Evaluation of Geosynthetics Reinforcement in Flexible Pavement Structures Using Accelerated Pavement Testing

Final Report
July 31, 2018

Authors:
Baoshan Huang, Ph.D., P.E.
The Edwin G. Burdette Professor
Department of Civil and Environmental Engineering,
The University of Tennessee

Hongren Gong, Ph.D.
Graduate Research Associate
Department of Civil and Environmental Engineering,
The University of Tennessee

Xiang Shu, Ph.D.
Research Assistant Professor
Department of Civil and Environmental Engineering,
The University of Tennessee

Sponsored by
The Tennessee Department of Transportation
Research Development and Technology Program
(Project#: RES 2013-30)

A Report From
Department of Civil and Environmental Engineering,
The University of Tennessee
Knoxville, TN 37996
Ph.: (865) 974-7713
Fax: (865) 974-2669

Table of Contents

List of Figures

List of Tables

Executive Summary

This project investigated the reinforcement performance of different types of geosynthetics placed at two locations of the aggregate base through a series of well-controlled accelerated pavement testing. To attain the target of accelerating the tests in a relatively short time period, a weak soil with a CBR value around 3 (%) was used to construct the subgrade of the pavement. A full-scale accelerated pavement testing facility was utilized to carried out all the accelerated tests, which has the ability to apply bidirectional load and a loading capacity higher than 9000 kips on each of the two wheels. A total of three rounds of tests were conducted to evaluate three different types of geosynthetics, which differed in their aperture shape, stiffness, and manufacturing mechanism. During the test of each round, the deformations at a certain interval of axle load passed were measured manually. The failure criterion of the testing was defined as reaching 1 inch of permanent deformation in the wheel path or reaching 100,000 axles, depending on whichever occurred first.

According to the accelerated pavement tests and the theoretical analyses carried out in the project. The following conclusions are reached:

- The utilization of geosynthetics to reinforce an unbounded aggregate base that rested on a weak subgrade was very efficient, while the effectiveness of the geosynthetical materials depended significantly on their aperture shape, stiffness, and manufacturing mechanism.
- Overall, in terms of the rutting performance, the lanes with geogrids installed at the bottom of the aggregate base performed the best, followed by the one with geogrids placed at the bottom of the aggregate base, and then the control that had no reinforcement in the base.
- Compared with the control lane, the permanent deformation of the lane with extruded biaxial geogrids placed in the middle of the aggregate base was reduced by 24%, and it was reduced by 37% for the lane had geogrids installed at the bottom of the base layer.
- Compared with the control lane, the rutting at the lane with woven biaxial geogrids installed at the bottom of the aggregate base was reduced by 13%, and it was reduced by 4% for the one with geogrids placed in the middle of the base layer.
- The construction quality is extremely critical to the success of the APT testing. During the construction process, great caution should be used in controlling the thickness of each of the layers, especially the thickness of the asphalt layer.
- The cost benefit analysis revealed that geogrids placed at the bottom of the aggregate base generated the highest overall benefit per unit cost. Compared with the control that had

no reinforcement, the extruded biaxial geogrids placed at the bottom of the base produced the highest overall benefit per unit cost and the highest rutting reduction per unit cost, followed by the triaxial geogrids placed at the same location if it had a similar thickness to its corresponding control section. The woven biaxial geogrids installed at the bottom of the base generated similar cost-benefit to the triaxial geogrids placed at the middle of the base. The woven biaxial geogrids that were placed in the middle of the base achieved only marginally higher benefit per unit cost than the corresponding control.

To optimize the using the geosynthetics as the base reinforcement material, it is recommended that in the future to include more materials combinations in the study, and thus to present a more comprehensive picture on the performance of geosynthetics as a reinforcement for the unbound granular base. Also, to ensure the success of APT testing, it would be worthwhile to pay more time and more attention to controlling the construction quality of the test sections, especially the thickness of each layer of the pavement.

Chapter 1 Introduction

1.1 Problem Statement

With the ever-increasing traffic volume and the ever-shrinking operational budget, maintain a well-functioning U. S. highway system is a great challenge facing the state department of transportation's (DOTs). Many states have been striving to explore alternatives to existing methods of designing, constructing, and rehabilitating flexible pavements. Use of geosynthetics reinforcement in base or subbase layers offers such an alternative. Many states have conducted studies to evaluate the improvements in performance of pavements reinforced with geosynthetics or geogrids in their bases or subbase layers. It is generally believed that use of geosynthetics reinforcement in base layers of pavement structure can extend the service life of flexible pavements and/or reduce the pavement's structural thickness.

Despite the many DOT studies on geosynthetics so far, there are still a lot of questions that need to be answered. Under what conditions can geosynthetics be mobilized to reinforce base or subbase layers? At what depths can the geosynthetics reinforcement be maximized? Unlike granular materials, geosynthetics have to be first mobilized (i.e., subjected to tensile forces) to exert their reinforcing effect on base layers. Without proper installation, geosynthetics may not be able to be mobilized, thus losing the reinforcement function. Similarly, if geosynthetics are installed relatively deep in the base layer, they may not be fully mobilized and thus their reinforcing benefits are not fully utilized. Accelerated pavement tests (APT) can simulate the stress and strain states of pavements in the field and thus can better mobilize the geosynthetics than small-size laboratory tests. This proposed research aims to use the accelerated pavement test pit at the University of Tennessee, Knoxville (UTK) to investigate under what circumstances the geosynthetics reinforcement can be mobilized in pavement base and how its reinforcing benefits can be maximized.

This proposed research may significantly benefit the economy of the State of Tennessee through use of geosynthetics reinforcement in flexible pavements:

(1) Offer alternative pavement design methods and technologies under special circumstances;

(2) Service life of pavements has the potential to be significantly extended;

(3) Pavement distresses will be reduced and pavement performance will be improved, resulting in improved public satisfaction through a better pavement condition;

(4) Structural thickness of pavement will be reduced, resulting in money-saving.

1.2 Project Objectives

The objectives of the proposed research are to:

(1) Determine the optimal location for geosynthetics reinforcement in pavement base layer using UTK test pit; and

(2) Compare the cost-effectiveness of geosynthetics-reinforced pavements with non-reinforced conventional flexible pavements.

Chapter 2 Literature Review

Nowadays, engineers are confronted with the pressure of maintaining and developing pavement infrastructure with limited budget. Due to the demonstrated benefits in reducing base course thickness, reducing permanent deformation, prolong pavement service life, geogrids have been applied extensively to pavement reinforcement in the last four decades. In order to investigate the mechanisms of and the optimal design approach of utilizing geosynthetics as base reinforcement materials, numerous agencies and universities have been motivated to conducted both laboratory and field research through full-scale or scale accelerated pavement testing.

2.1 Fundamental Basics of Geosynthetics

There exists numerous types of geosynthetics for pavement reinforcement. The most widely used one that has demonstrated effectiveness in improvement pavement performance was called geogrids (Webster, 1993; Koerner, 2012; Beranek, 2003; Al-Qadi et al., 1994; Perkins and Ismeik, 1997a; Perkins and Edens, 2003; Giroud and Han, 2004). The geogrids are defined as a geosynthetic material consisting of connected parallel sets of tensile ribs with apertures of sufficient size to allow strike-through of surrounding soil, or other geotechnical materials (Webster, 1993; Koerner, 2012). There are four major types of commercial geogrids, including extruded geogrids, woven geogrids, welded geogrids, and geogrid composites.

According to their configurations, there are two major types of geogrids used in base course reinforcement (Tang et al., 2008; Han et al., 2011; Beranek, 2003), which are the primary points of interest for the current project and research.

Uniaxial Geogrids extruded geogrids that are pre-tensioned in one direction are called uniaxial geogrids and are typically used in geotechnical engineering projects concerning reinforced earth and retaining walls.

Biaxial Geogrids Extruded geogrids that are pre-tensioned in two directions are referred to as biaxial geogrids and are typically used in pavement applications where the direction of principle stress is uncertain.

In general, the geogrids have traditionally been used in three different categories of application (Giroud and Noiray, 1981; Beranek, 2003; Han et al., 2011; Giroud and Han, 2004; Kwon et al., 2005; Kinney et al., 1998; Itani et al., 2016):

- Mechanical subgrade stabilization;

- Aggregate base reinforcement;
- Asphalt concrete overlay reinforcement.

Beranek (2003) and Perkins and Ismeik (1997b) reported that three fundamental reinforcement mechanisms have been identified involving the use of geogrids to reinforce pavement materials:

- Lateral restraint;
- Improved bearing capacity;
- Tensioned membrane effect.

A design approach for pavement reinforced with geogrids, which is similar to the method presented in the AASHTO 1996, was also presented in these studies (Beranek, 2003; Perkins and Ismeik, 1997b). They recommended that the **placement of the geogrids** should be dependent on the thickness of the aggregate base course, if thickness of aggregate layer ≤ 14 in. or (10 in.), place at the bottom, if the thickness of the aggregate layers is ≥ 14 or 10, place it in the middle of the aggregate course (Beranek, 2003).

2.2 Application of Geosynthetics in Pavement

2.2.1 Filed Tests

Fannin and Sigurdsson (1996) reported a field a study on an unpaved road on a soft subgrade. The performance of five sections were observed, one unpaved section as control, three section with geotextiles, and one with geogrid. Figure 2.1a showed a diagram of the test section in the study. The test section each has a width of 4.5m and length of 16m. The index of the subgrade soil is **OH** according to the Unified Soil Classification System (USCS); its undrained shear is about 45 kPa. A series of base course thicknesses were included in the study, which varied from 0.25m, 0.3m, 0.35m, 0.4m, and 0.5m.

Figure 2.1b is the load configuration used in the study, the pass speed of the vehicle is 7 km/h. Greatest performance is observed on pavement with thinner base course, as the thickness of base course increases the benefits diminishes. Geotextiles excels geogrid in thinner pavement due to the tensioned-membrane effect existed in the geotextiles, while geogrid outperforms the geotextiles on thicker pavement. Due to the inability to include the effect of initial compaction of the granular base, the analytical method generally overestimates the rut depth.

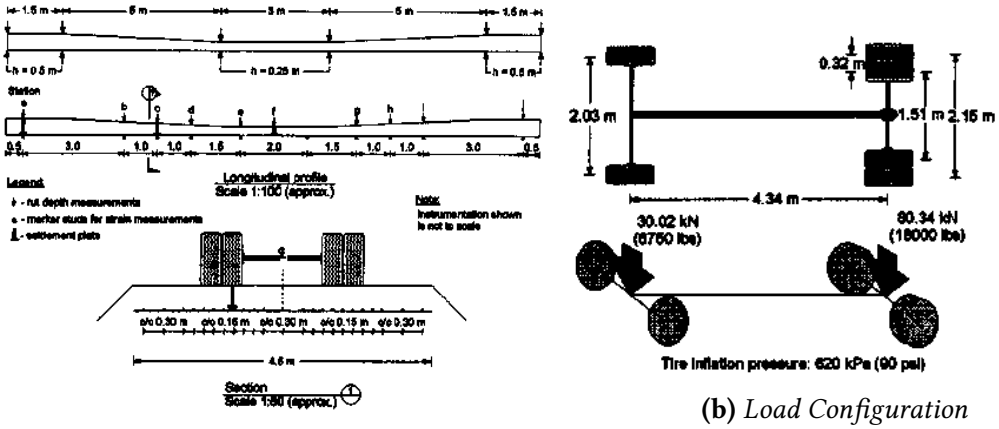

(a) *Test Section Layout*

(b) *Load Configuration*

Figure 2.1: *Layout of the Test Section and Load Configuration*

It is also observed that reinforcement plays more important role in thicker granular base course, in which the mobilization of the tensile strength is subject to influence of the interlock of the aggregate and the stiffness of the geogrid itself (Fannin and Sigurdsson, 1996).

There are other large scale field tests used to evaluate the performance of geosynthetics reinforced soil or subgrade not restricted to pavement construction, such as Kennepohl et al. (1985), Perkins (2002), and Demir et al. (2013), and among others.

2.2.2 Full Scale and Scaled Laboratory Test

Leng and Gabr (2002) used a scaled box to investigate the influence of two types of geogrids on the performance of pavements on soft subgrade soil. Figure 2.2 showed the schematic of the test box used in the study. The subgrade soil in the study was composed of a mixture of 85% Lillington Sand and 15% Kaolinite, its CBR is about 3-4. Surface deformation, vertical stresses at the interface and the center of the loading plate were monitored. Pressure cells were placed at four location at the interface, which are 0mm, 152mm, 305mm, and 457mm from the center of the loading plate.

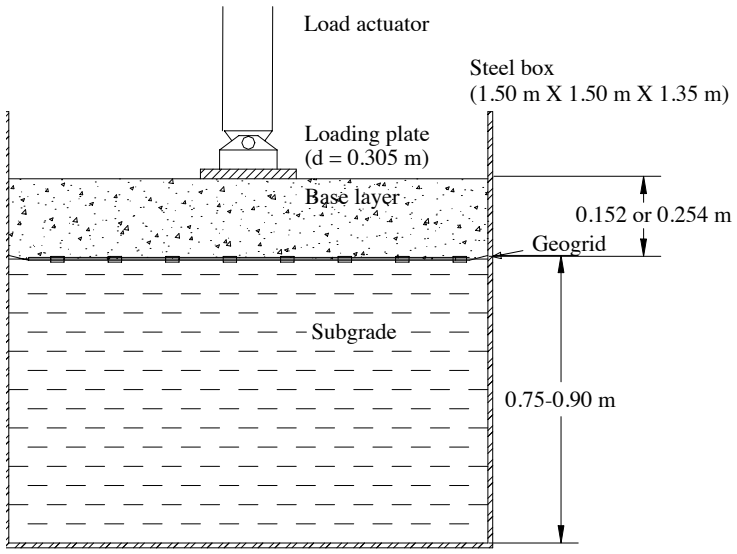

Figure 2.2: *Schematic of the Test Box (Leng and Gabr, 2002)*

It was found in the study that inclusion of geogrids decreases the maximum stress at the center of the loading plate and produces a more uniform stress distribution on the top of subgrade. Reduced vertical deformation of tests included geogrids demonstrated that the vertical stress on the subgrade decreased and thus is the vertical deformation of the subgrade. The inclusion of geogrids improved the shear resistance at the base-subgrade interface due to interlocking and lateral moving restraint of the aggregates.

Al-Qadi et al. (1994) presented experimental and analytical investigations on pavement with or without geosynthetics. Four test sections were included, three of two were reinforced with geotextile and one with geogrid, one without geosynthetics was served as control. The test sections were built upon a silty sand subgrade. A computer-controlled pneumatic system that is able to deliver a load of 55 kPa and a frequency of 0.5Hz through a rigid plate with a diameter of 30cm was used. The tests were conducted in a test pit with a size of 3.1m× 1.8m× 2.1m, Figure 2.3 showed a schematic of the test pit.

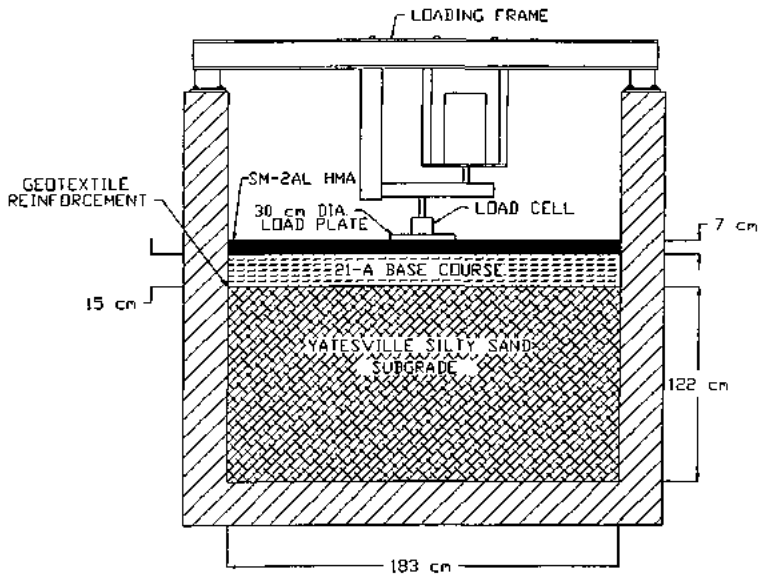

Figure 2.3: *Test Pit Schematic (7cm AC+15cm Stone+122 cm Soil (with a CBR of 4))*

It was noted in the study that the geosynthetics is able to distribute a concentrated load over a larger area to the subgrade, and hence improve the strength of pavement built upon weak soil. Another mechanism of the reinforcement of geosynthetics is the reduction in the plastic deformation.

In order to validate the mechanism of reinforcement of the geogrid and quantifying the effectiveness of geogrids, Al-Qadi et al. (2008) conducted a full scale accerated testing. In total, three cells of flexible pavement each with three test sections were constructed. The traffic loading was applied by a dual-tire with 44kN of load and a moving speed of 8 km/h. Load related censors were installed along the pavement centerline to monitor the dynamic response under the tire. Figure 2.1 showed the pavement structure of the test sections in the study. After trafficked, the test sections were trenched to examine the performance. It was observed in the study that geogrid is effective in confining the horizontal shear deformation of the aggregate layer. For a thicker base course, the optimal location to install the geogrid is the upper third of the layer, while the optimal location is at the base-subgrade interface for its thin counterpart.

Table 2.1: *Structure of the Test Section*

Pavement Test Cell Name	Section	Base Thickness (mm)	HMA Thickness (mm)	Length (m)	Geogrid (GG) Type and Location
A	A-1	203	76	6.1	GG1 @ subgrade–base interface
	A-2			6.1	GG2 @ subgrade–base interface
	A-3			6.1	Control
B/C	B-1	305	76	6.1	Control
	B-2			7.6	GG2 @ subgrade–base interface
	C-1		127	7.6	Control
D	D-1	457	76	6.1	GG2 @ 152 mm from top base
	D-2			6.1	GG2 @ subgrade–base interface & GG2 @ 152 mm from top base
	D-3			6.1	Control

Tang et al. (2008) reported that results from direct shear and pull-out tests are the most commonly used parameters depicting the soil–geogrid interaction characteristics. A scaled accelerated pavement tester (APT) was used in the study to evaluate the performance of geosynthetics reinforced flexible pavement. It is noted that the advantages of APT are the ability to conduct performance tests at relatively low costs over a short time period, and the ability to control the loading and environmental conditions. In their study, **biaxial** geogrid products were used.

The subgrade soil in the study is silty sand, which has an index of SW-SM as per ASTM classification system, or A-2-4 as per AASHTO. The base course is composed of dense-graded crushed stone, with 3.9% optimum moisture content, and maximum dry density of 2329 kg/m^3. A 27 kN/m^2 vertical pressure was applied for direct shear test. Figure 2.4 showed a schematic of the test setup in the study, as shown in Figure 2.4, the machine direction is parallel to the pull-out direction. A 6.9 kN/m^2 of normal pressure was also applied with a the pulling rate of 0.1 mm/min.

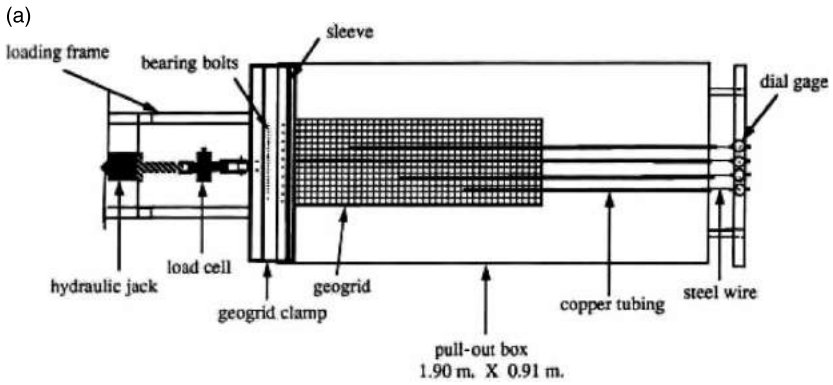

Figure 2.4: *Pull-out Test Setting-Up (after Tang et al. (2008))*

Fannin and Raju (1993) reported a study on pullout tests conducted on geosynthetic embedding in a dense, coarse sand sample. The tests in this study is displacement controlled with varied vertical pressure. Both geomembrane and geogrids are included.

Raju and Fannin (1998) reported a study using both displacement- and load-controlled pullout test with varied vertical pressure. Two geomembranes and three types of geogrids. The loading rate of load-controlled and displacement-controlled tests are 0.25 kN/(m $\cdot$ min^{-1}) and 0.5 mm/min.

- Pullout resistance is established with respect to a bond coefficient or interaction factor, which describes the interface bond mobilized between the geosynthetic and the backfill soil.
- The maximum pullout resistance in cyclic loading is greater than that observed in monotonic loading.
- Geosynthetics are thermo-viscoelastoplastic materials, which means their behaviour is both temperature and stress dependent.
- According to their data in the study, it is observed by the authors that pullout resistance may be independent of load frequency.

- The displacement to mobilize maximum pullout resistance of a grid is larger at higher values of confining stress.

Wu et al. (2015) investigated the performance of inclusion of geosynthetics in unbound granular base courses through loaded wheel tester (LWT). Two unbounded materials from Kansas were included, a type of river sand and a type of gravel. Four types of geogrids were investigated. Two types of tests were conducted, the LWT and cyclic plate loading tests. Before the tests were carried out, the unbound granular materials were compacted manually in the aluminum box with a size of **600mm** $\times$ **400mm** $\times$ **100mm**. To achieve a uniform compaction, the materials were divided into three layers. The rut depth was used as an indicator of the performance. In total, 16,000 cycles at a frequency of 2Hz were conducted for the LWT test. For different base materials, the magnitudes of the tests differ, 88N wheel and 138 kPa rubber hose pressure for the river sand, while 353N and 552kPa rubber hose pressure was used for the gravel.

It was observed in the study that LWT is a effective tool in assessing the performance base courses reinforced with geogrids. Meanwhile, LWT was demonstrated to be able to identify the optimal aperture size of a specific aggregates. It was also reported that the performance of a geogrid varies with the gradation of the aggregate being stabilized. Similar study were also reported by Han et al. (2011) and Zhang (2007).

2.3 Accelerated Pavement Testing

2.3.1 Palomino et al. (2010)

Palomino et al. (2010) used a one-third scale mobile load simulator to examine the effect of geogrids on the performance of flexible pavement. The load simulator is able to generate a wheel load of 2.7 kN and a contact pressure of 690 kPa (100 psi), which is equivalent to one-ninth of the standard full-scale single tire. The dimension of the test pit used in the study is 366cm (144in) in length, 206 cm (81in) in width, and 127 cm (50 in) in depth. The pavement structure of their test section is 4cm asphalt concrete, 10-cm aggregate base course, and 113-cm of soil subgrade. Three types of soil were included in their study, one with a label of CL (CBR 3) and another with a label of ML (CRB 1.5) per ASTM soil classification standard, or A-4(5) and A-4(4) per AASHTO standard.

In this study, three types of biaxial geogrids were used. To determine the physical and mechanical properties of the geogrids, the test procedure proposed by a ASTM standard were followed. The tensile strength at 2%, 5% strain and the ultimate strength were measured as per ASTM D 6637. The flexural rigidity as per ASTM D-1388 was tested as well. Because the behavior of geogrids installed in pavement will not experience as large strain as tested, a wide width test using a small displacement (less than 1% strain) was performed in both the machine and cross-machine direction of the geogrid, they found the tensile strengths in this two directions are significantly different. In order to characterize the aggregate-geogrid interface interaction, pullout test as per ASTM D-6796 was carried out in the machine direction of the geogrid. In addition, direct shear tests as per ASTM D-3080, which is commonly used to measure the friction angle and adhesion at the interface of soil and aggregate base, were conducted.

In this study, a total of five types of instruments were installed and series of tests were conducted to monitoring the performance of the test sections. To monitor the deflection at the surface of the subgrade, a array of linear variable differential transformers (LVDT) were installed. A comparison on LVDT from different manufactures were conducted, the one from Macro Sensors (GHSE-750-1000) were chosen for their tests. As a backup for measuring the deformation in the subgrade, potentiometers were customized and installed at the top of the subgrade. The potentiometers are useful in obtainin gthe elastic and permanent strain of the subgrade. Moreover, to obtained the vertical stress at the top of the subgrade, earth pressure cells were used to measure the dynamic and static deformation at the top of the subgrade. In their study, the hydraulic-type earth pressure cell from Geokon (Geokon 3500) were chosen. The strain in the geogrids is a important indicator of the mobilization status of the material. In their study, a foil type strain gauge from Omega Engineering (KFG-5-120-C1-11L3M3R). The strain gauges were attached to both bottom and top sides of the rib to consider the influence of bending. The location of the geogrids ribs had strain gauges installed was around the wheelpath of the load simulator. These instruments were all calibrated before put into testing. To monitor the temperature, thermocouples were installed in the middle of the asphalt layer. Apart from the instruments used, a lightweight deflectometer (Carl Bro^{TM} PRIMA 100) was used to determine the in-situ pavement layer modulus.

2.3.2 Al-Qadi et al. (2011)

Al-Qadi et al. (2011) uses full-scale accelerated testing facility to investigate the effectiveness of geogrids on the performance of low-volume flexible pavements. In this study, low-volume flexible pavement sections were constructed on a relatively weak subgrade which has a California Bearing Ratio (CBR) of %4, and a total of 170 sensors were used, namely, 18 pressure cells, 49 LVDTs, 12 strain gauges, 82 thermocouples, 10 TDRs and 2 peizometers. These sensors were used for the purpose of obtaining the stress, strain, deflection, moisture, temperature and pore water pressure. The Accelerated Transportation Loading ASsembly (ATLAS) were utilized to applied the accelerated dual-tire load, which operates at a speed of 8 km/h , a tire pressure of 690 kPa, and a load of 40 kN. However, five different load levels at 26, 35, 44, 53, 62 kN, and two speeds (8 and 16 km/h). In addition, three different tire inflation were also included: 550, 690, and 750 kPa to test the responses of the sensors before starting the pavement performance test. For their study, the failure of the pavement was defined by a 50-mm surface rutting. To find the optimal placement of the geogrids, the geogrids were installed two different locations, one at the base-subgrade interface, and another at top one-third of the base course. After the completion of the testing, deep trench was cut in the area showed significant distress to quantity layer thickness, the location and condition of the interface, and the location of the geogrids.

2.3.3 Webster et al. (1998)

Webster (1993) from U.S. Army Corps of Engineers performed a study for base-reinforced flexible pavement. A total of 2 lanes each with 4 test items were constructed. Instrumentation of the test section consisted of four sets of Multi-Depth Deflectometer (MDD) modules installed in test items I and 2 of traffic lanes and 2. Figure 19 shows a layout of the MDD test locations. The

MDD is an LVDT deflection measuring device which is retrofitted into the pavement layers. In this study, the failure of a test item was defined as **one inch of rutting**. However, traffic was usually continued on a test item until **three inches** of rutting occurred or until each item in the traffic lane reached one inch of rutting. As reported in their study, the rut depth included both the permanent deformation and upheaval within the traffic lane. Test traffic was applied through a 30-kip single-wheel-assembly test cart. The tire load was 30,000 lb with a contact area of 442 sq in. The measured tire contact width was 17.25 in. Two types subgrade soils were tested, one with a design CBR 3 to represent a weak support, an the other with a design CBR 8 to represent a strong support. Nondestructive tests were performed on each traffic lane with the Dynatest model 8000 falling weight deflectometer (FWD), and the impulse stiffness modulus was obtained this test.

2.4 Theoretical Analyses

2.4.1 Finite Element Methods

Kwon et al. (2008) reported that an increase in horizontal confinement resulted in significant increases in the moduli of the base and subgrade layers in the vicinity of the geogrid reinforcement. These residual stresses provided both confinement and particle interlock. According to Uzan (1985), these horizontal residual stresses were measured to be as high as 14-35 kPa in cohesiveness granular materials. Barksdale and Alba (1993) also reported 21 kPa horizontal residual stresses in the 305mm thick granular base obtained from field measurements due to the application of an 8.9 MN (10 ton) vibratory compactor.

It was observed that,

- Relatively high values of reinforcement properties and improved interface analysis techniques were needed to best demonstrate the experimentally observed geogrid benefits.
- Residual compressive strain built in the aggregate base could help to explain the benefits of geogrid.
- Small geogrid movement could lead to permanent residual stresses locked-in around the geogrid.
- The area of locked-in permanent residual stresses were restricted to approximately 10 cm above and below the geogrid.
- Two interface: geogrid-base and geogrid-subgrade, typically the shear stresses develop at the base-geogrid interface.
- Stiffening effect due to inclusion of geogrid cannot be properly simulated by assigning constant residual stresses throughout the entire base layer.

  Perkins and Edens (2002) proposed a distress model for geosynthetics reinforced pavements using the FEM. They reported that the reinforcement of the geosynthetics come from confinement of the unbound aggregate layer, resulting in a lower vertical stress and improved

load spreading on the subgrade layer, and reduced **shear stress on and shear strain** in the top of the subgrade and reduced vertical strain in the aggregate and subgrade layers. The geosynthetic was modeled by **four-node membrane elements** that have the property of containing tensile load carrying capacity, but have no resistance in bending or compression. Increase in bulk stress, in return leads to an increase in **stiffness** of the aggregate layer.

- Traffic benefit ratio (TBR) and base course reduction Ratio (BCR) were used to described the benefits achieved through the inclusion of geogrids.
- It is noted in the study that the primary reason for lack of usage were the absence of a suitable design method for defining reinforcement benefit and the corresponding inability to define cost-benefit for reinforced pavement systems.
- It is expected that a **decrease of the apparent tensile modulus** results in greater lateral movement of the base aggregate and greater **shear strain** induced in the top of the subgrade.
- Reduction of the shear modulus results in greater movement of the geosynthetic in **radial directions** off the principal axes of the material and a corresponding reduction in reinforce- ment benefit.
- **Eight-node hexagonal solid elements** were used for all material layers.

Kwon et al. (2009) developed a finite element model to analyze geogrid reinforced flexible pavement. To obtain results in good agreement with field tests, three major factors were included in the FEM model, 1) the nonlinear, stress-dependent behavior of unbound granular materials such as the aggregate base and subgrade soil were considered; 2) the anisotropic behavior of the aggregate base; 3) residual stress locked in geogrid after compaction and preloading. The results generated via FEM were compared with those measured from full scale field test loaded by the Advanced Transportation Loading AsSembly (ATLAS). After trafficked, trenches were excavated in the test sections to examine the performance.

In total, nine test sections were included to investigate two types of geogrid and different base course thickness which range from 20.3cm (8 in) to 45.7cm (18 in). Figure 2.5 showed a schematic of the test section and the location of measured response. In this field study, the subgrade soil has a index of ML-CL per USCS, and its average plasticity index is 5. The CBR of the subgrade is about 4.

It was observed in the study that inclusion of geogrid significantly enhances the pavement structure. At the interface of unreinforced section, noticeable intermixing between the subgrade soil and the aggregate course were seen. The developed FE model yields results in good agreement with the measurements. The residual stress locked in or around the geogrid is dependent on the aggregate size and the type of geogrid used.

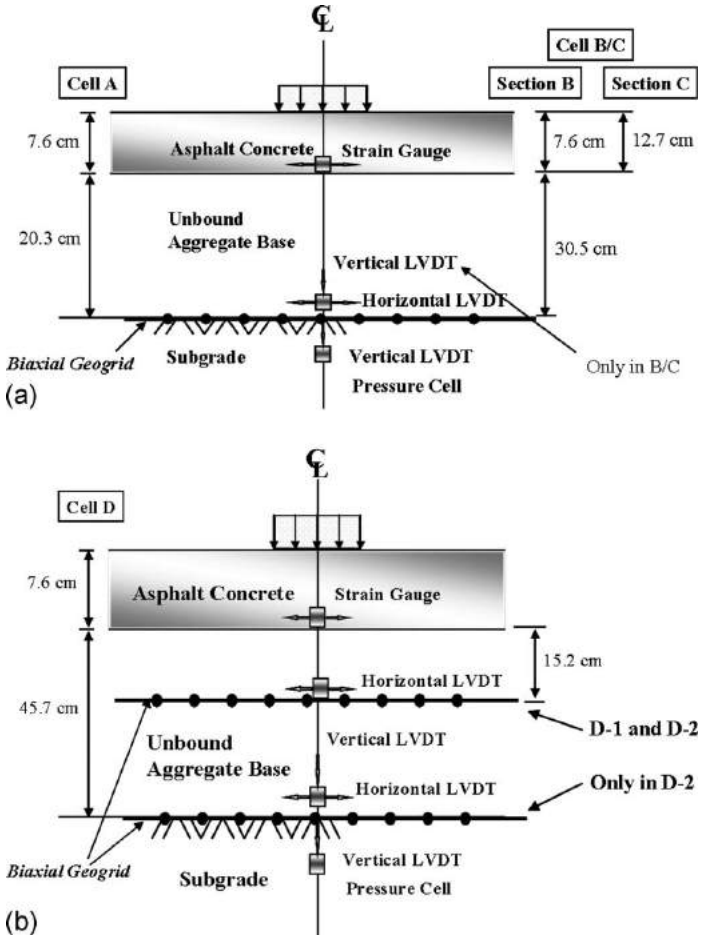

Figure 2.5: *Locations of Measured Responses*

2.4.2 Discrete Element Analyses

The discrete element method (DEM) was proposed by Cundall and Strack (1979), which has been widely used to simulate the interactions between particles in a micro scale. The DEM is capable of capturing the evolution of the inter-particle contact forces and displacement of particles, which are not able to implement through laboratory test or continuum mechanics such as finite element methods (FEM). In terms of mathematical formulation, the continuum problems involves the constitutive law, balance principles, boundary condition and/or initial conditions. However, as to the problems of discontinua (discontinuum), its mathematical formulation involves the interaction law between particles and balance principles (Munjiza, 2004).

McDowell et al. (2006) reported a study using discrete element method through PFD3D. In the study, the responses of the triaxial test were simulated to serve as a benchmark. In order to generate realistic triaxial shear strength of triaxial test, several shapes of clumps were simulated via overlapped spheres rather than single spheres. It was found that the responses from the **eight-ball cubic clump** model agrees well the laboratory triaxial test results. The eight-ball cubic clump model for aggregate along with geogrid modelled with spherical particles bonded

together by contact and parallel bonds were used to simulate the pullout tests. The dimension of box in the DEM model for pullout test is 18cm×18cm×70cm(depth), as shown in Figure 2.6. Within this model, 40,000 balls were used to form the geogrid, while about 50,000 balls were used to produce a well graded aggregates with a size range from 20mm to 180mm.

The effect of the aperture size of the geogrid with respect to the size of aggregates is investigated through DEM, it was found that *a ratio of aperture size to the aggregate size about* **1.4** generates the maximum interlock and peak resistance. It was observed in the study that DEM is able to generate realistic predictions of the peak pull-out resistance and the displacement necessary to mobilise the peak pull-out force. However, at small displacements the pullout resistance is less than the one measured via experiments.

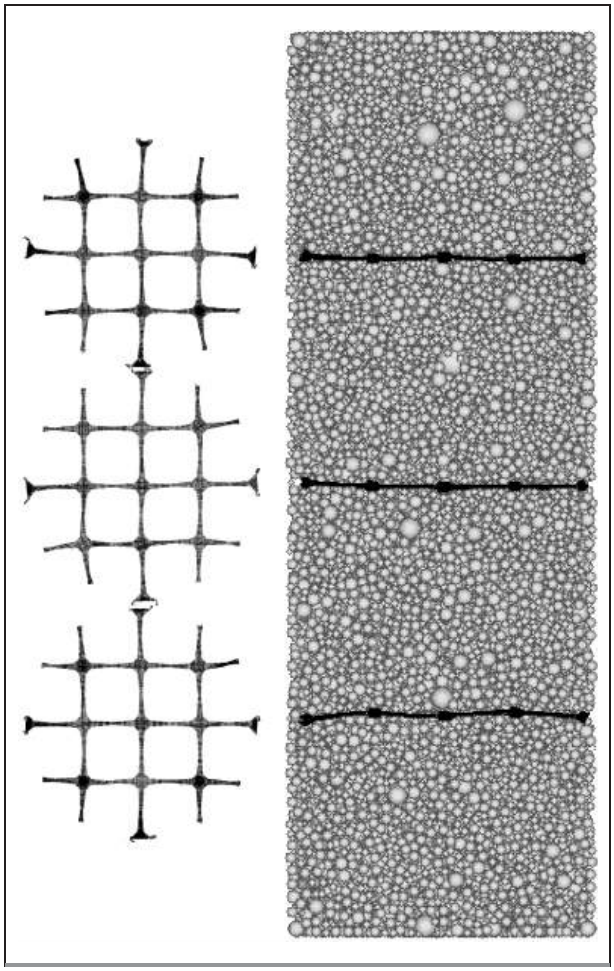

Figure 2.6: *Deformed Triaxial Sample with Three Geogrids Layers (McDowell et al., 2006)*

2.5 Design Approaches

Perkins et al. (2009) presented a Mechanistic-Empirical based on the original MEPDG model. New components for the reinforcement are introduced and include,

- Structural elements for the reinforcement
- A material model for the reinforcement;
- A model for reinforcement–aggregate shear interaction;
- Additional response modelling steps that account for the influence of the reinforcement on lateral confinement of the base aggregate during construction and subsequent traffic loading;
- A modified permanent deformation damage model used for aggregate within the influence zone of the reinforcement.

Perkins and Edens (2003) developed a Mechanistic-Empirical design approach for flexible pavement reinforced with geosynthetics. A parametric study for the M-E design method was presented. In the design model, structure number (SN) from the AASHTO1993 is related to the traffic benefit ratio (TBR), which is defined as the increase in service life of geosynthetics reinforced to unreinforced pavement. The parameters included are thickness of the structural section, strength or stiffness of the subgrade, tensile modulus of the geosynthetics and other parameters related to the geosynthetics. The model is then calibrated by the measurements from large-scale reinforced pavement sections. It was observed in the study that the M-E model is capable of capturing the sensitivity of parameters. However, the prediction yields from the model is conservative compared to the test results. Also, the model assumes the placement of the geosynthetics is located at the base-subgrade interface, which limits its applicability. In order to generate more realistic prediction, more accurate materials model for asphalt concrete, unbounded aggregate base, subgrade soils, and the loading condition are needed.

Perkins and Ismeik (1997a) reviewed more than thirteen researches concerning inclusion of geosynthetics in flexible pavement or using geosynthetics to reinforce unbound granular materials all around the world.

- The use of geosynthetics could date back to the late 1970s, when its mainly used to reinforce unpaved road. Its major functions are filtration, separation, and drainage.
- Studies involving geosynthetic reinforcement of roadways have identified three potential reinforcement functions: lateral restraint, increased bearing capacity, and tensioned membrane.
- Geotextile outruns the geogrid in solving separation and filtration problems.
- It is critical to considering data correction for deformation after the first 25 cycles.
- These results tend to suggest that the differences in layer properties between the sections was greater than that which could be accounted for by the parameters used to define these properties and/or the analysis technique used to compare sections was not able to account for the property differences observed.
- Machine direction is the one that the geosynthetics rolls.

Perkins et al. (2009) proposed a design Mechanistic-Empirical model base on the Mechanistic-Empirical Methods developed in the NCHRP 1-37A project. The new components for the model including:

- Structural elements for the reinforcement;
- Material model for the reinforcement;
- Model for reinforcement-aggregate shear interaction.

Based on the review of extensive existing studies, they also observed that,

- Even though it is well accepted that geosynthetics help to enhance the pavement structure and prolong pavement life, the absence of well recognized design methods limited its application.
- Conventional empirical method is not adequate for pavement covered with high quality asphalt mixture, which is developed based on the experience of unpaved low traffic volume roads.
- Central to mechanistic-empirical design methods are mechanistic pavement response models and empirical damage models that relate pavement response to pavement performance.
- Damage estimated or benefit value estimated by empirical model is too conservative.
- Reinforcement was modeled as isotropic linear elastic. Due to its direction-dependent mechanical properties, a method based on a work-energy principal was used to convert orthotropic into isotropic constant.
- Coulomb friction model was used to model the reinforcement-aggregate interaction.
- Experimental data and theoretical considerations with simplifying approximations have been used to show the equality between *the ratio of the permanent to resilient strain in the reinforcement* to the ratio of residual to transient shear stress on the reinforcement-aggregate interface. $\frac{\varepsilon_p}{\varepsilon_v} = \varepsilon_{o-r} e^{-\left(\frac{\rho}{N}\right)}$ (Tseng and Lytton (1989)).

$$\tau_r = \tau_t \frac{\varepsilon_p}{\varepsilon_r} \tag{2.1}$$

$$\log(\frac{\varepsilon_p}{\varepsilon_r}) = \log(A) + B \log\left(\frac{N}{N_{25mm}}\right) \tag{2.2}$$

Where :

$\tau_r =$ residual shear stress on interface

$\tau_t =$ transient shear stress on interface

$\varepsilon_p =$ permanent strain in the reinforcement

$\varepsilon_r =$ resilient strain in the reinforcement

$N/N_{25\ mm} =$ ratio of actual traffic passes to passes necessary for 25 mm permanent deformation.

$A,\ B =$ geosynthetics strain growth parameter

- Conventional finite element response models consisted of involving the *direct inclusion of structural elements for reinforcement sheet* and contact surfaces between the reinforcement and surrounding materials.
- A response model modules have been developed to yield an increase in aggregate confinement during compaction and traffic loading.
- Geosynthetics reinforcement results from confinement and restraint of the aggregate, no direct measurement of the residual horizontal stress has been reported. Because it is difficult to measure the residual shear stress directly, the modeling methods used are partially physically artificial but necessary given the limitations of the material models used.
- To model the restraining effect of the geosynthetics to the aggregate during compaction, a procedure was developed involves assigning thermal contractive properties to the reinforcement sheet and creating shrinkage of the material by applying a temperature decrease. Cyclic pullout tests described by Cuelho and Perkins (2005) and Moraci and Cardile (2012) were performed to evaluate the optimum values of E_{slip} and μ for the interaction models of different geosynthetic materials. These new parameters should be applied only in cases where the mobilized friction angle of 30° is exceeded, since a reduction in permanent deformation of reinforced aggregate base materials were observed only for aggregates with friction angles greater than this.

Kwon and Tutumluer (2009) reported that the main mechanism of geogrids reinforce unbound aggregate base and subbase layers of flexible pavement is the geogrid aggregate interlock.

- As paving material costs increase, thickness reduction and cost savings using geosynthetics become more attractive alternative solutions for many roadway projects.
- The geosynthetic reinforcement is not included in the current version of MEPDG, due to the fact that no sufficient evidence demonstrated its inclusion provides benefits through proper mechanistic response and field-validated performance models.
- Within the context of mechanistic(M)-empirical(E) pavement design, there should be a response concerning the geogrids, which should be identified through a realistic and accurate geogrid base reinforcing mechanism for lowering such a critical pavement response, namely, the procedures of M-E $\Rightarrow$ Critical Response $\Rightarrow$ Geogrids Benefits $\Rightarrow$ Pavement Performance.
- To implement the geogrids reinforced aggregate base in the M-E pavement design, it is apparent that the a critical issue is to incorporate the effect of the enhanced stiffness into the mechanical analysis, and to consider how to maintain the gained stiffness through the inclusion of geogrids.
- The three primary mechanisms are; a) lateral restraint of aggregate particles; b) improved overall bearing capacity of the subgrade; and c) the tensioned membrane effect the mobilized geogrids
- The relative size of the aggregate particles and there gradation compared with the grid aperture had an influence on the size of the rupture zone.

- Commonly used linear elastic layered solutions are limited in demonstrating geogrid benefit because in the linear elastic analysis, modulus of the base or subgrade is a constant but not a function of the stress state.
- The weakest part of the pavement structure is the layer interface of the aggregate base course and the subgrade. The design strength of the aggregate base cannot be achieved due to the punching down of the aggregate into the subgrade soil.
- Conventional FWD backcalculation procedure is unable to predict realistic results due to using elastic layer system.
- The DCP was used to estimate thickness and in-situ bearing capacities of base and subgrade materials.

2.6 Summary

This part reviewed many studies on the inclusion of geosynthetics as reinforcement for the unbounded aggregate base. The studies reviewed could be divided into four major categories: 1) laboratory testing; 2) theoretical analysis using finite element method (FEM) or discrete element method (DEM); 3) Empirical and Mechanistic-Empirical design methods for flexible pavement reinforced by geosynthetics; 4) approaches for pavement design including geosynthetics.

In general, there exists three mechanisms for explaining the reinforcement of the geosynthetics included in the pavement, including the lateral restraint of the aggregates, enhanced bearing capacity caused by stiffness enhancing in the vicinity of the geosynthetics, more evenly distributed load on the subgrade as a result of the tensioned membrane effects. In addition, many studies also investigated the benefits of inclusion of geosynthetics in low traffic volume pavements with thin pavement structure. To identify and quantify those benefits, field observations were designed and laboratory testing method such as scaled and full scale accelerated pavement testing, small scale pull-out test, loaded wheel tester (LWT), along with numerical simulation such as finite element analysis and discrete element analysis.

Although an extensive amount of studies have been conducted, which based either on laboratory testing or numerical simulations, on using geosynthetics as pavement reinforcement materials, many critical problems are still left unsolved. Issues need to be addressed including the optimum placements of geogrids with varied aperture shapes, different manufacturing mechanisms and physical properties such as rib stiffness, as well as the geosynthetic products that match best with unbounded aggregate materials of varied gradations.

Chapter 3 Materials Testing and Pit Boundary Effects Analysis

3.1 Soil Engineering Properties Tests

In total, six soil samples were provided by TDOT for testing. Particle size distribution tests were conducted for all six samples. Then the soil samples were classified by AASHTO or ASTM soil classification system. In addition, three soil samples were tested for their liquid limits and plasticity limits. The names of the soil samples were used as it labeled when provided for testing, which are top#1 soil, top#3 soil, clay#2 soil, Conveyor-Belt, Pit, and Non-Vulcan.

The AASHTO Soil Classification System was developed by the American Association of State Highway and Transportation Officials (AASHTO), and is used as a guide for the classification of soils and soil-aggregate mixtures for highway construction purposes. The classification system was first developed by Hogentogler and Terzaghi in 1929, but has been revised several times since.

3.1.1 Top#1 Soil

Table 3.1 gives the size distribution of the Top#1 soil. Figure 3.1 indicates the size distribution curve for this soil. As indicated, there are 87.8% of particles passing the #4 sieve. The classification of this soil as per the ASTM and AASHTO standards are given in Table 3.4. As given in Table 3.4, this soil has an index of ML as per the ASTM standard, and it is a sandy silt (A-1-b) as per the AASHTO, which is an excellent soil as subgrade. The purpose of this test is to identify soft soil that meets the accelerated testing purpose of the project, hence, this soil is not a good candidate for construction the test pit.

3.1.2 Top# 3 Soil

Table 3.2 gives the size distribution of the Top#1 soil. Figure 3.2 indicates the size distribution curve for this soil. As indicated, there are 75.6% of particles passing the #4 sieve. The classifications of this soil as per the ASTM and AASHTO standards are given in Table 3.4. As given in Table 3.4, this soil has an index of CL-ML as per the ASTM standard, and it is a sandy silt (A-1-a) as per the AASHTO, which is also an excellent soil as subgrade. Hence, this soil is also not appropriate for the test section.

Table 3.1: *Particle size distribution for Top#1 soil*

Sieve Number	Sieve Size, mm	Retained, g	Passing,%
1”	25	0	100
3/4”	19	25.6	97.6
1/2”	12.7	12.3	96.4
3/8”	9.51	11.5	95.3
1/4”	6.35	32.1	92.2
#4	4.76	47	87.8
#8	2.38	177.5	70.9
#10	2	55.9	65.6
#16	1.19	181.5	48.3
#20	0.841	104.6	38.4
#30	0.595	74.8	31.2
#40	0.42	58.6	25.7
#50	0.297	44.4	21.4
#100	0.149	72.5	14.5
#200	0.075	33.9	11.3
<#200	<0.075	119	
Total		1051.2	

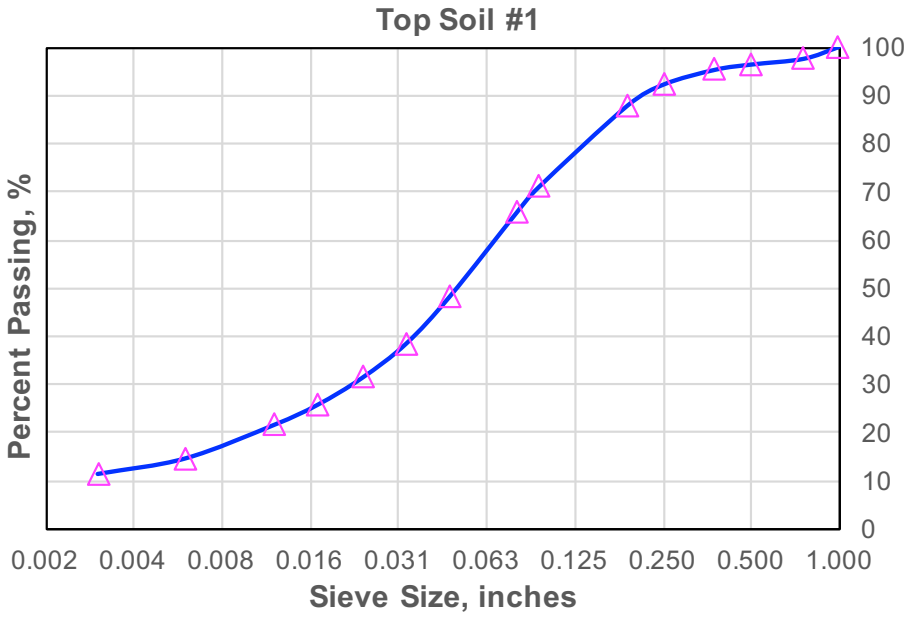

Figure 3.1: *Size distribution curve for Top soil# 1*

Table 3.2: *Size distribution for Top Soil# 3*

Sieve Number	Sieve Size, mm	Retained, g	Passing,%
1”	25	20.8	99.3
3/4”	19	9.3	99
1/2”	12.7	93.3	96
3/8”	9.51	122.5	92.1
1/4”	6.35	268	83.5
#4	4.76	244.8	75.6
#8	2.38	974.5	44.3
#10	2	207.6	37.6
#16	1.19	411.1	24.4
#20	0.841	200.5	17.9
#30	0.595	143.5	13.3
#40	0.42	101.9	10
#50	0.297	77.4	7.6
#100	0.149	105.4	4.2
#200	0.075	45.4	2.7
<#200	<0.075	84.3	
Total		3110.3	

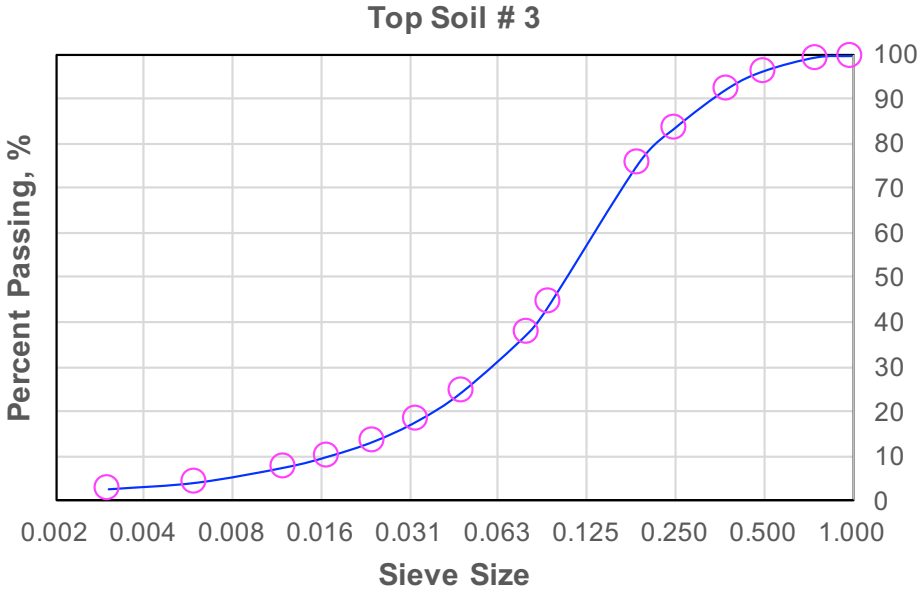

Figure 3.2: *Size distribution curve for Top Soil# 3*

3.1.3 Clay Soil # 2

Table 3.3: *Size distribution for clay soil #2*

Sieve Number	Sieve Size, mm	Retained, g	Passing,%
1”	25	0	100
3/4”	19	7.5	99.5
1/2”	12.7	1.7	99.4
3/8”	9.51	17.6	98.2
1/4”	6.35	54.4	94.5
#4	4.76	56	90.8
#8	2.38	359.3	66.6
#10	2	90.4	60.5
#16	1.19	197.8	47.2
#20	0.841	121.4	39
#30	0.595	0	39
#40	0.42	198	25.7
#50	0.297	68.8	21.1
#100	0.149	103.4	14.1
#200	0.075	71.4	9.3
<#200	<0.075	138.1	
Total		1485.8	

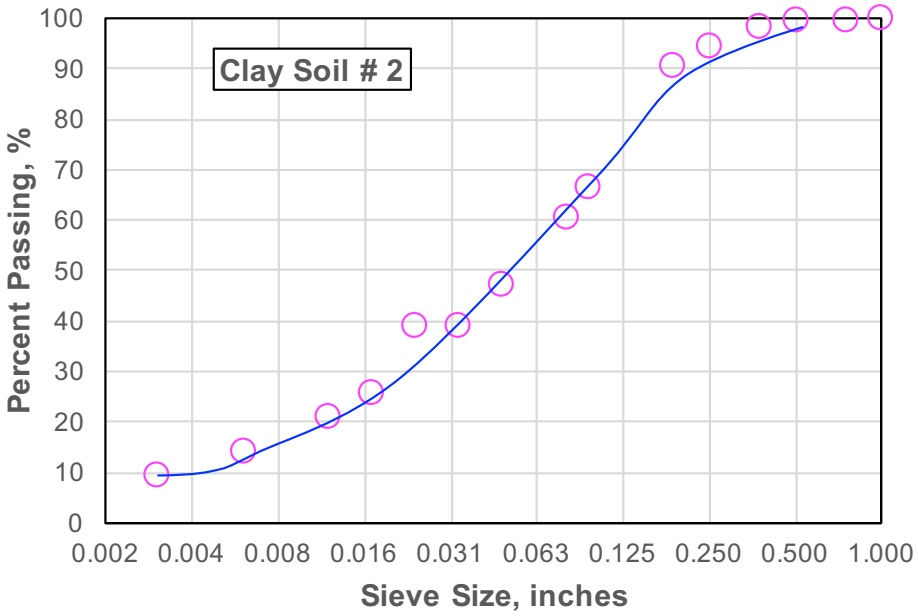

Figure 3.3: *Size distribution curve for Clay soil#2*

According to the AASHTO soil classification, and the particle distribution for the three soil

Table 3.4: *Summarization of soil test results*

Soil Name	LL, %	PL, %	PI, %	Classification
Top Soil #1	23.7	20.6	3.1	ASTM: ML, Sandy silt AASHTO: A-1-b, excellent soil as subgrade
Top Soil #3	30.9	24.7	6.2	ASTM: CL-ML, Sandy silty clay with gravel AASHTO: A-1-a, excellent soil as subgrade
Clay Soil #2	28.7	27.9	0.8	ASTM: ML, Sandy silt AASHTO: A-1-b, excellent soil as subgrade

samples above, the classification results are shown in Table 3. The liquid and plasticity test results are also presented in Table 3. As the classification results in Table 3 shown, there are a large portion of sandy particles in them, especially for Top Soil#3, particles in the size of gravel was found. Therefore, these three soils are very good sources to build strong subgrade. However, in order to observe the effect of the geosynthetics on the performance of asphalt pavement, the research team suggested to use a weak soil which has a California Bearing Ratio (CBR) as close to 3 as possible. Therefore, these three soils are not appropriate for this project.

3.1.4 Conveyor-Belt Soil

Table 3.5

Sieve Size	Mass Pertaining, g	Passing,%
3/4”	32.5	98.7
3/8”	75.2	95.5
NO.4	81.6	92.1
NO.10	206.9	83.6
NO.20	428	65.8
NO.40	1437.8	6.1
NO.50	39.8	4.5
NO.100	56.5	2.1
NO.200	29	0.9
<NO.200	22.7	
Total	2410	

Because less than 35% of the particles pass the NO.200 sieve, and less than 30% pass the NO.40 sieve, thus it is a type of A-1 soil. In addition, less than 15% of the particles pass NO.200, but more than 50% of them passed the NO.10 sieve, thus Conveyor-Belt is a type of A-1-b. Typically, the bearing capacity of subgrade using this soil is strong.

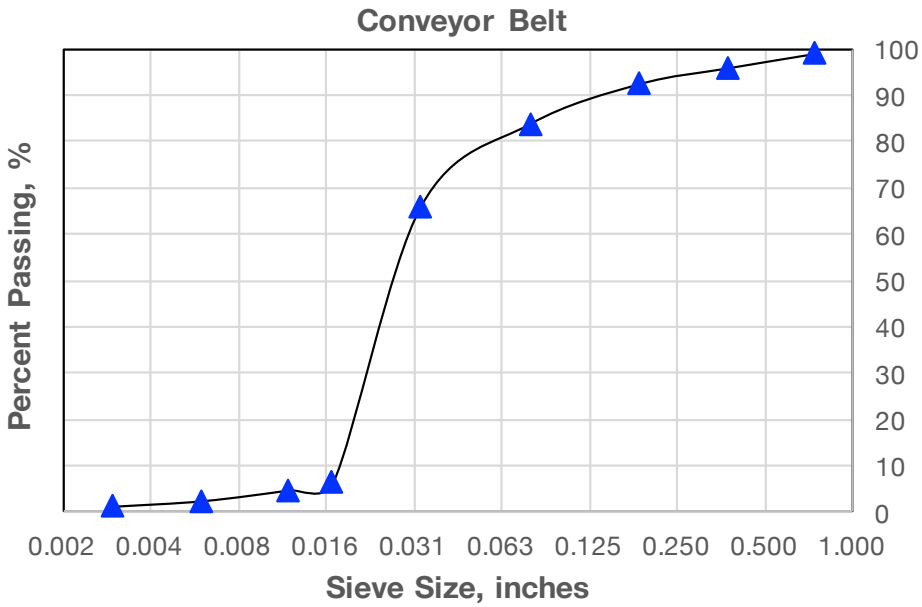

Figure 3.4: *Particle gradation curve for Conveyor-Belt soil*

3.1.5 Non-Vulcan Soil

Table 3.6: *Particle size distribution of Non-Vulcan soil*

Sieve Size	Mass Pertaining, g	Passing, %
3/4”	57.9	96.6
3/8”	84	91.7
NO.4	303	74
NO.10	474.8	46.3
NO.20	346.5	26
NO.40	166.2	16.3
NO.50	60.5	12.8
NO.100	90.3	7.5
NO.200	57.2	4.2
<NO.200	71.2	
Total	1711.6	

Since less than 35% of the mass passed the NO.200 sieve, thus it should be one type of A-1. Plus, less than 30% passed the NO.40 sieve, and less than 15% of them passed the No.200 sieve. Besides, less than 50% passing NO.10, thus it is a type of A-1-a.

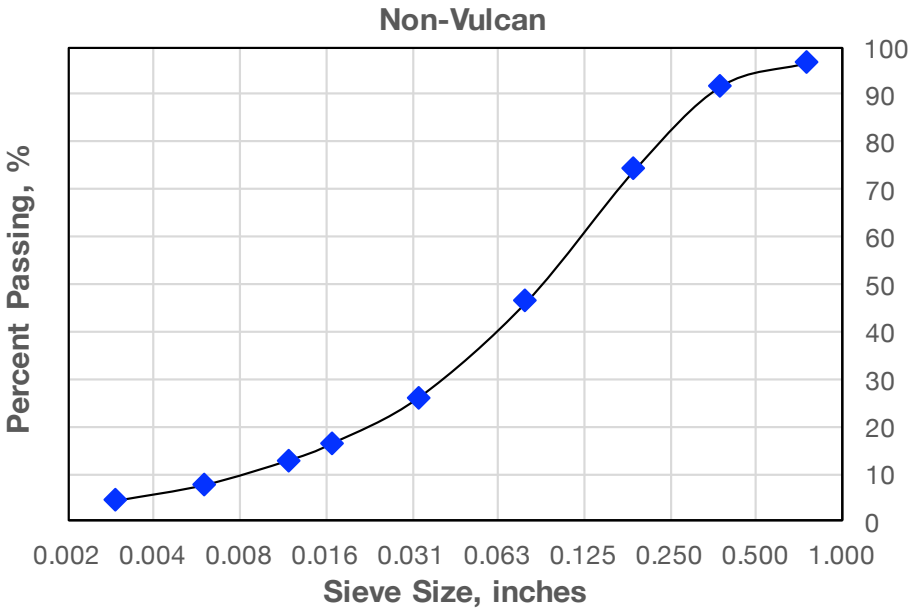

Figure 3.5: *Particle gradation curve for Non-Vulcan soil*

Table 3.7: *Particle size distribution of PIT soil*

Sieve Size	Mass Pertaining, g	Passing, %
3/4”	15.3	98.9
3/8”	25.9	96.9
NO. 4	189.3	82.8
NO.10	403.9	52.8
NO.20	340.9	27.4
NO.40	165.3	15.1
NO.50	52.9	11.1
NO.100	70.6	5.9
NO.200	36.1	3.2
<NO.200	42.9	
Total	1343.1	

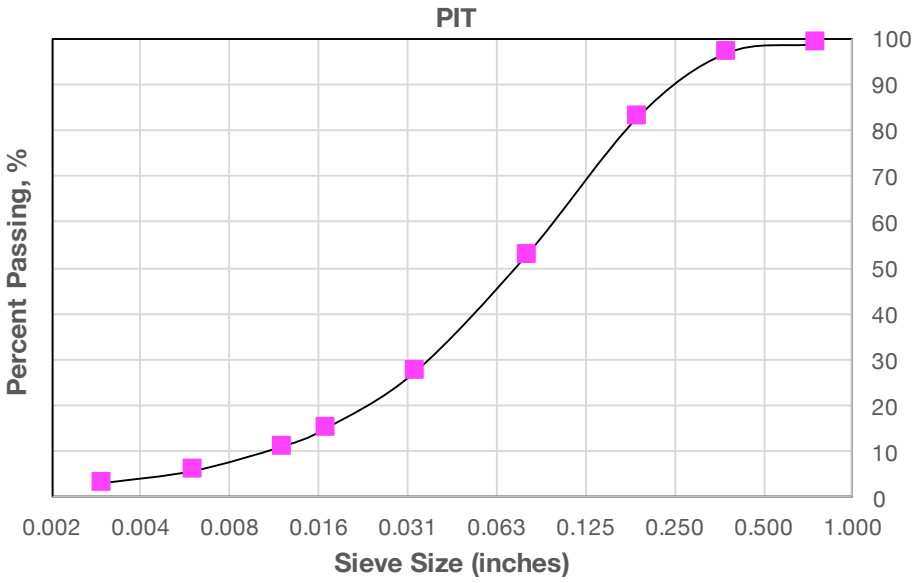

Figure 3.6: *Particle size distribution curve for PIT soil*

3.1.6 Pit Soil

Because there are less than 35% passing NO.200, and less than 50% passing NO.40, thus it is a A-1 soil. Less than 30% passing NO.40, less than 15% passing NO.200, but more than 50% passing NO.10, thus PIT is A-1-b. This is also an excellent soil for constructing a strong subgrade, and thus not a desirable candidate for this project.

3.1.7 Potential location of weak soil

In our previous project for determining resilient modulus of subgrade soil, soils from nine counties were tested, the classifications of the soils range from A-1 to A-7. From our database, it is noted that, A-7-5 was found in Giles County at station #270. Also, in Knox County at Station#400, Station #500, and Station Rutledge Pike, A-7-6 soil were identified. In addition, at Station #618 in the County of VanBuren, A-7-6 soil was used as well. These locations may be good resources of weak soil for this project.

3.2 Properties of Subgrade Soil in Test Pit

3.2.1 Atterberg Test

A portion of the subgrade soil that passing the No. 10 sieve was used in the Atterberg tests (Figure 3.7). To determine the liquid limit, five sets of test are needed. These five sets of test correspond to five different moisture contents, which were used to determine the liquid limit through regression. For each test set, three soil samples were prepared. The samples were then

dried in an oven to obtain the corresponding moisture content. As shown in Figure 3.8, the liquid limit of the subgrade soil is 35. The plasticity limit was determined by hand rolling, which is 21 for the subgrade soil. The plasticity index, which is the difference between the liquid limit (LL) and the plasticity limit (PL), is LL-PL=14.

Figure 3.7: *Atterbeg Test of Subgrade Soil*

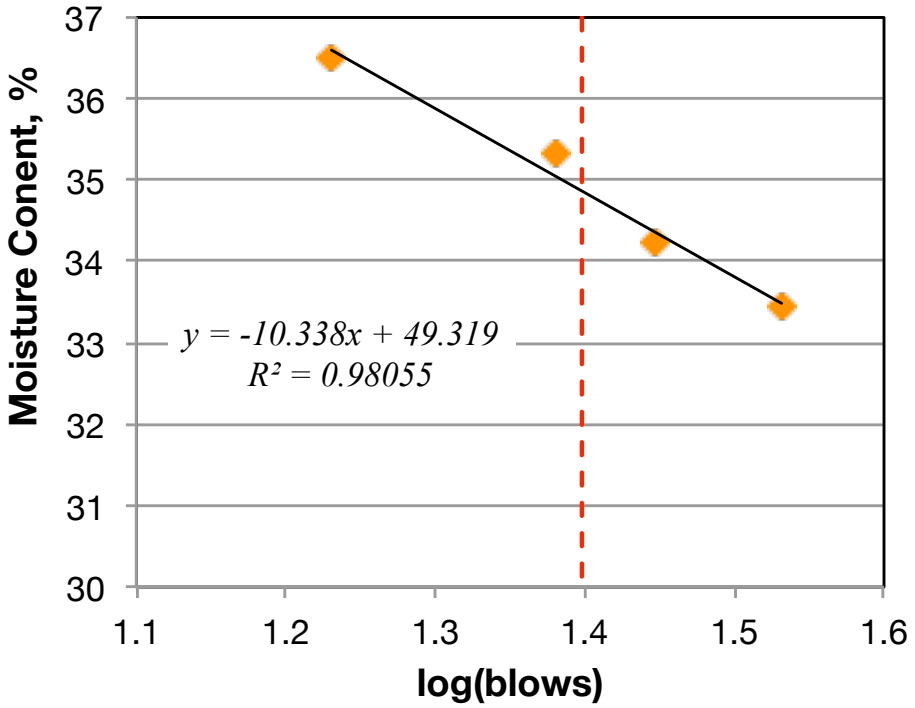

Figure 3.8: *Atterbeg Test of Subgrade Soil*

3.2.2 Gradation of Soil Used in Constructing Testing Pit

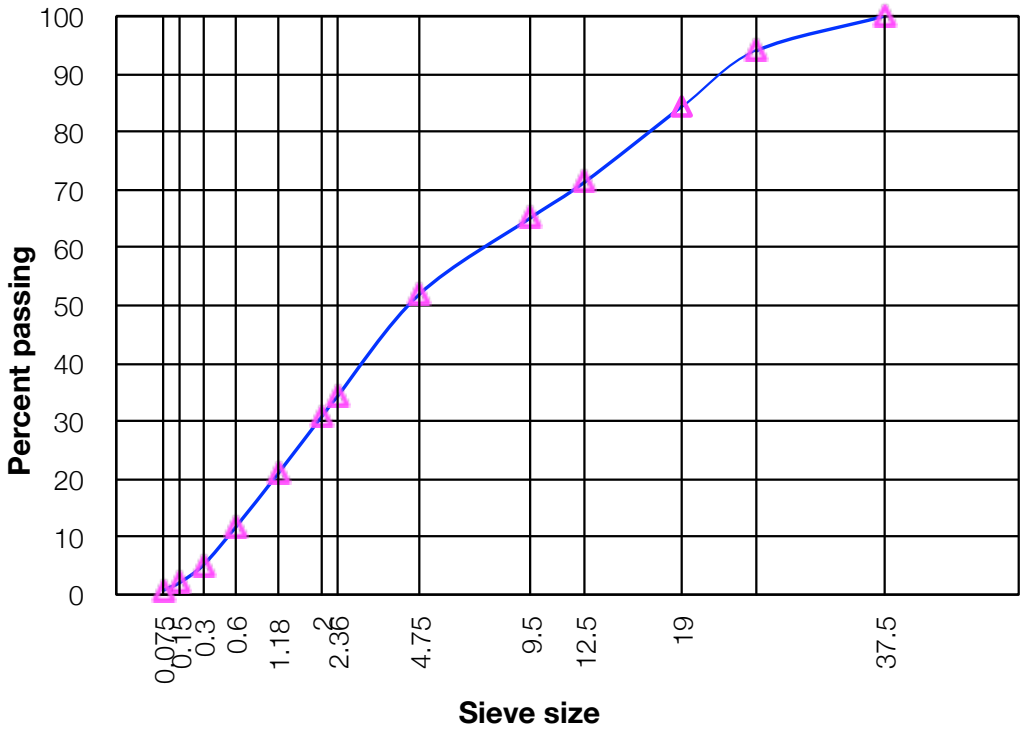

Figure 3.9: *Gradation of Subgrade Soil Used in Test Pit*

As shown in Figure 3.9, D85 is close to 9.5mm, while the D50 is approximately 0.026mm. D85 is the sieve size that 85 percent of aggregate particles are able to passing through. Similarly, D50 is the sieve size that 50 percent of the aggregate particles are able to passing through. D85 and D50 are important parameter in pavement drainage design, especially for seepage. It determines whether a geo-fabric is needed to control the movement of the fine particles. The PL and LL are 21 and 35, respectively. Since the PI=PL-LL=14, which is greater than 7, a geo-fabrics may be unnecessary. As the sieve analysis results indicate that the index of soil should be A–6 as per AASHTO standard or CL as per ASTM standard (sandy lean clay with gravel) (Figure 3.9). For a CL soil, its range of CBR is 2-17.

3.2.3 Gradation of Aggregate in Stone Base

Using a method similar to the one used in determining the particle size distribution (PSD) of subgrade soil, the PSD of base aggregate stone was obtained. Figure 3.10 shows the gradation curve of the aggregate base layer. The gradation of base aggregate is essential in choosing the appropriate geogrid products.

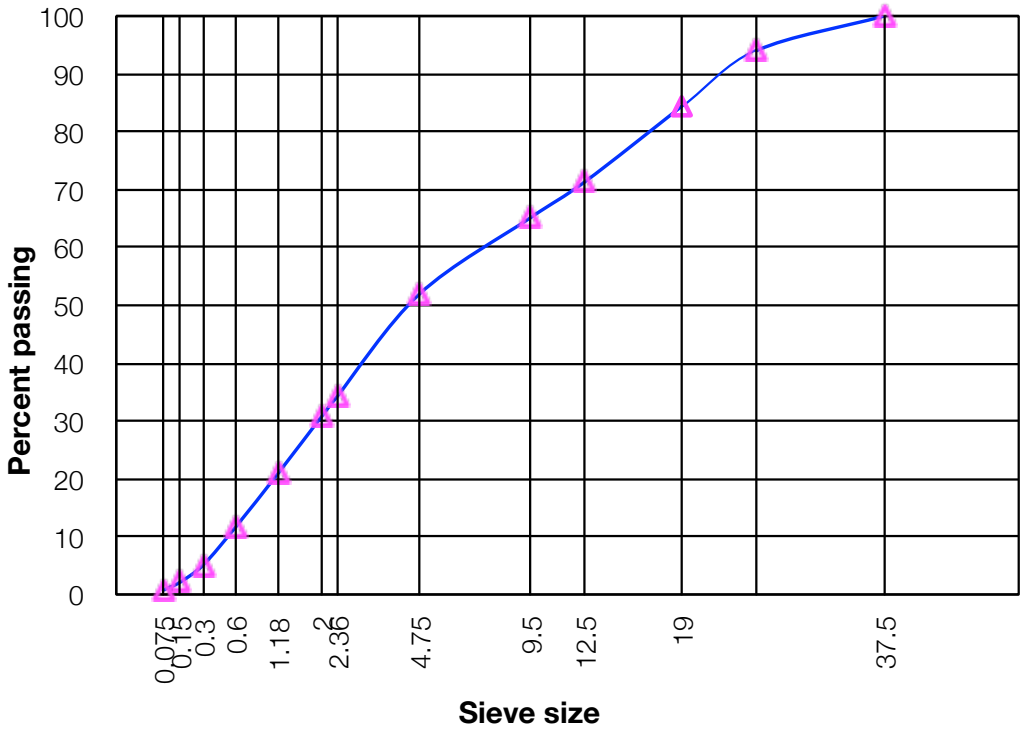

Figure 3.10: *Gradation of Aggregate in Stone Base*

3.3 Geosynthetics Properties

A total of three types of geosynthetics were used in the project, which were respectively obtained from Tensar, Maccaferri, and Huesker. As per the objectives of the projects, these purposely selected geosynthetics products differed in opening shape, rid stiffness, and the manufacture mechanism.

3.3.1 Tensar Tri-axial Geogrids

With its unique triangular structure, TriAx Geogrid represents a revolutionary advancement in geogrid technology. Its multi-directional properties leverage triangular geometry, one of construction's most stable shapes, providing greater stability and stiffness. The change from a rectangular to a triangular grid aperture, coupled with an increase in rib thickness and junction efficiency, offers the construction industry a better alternative to conventional materials and practices.

The potential merits of using geosynthetics as the base reinforcement for pavements:

- Better interlock and confinement;
- Triangular aperture geometry;
- Junction integrity and efficiency;

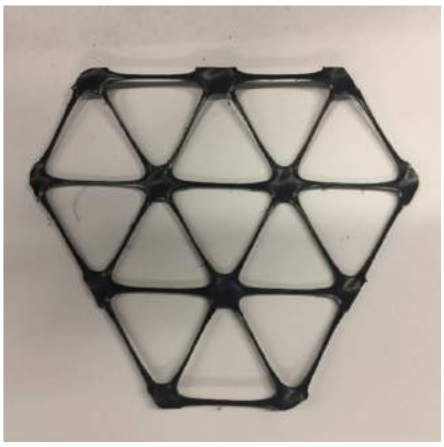

Figure 3.11: *Illustration of Tensar TX5 Geogrids*

- Superior performance for paved and unpaved roads;
- Less stress on subgrades;
- Enhanced "snowshoe effect" (better stress spreading);

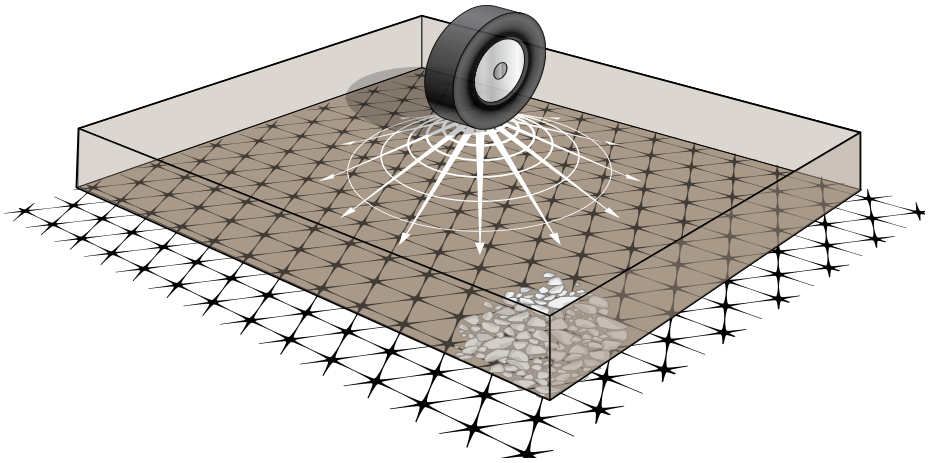

Figure 3.12: *Load Spreading Effects of Tensar Triaxial Geogrids (Credits of Tensar)*

3.3.2 Maccaferri Bi-Axial Geogrids

As Maccaferri reported that the MacGrid EG Series geogrids are able to provide interaction with different types of soils and fill material, especially granular soils. The actual benefits realized through the use of geogrids, depend on the type of soil being used with the geogrids. The installation of MacGridTM EG helps to improve the load bearing capacity of existing soils, creating more predictable stabilization conditions for future construction. Situations that would benefit from the use of TM MacGrid EG include:

Table 3.8: *Mechanical Properties of Tensar TX-5 Geogrids*

Properties	Tensar Biaxial	Tensar TX-5
Tensile Strength at 5% (kN/m)	30	-
Radial Stiffness at 0.5% (kN/m)	-	270
Radial Secant Stiffness at 2% Strain (kN/m)	-	250 kN/m
Junction Efficiency (%)	90	95
Aperture size (mm)	32×31	$46 \times 46 \times 46$

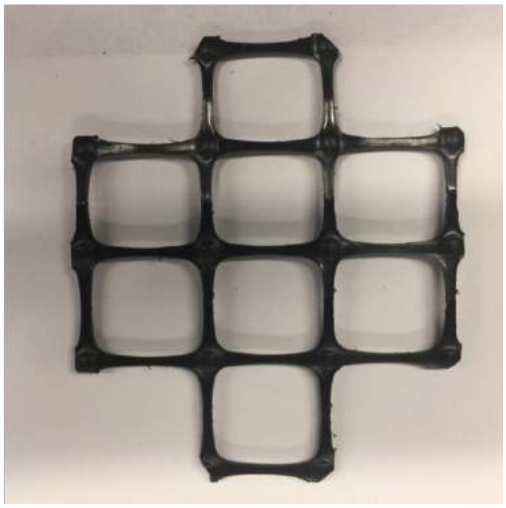

Figure 3.13: *Illustration of Maccaferri Bi-Axial Geogrids*

Table 3.9: *Mechanical Properties of Maccaferri Biaxial Geogrids (MacGrid 30S)*

Mechanical Properties	Test Method	Unit	Values	Notes
Tensile Strength (Longitudinal)	EN ISO 10319 ASTM D 6637	lb/ft (kN/m)	2050 (30)	(1)
Tensile Strength at 2% Strain (Longitudinal)		lb/ft (kN/m)	720 (10.5)	(4)
Tensile strength at 5% Strain (Longitudinal)		lb/ft (kN/m)	1440 (21)	(4)
Tensile Strength (Transverse)		lb/ft (kN/m)	2050 (30)	(1)
Tensile Strength at 2% Strain (Transverse)		lb/ft (kN/m)	720 (10.5)	(4)
Tensile Strength at 5% Strain (Transverse)		lb/ft (kN/m)	1440 (21)	(4)
Junction Strength Efficiency	GRI CG2	%	95	(1)
Flexural Rigidity	ASTM D1388	mg-cm	3,900,000	(1)
Aperture Stability	COE Method	m-N/deg	1.43	(1)

3.3.3 Huesker Bi-Axial Geogrids

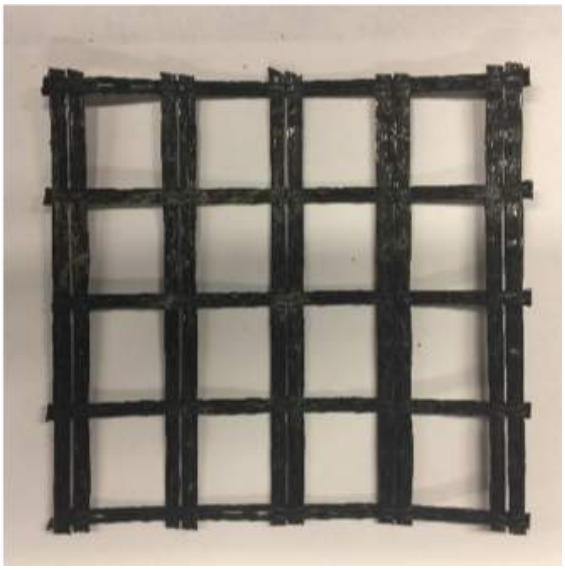

Figure 3.14: *Illustration of Huesker Geogrids*

According to Huesker, the Fornit geogrids offer an excellent tensile reinforcement in an aggregate base layer for both paved and unpaved roads. With the tensile element distributing the applied loads over a larger area, Fornit geogrids reduce the subgrade bearing capacity requirement. Also, the Fornit ® geogrids are ideally suited for maintaining the integrity of the road construction under repeated wheel loading. Lateral displacement of the aggregate is restricted by its interlocking with the grid, proved by interface shear strength testing. The aggregate layer is supported by the geogrid mesh, which provides a bridging function as well as spreading any applied wheel loading over a much wider surface area, thereby increasing its bearing capacity.

Fornit ® 20/25 is comprised of polypropylene yarns and has been developed to stabilize poor soils by providing tensile reinforcement and soil separation. They confine and strengthen road base aggregate thereby reducing the required base thickness. Fornit ® 20/25 is easy to install and resistant to freeze-thaw conditions, soil chemicals and ultra-violet exposure. Fornit ® 20/25 is produced in Huesker's ISO 9001 certified facility.

PROPERTY	TEST METHOD	ENGLISH units[1]	SI units[1]
Mass/Unit Area	ASTM D-5261	7 oz/yd^2	240 g/m^2
Aperture Size	Measured	1.35 x 1.35 inch	35 x 35 mm
Ultimate Wide Width Tensile Strength			
Machine Direction (MD)	ASTM D-6637	2,055 lb/ft	30 kN/m
Cross Machine Direction (CMD)	ASTM D-6637	2,055 lb/ft	30 kN/m
Elongation at Break	ASTM D-6637	6%	6%
Wide Width Tensile Strength @ 2%			
Machine Direction (MD)	ASTM D-6637	822 lb/ft	12 kN/m
Cross Machine Direction (CMD)	ASTM D-6637	822 lb/ft	12 kN/m
Wide Width Tensile Strength @ 5%			
Machine Direction (MD)	ASTM D-6637	1,640 lb/ft	24 kN/m
Cross Machine Direction (CMD)	ASTM D-6637	1,640 lb/ft	24 kN/m
Tensile Modulus @2%			
Machine Direction (MD)	ASTM D-6637	41,100 lb/ft	600 kN/m
Cross Machine Direction (CMD)	ASTM D-6637	41,100 lb/ft	600 kN/m
Tensile Modulus @ 5%			
Machine Direction (MD)	ASTM D-6637	32,800 lb/ft	480 kN/m
Cross Machine Direction (CMD)	ASTM D-6637	32,800 lb/ft	480 kN/m

[1] MARV - Minimum average roll values are based on a 95% confidence level.

Standard Roll Size: 17.06 ft (5.2 m) wide x 328.1 ft (100 m) long = 622 yd^2 (520 m^2)
Weight: 285 lb/roll (130 kg)

Figure 3.15: *Mechanical Properties of Huesker Fornit 20/25 Geogrids (merits of Huesker)*

3.4 Test Pit Boundary Effect Anlaysis with FEM

3.4.1 Model Dimension

A finite element model (FEM) using ABAQUS was used to establish the wall effect of the test pit on the test section. The dimension of test pit is 20 feet in width, 20 feet 8 inches in length, and 6 feet in depth. A FEM model of size 6ft × 6ft × 6ft is used, after considering the symmetry in the problem. As shown in Figure 7, the dimension in Y-direction is 6ft, while the dimensions of the model in X- and Z-direction are the same, which is 5ft. A rectangular load of the size 0.196 m (in Z direction)×0.135m (in X direction) is applied at the center of the model, the amplitude of the load is 0.707 MPa. The left wall and back walls, and the bottom face of the model are fixed for all direction of movement, while the front face and right faces are fixed for motions in Z and X direction. In order to obtain accurate enough prediction of mechanistic response at the boundaries, a fine mesh is introduced, with a total of 525,525 elements.

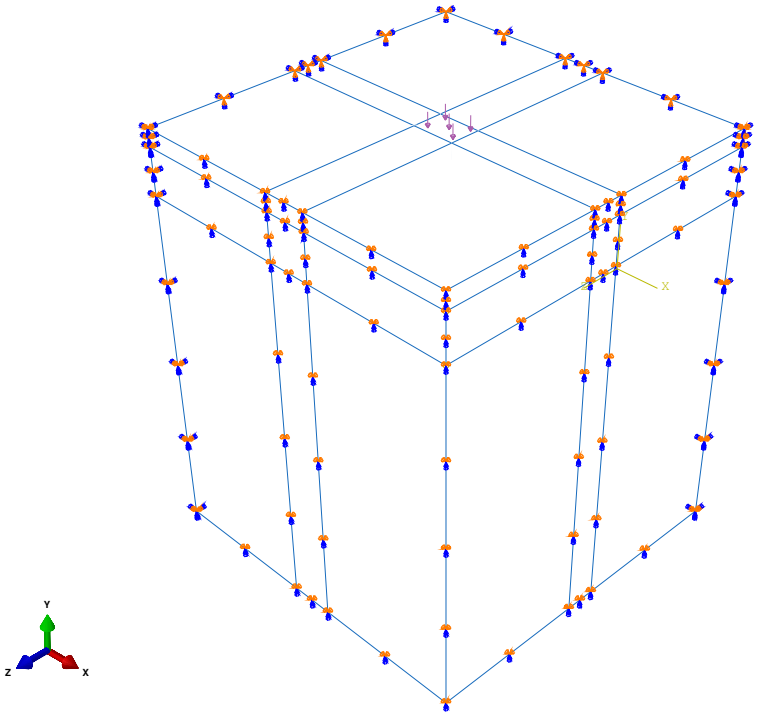

Figure 3.16: *Load and boundary condition of the FEM model*

Table 3.10: *Pavement structure of the FEM model*

Material	Thickness	Young's Modulus	Poisson's ratio
Asphalt Concrete	3 inches	4000 MPa (580,150 psi)	0.35
Aggregate	8 inches	200 MPa (29,000 psi)	0.4
Soil	61 inches	20 MPa (2,900 psi)	0.4

3.4.2 Critical Stress and Strain

Vertical Deflection

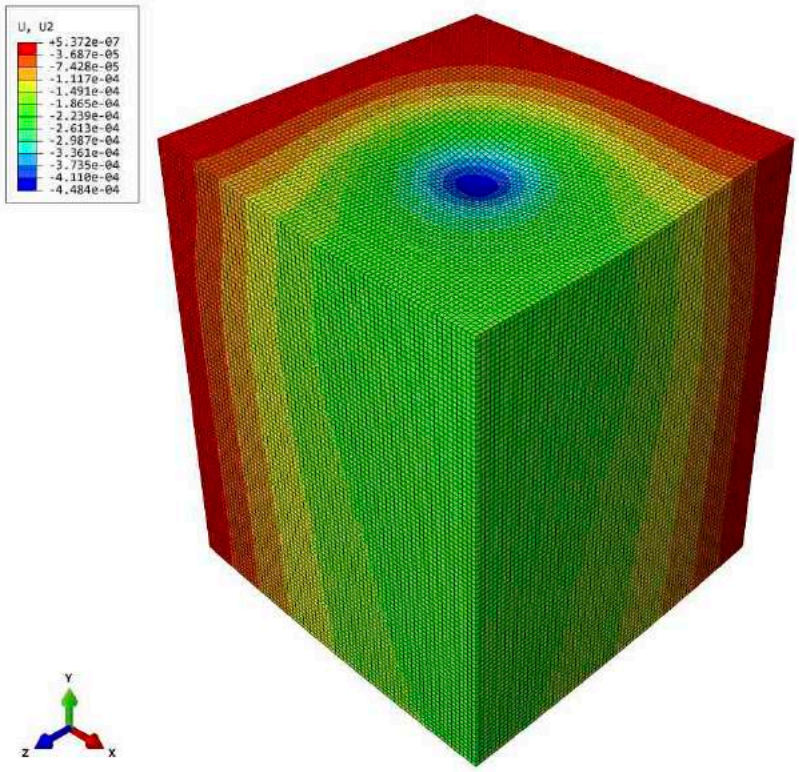

(a) *Deflection Contour Plot*

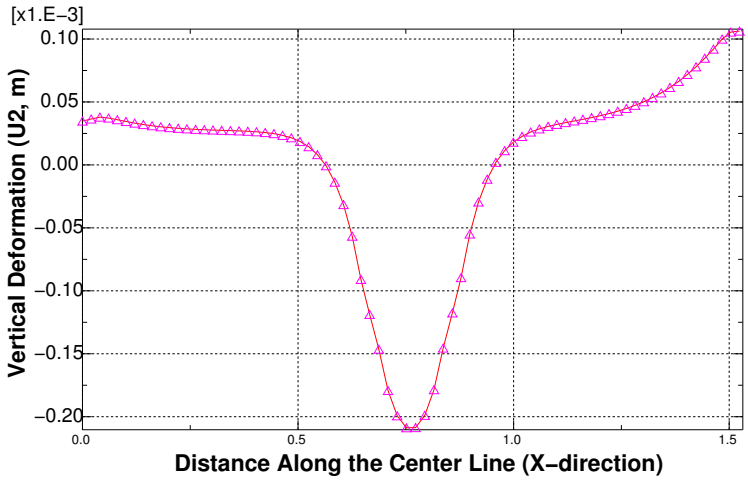

(b) *Deflection Basin*

Figure 3.17: *Vertical displacement (U2) of test section under wheel load*

Figure 3.17 Showed a contour plot of the vertical displacement (Y-direction), it is seen that

when load is applied at the center of the test section, the displacement at the surface of the boundary is extremely small and even negligible. Under this condition, when the load is applied at the center of the test section, the effect of the wall on the mechanistic responses at the center of the section is negligible. If an influence width is to be proposed, then about 0.25m (0.82 ft) from the wall is free of influence from the load at the center.

Compressive Strain

Figure 3.18 showed a contour plot and line plot for the vertical strain along the center in the X-direction. It is seen in Figure 3.18, the vertical strain in the vicinity of the wall is extremely small, there is an area, which is about 0.5m (1.64 ft) from the wall, free of influence from the load applied at the center. As is seen in Figure 3.18 , the influence depth is about 0.28 m (0.92 ft), which is approximately the depth of the asphalt mixture layer and the aggregate layer.

Compressive Stress

Figure 3.19 showed a contour plot and line plot of the vertical stress (S22) along the center in X-direction, it is seen in Figure 3.19, noticeable S22 values are located within a small area around the load center. In terms of vertical stress (S22), the FEM model is free of influence from the wall effect.

Tensile Strain (Along Traffic Direction)

Unlike the vertical stress and displacement, as shown in Figures 3.18 and 3.19, there are some large strain values along the top edge of the wall. It is seen from the line plot in Figure 3.20, the influence width in terms of tensile strain (E11) is about 0.25 m (0.82 ft).

Tensile Strain (Cross-Traffic Direction)

Shown in Figure 3.21 are a contour plot and a line plot of the horizontal stress (S11) along the center line of the model in X-direction. It is seen in Figure 3.21, there are some large tensile stresses along the edge of the surface. Therefore, in terms of tensile stress, the effect of the wall on the stress in the vicinity of the wall is not negligible, the influence width of the wall is about 0.5m (1.64 ft).

In all, the vertical stress (S22), strain (E22), displacement (U2) are free of the influence from the wall of the test pit. However, the influence of the wall of the test pit on the tensile stress (S11) and strain (E11) are not negligible. In terms of tensile stress (E11), the influence width of the wall is about 0.25 m(0.82ft). However, from the tensile strain perspective, the influence width of the wall is about 0.5m (1.64ft).

3.4.3 Summary

According to the FEM analyses presented above, the influential range of the APT wheel loading would be less than 1 foot from each edge of the test pit. Also, given the geometry of the test pit (20ft (wide) $\times$ 20.8ft (long)), to consider the boundary effect of the concrete wall on the test pit,

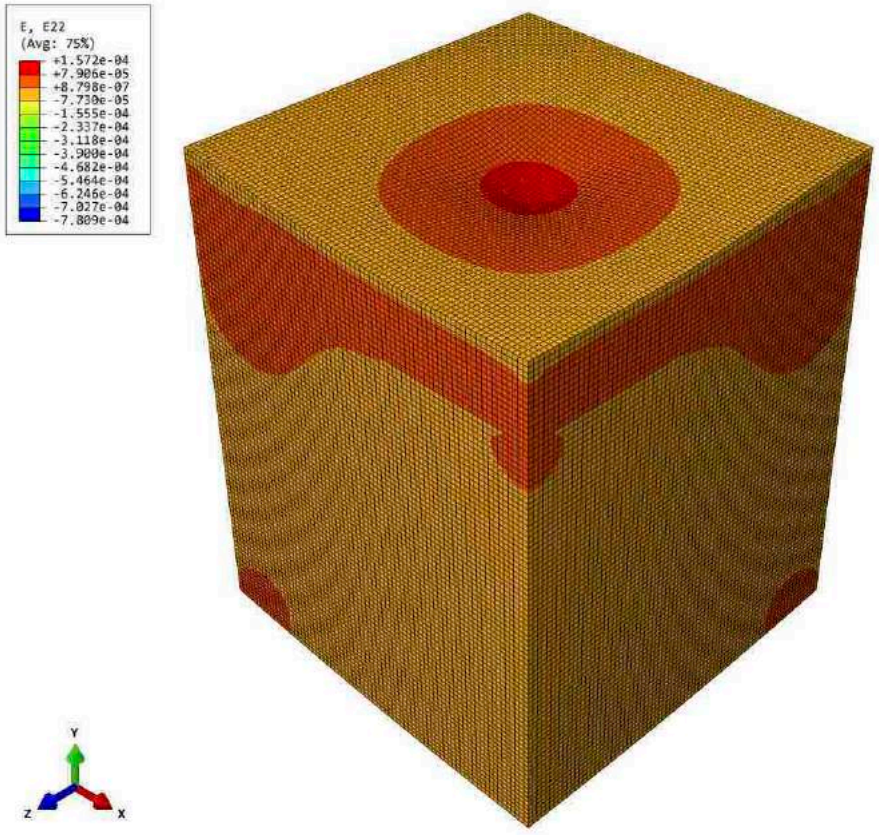

(a) *Compressive Strain Contour*

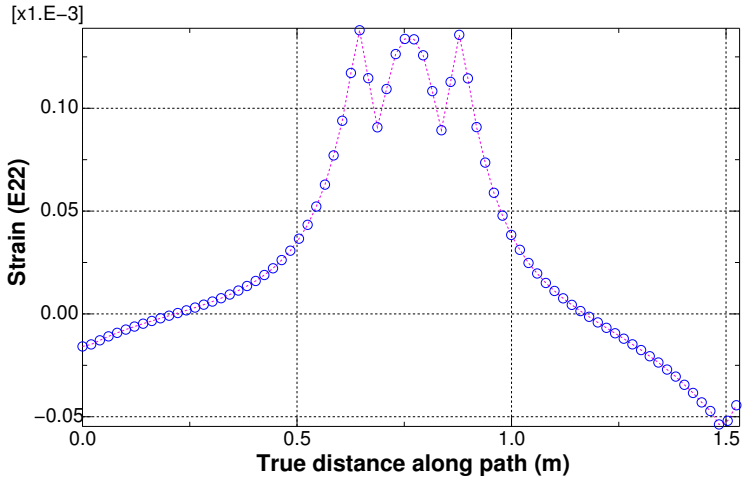

(b) *Compressive strain curve*

Figure 3.18: *Vertical strain along the center line (in X-direction)*

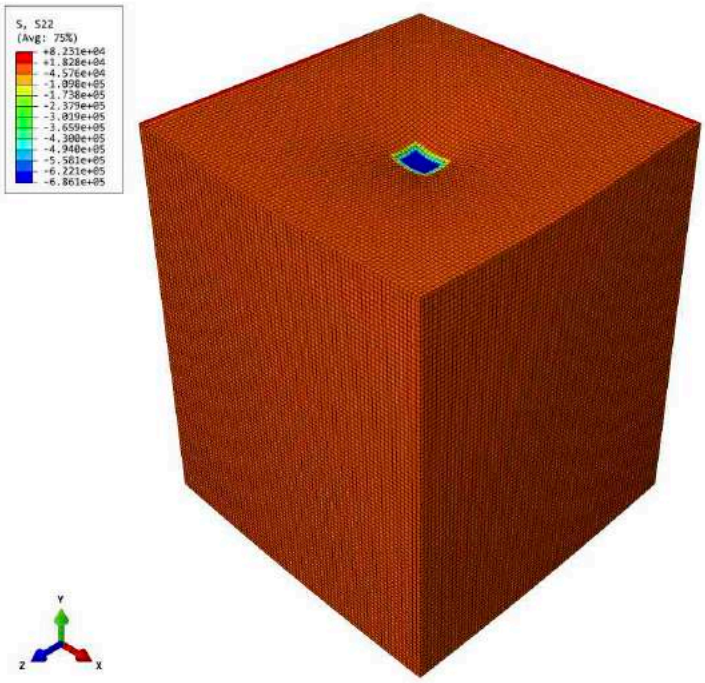

(a) *Compressive Stress Contour Plot*

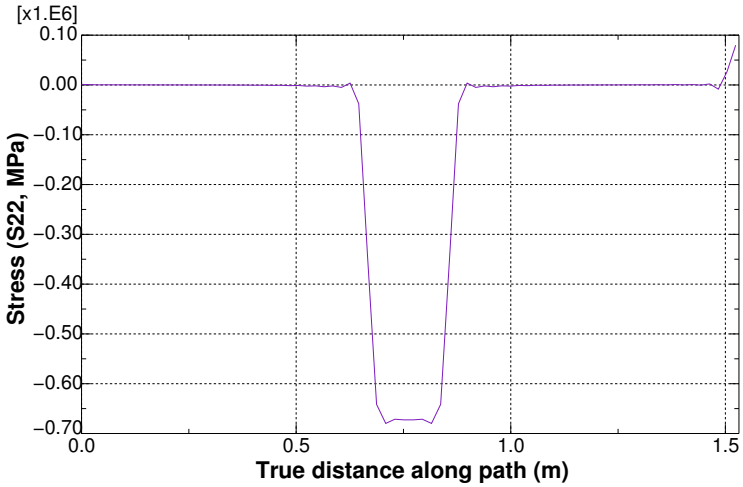

(b) *Compressive Stress Curve (along cross-traffic direction)*

Figure 3.19: *Vertical stress (S22) along the center line (along cross-traffic direction)*

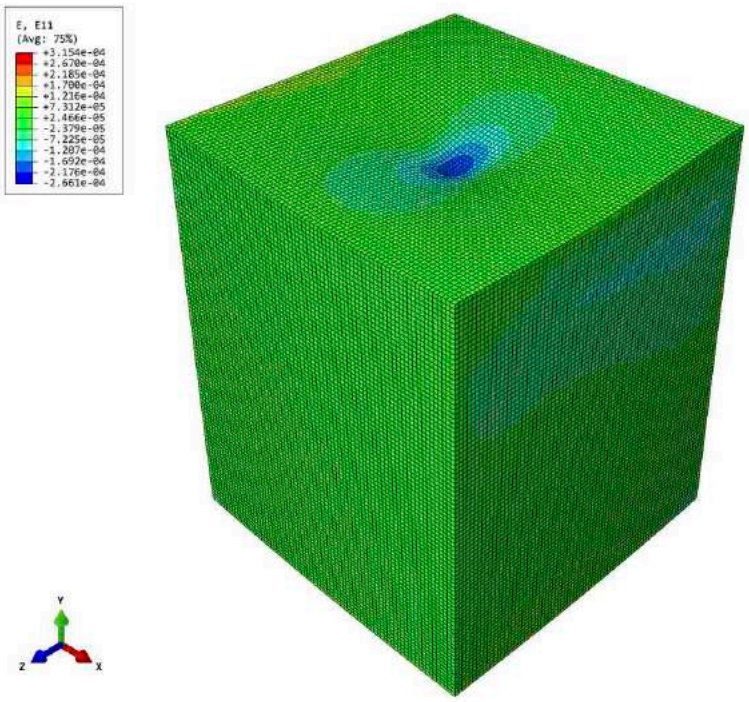

(a) *Tensile Strain Contour Plot (along cross-traffic)*

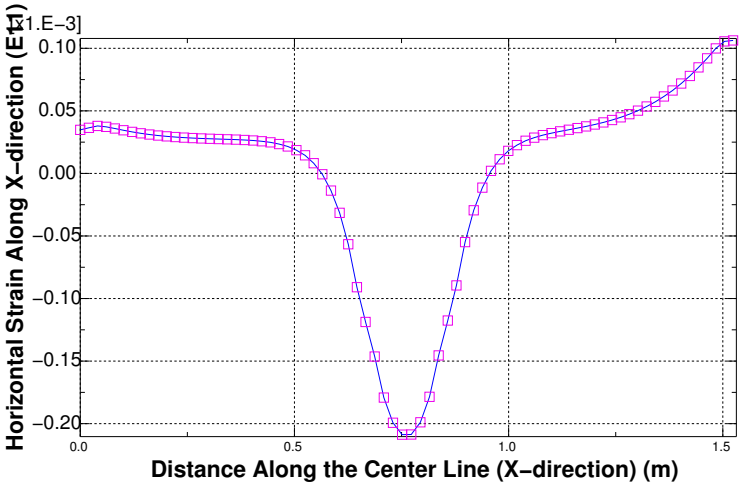

(b) *Tensile strain curve*

Figure 3.20: *Horizontal strain (E11) along the center line (in X-direction)*

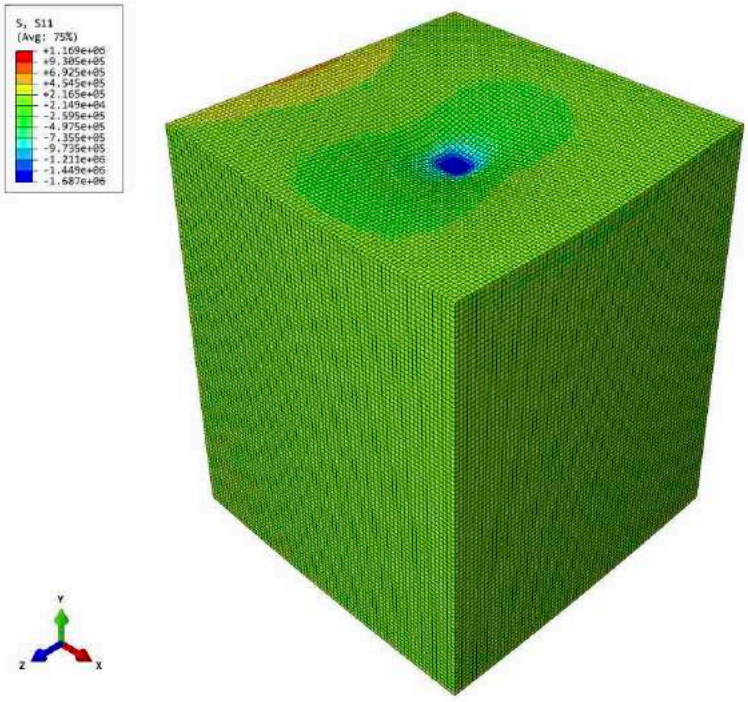

(a) *Tensile Stress Contour Plot (along cross-traffic direction)*

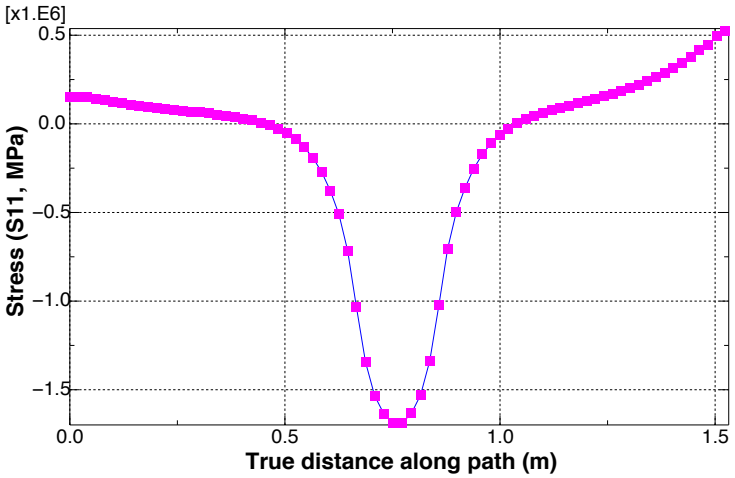

(b) *Tensile Stress Curve*

Figure 3.21: *Horizontal stress (S11) along the center (in X-direction)*

a foot of space was remove from each side of the test pit. Hence, after considering the boundary effect of the test pit and the equal lane width used for the test sections of the project, the lane width was set to 6 feet (18ft/3).

Chapter 4 First Round of APT Testing

4.1 Test Experiment Design

Figure 4.1 shows the pavement structure for the first phase of the test. Figure 4.3 shows a schematic of the lanes divided and the locations for density and dynamic cone penetrator (DCP) tests. Figure 4.3 shows the placement of the geogrids.

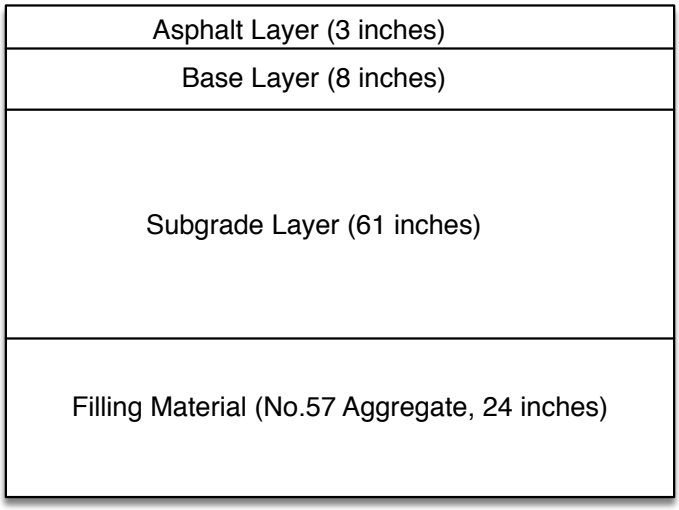

Figure 4.1: *Schematic of Pavement Strucutre*

4.2 Test Section Construction

Figure 4.4 through Figure 4.8 show the process for the test section construction. To simulate the real construction conditions in the field, all of the construction equipment was the same as those involved in the real-world construction project. In this project, the subgrade and aggregate base were compacted by a steel drum roller compact. During the compaction of the aggregate base, vibration was applied to achieve a high level of density, while no vibration was used during the compaction of the subgrade soil to avoid over densifying the subgrade.

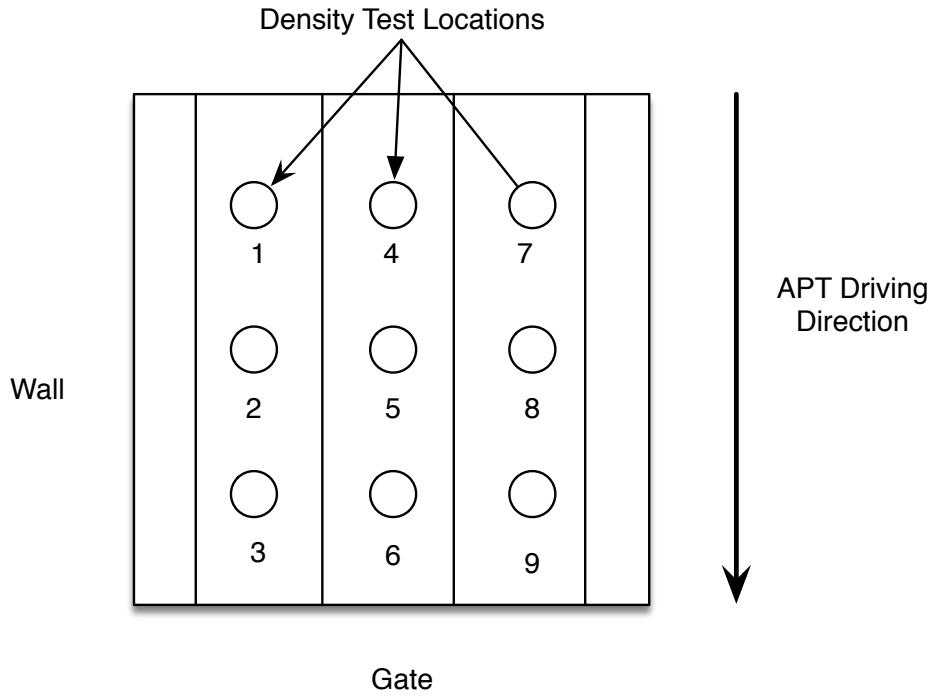

Figure 4.2: *Locations Density Measurements*

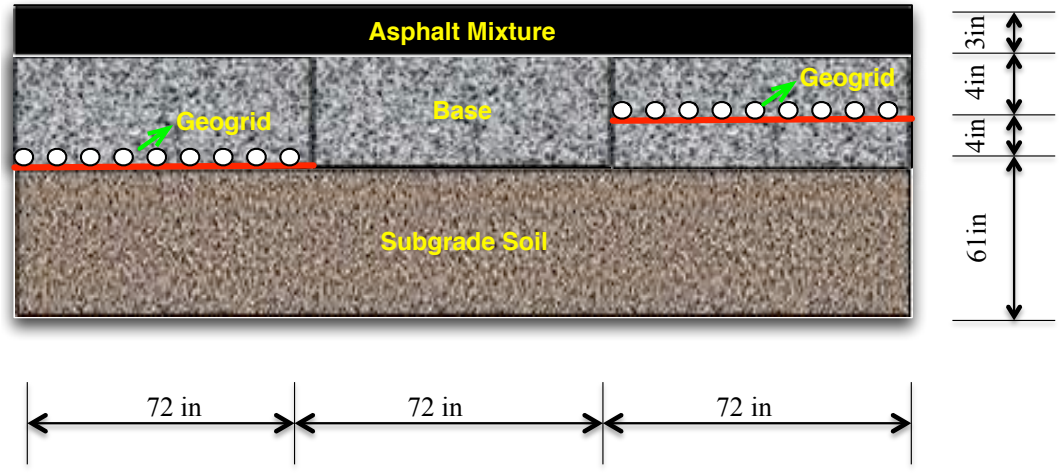

Figure 4.3: *Test Lanes Layout*

Figure 4.4: *Leveling Test Pit for Subgrade Construction*

Figure 4.5: *Placing Subgrade Soil*

(a) *Geogrid in Middle of Aggregate Base* **(b)** *Geogrid at Bottom of Aggregate Base*

Figure 4.6: *Placing Geogrids on Each Side of Test Pit*

(a) *Subgrade Soil Compaction* **(b)** *Aggregate Base Compaction*

Figure 4.7: *Placing Geogrids on Each Side of Test Pit*

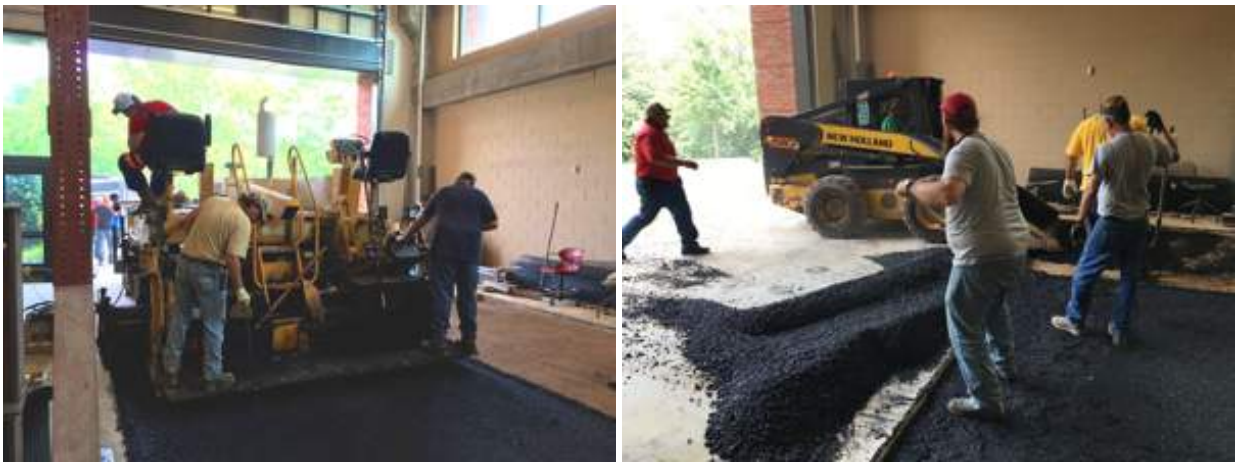

Figure 4.8: *Placing Asphalt Mixture*

4.3 Density Measurements After Constuction

The density, in-field moisture content, and compaction degree of the subgrade soil were measured after application of each layer of soil. To control the uniformity and quality of the compaction, the nuclear gauge test was conducted on nine different locations (Fig 4.2). Overall, the average moisture content is 18.9%, while the compaction degree is 80.4% (Figure 4.10). To make this the strength of the subgrade weaker, a high moisture content and relative lower compaction degree is helpful. The dynamic cone tests (Figure 4.11) were also performance on the same locations as the density measurement using nuclear gauge (Figure 4.9). The DCP test results could be related to California bearing ratio (CBR) using a relation as follows:

Figure 4.9: *Test of Density and Compaction Degree of Subgrade Soil Using Nuclear Gauge*

$$\log \mathrm{CBR} = 2.46 - 1.12 \log \mathrm{DPI} \text{ or } \mathrm{CBR} = 292/(\mathrm{DPI}^{1.12}) \tag{4.1}$$

γ=79.3% **ω** =19.6% ①	γ=77.5% **ω**=17.5% ④	γ=79.1% **ω**=19.7% ⑦
γ=82.3% **ω**=19.2% ②	γ=80.5% **ω**=14.6% ⑤	γ=87.8% **ω**=18.7% ⑧
γ=75.5% **ω**=21.7% ③	γ=79.7% **ω**=19.6% ⑥	γ=82.1% **ω**=18.5% ⑨

Figure 4.10: *Nuclear Gauge Measurements of Moisture Content and Compaction Degree of Subgrade*

Figure 4.11: *Dynamic Cone Test for Bearing Capacity of Subgrade*

where, DPI is defined as the vertical movement of the DCP cone produced by one drop of the hammer, expressed in mm/blow (inch/blow). Stiffer or stronger soils have a lower DPI.

Fig 4.12 shows the distribution of CBR along the penetration depth in the aggregate base and subgrade. Due to the existence of coarse stone particles, there are some extreme values, such as those values greater than 100. During the construction process, a large number of large coarse aggregates was found in the subgrade soil, this makes the DCP test results looks large, but at those spots without large coarse aggregates, the CBR is around 3-6.

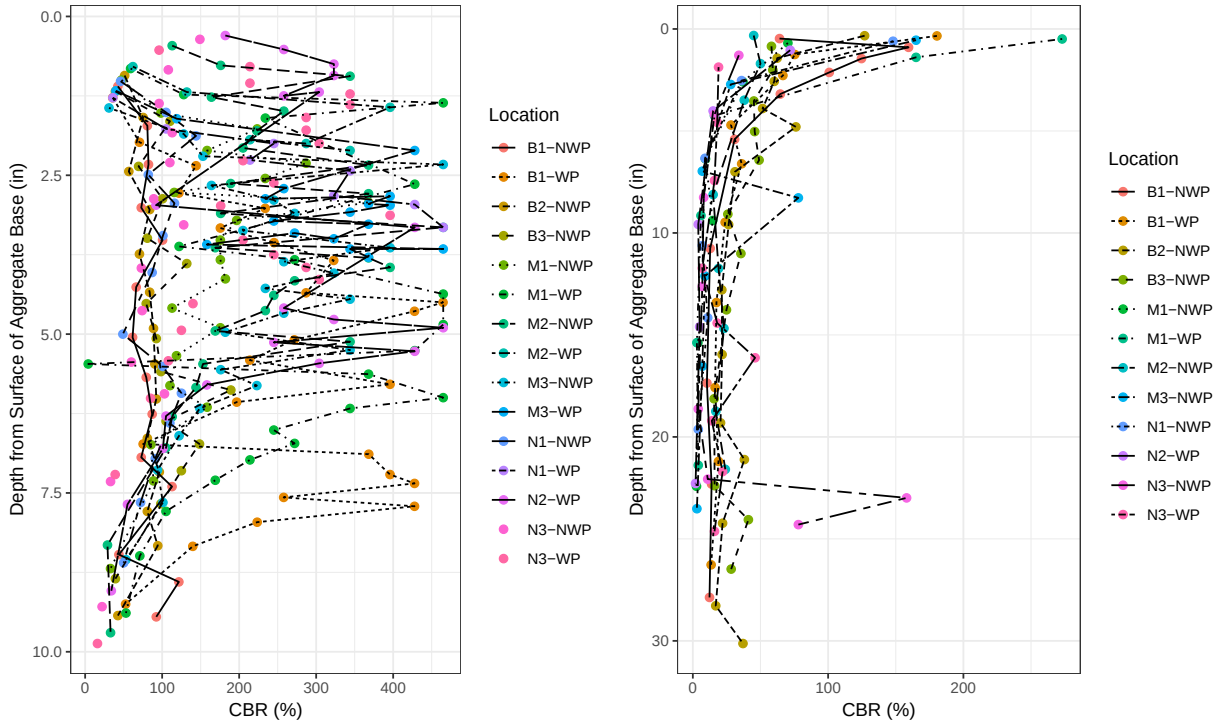

(a) *Aggregate Base* **(b)** *Subgrade*

Figure 4.12: *Distribution of CBR along the Depth*

4.4 APT Testing Profiles

The control lane which sits in the middle of the test section was trafficked with a unidirectional rolling wheel load from the APT. At certain numbers of axle load repetitions, the surface deformation was measured using a profilometer (Figure 4.13). The profilometer has a length of 8 feet, which is sufficient to cover the width of the lane (six feet) under testing.

For the convenience of measuring the profile, a grid with a interval of one foot between each line in both the horizontal and vertical directions was drawn on the test section. In addition, the elevation at the center of the each wheel path was taken as well. Therefore, there are nine locations used to determine the profile of a cross section and a total of 19 cross sections were divided in each lane. In order to refer, compare and plot the profile of the three lanes after trafficking, the locations to be profiled were labeled. The label consists of a letter and three numbers. The control

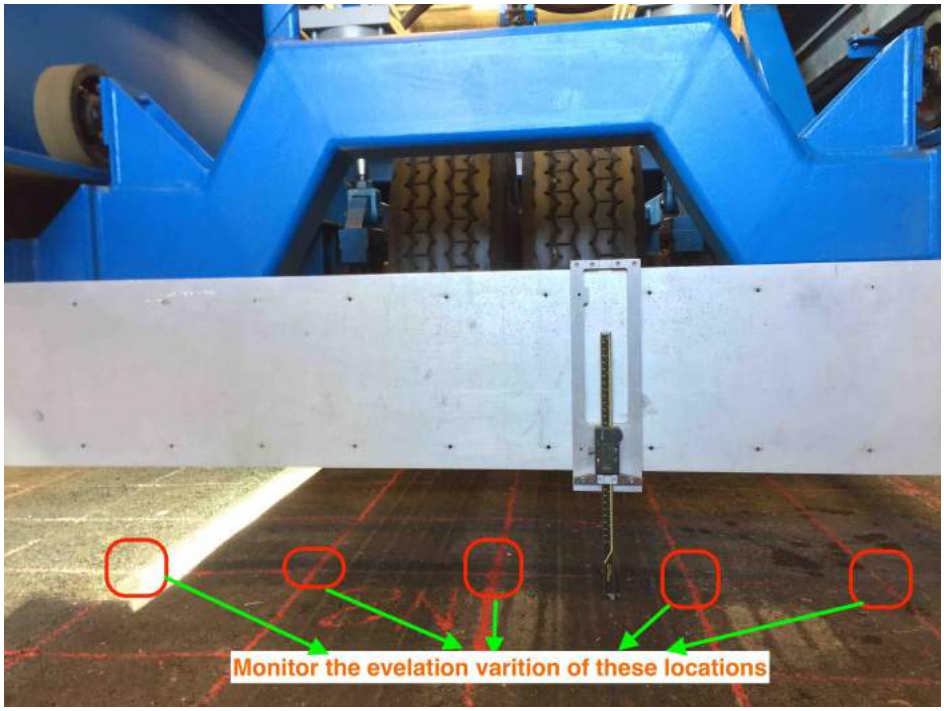

Figure 4.13: *Measuring the Profile of the Section Using Profilometer*

lane was assigned with a letter of "N", while the lane with geogrids installed at the bottom of the aggregate base (AB) was assigned with a letter of "B", and the one with geogrids installed at the middle of the AB was given a letter of "M". Considering the potential variation in compaction quality at different part of the lane, each lane was then divided into three subsection, from the easternmost to the westernmost direction, the subsection has a number of 1, 2, and 3, respectively. Hence, each subsection has seven line in both the horizontal and vertical directions. The overlapped lines of the subsections or lanes shared the same label, for instance, for subsection N1, the line labeled Col-7 (N1-7) is actually also the line (M1-1) of the subsection M1. Therefore, it is convenient to refer a specific location with a label like N_{1-34}, which indicates this location is in the first subsection of the control lane and has a row number 3 and a column number 4. For a interval of axle repetitions, the elevation at the locations where the horizontal and vertical lines cross were obtained for each interval, as illustrated in Figure 4.13.

Figure 4.14 shows the labels of the grid lines. In addition to the lines drawn on the test section, two extra lines (Col-4.5 and Col-3.5) which is the centerline of the two wheel paths were included as well. The permanent deformation or the variation in elevation at each location can be obtained from the difference between the intervals of axle load repetitions.

For the locations with row numbers 1 and 2 in the subsection N1 (Box N1), they are unlikely to vary with the repetitions of axle loading, because the wheel never reach this area. For this reason, the elevations of these locations were omitted. After exploring with the measured profiles, it was found only the locations with columns of 3, 3.5 (wheel path centerline), 4, 4.5 (wheel path centerline), and 5 have evident changes in elevations as the axle repetitions increases. Therefore, only the profiles for locations with these column numbers are reported. The elevations reported here are the distances from the bottom of the beam of profilometer to the pavement surface, thus

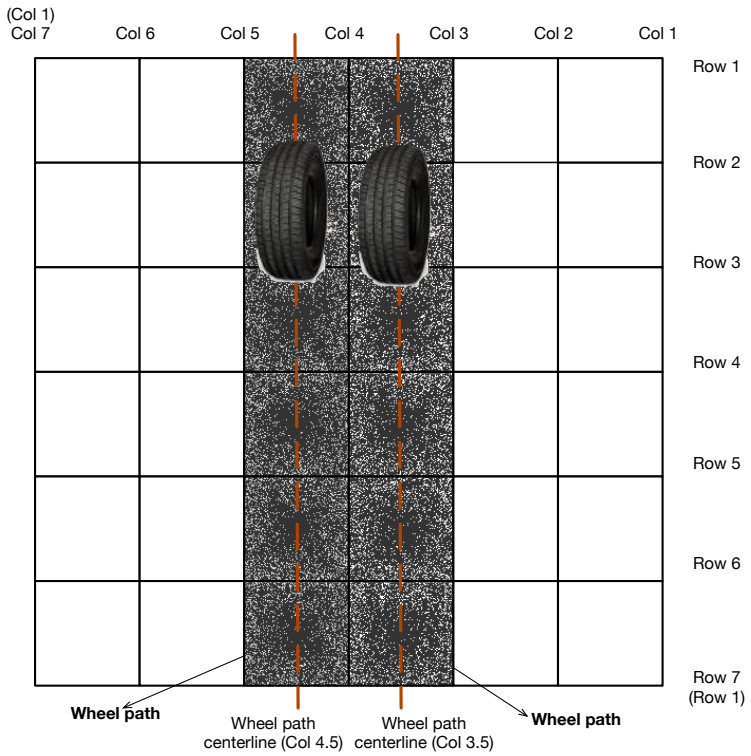

Figure 4.14: *Profiling Locations (Subsection N1)*

as the rutting develops, the elevations of profiling locations are expected to increase. Besides, a regular pattern was found that more variation happened in the first three or four measurements. Overall, the minimum elevation occurred the third or fourth measurement, except for the locations with column number 3.5 and 4.5 in the subsection N3.

For the locations with row numbers 1 and 2 in the subsection N1 (Box N1), they are unlikely to vary with the repetitions of axle loading, because the wheel never reach this area. For this reason, the elevations of these locations were omitted. After exploring with the measured profiles, it was found only the locations with columns of 3, 3.5 (wheel path centerline), 4, 4.5 (wheel path centerline), and 5 have evident changes in elevations as the axle repetitions increases. Therefore, only the profiles for locations with these column numbers are reported. The elevations reported here are the distances from the bottom of the beam of profilometer to the pavement surface, thus as the rutting develops, the elevations of profiling locations are expected to increase. Besides, a regular pattern was found that more variation happened in the first three or four measurements. Overall, the minimum elevation occurred the third or fourth measurement, except for the locations with column number 3.5 and 4.5 in the subsection N3.

The profiles of the aforemethioned locations are presented in the Appendix. As shown in the profiles of the locations with a column number of 3, the trafficked pavement surface has gone downward about half inch. Similar patterns are displayed for all three subsections, namely, N1, N2, and N3. For the profiles of locations with a column number of 3.5, the data from subsection N3 seem to have captured the trend of rutting development. Because as the axle load repetitions increase, the elevation will increases then approach to a steady state. As per the profilometer used in this project, a increase in the elevation indicates a increase of rutting, while a decrease in

elevation implies a upheaval happened at that location, as illustrated in Figure 4.15.

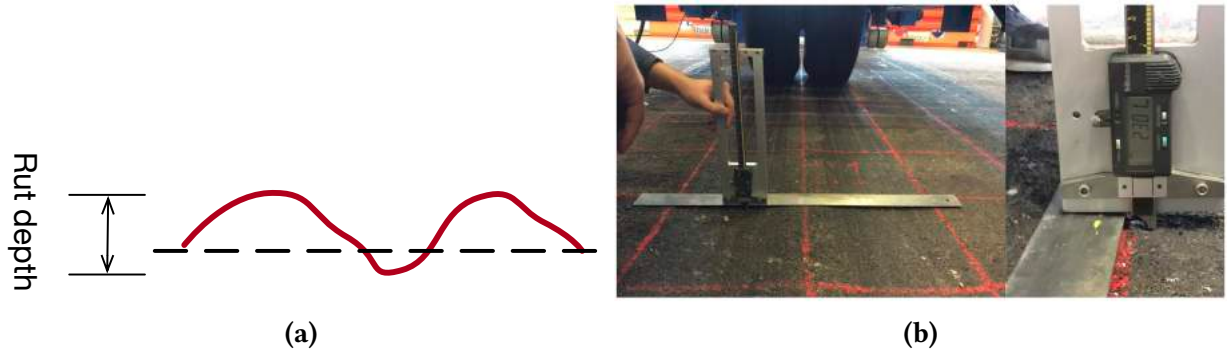

(a) (b)

Figure 4.15: *Rutting: (a) Illustration of Rutting Development and (b) Measuring Rutting with Straight Edge*

4.5 PROFILE OF THE TRAFFICKED TEST SECTIONS

For the convenience of comparing the profile measurements with the rutting depth, the reading of elevation from the profilometer was subtracted by 7.2 inches, which was the elevation reading of the profilometer when it was placed on a flat surface. For the convenience of referring the sections, the section with geogrid installed in the middle of the base layer was labeled as M, the other with geogrids reinforcement was assigned a label of B, and the control section had a label of N.

4.5.1 Results of Control Section

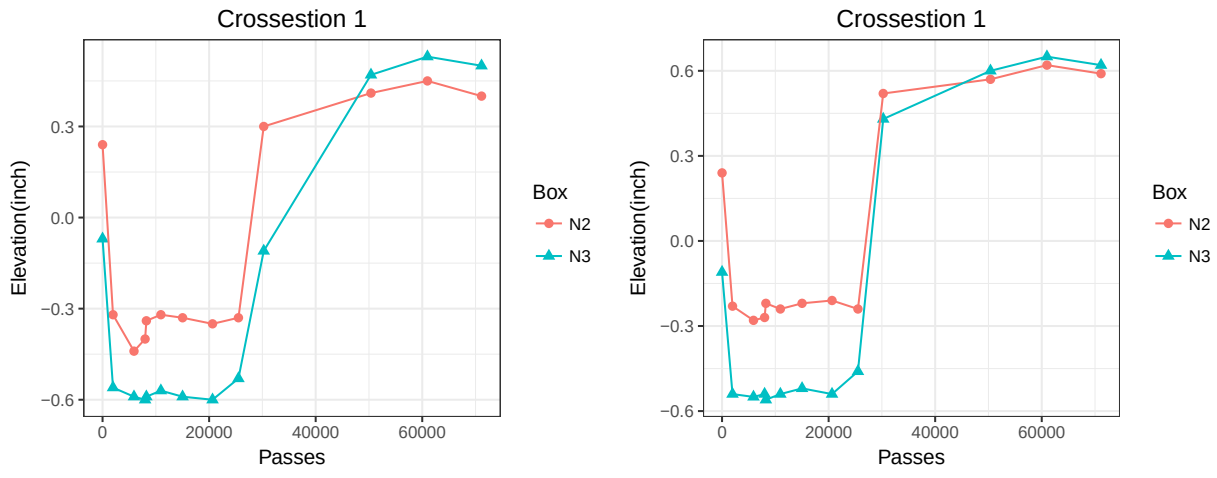

(a) (b)

Figure 4.16: *Adjusted Profile of control lane, (a): left wheel path center; (b): right wheel path center*

Figure 4.16 plots the adjusted profiles versus the load repetitions. It was observed that after about 71,000 axle load repetitions, the permanent deformation accumulated was about 1.0 inch in the right wheel path; and it was around 1.3 inch for the left wheel path.

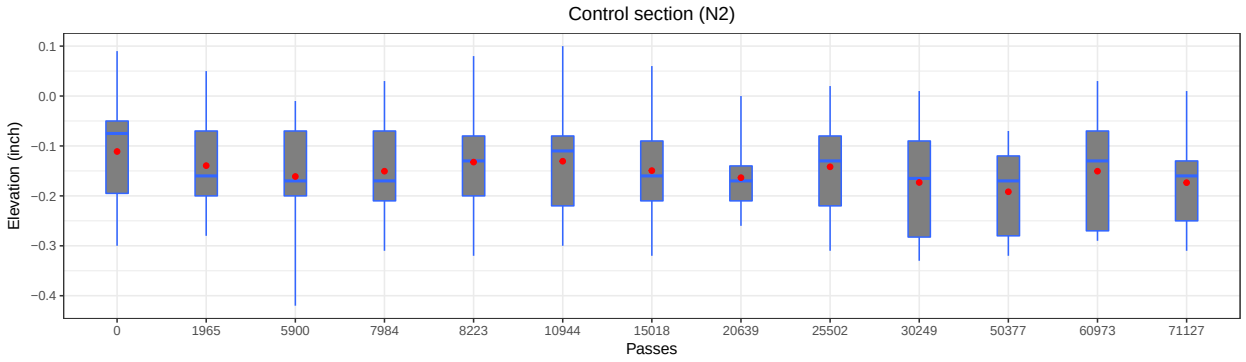

Figure 4.17: *Boxplot for profile of cross section 2 (Column number = 2)*

Figure 4.17 plots the adjusted profiles versus the load repetitions. It was seen that after about 71,000 axle load repetitions, the permanent deformation accumulated was about 1.0 inch in the right wheel path; and it was around 1.3 inch for the left wheel path.

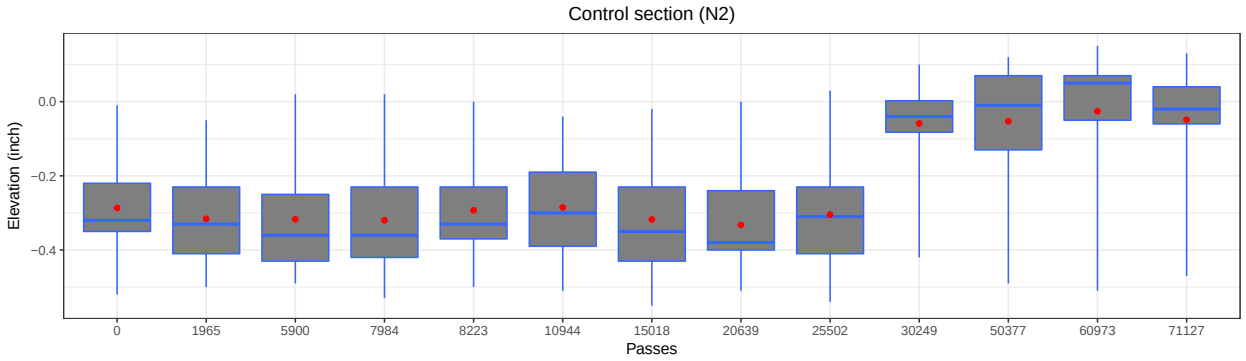

Figure 4.18: *Boxplot for profile of cross section 3 (Column Number = 3)*

Figure 4.18 shows the longitudinal profile of cross-section 3. It is seen that as the cross-section getting closer to the wheel-paths (column number = 3.5 or 4.5), the change in profile becomes significant. For this cross-section, the change of adjusted elevation from the start to the end of test is only 0.28 inch.

Figure 4.19 and Figure 4.20 show the longitudinal profile vary with the axle load numbers. It was observed that there was a stage in each graph. This was due to the fact that at the start of the testing until axle repetitions reached 25,502, the air pressure in the cylinder that apply the axle load to the pavement was 40-psi only. After 25,502 axle repetitions, an air pressure of 100-psi was used to speed up the test. After around 71,000 axle repetitions, a rutting depth of 2.0 inches was observed which led to the termination of the testing on this section. For the left wheel path, as the axle load number reaches 71,127 passes, the change in the adjusted elevation is 1.01 inches (Figure 4.20). As to the right one, when axle load number reach 71,127 passes, the change in the adjusted elevation was 0.82 in.

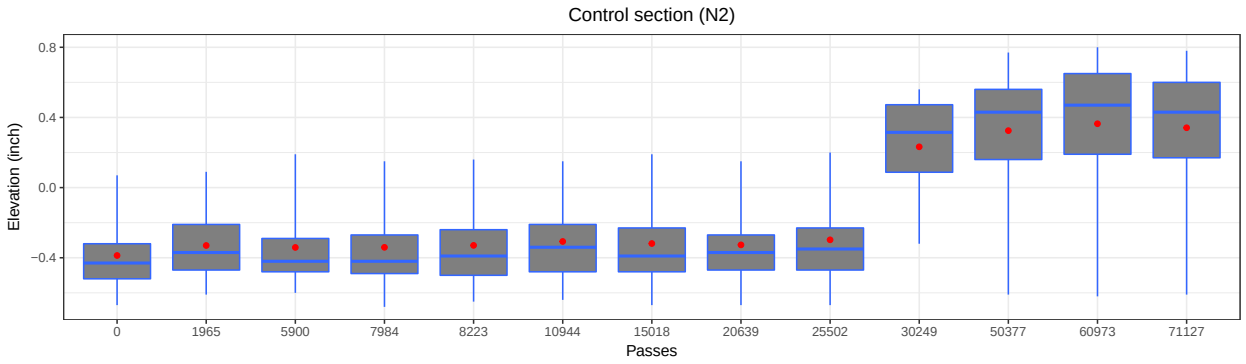

Figure 4.19: *Boxplot for profile of cross section 4.5 (Column Number = 4.5)*

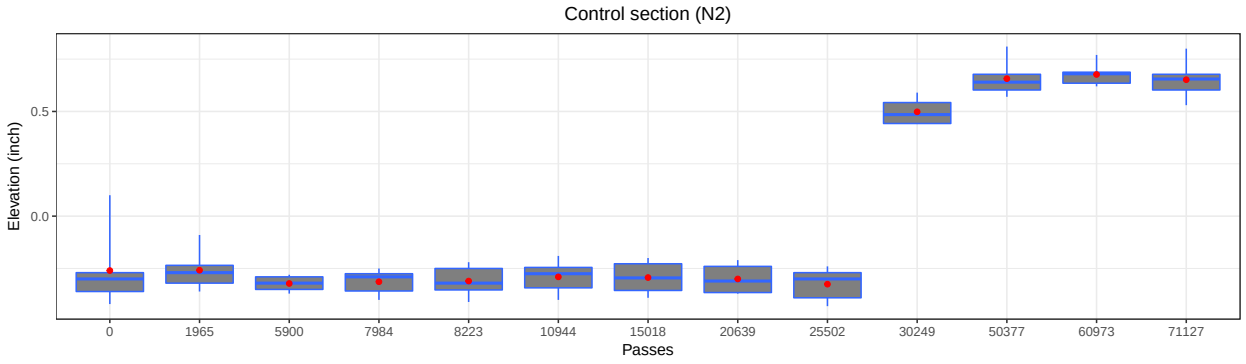

Figure 4.20: *Boxplot for profile of cross section 3.5 (Column Number = 3.5)*

4.5.2 Section with Geogrid in the Middle of Aggregate Base

The test on the section with geogrid installed in the middle of the base layer (section-M) was conducted after the failure of the control section. This section developed a rutting depth of 2.1 inches after 104,488 axle load repetitions. It was seen in Figure 4.22, from the start of the test to the failure of the section, the change in adjusted elevation of this cross-section was 0.78 inch. As shown in Figure 4.23, for the left wheel path (column 4.5), the change in adjusted elevation from the start of testing to the finish was 0.88 inch. This was smaller than the control section (1.01 inch), and demonstrated the effectiveness of geogrid in the section M.

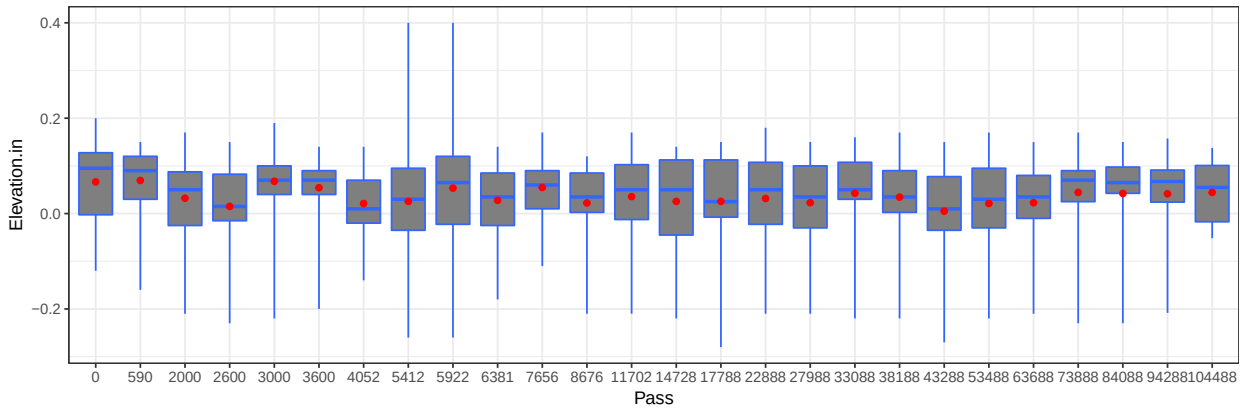

Figure 4.21: *Boxplot for profile of cross section 2 (Column Number = 2)*

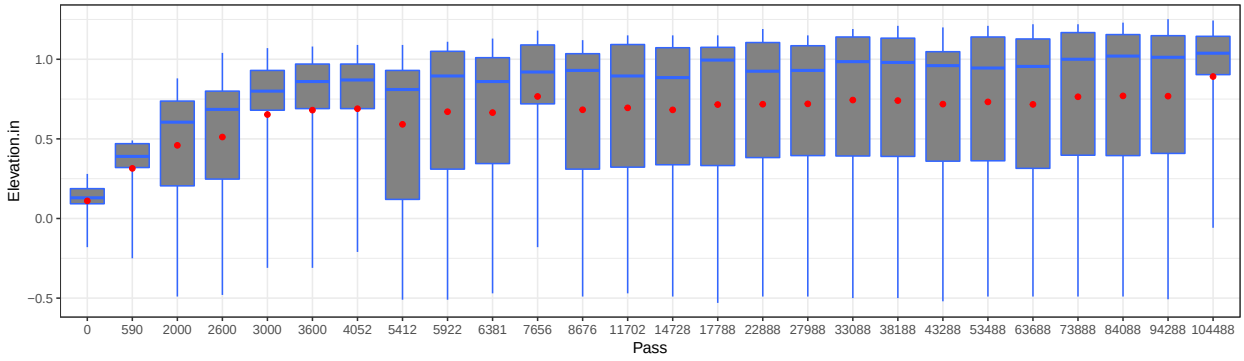

Figure 4.22: *Boxplot for profile of cross section 3.5 (Column Number = 3.5)*

Figure 4.21 shows the boxplot for the profile of cross section 2 in the section M. Due to the fact that this cross section is quite far from the wheel path (more than 1.5 feet), the profile seemed to keep unchanged as the axle repetitions increases. This was in turn verified accuracy of that the measured profiles, because the mean elevations of this cross-section at different loading passes remains stable. From zero loading pass to 104,488 loading passes, the change in the adjusted elevation in this cross-section was only 0.04 inch. This indicated that the traffic loading had very little effect on this area.

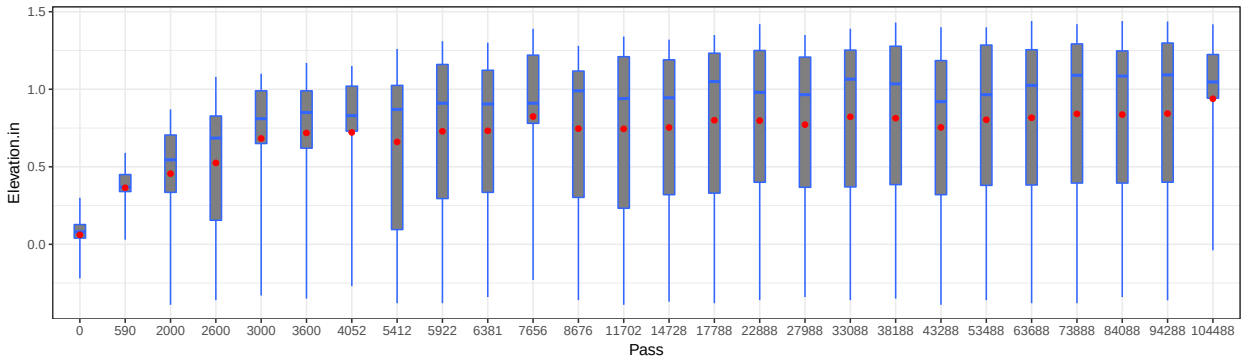

Figure 4.23: *Boxplot for profile of cross section 4.5 (Column Number = 4.5)*

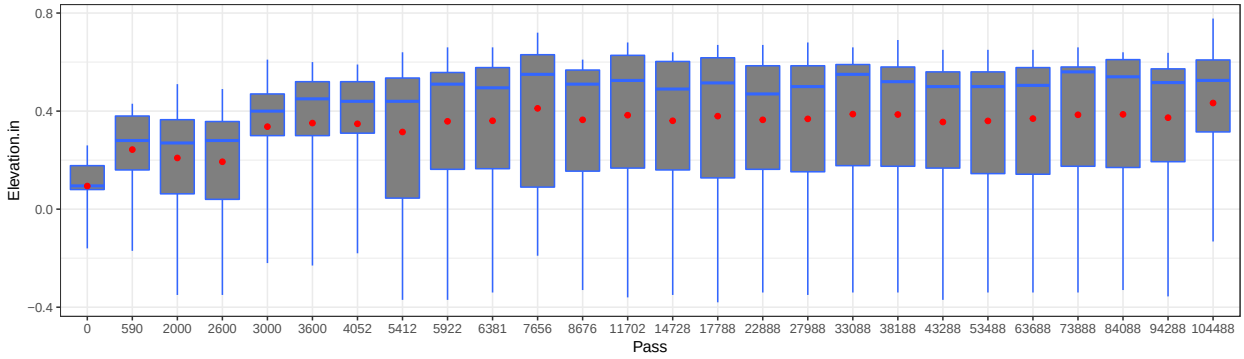

Figure 4.24: *Boxplot for Profile of Cross Section 3 (Column Number = 3)*

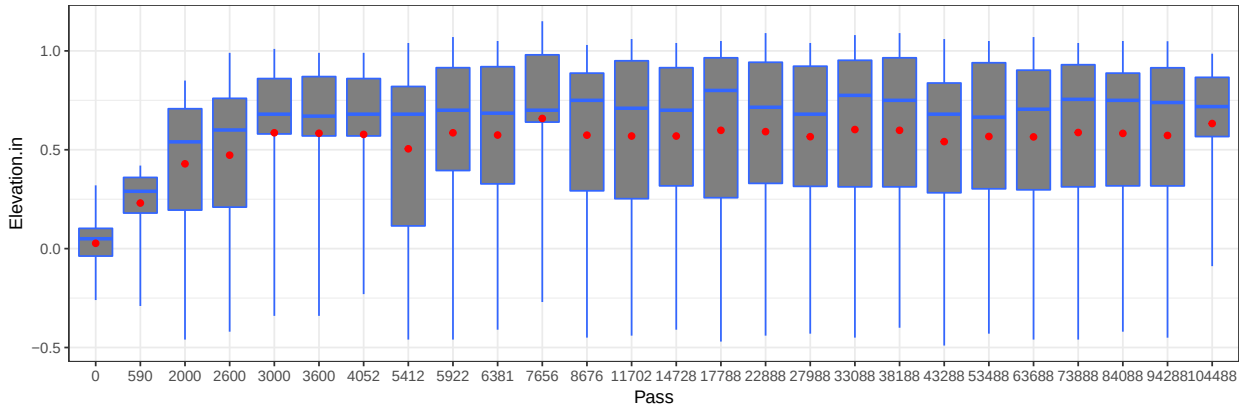

Figure 4.25: *Boxplot for Profile of Cross Section 4 (Column Number = 4)*

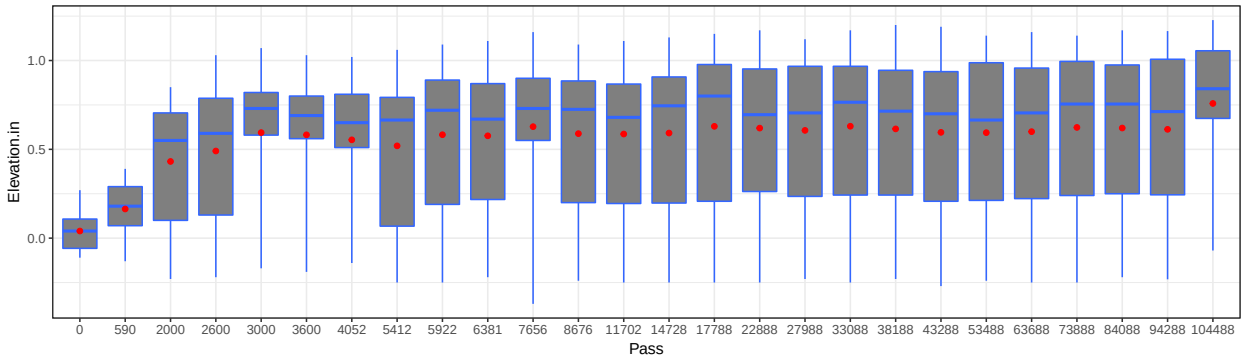

Figure 4.26: *Boxplot for Profile of Cross Section 5 (Column Number = 5)*

As shown in Figure 4.24 and Figure 4.25, for the cross-section adjacent to the wheel path, the change in adjusted elevation is obvious, though the changes are smaller than those of the wheel-paths. The change in adjusted elevation for the cross-section 3 is 0.72 inch, and it is basically the same for the cross-section 5 (Figure 4.26).

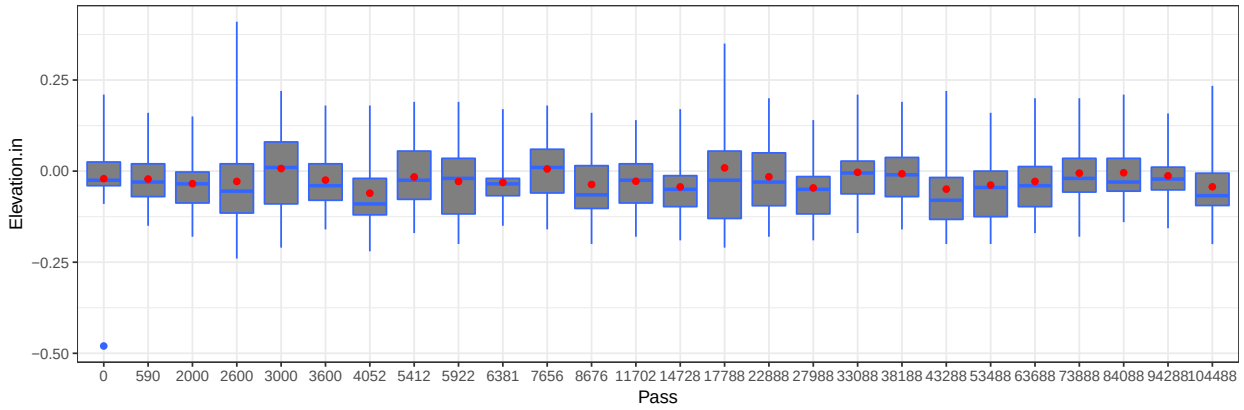

Figure 4.27: *Boxplot for Profile of Cross Section 6 (Column Number = 6)*

It was seen in Figure 4.27 the change in profile for the cross-section 6 was marginal, which was less than 0.1 inch. This was also an indication of the consistency of the profile measurement work.

4.5.3 Section with Geogrids at the Bottom of Aggregate Base

For the section with geogrid installed at the bottom of the aggregate base layer (section-B), serious cracking begun to occur at 4000-axle load passes. The cracking occurred outside of each wheelpath, as shown in Figure 4.28. As the load repetitions increase to 8,782 passes, the maximum width of the cracking increase from 0.25 inch to 0.5 inch. Furthermore, the rutting depth of this section develops rapidly as the axle load repetitions increases. When the load repetitions reaches 8,782, the maximum rutting depth became as high as 2.5-inch.

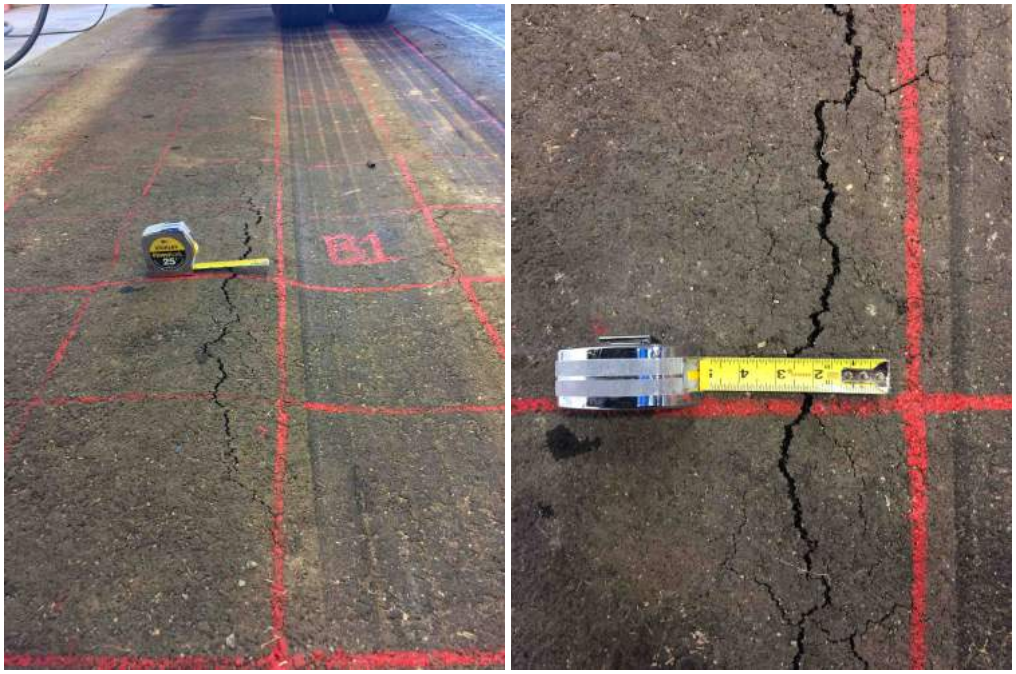

Figure 4.28: *Cracks on Section with Geogrids at the Bottom of Base Layer*

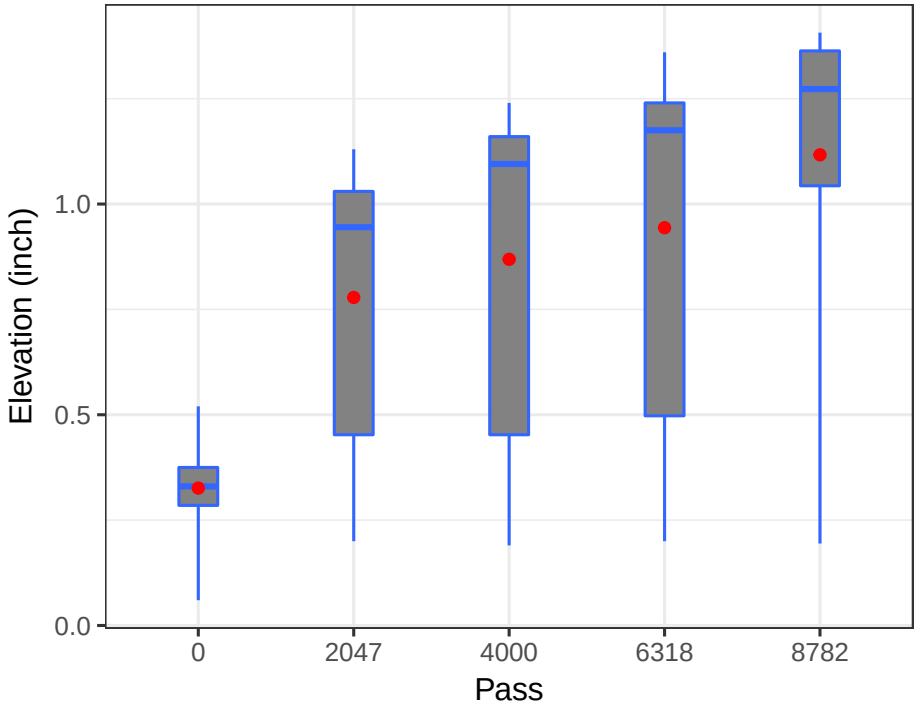

Figure 4.29: *Boxplot for Profile of Left Wheel Path Center (Column Number = 4.5)*

Figure 4.29 shows a boxplot for the profile of the left wheel path of the section-B. When the axle load repetitions increased to 8,782, the change in adjusted elevation of this cross-section is 0.78-inch. However, the change for the right wheel path is smaller, which was only 0.23-inch.

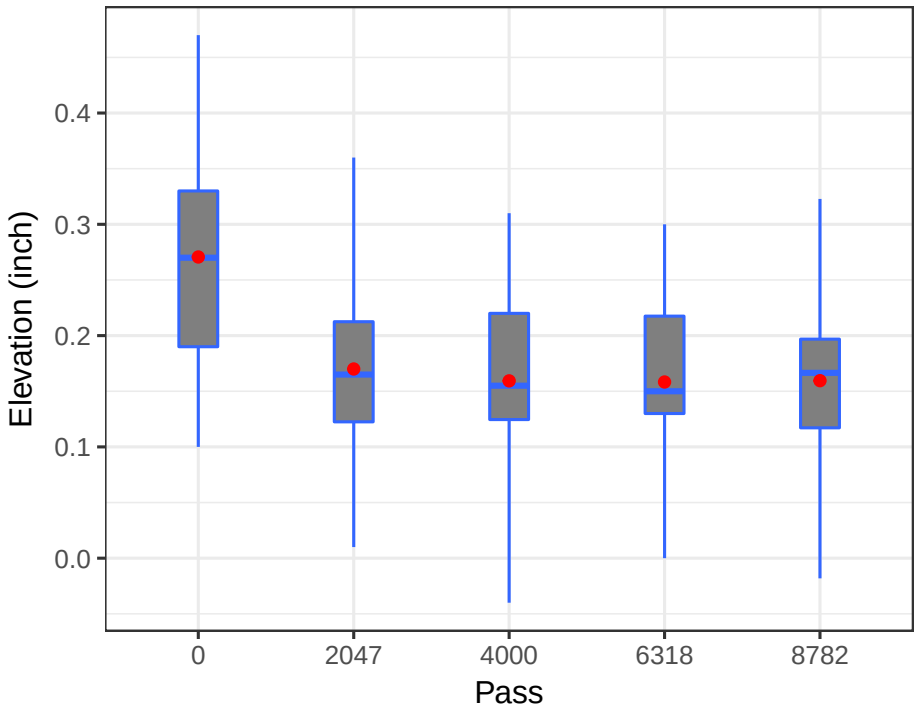

Figure 4.30: *Boxplot for Profile of Left Wheel Path Center (Column Number = 3)*

Figures 4.30 through 4.32 show the profile of the cross-sections next to the two wheel-paths. It was observed that the change in adjusted elevation was pronounceable. This was due to the large deformation accumulated at a relatively short period of time, and the depression in the wheel-path area was accompanied by the bulging in the adjoining area, such as those in cross-section 3, 4, and 5. This was different from the control and the section M. A probable reason for the control section achieved good compaction quality was that the machinery had enough space to maneuver and apply the compaction. Although, due to limited space for compaction, the moisture content and thickness variations in this section may also have caused the difference in the construction quality of section B. Figure 4.33 plots the elevation variation of cross-section 6 with the axle load repetitions. It was clearly shown that the elevation increases consistently as the axle load repetition increases.

4.6 Falling Weight Deflectometer Test Before APT Testing

A falling weight deflectometer borrowed from the TDOT was used to performed the deflection tests. The FWD is manufactured by Dynatest, and the model of this FWD is 8002-200. The FWD is a device to simulate deflection of a pavement surface caused by a fast moving truck. The

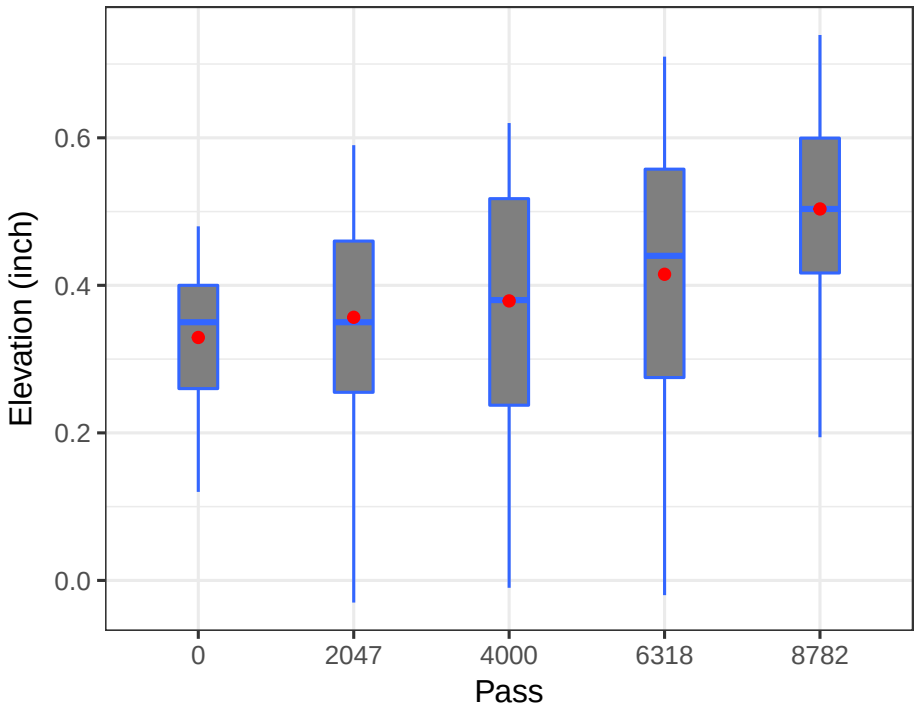

Figure 4.31: *Boxplot for Profile of Left Wheel Path Center (Column Number = 4)*

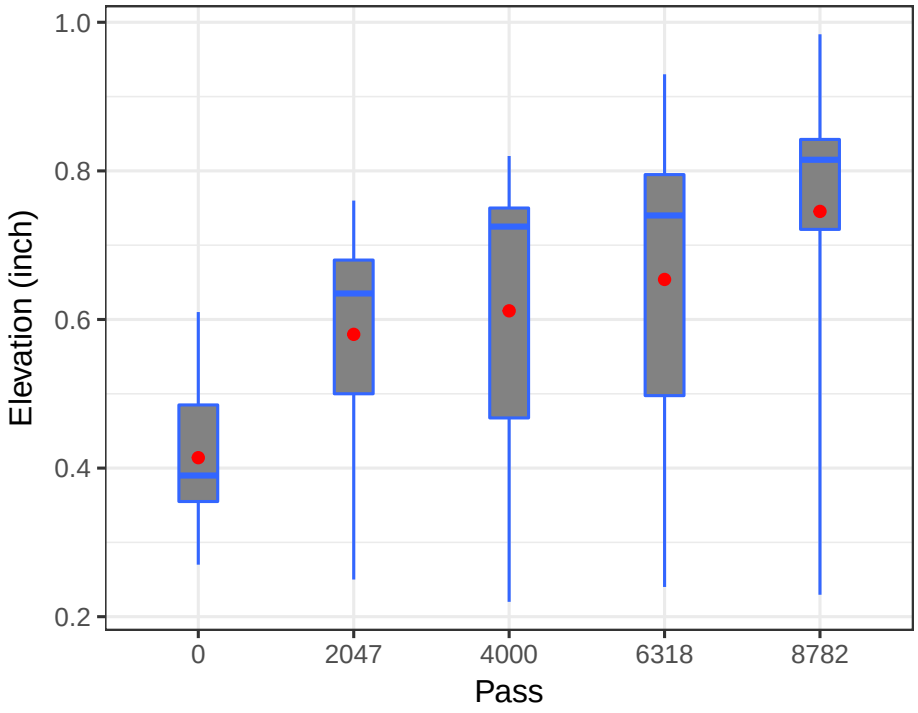

Figure 4.32: *Boxplot for Profile of Left Wheel Path Center (Column Number = 5)*

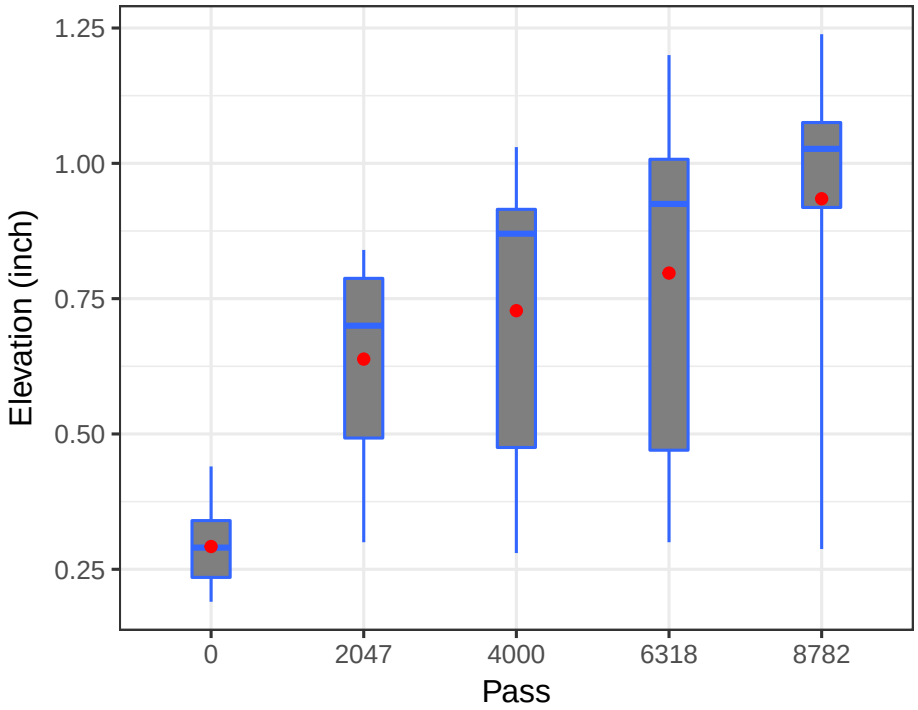

Figure 4.33: *Boxplot for Profile of Left Wheel Path Center (Column Number = 6)*

FWD generate a load pulse by dropping a weight. This load pulse is transmitted to the pavement through a 30-centimeter (cm) diameter circular load plate. Figure 4.34 showed the FWD trailer used for the deflection test.

Figure 4.34: *Falling Weight Deflectometer (model#: 8002-200)*

Table 4.1 shows the distance of the seven sensors regarding the center of the loading plate.

The first sensor, D1, is mounted at the center of the loading plate. Generally, four drops were applied at each station, namely, the location where the loading plate was rested on. The load applied at each drop is different, which increases drop by drop. As shown in Figure 4.35, the drop load increased from 380 kPa for the first drop to 928 kPa for the fourth drop. Obviously, as the drop load increase, the deflection increases. Figure 4.35 gives the deflection basins of resulted from the four drops.

Table 4.1: *FWD Geophone Locations (unit: mm)*

D1	D2	D3	D4	D5	D6	D7
0	203	305	457	610	914	1219

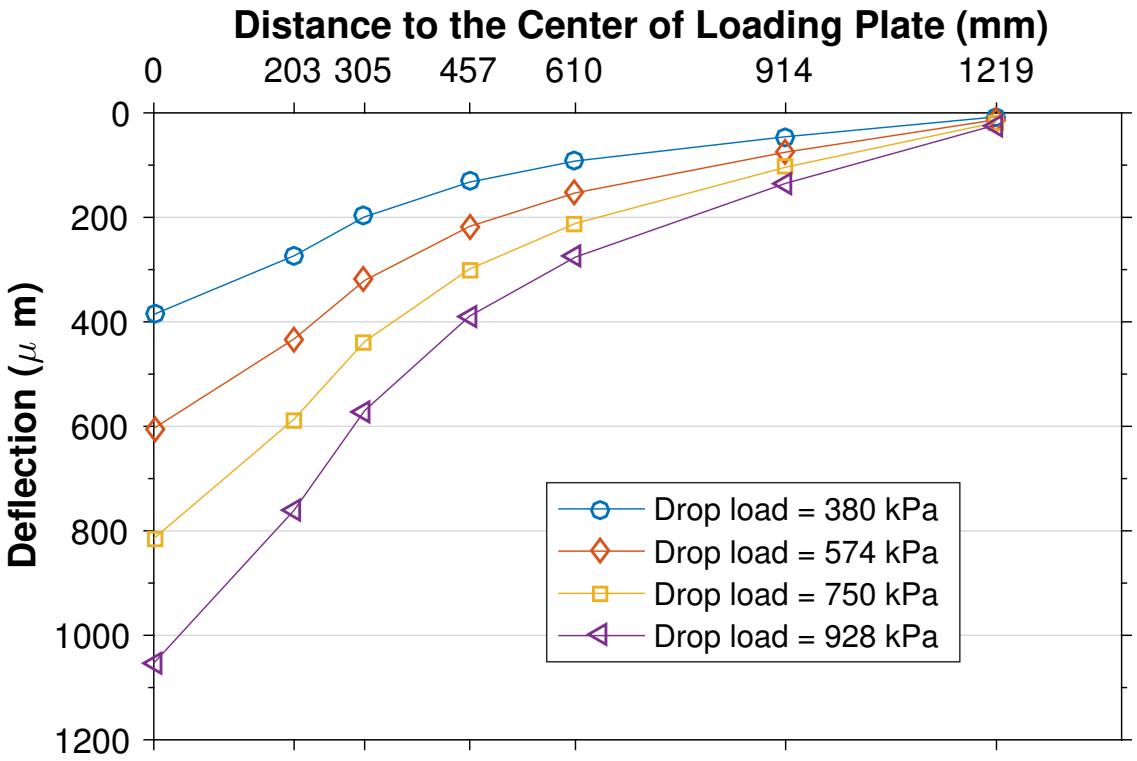

Figure 4.35: *Deflection Basins of Different Load Levels*

Figure 4.36 shows the time history plots for the stresses under the loading plate of FWD. As seen in Figure 4.36, the stresses under the loading plate increase as the load increases. The plots in Figure 4.36 is also in line with the observation that FWD simulates the nature of the loading applied by a fast moving vehicle, which is an impulse load.

Figure 4.37 shows the locations at the test pit where the FWD tests were conducted. As reported previously, the geogrids were placed at the two sides of the test pit, whereas the middle lane was used as the control which used no geogrid. For each location, two consecutive tests

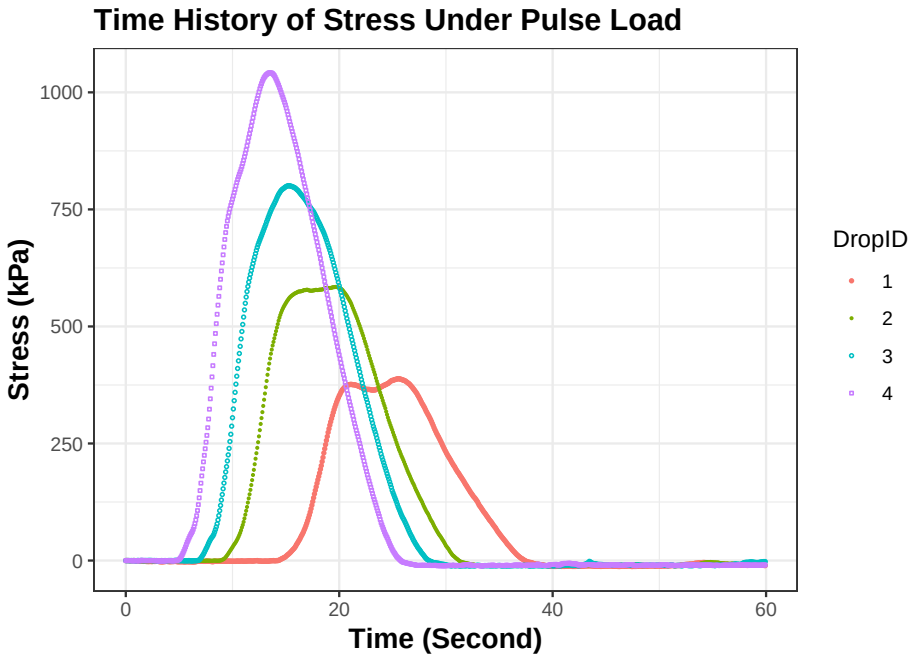

Figure 4.36: *Time History of Stress Under a Pulse Loading*

were conducted, and the results were then averaged to account for potential operation errors. The resulted deflections were used for two kinds of analyses, moduli backcalculation and direct deflection basin comparison. As expected, when the geogrids were mobilized in the aggregate base course, the moduli of the base course will be increased due to the reinforcement of the geogrid. However, the FWD deflection test may not be able to detect this reinforcement due to the nature of the deflection test. Because unlike the truck loads applied to pavement which include vertical pressure, horizontal and longitudinal shear stress, the FWD applies only vertical pressure.

Numerous computer programs are available for back-calculating the layer properties of the pavement through FWD deflection basins. The MODULUS developed by the Texas Transportation Institute (TTI) is one of the most popular one. The version 6.1 of MODULUS was used in this analysis. Figure 4.38 shows the interface of the back-calculation routine of the MODULUS program. It is documented in the manual of the MODULUS, when the thickness of asphalt mixture layer is less or equal to three inches, the backcalculated moduli of the asphalt layer will be fixed Liu and Scullion (2001) . In other words, the maximum of the range for the moduli of the asphalt layer is equal to its minimum. As shown in Figure 4.38, the range of moduli of the asphalt mixture was set to 720 to 1040 ksi. Since the thickness of the asphalt layer in the test pit is three inches, the backcalculated the modulus of the asphalt layer would be fixed at 720 ksi. This is acceptable for the tests in this study, because it is the moduli of the aggregate base layer is of interest.

Figure 4.39 shows the backcalculated moduli of the aggregate base course using only the deflection basins resulted from the largest drop loads. As is seen in Figure 4.39, the moduli of base course in the lanes at both sides which including geogrid are similar. However, the moduli of the base course is much larger in the middle lane (control) which used no geogrids. This is

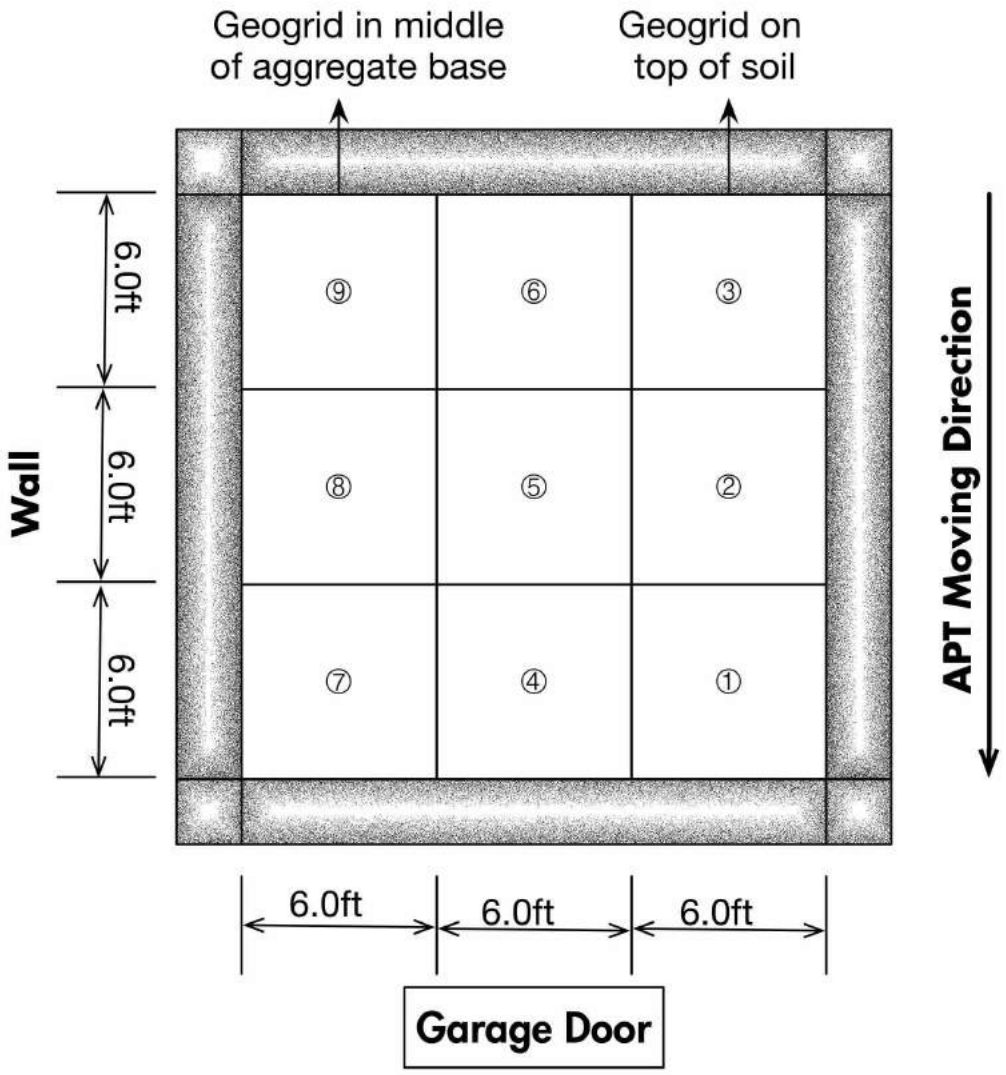

Figure 4.37: *FWD Test Locations Layout*

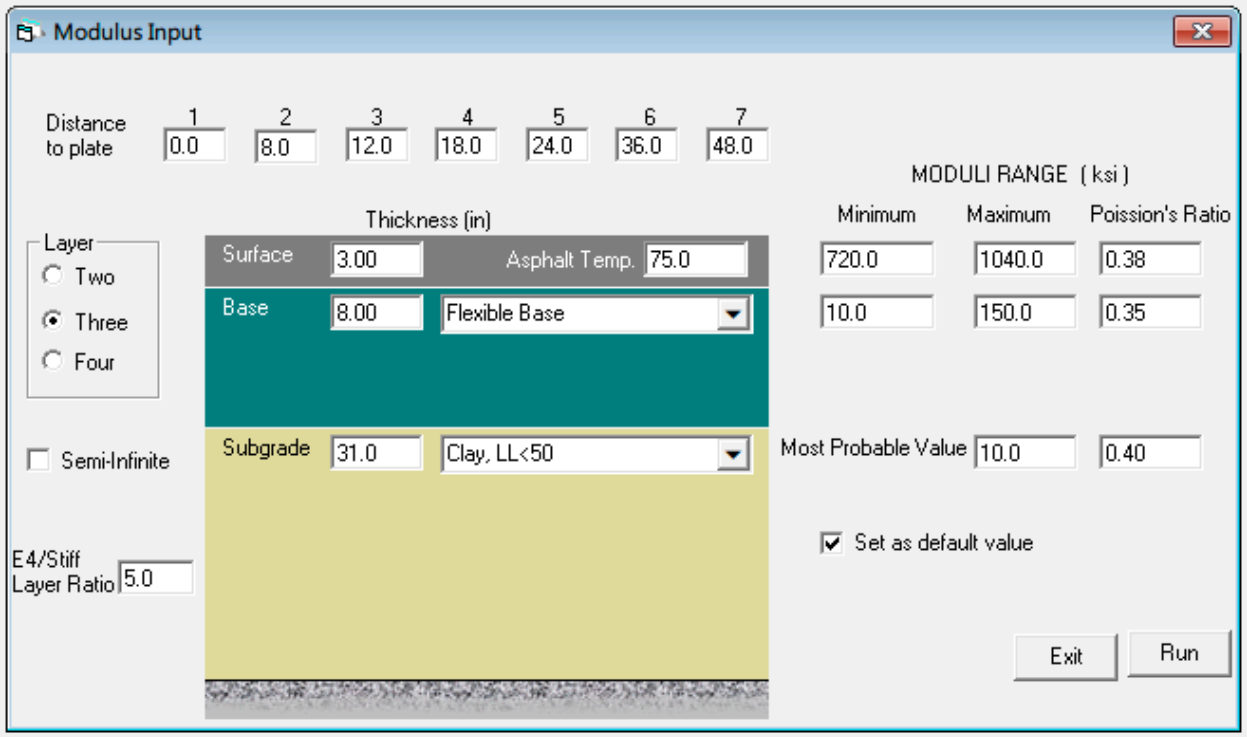

Figure 4.38: *Moduli Backcalculation Using MODULUS*

unrealistic, if all the three lanes were constructed uniformly, then even the geogrids have no reinforcement on the aggregate base, the back-calculated the moduli of the base course should be similar. To verify that this difference between the lanes with geogrids and the control was not caused by operation errors, two runs of tests conducted at different days. Still, the results of the two runs of tests showed the same trend. Therefore, the operation error is not the cause of this. There are several reasons contributed to this abnormal trend, which could be,

- The errors introduced by the MODULUS;
- The boundary effect of the walls in the test pit;
- The differences in compactions resulted from nonuniform construction;
- There are more rocks in the middle lane than the two lanes in the sides;

To find whether the MODULUS program has caused this abnormal difference, the deflection basins at different locations were compared directly.

Figure 4.40 shows the plots for the deflection basins at different locations of the test pit. The top row indicates the locations of 3, 6, 9, while the middle row represents the locations of 2, 5, 8, and the bottom row includes the locations of 1, 4, 7 in Figure 4.37, respectively. The lanes labeled as B and M indicate the geogrids at the bottom and middle, respectively. Whereas, the lane labeled as N indicates no geogrids was used, which is the control lane. As observed in Figure 4.40, the deflections at the locations in the control lane are the smallest, especially for the locations in the middle row and the bottom row. It was also found in Figure 4.40 that the base course moduli

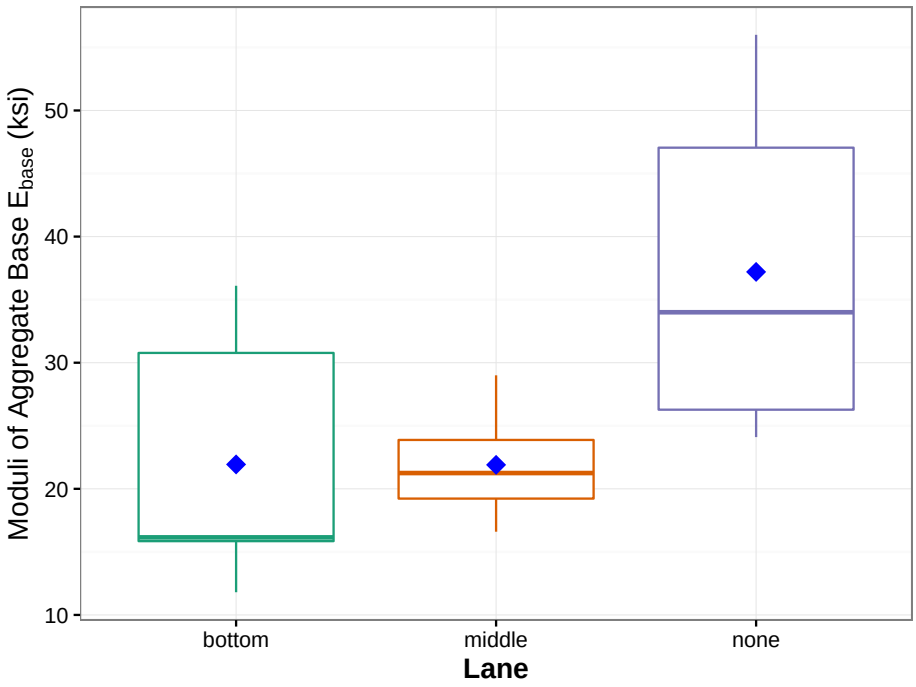

Figure 4.39: *Backcalculated moduli of the aggregate base course*

of both lanes with geogrids are very similar, which implies that the FWD test may not capable of detecting the difference in reinforcement produced by the geogrids. Regarding the boundary effect of the walls in the test pit, it is believed that the locations in the middle row are affected at the least degree. However, as indicated in Figure 4.40, the deflections at the control are the smallest, followed by the lane has geogrids in the middle of the aggregate base course, and then the lane with geogrids placed at the top of the subgrade. The same observation applies to the three rows of locations. However, since only location 5 is free of the effect of the boundary, it is possible that the boundary effect of the walls contributed to this problem.

In this study, two deflection basin parameters apart from the deflections themselves were investigated. As reported by Xu et al. (2002), the base damage index (*BDI*) and base curvature index (*BCI*) are closely correlated to the base course. The base damage index (*BDI*), which is defined as, $BDI = D300–D600$, is the most sensitive parameter for the base modulus. The base curvature index (*BCI*), which is defined as $BCI = D600–D900$, is ranked the second most sensitive parameter for both base and subgrade.

Figure 9 shows the box-plots for the base curvature indices (BCI) of the deflection basins collected at the three different lanes. Similar to a single deflection value, a lower BCI indicates a stronger structure. It is seen in Figure 9 that the BCI of the control lane (N) has the lowest BCI, while the BCI of two lanes with geogrids (B and M) are similar.

Similar to the BCI, lower value of BDI indicates stronger structure. As observed in Figure 4.42, the control lane has the lowest BDI, followed by the lane with geogrids at the bottom of the base course. The BDI of the lane has geogrids in the middle of the aggregate base course showed the highest BDI, but the difference between the two lanes with geogrids is less than 8%. Clearly, the information provided in Figure 4.42 and Figure 4.42 is similar to those presented in Figure 4.40.

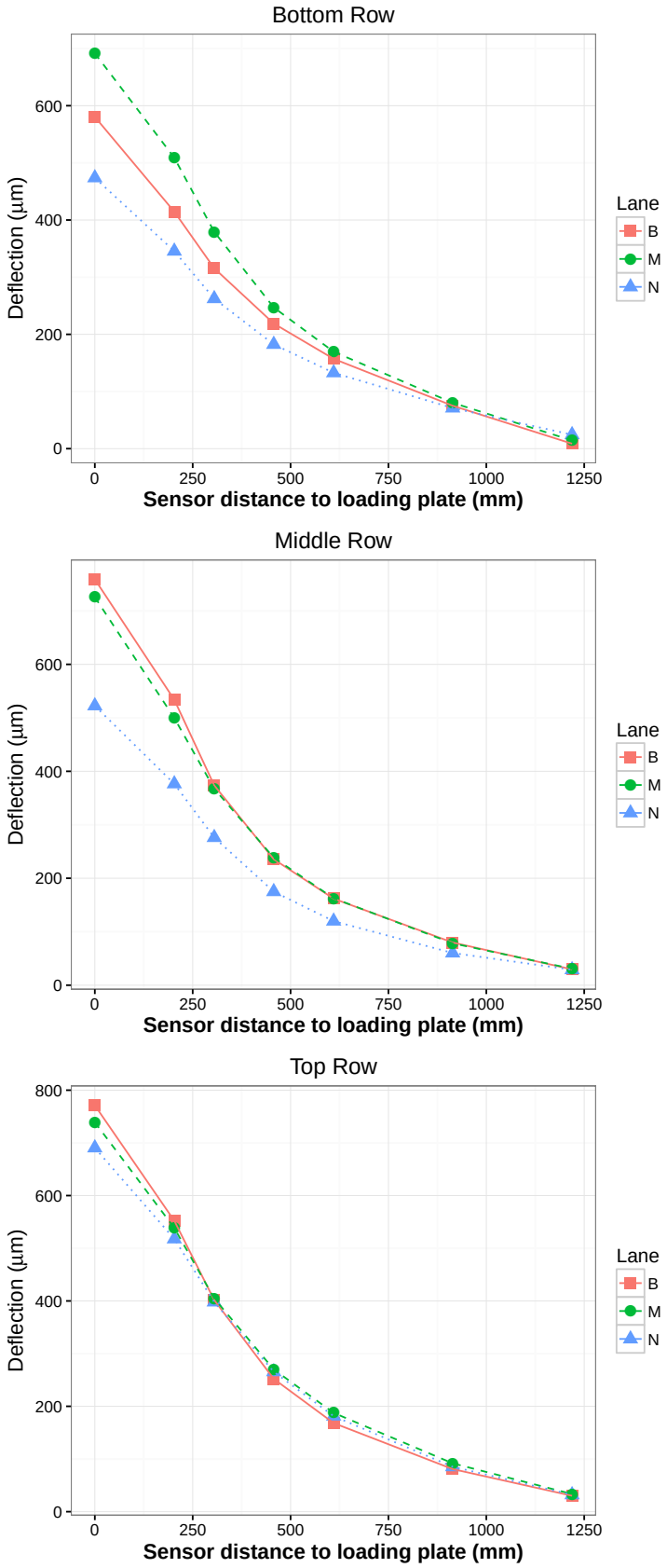

Figure 4.40: *Comparison of the deflection basins at different locations*

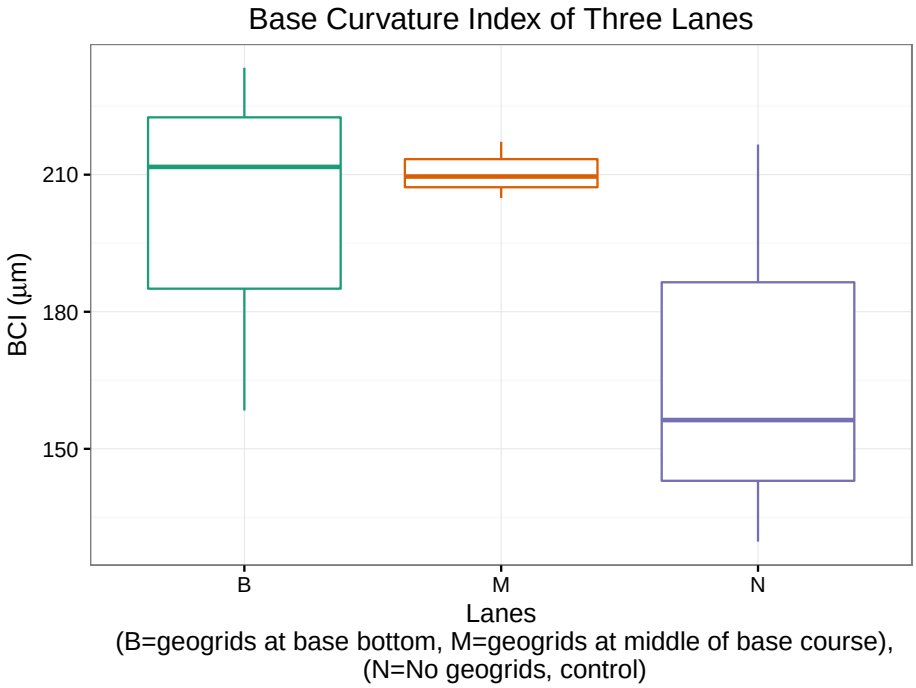

Figure 4.41: *Base Curvature Indices of the Three Lanes*

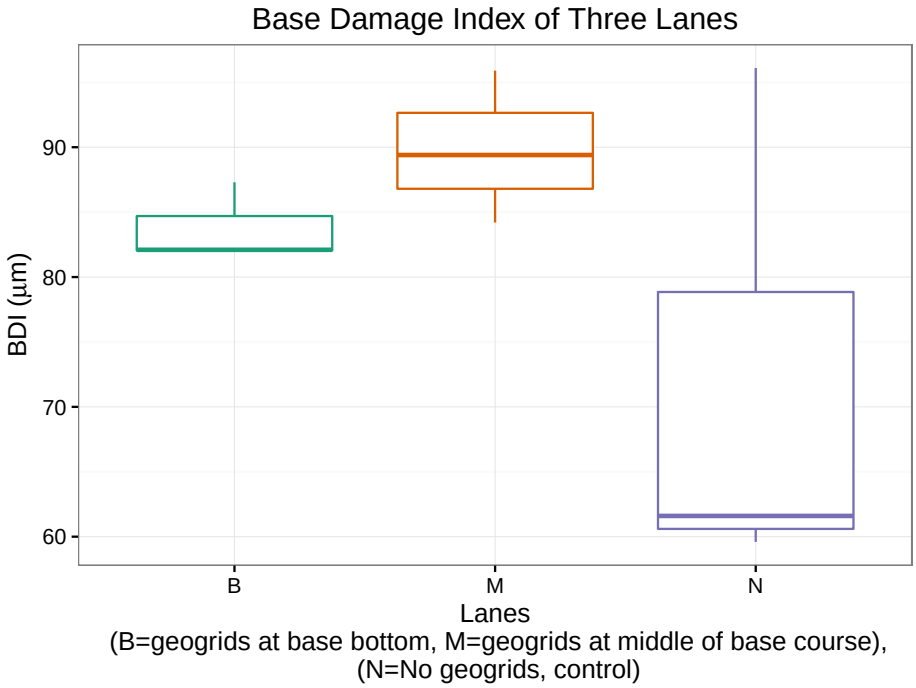

Figure 4.42: *Base Damage Indices of the Three Lanes*

According to the analyses above, the operation error of the FWD is believed not to be the cause of this problem. Thus, probable causes of this problem are the non-uniformity in the compaction of the subgrade and aggregate base and the boundary effect of the walls in the test pit. In other words, the FWD may not be able to detect the reinforcement effect of the geogrids.

4.7 Falling Weight Deflectometer Tests After APT Testing

FWD tests were conducted in the ruts and the adjacent area where no rutting happened (Figure 4.43). The motivation for collecting deflection information at both the loaded and unloaded areas is to see whether the stiffness of the granular materials is different in these areas. Thus, it will help to recognize that a large deformation is beneficial to mobilize the geogrid and then contribute to the reinforcement of the granular base and the whole pavement structure.

Figure 4.43: *FWD Tests on Different Locations*

4.7.1 Summary of FWD Tests

Falling weight deflectometer tests were conducted at all the three lanes of the test pit. The moduli of the aggregate base course were back-calculated using the MODULUS program. It was found

that the moduli of the base course of the two lanes with geogrids are very similar. However, the moduli of the base course of the control lane which use no geogrids are the highest. Possible causes of this dilemma are the boundary effect of the walls of the test pit, non-uniformity in compaction of the aggregate base course and the subgrade, and the variation of soil particle size.

4.8 Forensic Trenching

4.8.1 Core Heights

To identify the failure mechanism of the test section, cores were drilled in both the wheel and non-wheel path area of each lane, as such a total of eighteen cores were taken. The heights of the cores were measured to verify the designed thickness of asphalt layer. It is a common practice to use water to cool the bit during the core process. However, the holes left by the coring test will later be used for the dynamic cone penetrator (DCP) test, and the introduction of water in the hole will soften the aggregate base and even the subgrade. To address this dilemma, a vacuum was employed during the coring process to minimize the amount of seeping into the interior of the pavement structure. Figure 4.44 illustrates the core drilling process. Figure 4.45 shows the height of cores taken from both the wheel path and non-wheel path area. As indicated, the minimum thickness was from the Lane B, which is around 2.8 inches, whereas the largest thickness value is from the control lane, which was about 4.75 inches, the difference between these two is as high as 2 inches, which would make a big difference in resisting to permanent deformation when APT loading was applied. It was also seen from Figure 4.45 that the average thickness of asphalt layer of the Lane-M is 4.1 inches and was quite consistent, as confirmed by the small widths of whisker in the box-plots.

Figure 4.44: *Core Drilling (Round 1)*

4.8.2 DCP Testing on Trafficked Test Sections

With the holes left from the coring test, the dynamic cone penetrator test was performed. The dynamic cone penetrator test is a well-accepted method to determine the on-site stiffness of un-

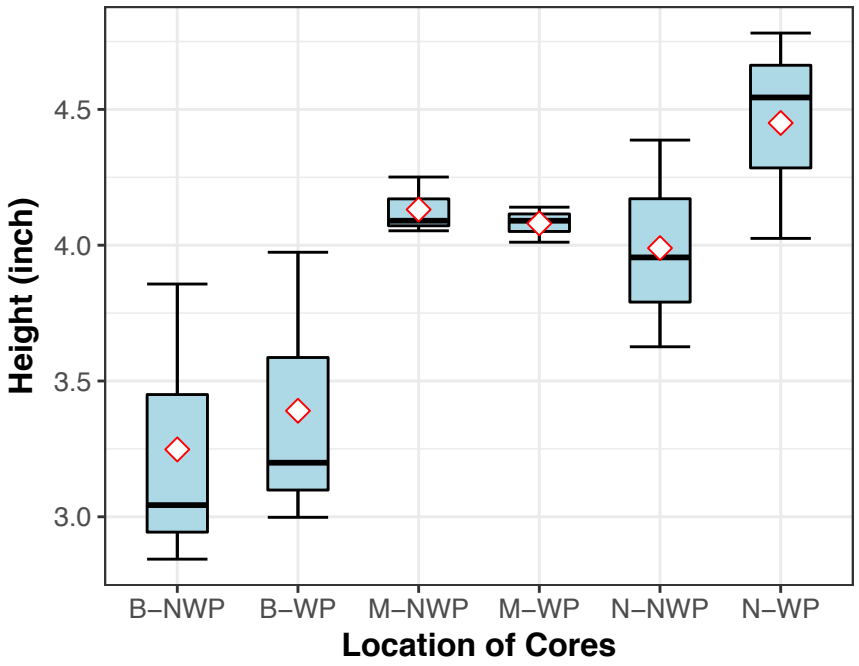

Figure 4.45: *Heights Distribution of Cores Drilled*

bounded granular materials, and its output has a very good correlation with California bearing ratio, which is again closely tied to the resilient modulus of granular materials.

Figure 4.46 shows the CBR values computed from the penetration indices of the DCP tests. As is seen in the plots, the CBR values of the subgrade in all three lanes are quite similar, and the range of the CBR is 3% to 15%. It is noted that there is an exceptionally large value in the non-wheel path area of the control (Figure 4.46a), which is probably an anomaly value due to the presence of large stone particles. As to the CBR values for the aggregate base, the CBR values in the non-wheel path area of Lane-M is the largest, followed those of the control lane. Again, the Lane-B has the smallest CBR value for its aggregate base. For the wheel-path area, the repeated APT wheel loading exerted still more compaction after the construction, which makes it more difficult to penetrate through the aggregate base for most of the test locations, thus very few observations were taken from these areas. As indicated in Figure 4.46c, due to insufficient in observations, the CBR value of aggregate base in the Lane M is smaller than the Lane B and control lane. However, the real situation is different, during the DCP testing, it is in the wheel-path area of the Lane-M we experienced the most difficulty in penetrating through the aggregate base. As is also indicated in the plots, the Lane M and control have similar CBR values.

Figure 4.47 shows overlapped plots for the computed CBR values from DCP test results. Overall, the Lane-M has the largest CBR value in the aggregate base of non-wheel path area, while the values in the Lanes M and N are similar. Regarding the stiffness of aggregate base in the wheel-path area, due to limited observations, it is difficult to tell which lane has the largest CBR value in the aggregate base. For the stiffness of subgrade in the non-wheel path area, the two lanes inclusive of geogrid show higher CBR value than the control. Likewise, for the stiffness of subgrade in the non-wheel path area, due to the difficulty in penetrating through the aggregate base in the wheel-path area, it is difficult to compare the stiffness of subgrade in these areas as

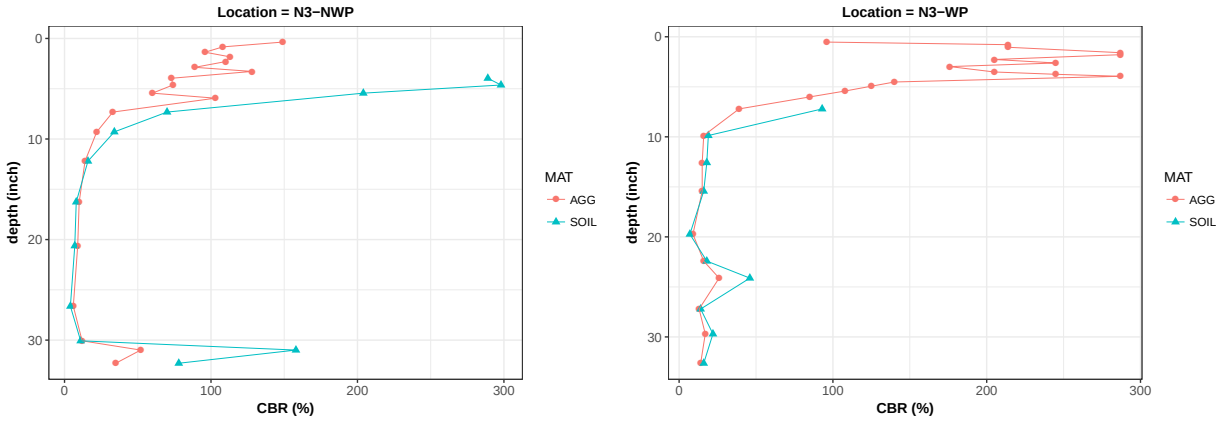

(a) *Control*

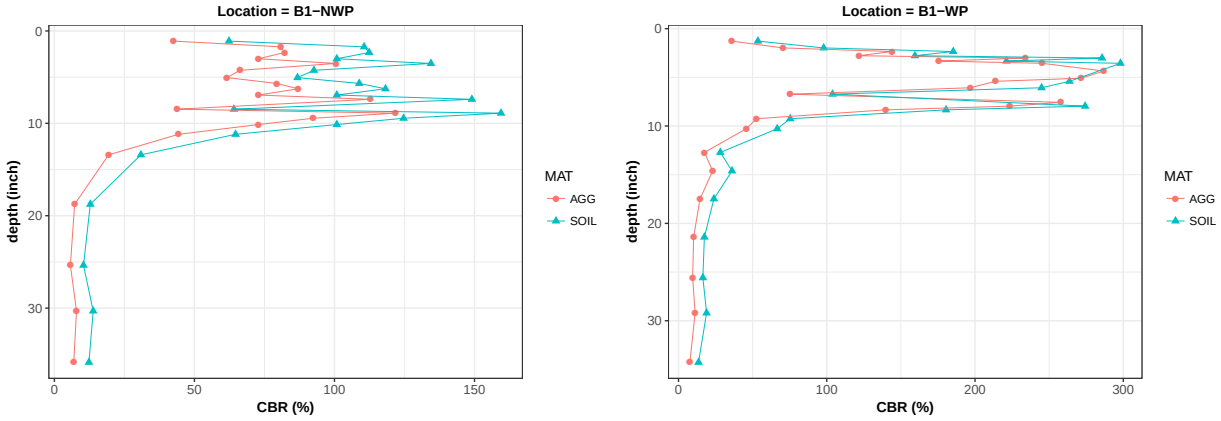

(b) *Lane B*

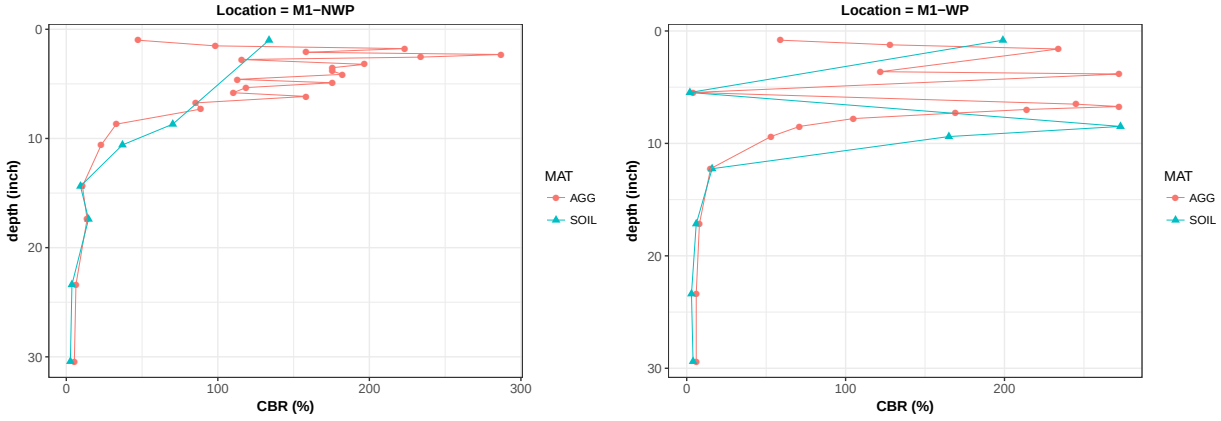

(c) *Lane M*

Figure 4.46: *CBR Values Calculated Using Penetration Indices from DCP test*

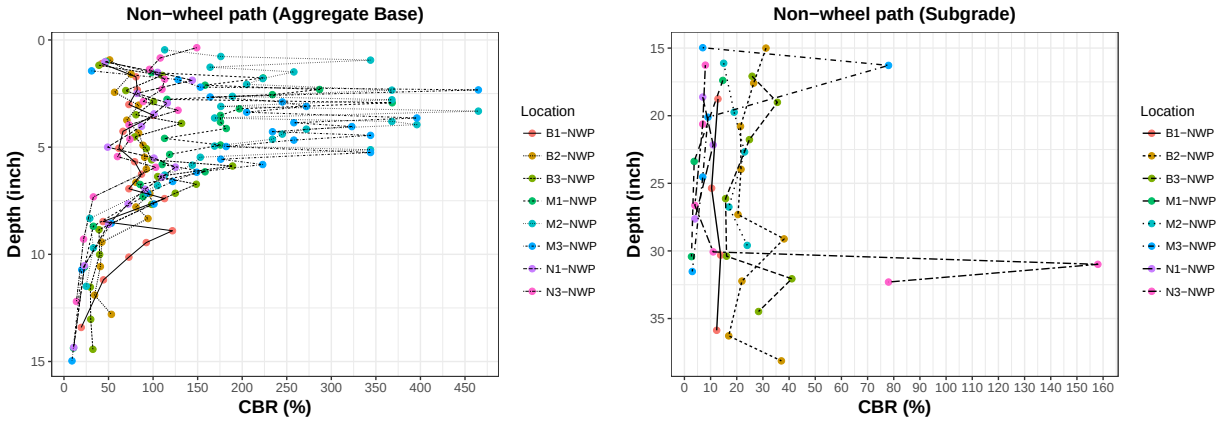

(a) *Non-Wheel Path*

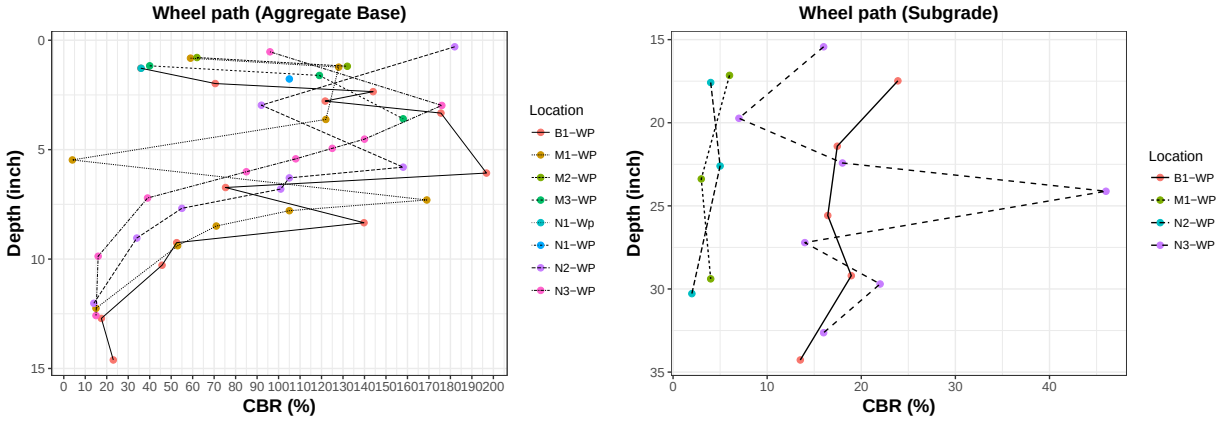

(b) *Wheel Path*

Figure 4.47: *Overlapped Plots for CBR Values in ALL Three Lanes*

well.

4.8.3 Cutted Cross Section

A forensic trenching investigation was conducted to find the causes for the failure of the pavement test sections under APT trafficking. Figure 4.48 gives an overview of the cut test pavement. It is obvious that the thicknesses of control lane and the lane with geogrids in the middle of aggregate base were significantly thicker than the one with geogrids at the bottom of the aggregate base layer. In addition, the thickness of the aggregate base in the control lane seems to be the largest, which may be the principal reason for the worst rutting resistance observed on Lane B.

Figure 4.48: *Overview of Cutted Test Pit (Round 1)*

Figure 4.50a depicts the thicknesses varies along the cross section. As indicated, the cross sectional thickness of Lane B was around 3.5 inches, and the median thickness of this lane was only slightly greater than 3 inches. However, the largest cross section thickness of Lane M was greater than 5.3 inches and a median thickness of 4.2 inches. The control section was also found significantly thicker than the Lane B, which had a largest cross section thickness of 5.1 inches and a median thickness of 4.1 inches.

Figure 4.49: *A Close-Up View of Geogrids Placement*

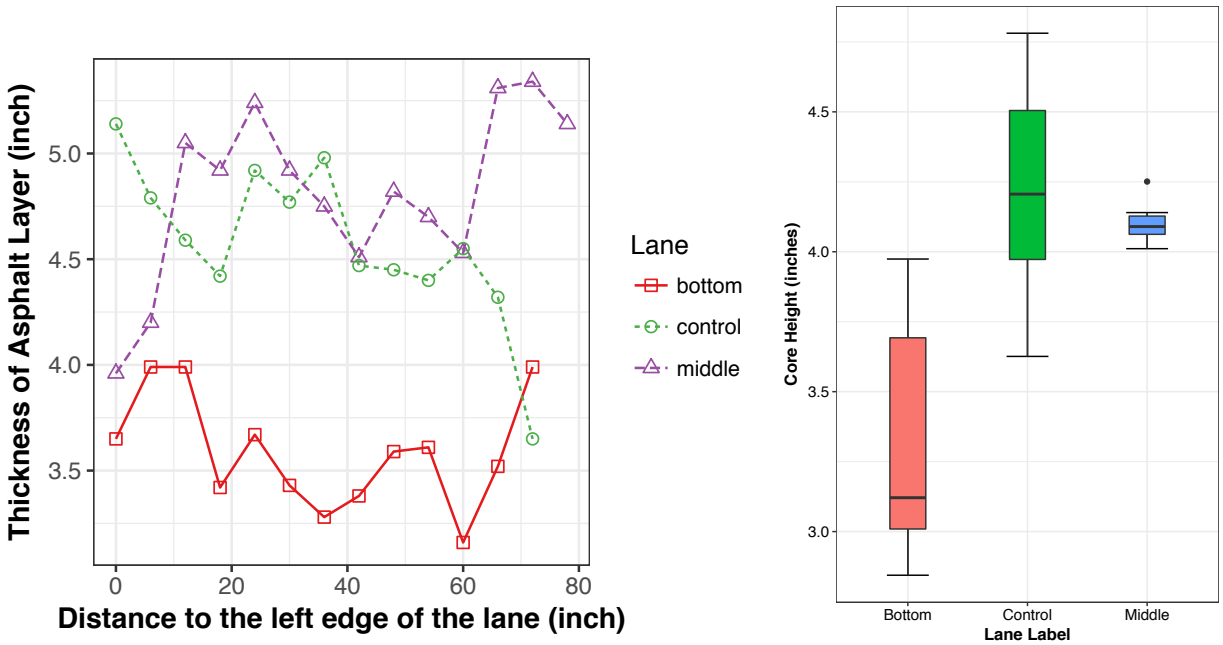

(a) *Cross Section Thickness* **(b)** *Aggregated Thickness*

Figure 4.50: *Aggregated Cross Section Asphalt Layer Thickness*

4.9 Summary

In the first round of the APT testing, a type of triaxial geogrids was employed as the base reinforcement material. Overall, the inclusion of geosynthetics significantly improved the rutting resistance of the test sections. Compared with the control section that has no geosynthetic reinforcement, the permanent deformation of Lane M was reduced by 20%. However, due to the considerably thinner asphalt thickness (compared with Lane M and control), Lane B was premature after 10,000 axle load repetitions.

Chapter 5 Second Round of APT Testing

5.1 Test Section Construction

Upon removing the pavement tested in the first round, about two feet of soil from the top of the existing subgrade was taken out as well. Before placing the new pavement in the test pit, new subgrade soil has to be refilled and compacted. Figure 5.1 through Figure 5.5 depict the reconstruction process of the subgrade. Given the lesson learned in the first round of the testing, more caution was used in control the thickness of each layer of the pavement during the second round. As shown in Figure 5.4, after placing each lift of material, the thickness was checked with a rope measure. In addition, because in the vicinity of the edge area, it is difficult for both the caterpillar excavator and the steel wheel roller to get good contact with the soil in this region, a hand-held vibrator was used to compact and level these areas (Figure 5.5). After the compaction, the density of the subgrade was checked with a nuclear gauge in nine locations (three locations in each lane), as shown in Figure 5.6.

Figure 5.1: *Refilling Subgrade Soil*

Figure 5.2: *Pre-Compacting Refilled Subgrade Soil with a Caterpillar Excavator*

Figure 5.3: *Compacting and Leveling Subgrade Soil with a Steel Wheel Roller*

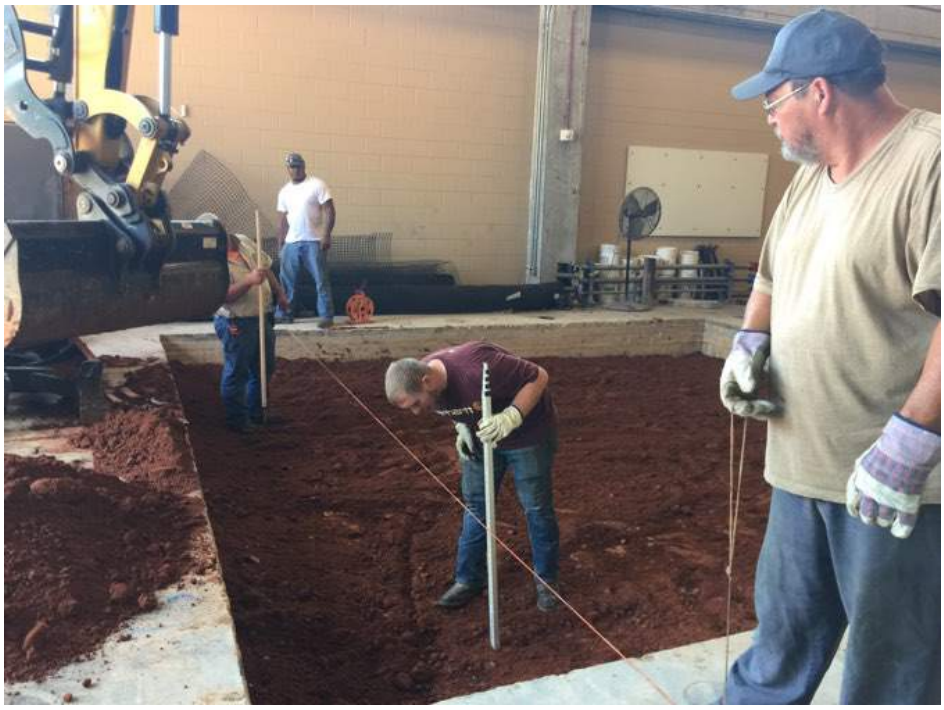

Figure 5.4: *Controlling the Thickness of Subgrade*

Figure 5.5: *Compacting the Edge Area with a Hand-Held Vibrator*

Figure 5.6: *Checking Subgrade Density with a Nuclear Gauge*

5.2 Thickness Verification

In order to verify the thickness of asphalt layer, cores were drilled at each end of the test pit (east and west). Two cores were taken from each lane, which amount to six cores in total. Figure 5.7 shows the location of coring at one end of test section. After taking the cores, the thicknesses of the cores were compared, as shown in Figure 5.8. Figure 5.9 indicates a layout of the test sections. The cores were taken at the east and west ends of the test section. It is seen that the thicknesses of asphalt layer of the three lanes is quite close, with the thickness of the lane with geogrids. Table 5.1 provides the measured heights of the cores from the three lanes, and it is found that the lane B has the thickest asphalt layer, followed by the lane M and the control lane. However, given the maximum nominal aggregate size of the asphalt mixture, these differences in thickness could be considered as insignificant.

Table 5.1: *Core Height at Different Locations*

	Lane-Control (inch)	Lane-Bottom (inch)	Lane-Middle (inch)
Core-1	3.75	4.25	4.0
Core-2	4.0	4.25	4.25
Average Height	3.88	4.25	4.13

Figure 5.7: *Coring Test Conducted to Verify Asphalt Layer Thickness*

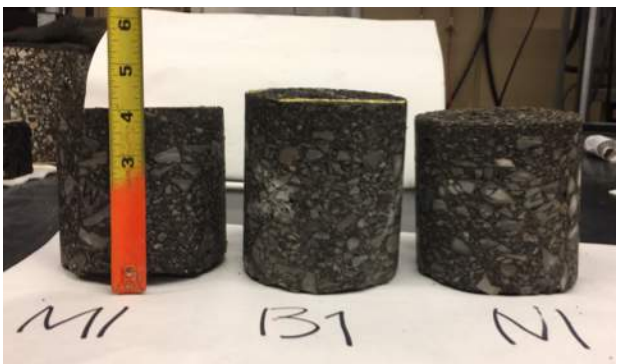

(a) *West Side of Lane*

(b) *East Side of Lane*

Figure 5.8: *Verification of asphalt layer thickness (B: lane B; M: lane M; N: control)*

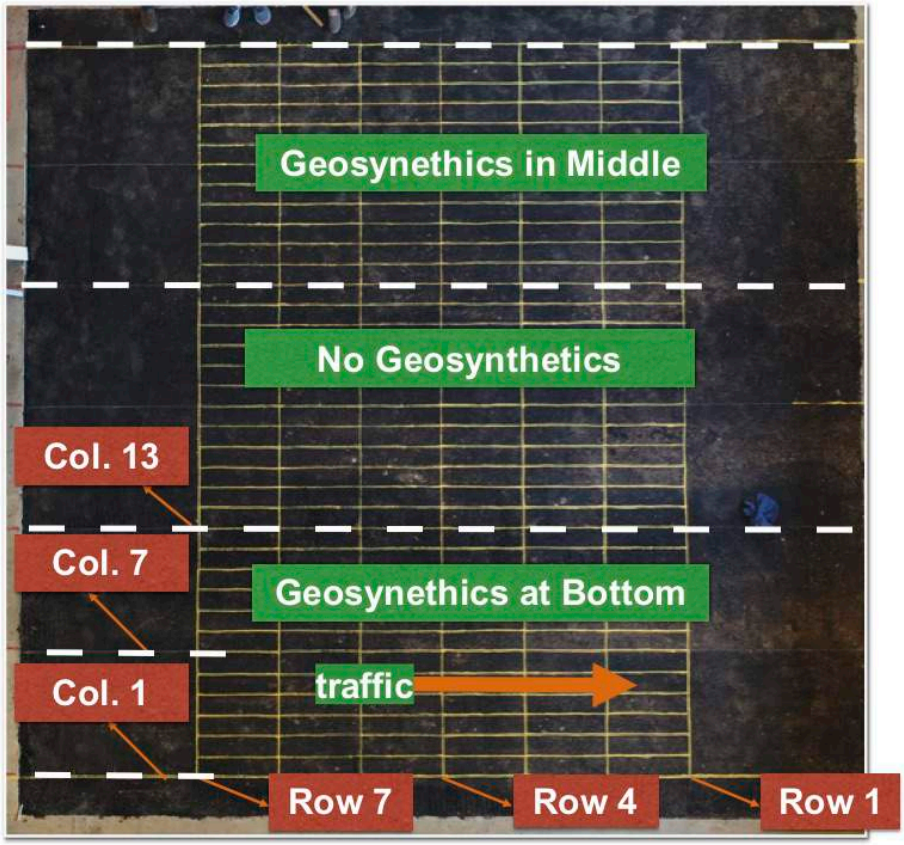

Figure 5.9: *Profile Grids*

5.3 APT Testing Profiles

5.3.1 Control Lane

Deformation Curves

Figure 5.10 through Figure 5.14 show the transverse profiles vary with the axle load repetitions in the control section. The cross-sections row-6 and row-7 (not shown) were found to have the least deformation. After 100,000 axle load repetitions, the deformations in these two cross-sections are less than 0.25 inch. The largest deformation was found in the row-1, which is 0.96 inch, followed by row-2 and row-3, where the deformations are 0.94 inch and 0.9 inch, respectively.

Aggregated Profiles Results in Box-plots

Figure 5.15 through Figure 5.27 show the changes of longitudinal profile due to the accumulation of axle load repetitions in terms of box-plots. Each boxplot in these plots indicates the average profile across all seven transverse cross-sections. The diamond in the boxplot indicates the mean of the profiles, while the bar in the box represents the median of the profiles. Often, the median is more robust to the influence of anomaly values. As is seen, sections that are away from the wheel

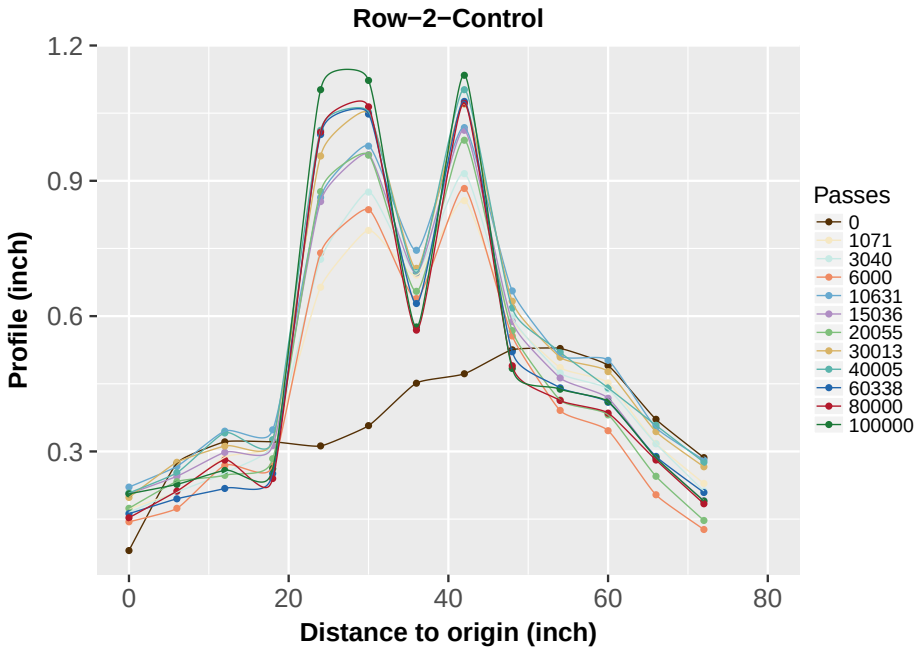

Figure 5.10: *Profile of Cross-Section-2 in Control Lane (Row-2)*

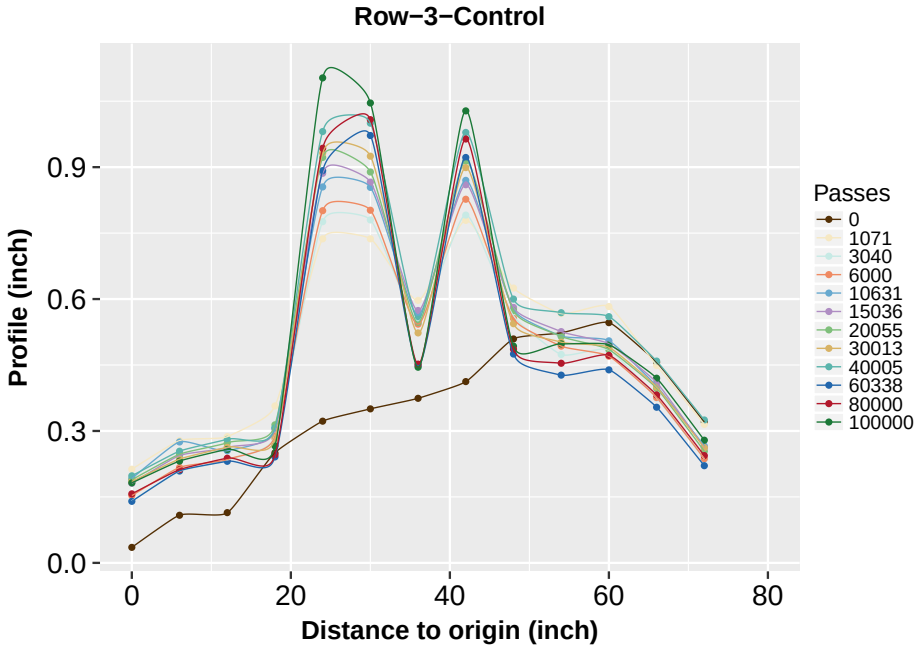

Figure 5.11: *Profile of Cross-Section-3 in Control Lane (Row-3)*

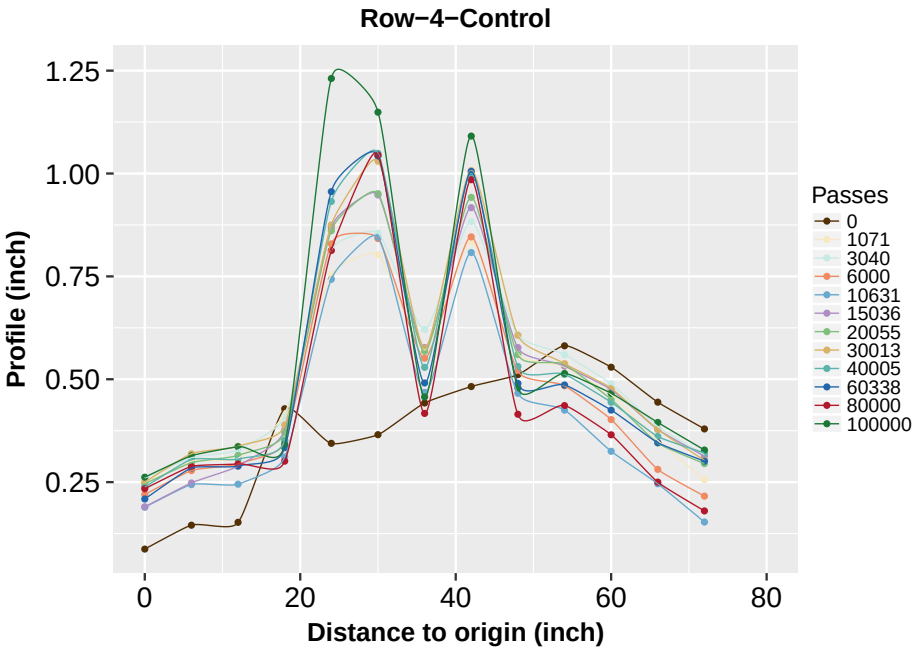

Figure 5.12: *Profile of Cross-Section-4 in Control Lane (Row-4)*

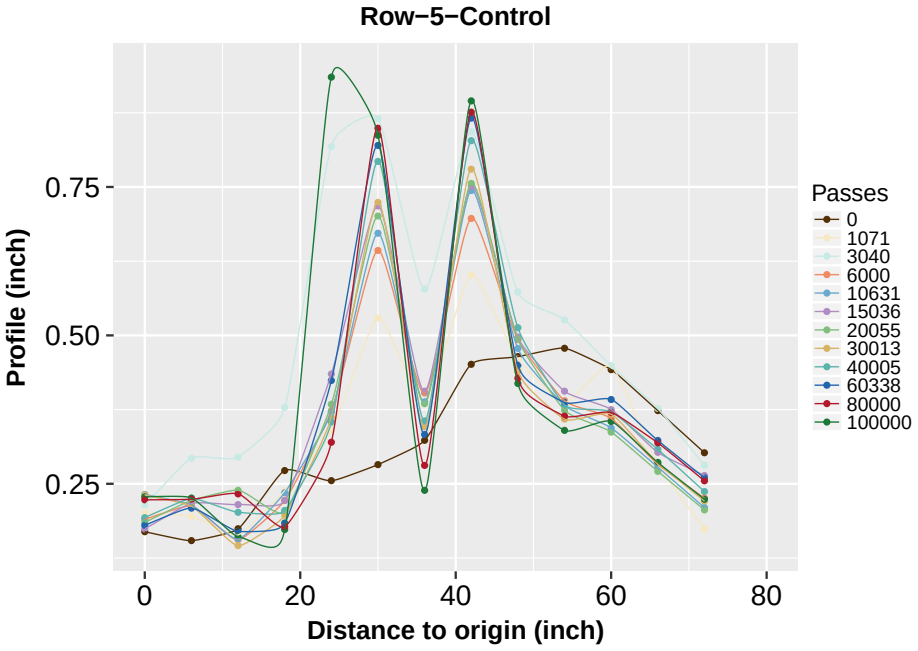

Figure 5.13: *Profile of Cross-Section-5 in Control Lane (Row-5)*

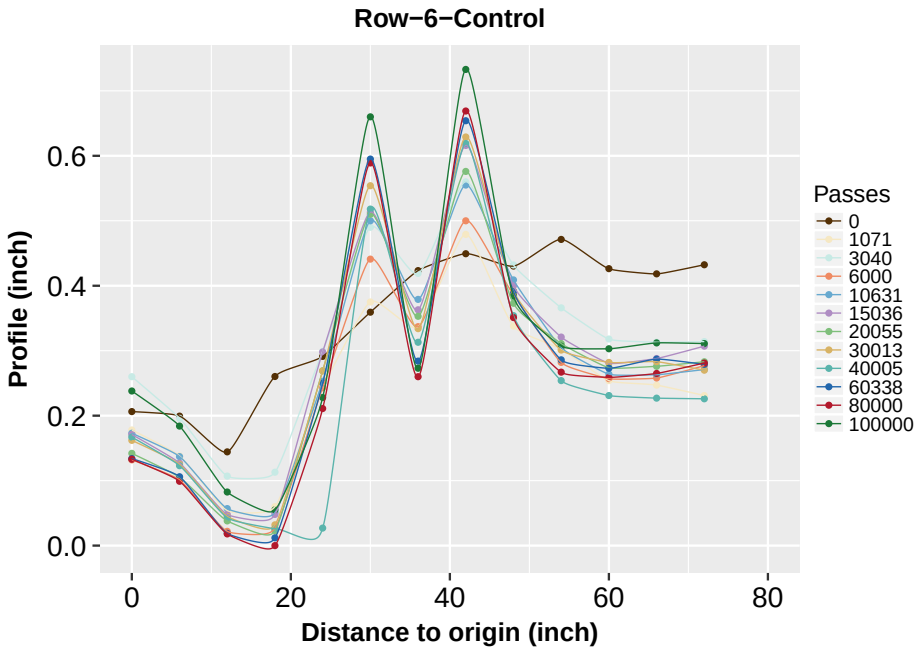

Figure 5.14: *Profile of Cross-Section-6 in Control Lane (Row-6)*

paths experienced very few deformation, as the medians of the profiles remain almost constant. These cross-sections include column-1 through column-3, and column-9 through column-13. For column-9 through column-13, the average profiles measured before trafficking seem to be slightly higher than those after trafficking, which was probably resulted from measuring error. As expected, the largest deformation occurred in the vicinity of the two wheel-path areas. The largest change in the profile's median value was found in column-5 (Figure 5.19), which is about 0.89 inch.

5.3.2 Aggregate at Bottom of Aggregate Base (Lane B)

Deformation Curves

Figure 5.28 through Figure 5.32 are the transverse profiles for the lane with geogrid installed at the bottom of the aggregate base (Lane B). It was observed that the deformations measured at cross-section 2 through 5 were similar, which are around 0.5 inches. The cross-section 6 (Figure 5.32) had the smallest deformation. Compared to the control lane, the largest deformation in the lane-B was only 50% of that of the control lane.

Aggregated Profiles in Box-Plots

Figure 5.33 through Figure 5.45 show the longitudinal profiles change with the axle load repetitions for the Lane B. Similar to the situation in the control lane, very few deformations were found in the longitudinal profiles that are away from the wheel-path areas. These cross-sections include column-1 through column-5, and column-10 through column-13. The columns that expe-

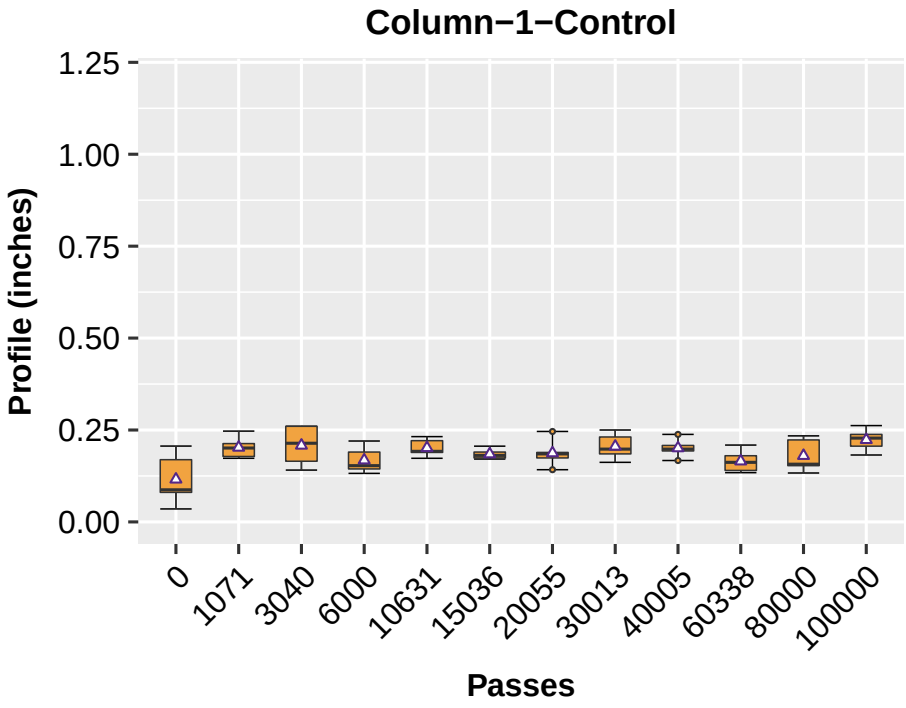

Figure 5.15: *Longitudinal profile change with axle load repetitions (Column-1)*

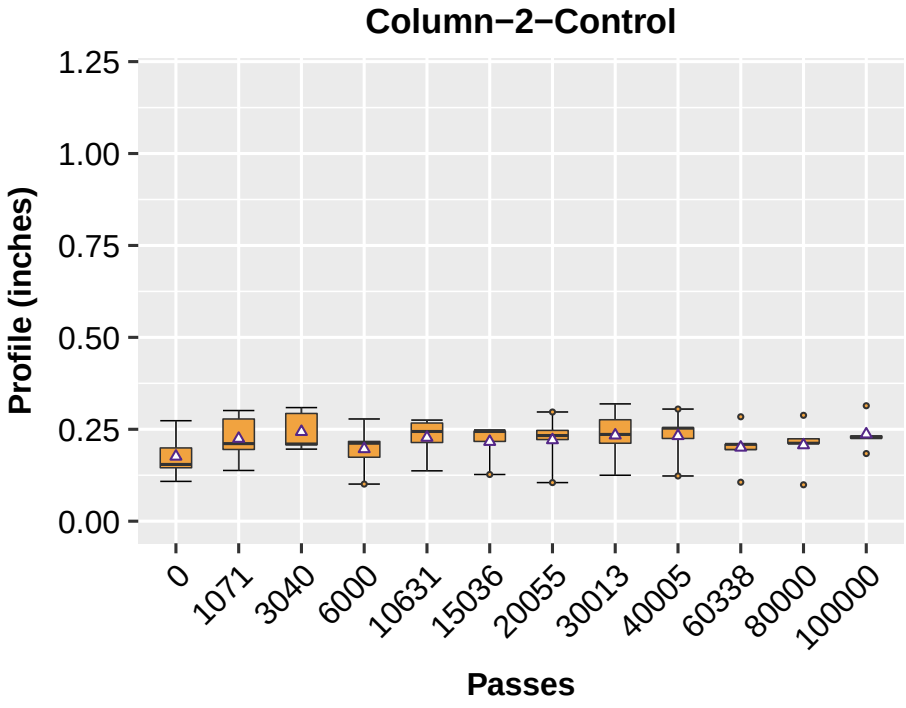

Figure 5.16: *Longitudinal profile change with axle load repetitions (Column-2)*

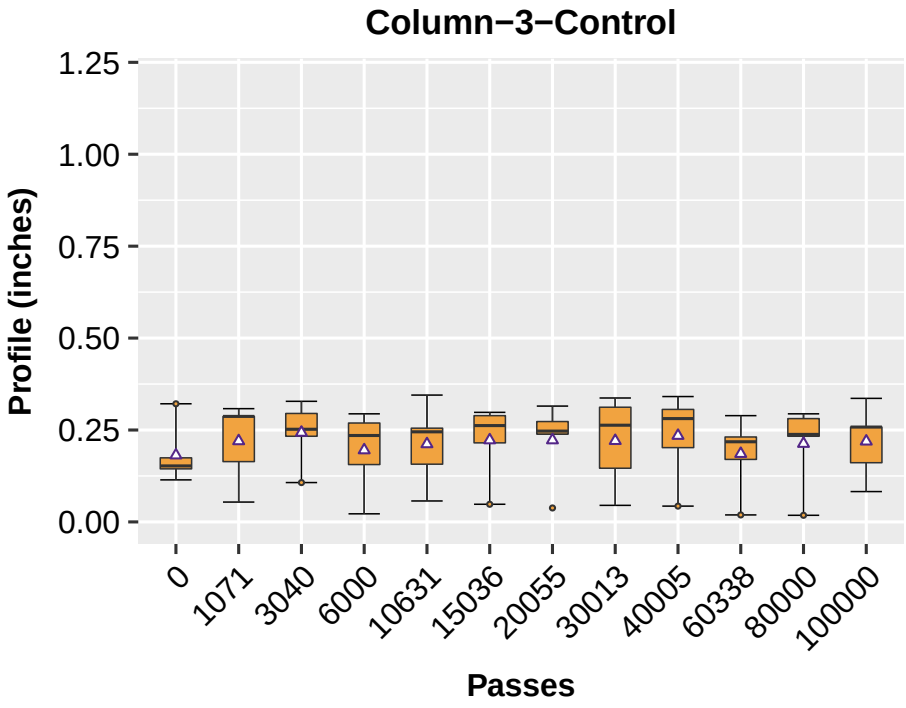

Figure 5.17: *Longitudinal profile change with axle load repetitions (Column-3)*

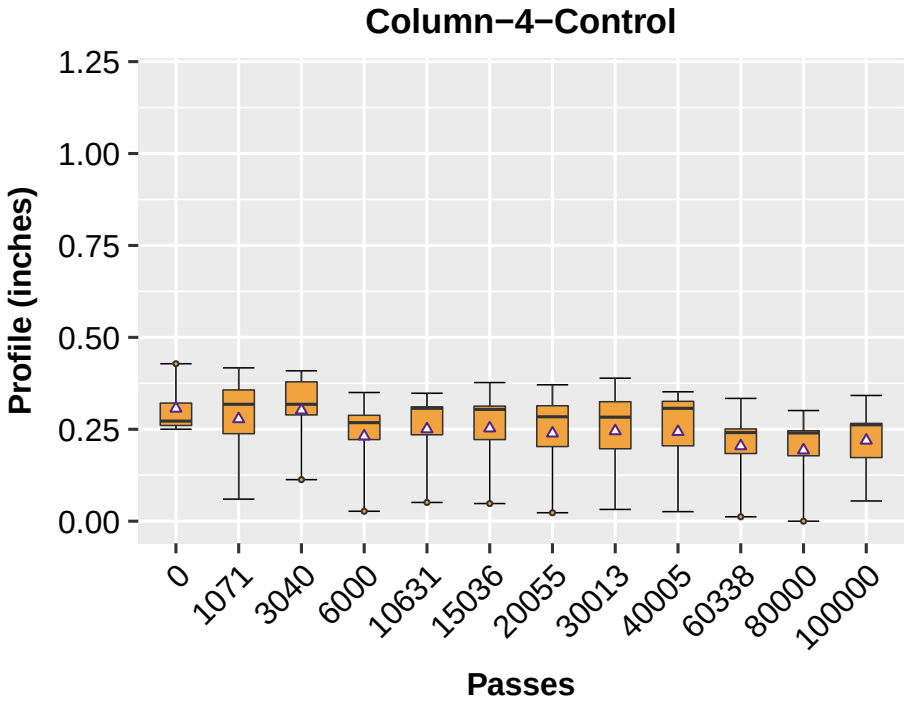

Figure 5.18: *Longitudinal profile change with axle load repetitions (Column-4)*

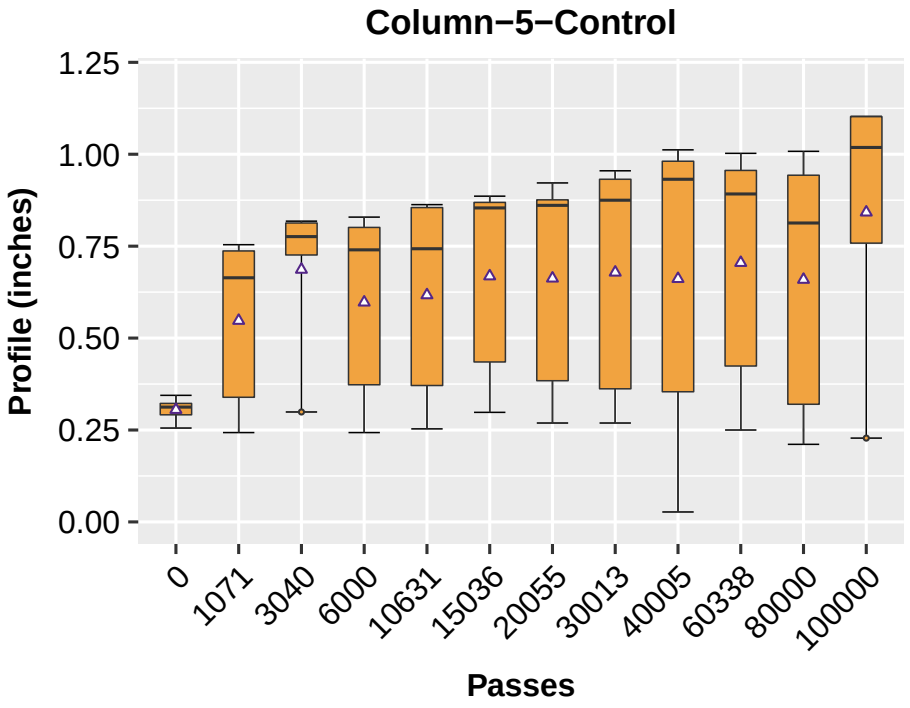

Figure 5.19: *Longitudinal profile change with axle load repetitions (Column-5)*

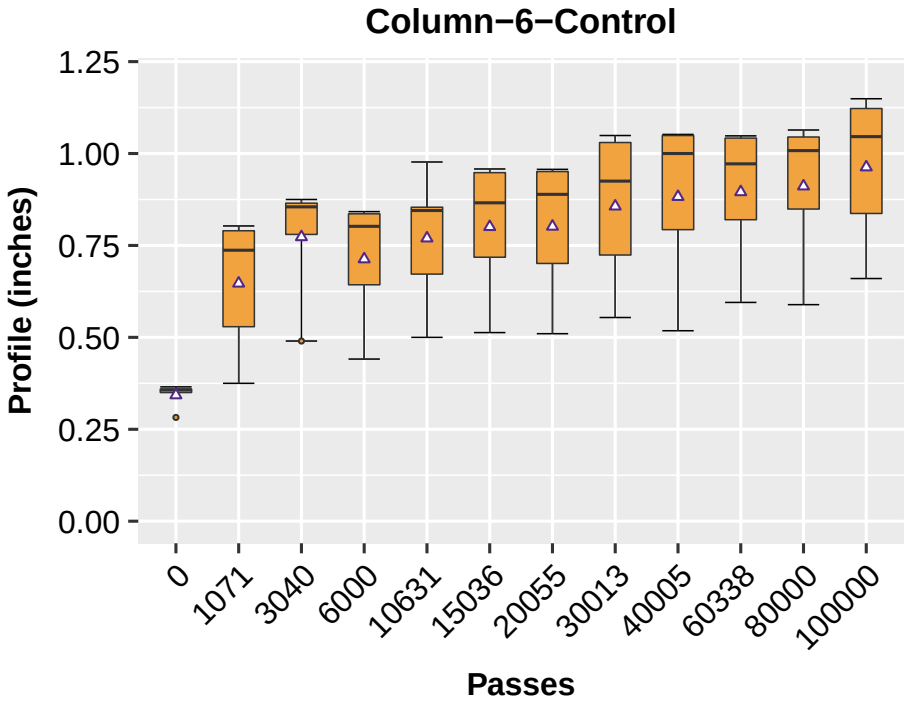

Figure 5.20: *Longitudinal profile change with axle load repetitions (Column-6)*

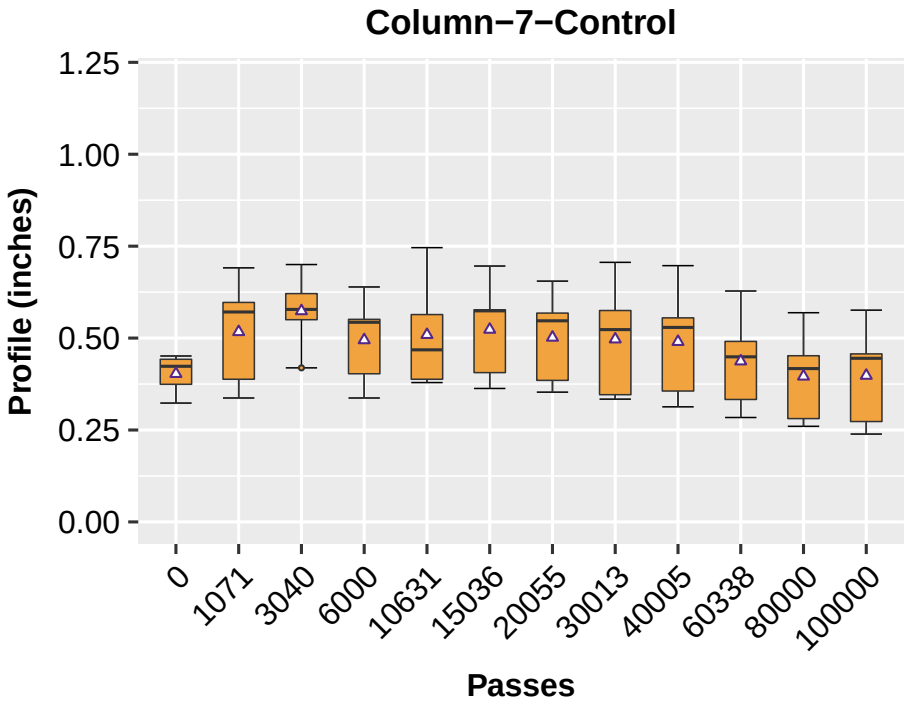

Figure 5.21: *Longitudinal profile change with axle load repetitions (Column-7)*

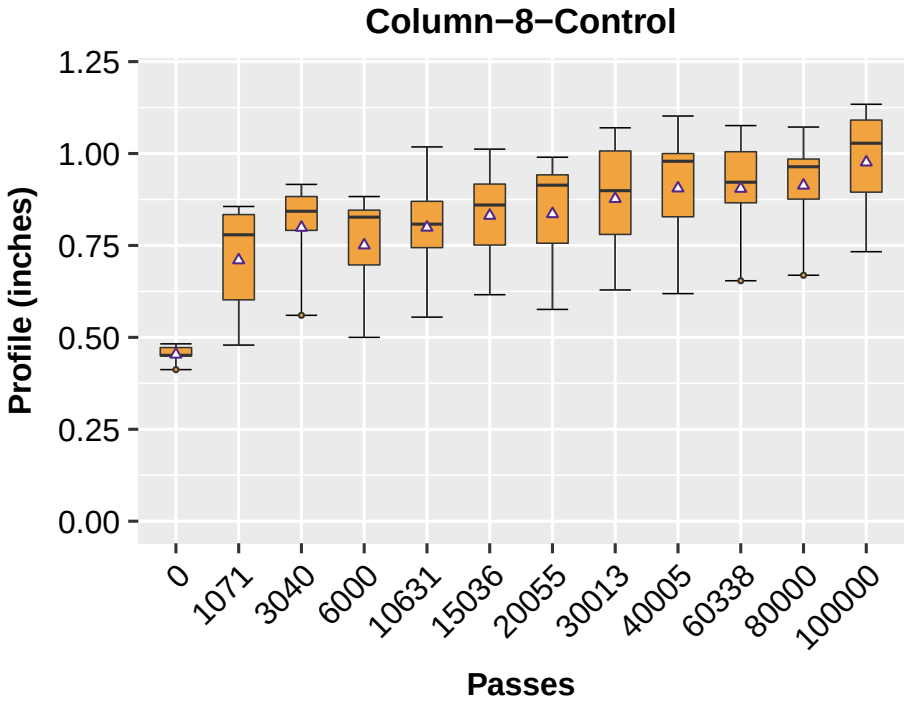

Figure 5.22: *Longitudinal profile change with axle load repetitions (Column-8)*

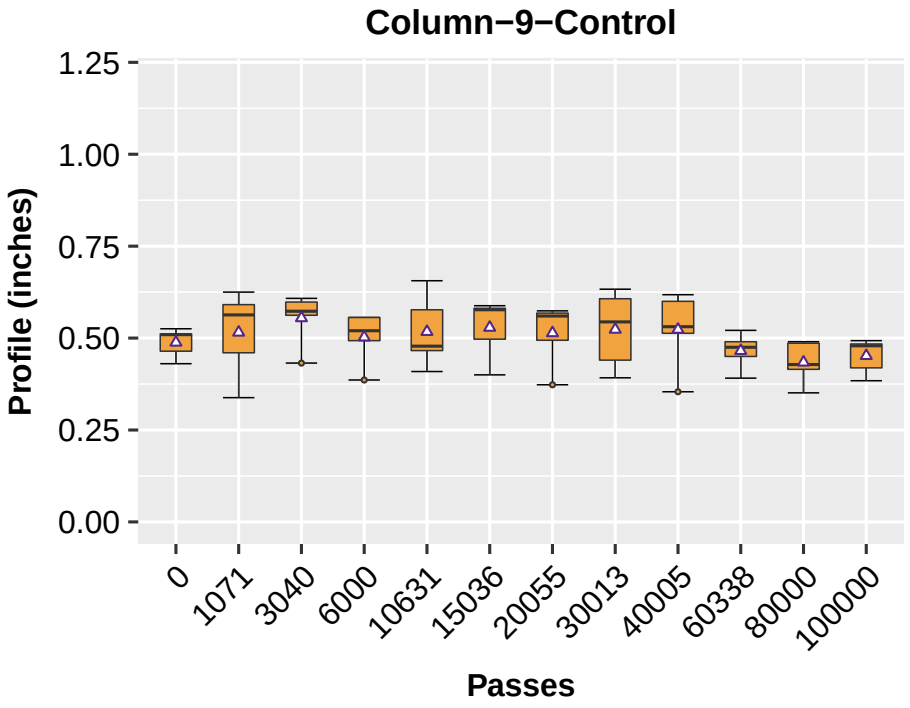

Figure 5.23: *Longitudinal profile change with axle load repetitions (Column-9)*

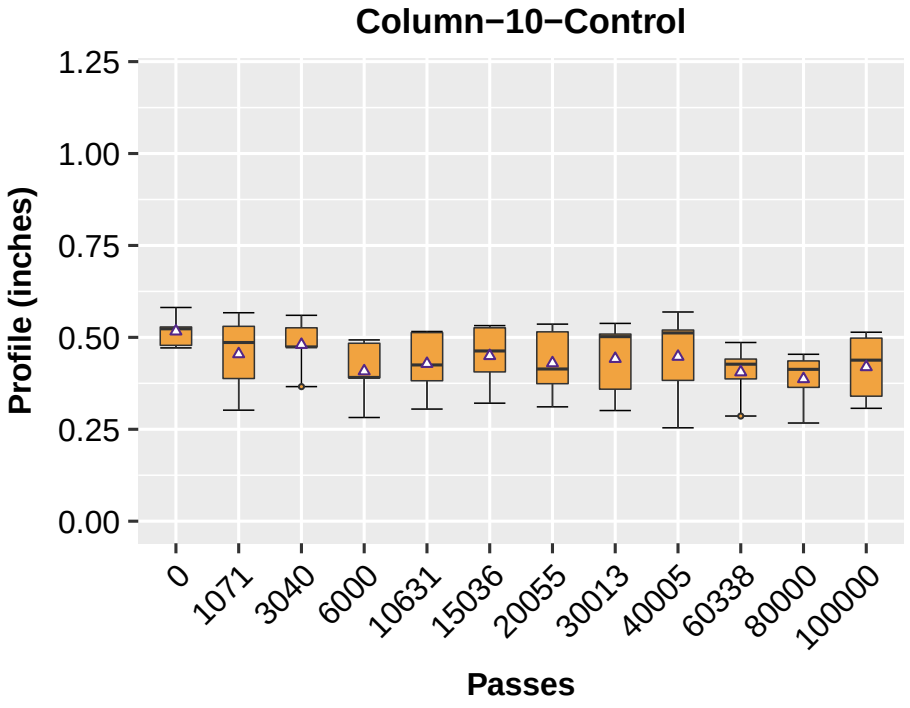

Figure 5.24: *Longitudinal profile change with axle load repetitions (Column-10)*

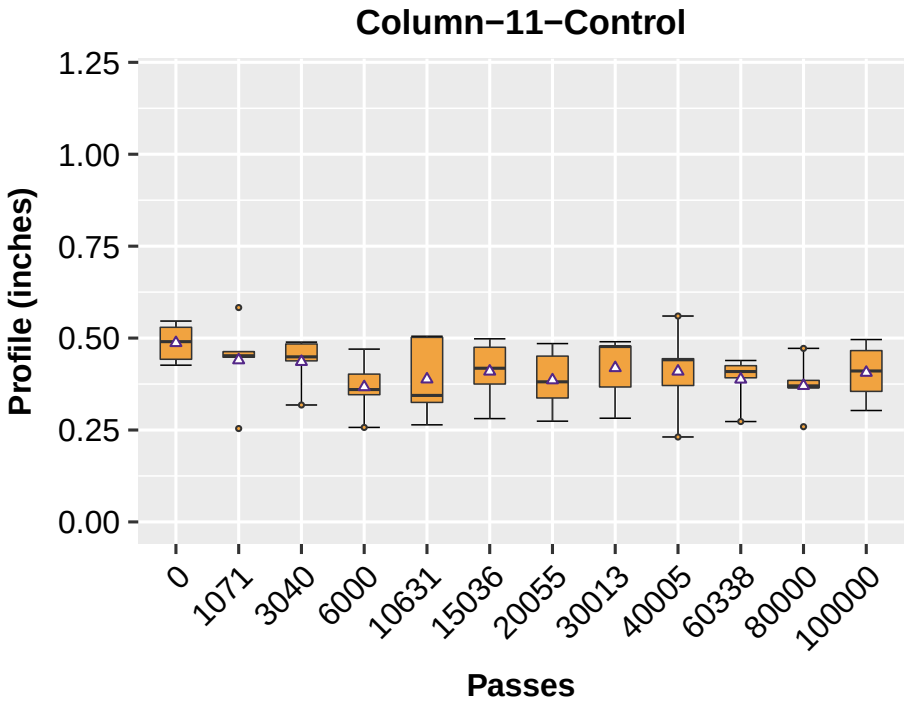

Figure 5.25: *Longitudinal profile change with axle load repetitions (Column-11)*

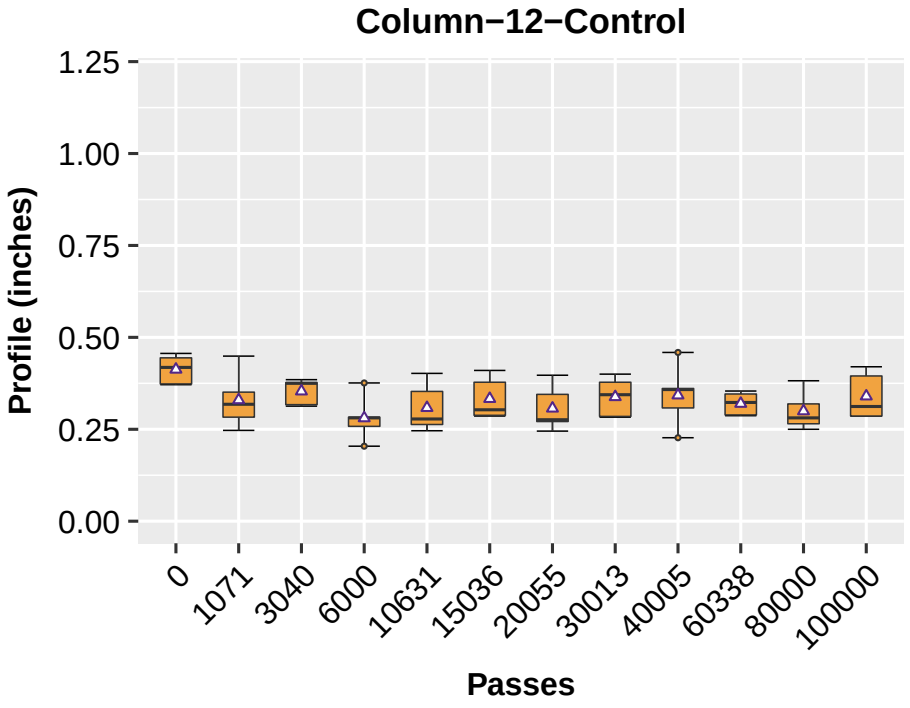

Figure 5.26: *Longitudinal profile change with axle load repetitions (Column-12)*

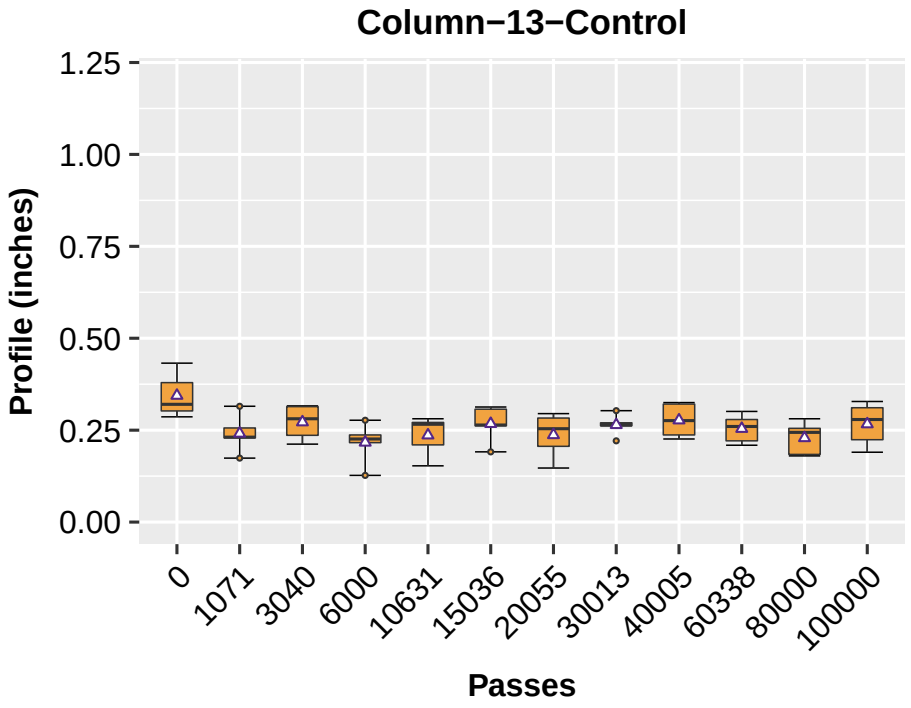

Figure 5.27: *Longitudinal profile change with axle load repetitions (Column-13)*

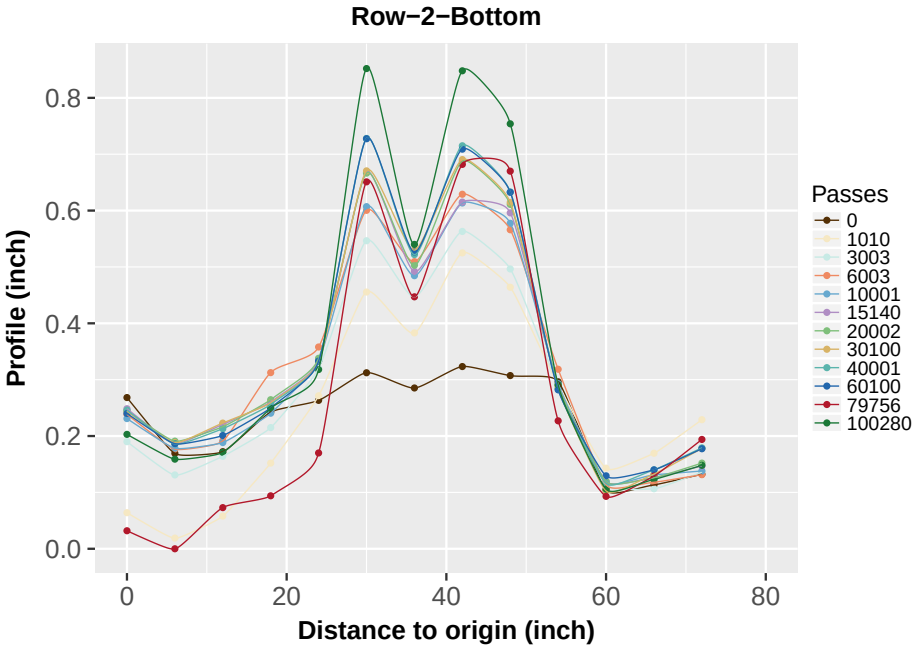

Figure 5.28: *Profile of Cross-Section-2 in Bottom Lane (Row-2)*

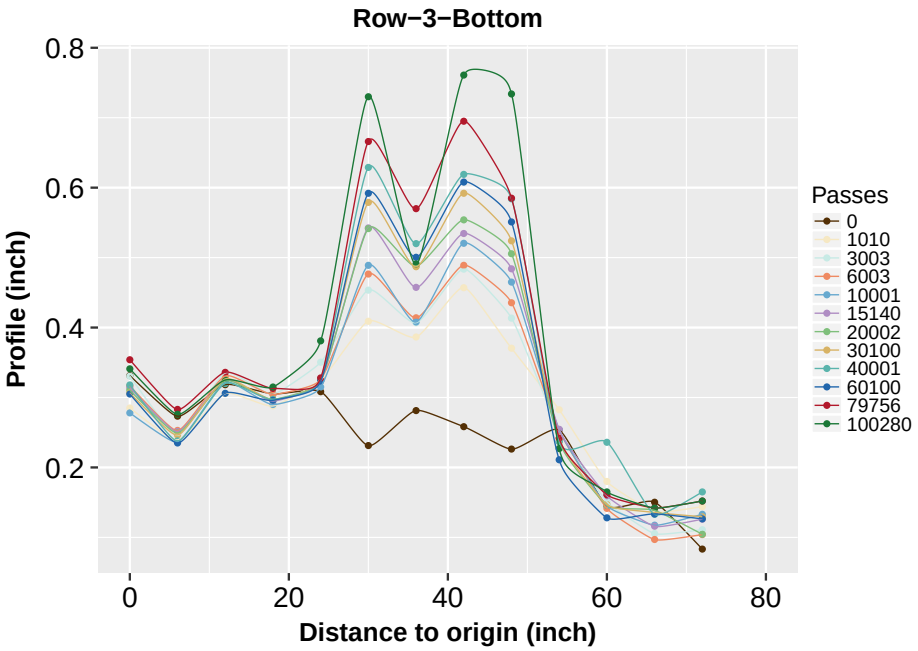

Figure 5.29: *Profile of Cross-Section-3 in Bottom Lane (Row-3)*

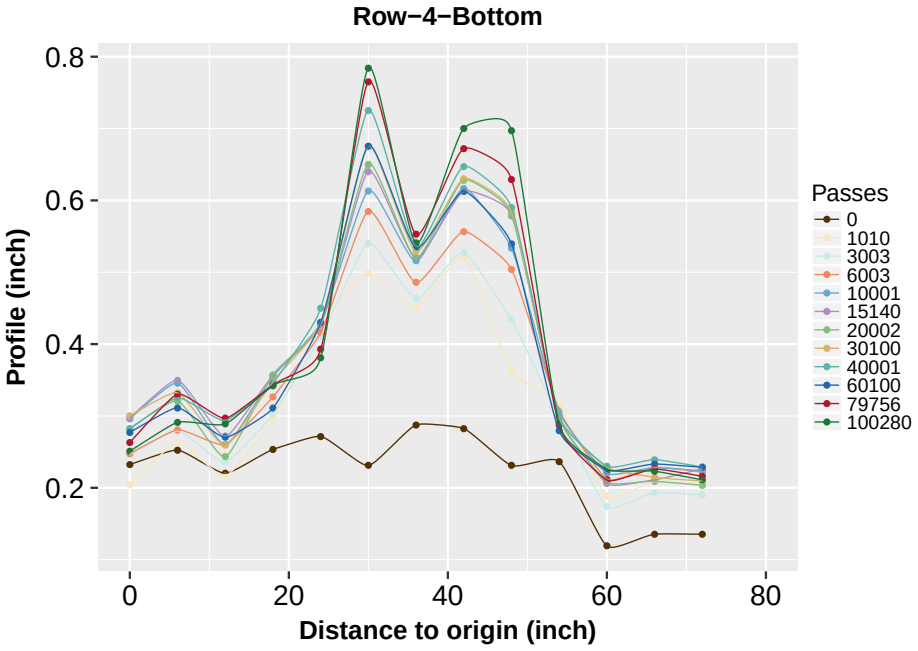

Figure 5.30: *Profile of Cross-Section-4 in Bottom Lane (Row-4)*

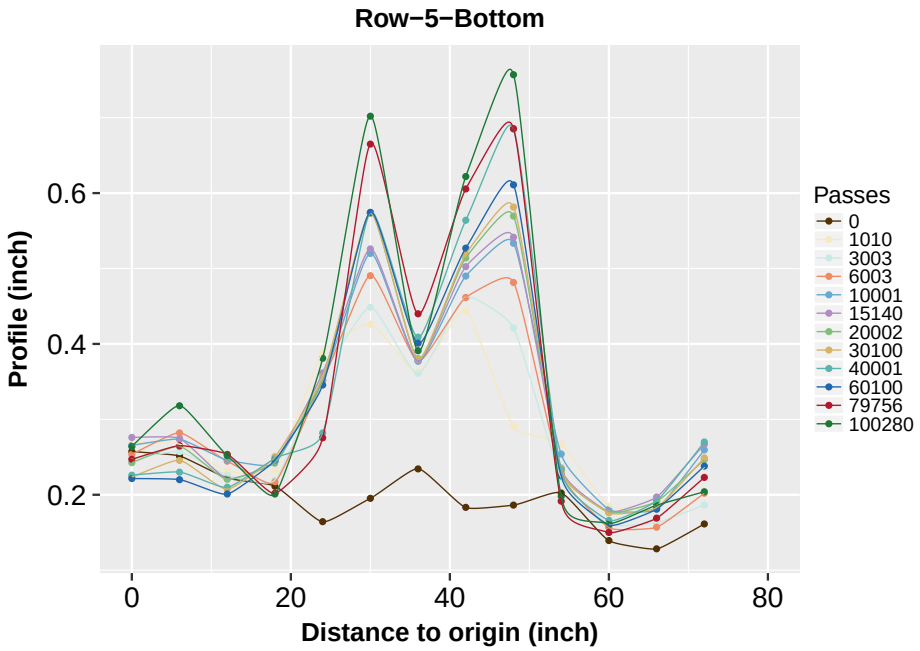

Figure 5.31: *Profile of Cross-Section-5 in Bottom Lane (Row-5)*

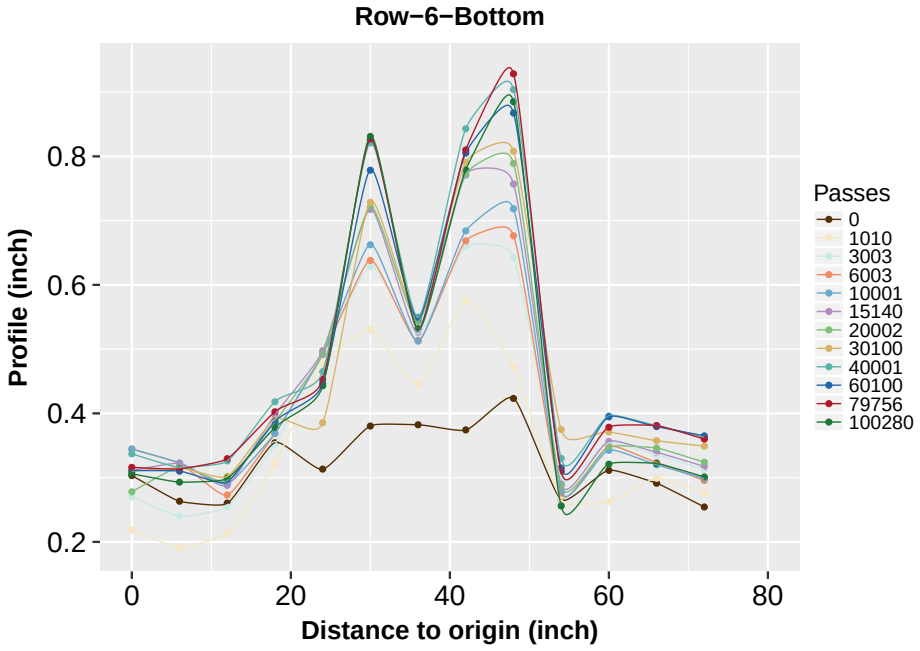

Figure 5.32: *Profile of Cross-Section-6 in Bottom Lane (Row-6)*

rienced an appreciable amount of deformation were column-6 through column-9. The column-9 had the largest median deformation, which was around 0.45 inch and was about one-half that of the control lane (0.89 inch).

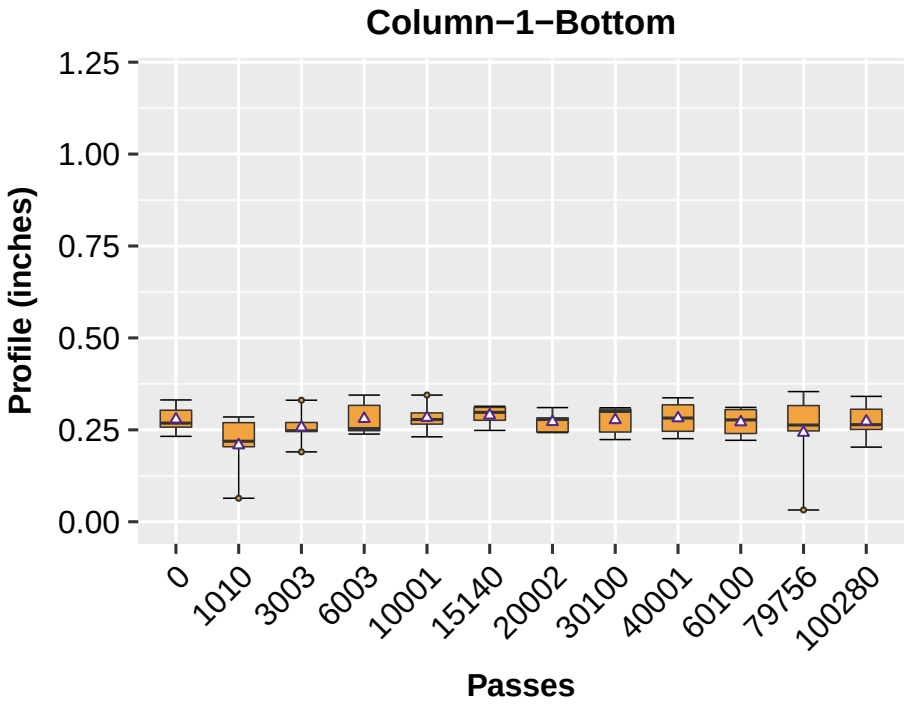

Figure 5.33: *Longitudinal profile change with axle load repetitions (Column-1)*

5.3.3 Aggregate in Middle of Aggregate Base

Deformation Curves

Figures 5.46 through 5.50 provide the changes in horizontal profiles with the axle load repetitions. The largest deformation was found in the second horizontal profile (Row-2-m), which reaches as high as 0.81 inch. The deformation in horizontal cross-sections four and five are also quite high, which are 0.64-in and 0.58-in, respectively.

Aggregated Profiles in Box-Plots

The aggregated profile results for the lane with geogrids placed in the middle of the aggregate base (Lane M) are shown in Figures 5.51 through 5.63. To measure the changes in the profiles of the test section as the axle load repetitions increases, grids were draw on the surface of the test lanes. For each lane, there are thirteen longitudinal cross-sections which are in align with the direction of traffic, and a total of seven horizontal cross-sections were included. For the Lane M, most of the deformations were found in the vicinity of the wheel path area. The largest permanent deformation was found in the fifth longitudinal cross-section, which had an average permanent

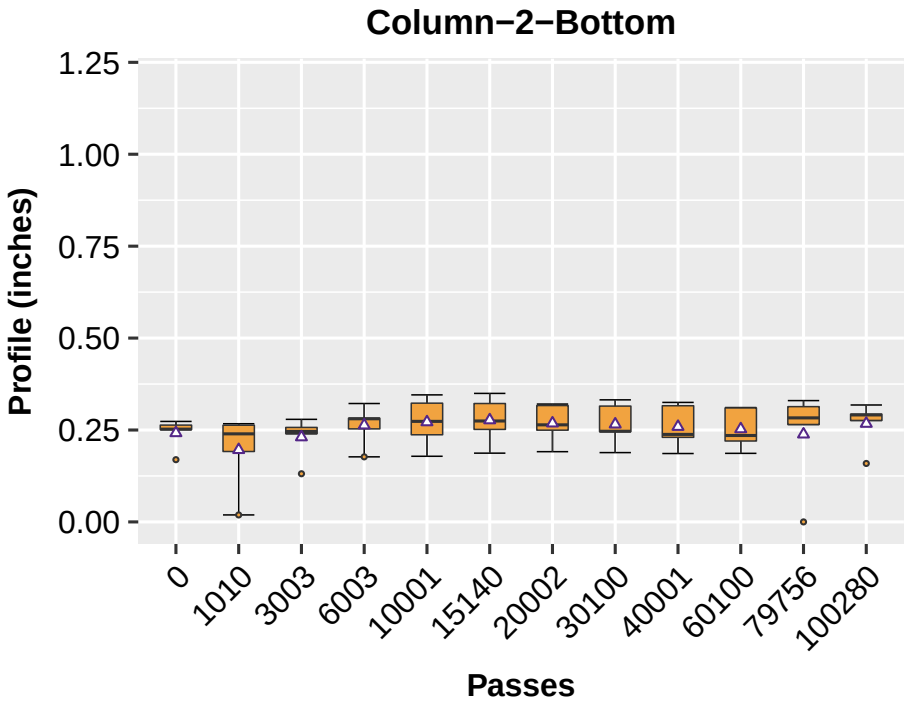

Figure 5.34: *Longitudinal profile change with axle load repetitions (Column-2)*

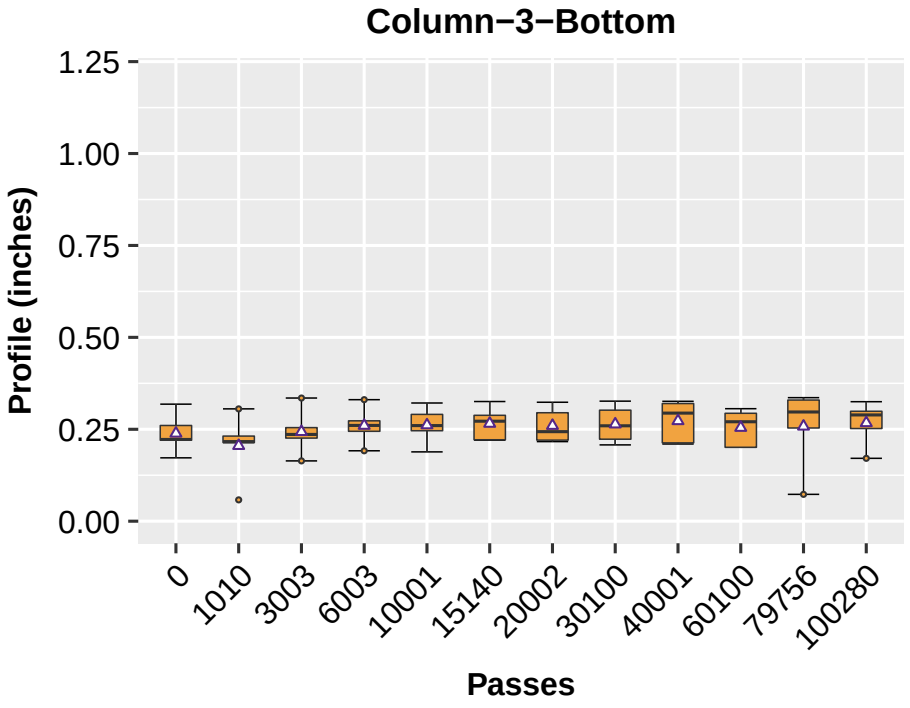

Figure 5.35: *Longitudinal profile change with axle load repetitions (Column-3)*

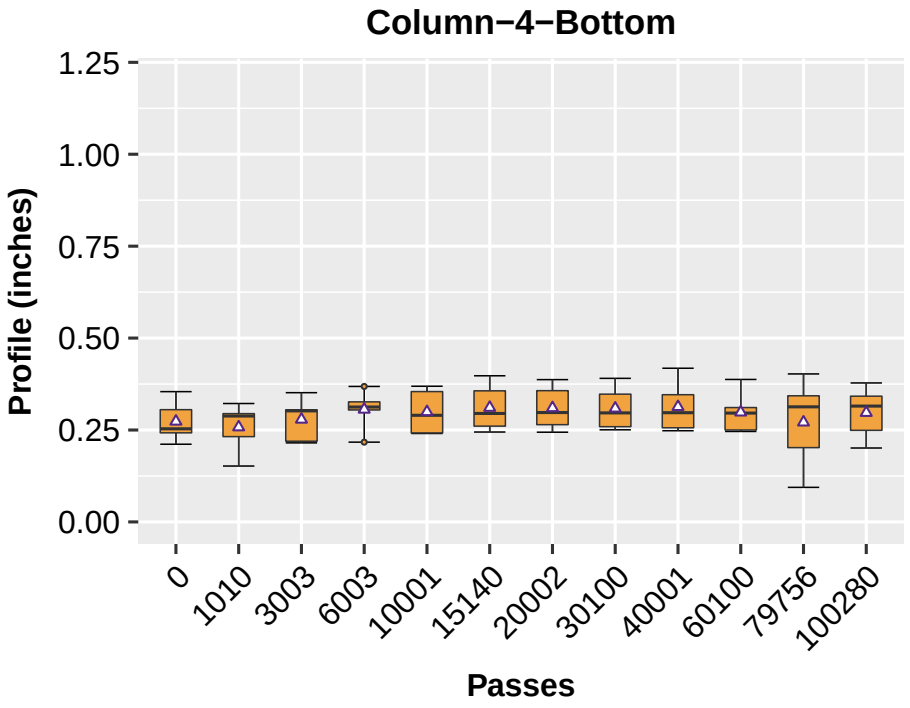

Figure 5.36: *Longitudinal profile change with axle load repetitions (Column-4)*

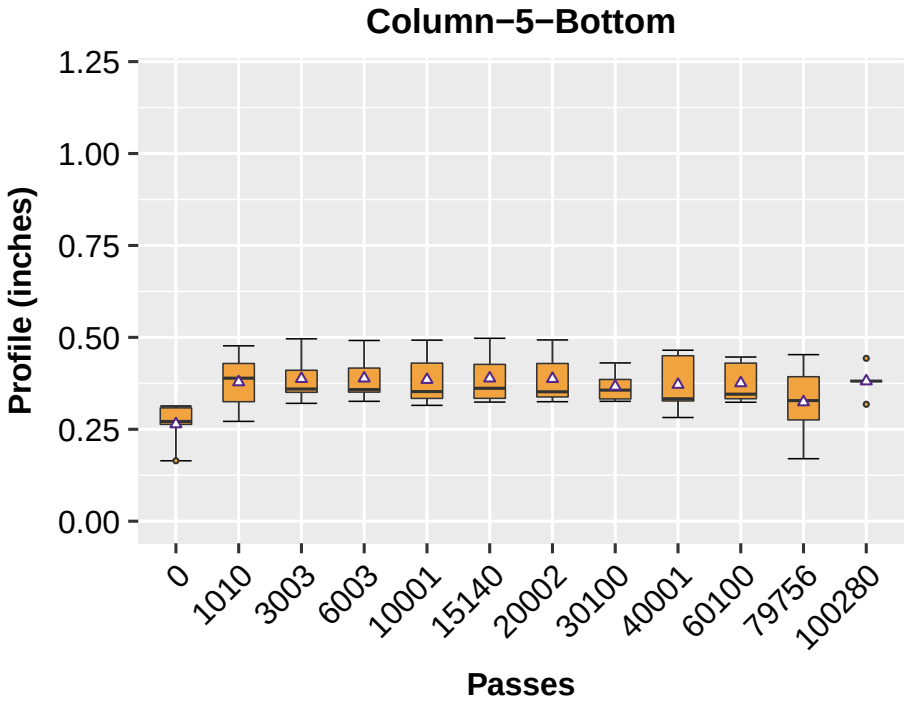

Figure 5.37: *Longitudinal profile change with axle load repetitions (Column-5)*

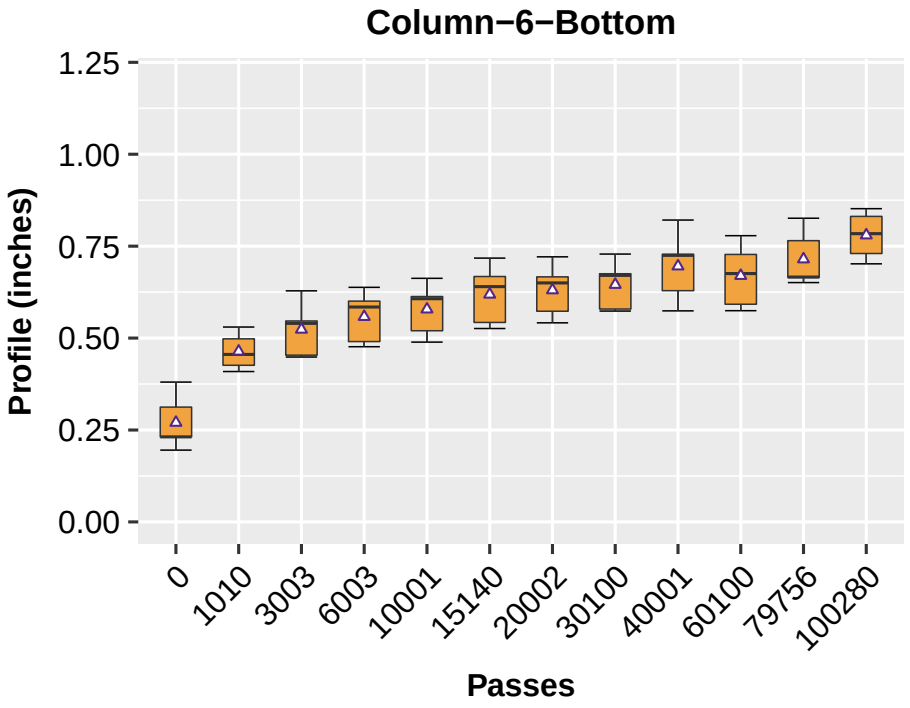

Figure 5.38: *Longitudinal profile change with axle load repetitions (Column-6)*

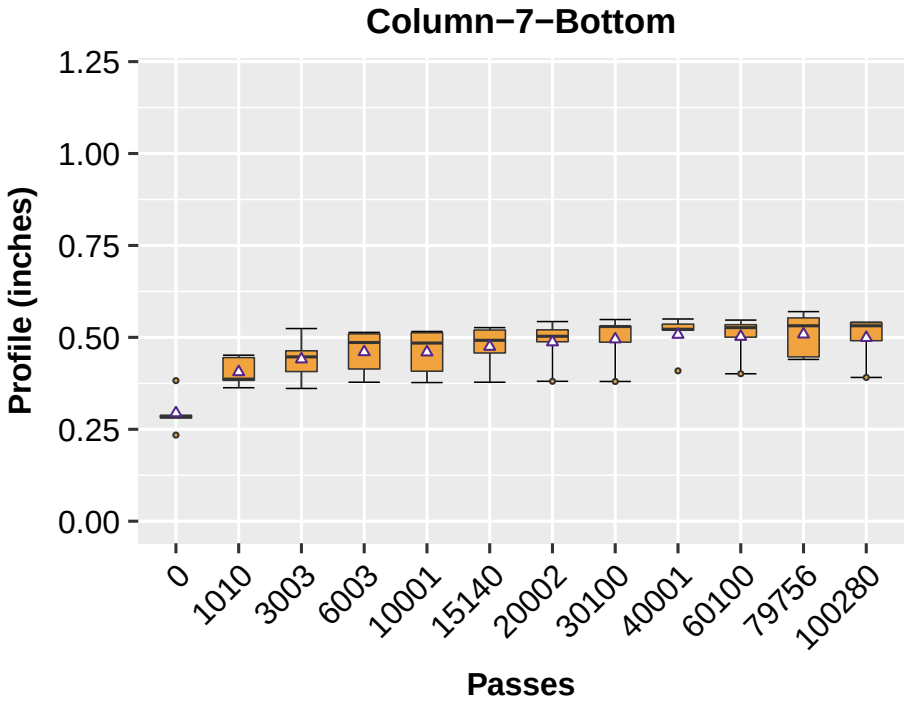

Figure 5.39: *Longitudinal profile change with axle load repetitions (Column-7)*

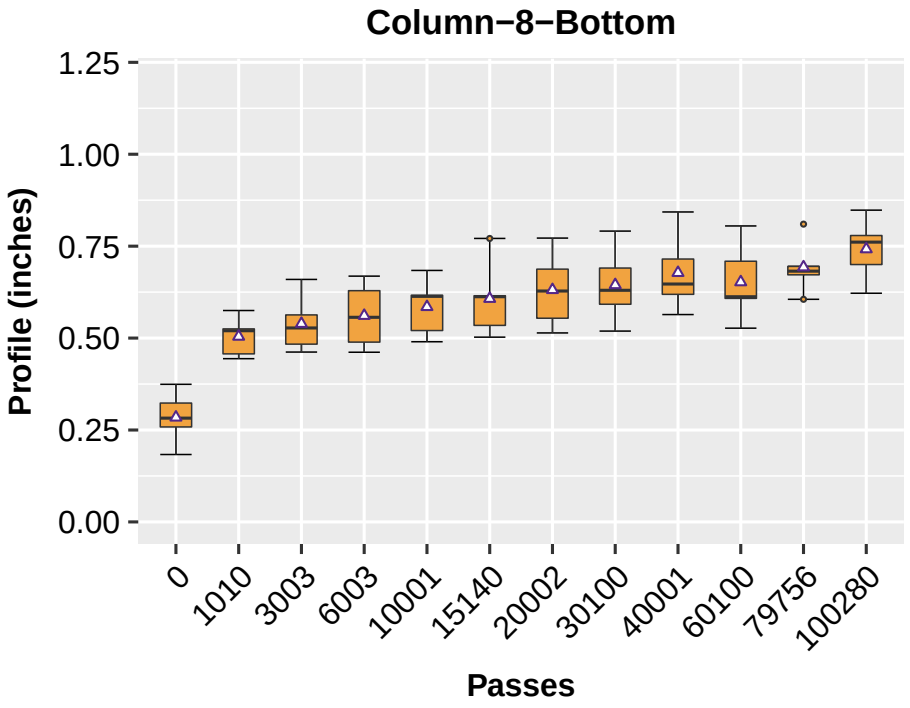

Figure 5.40: *Longitudinal profile change with axle load repetitions (Column-8)*

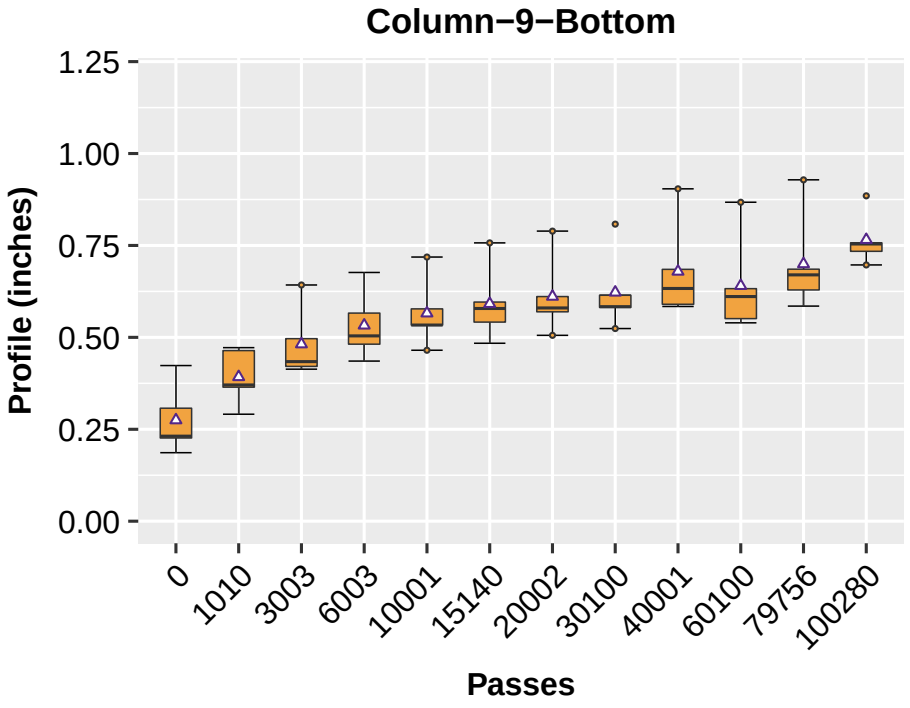

Figure 5.41: *Longitudinal profile change with axle load repetitions (Column-9)*

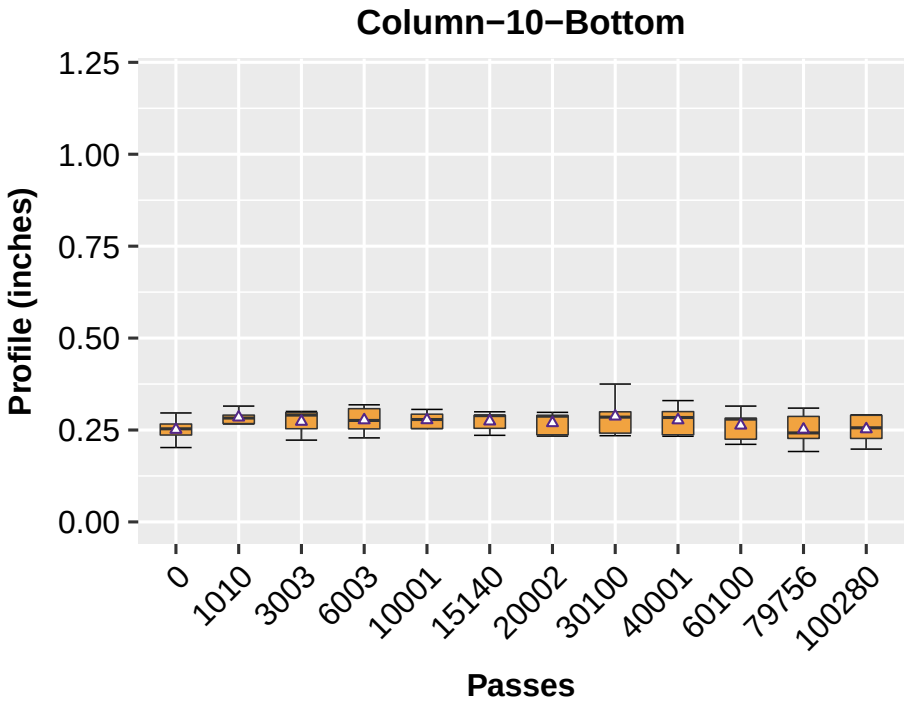

Figure 5.42: *Longitudinal profile change with axle load repetitions (Column-10)*

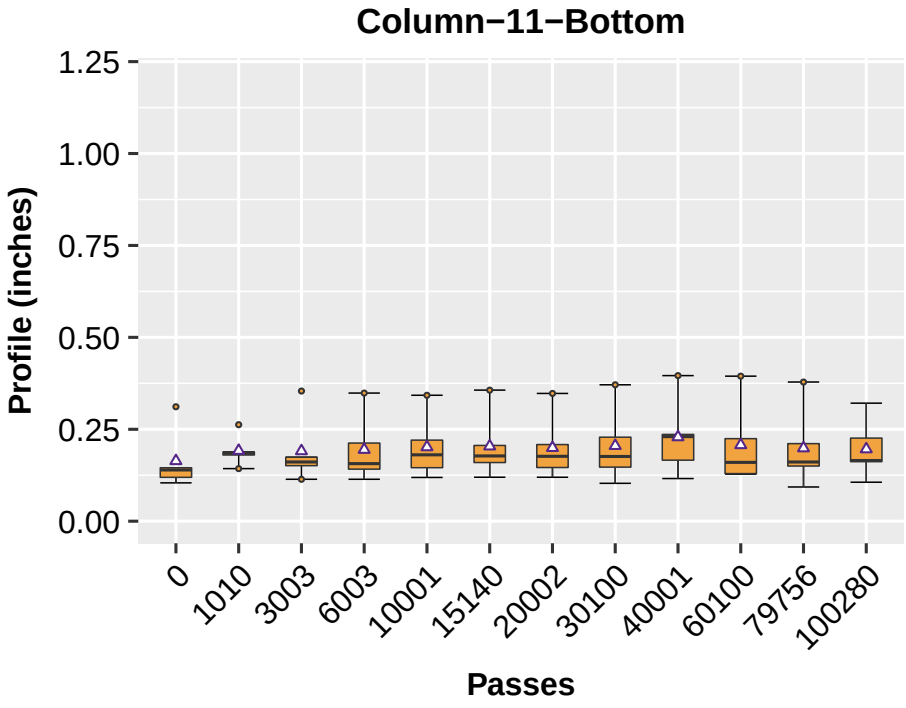

Figure 5.43: *Longitudinal profile change with axle load repetitions (Column-11)*

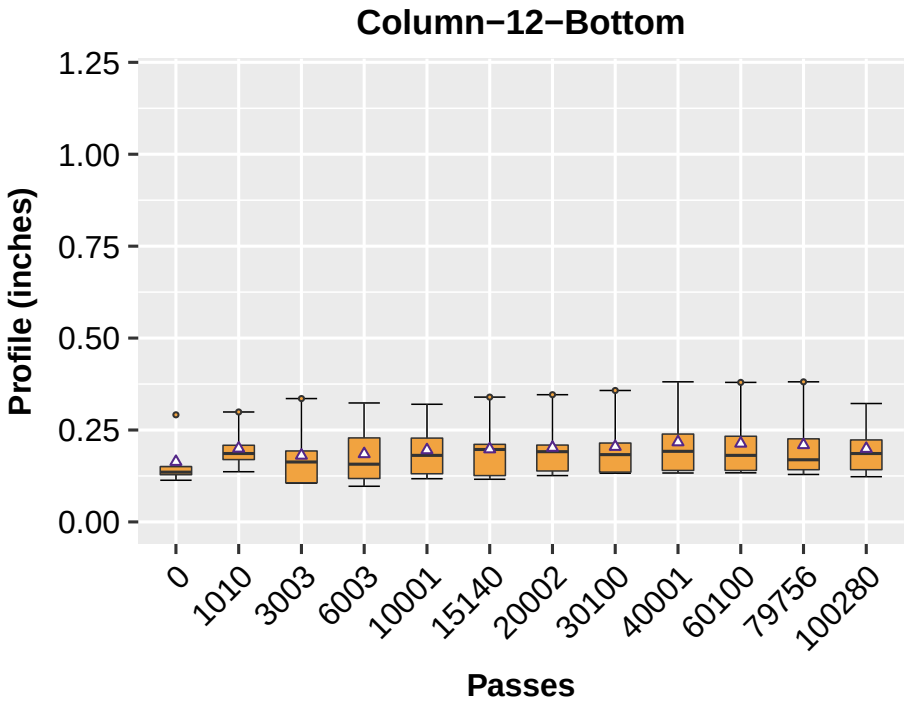

Figure 5.44: *Longitudinal profile change with axle load repetitions (Column-12)*

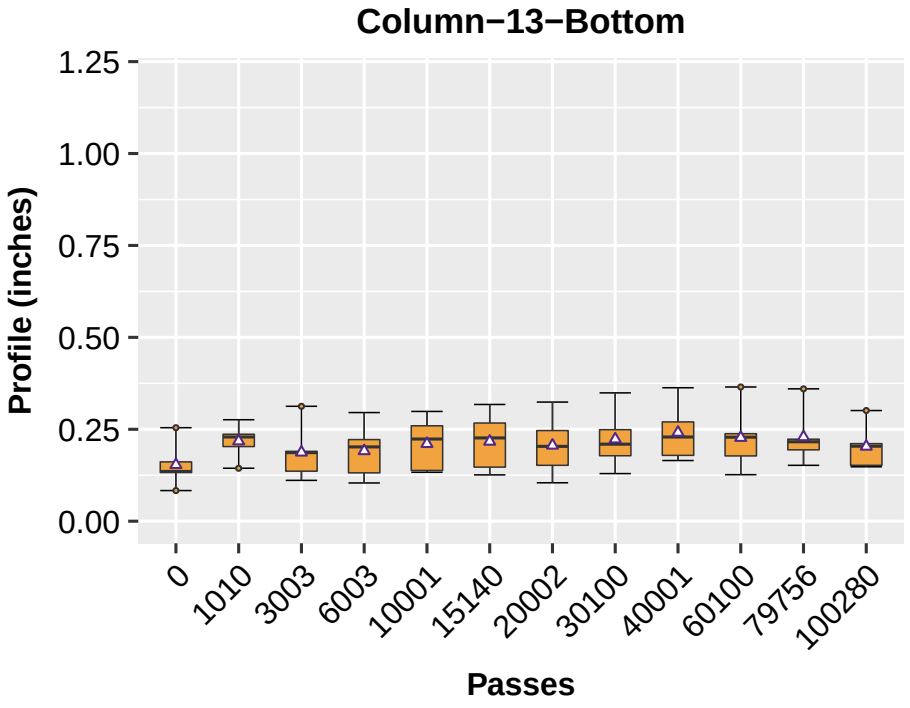

Figure 5.45: *Longitudinal profile change with axle load repetitions (Column-13)*

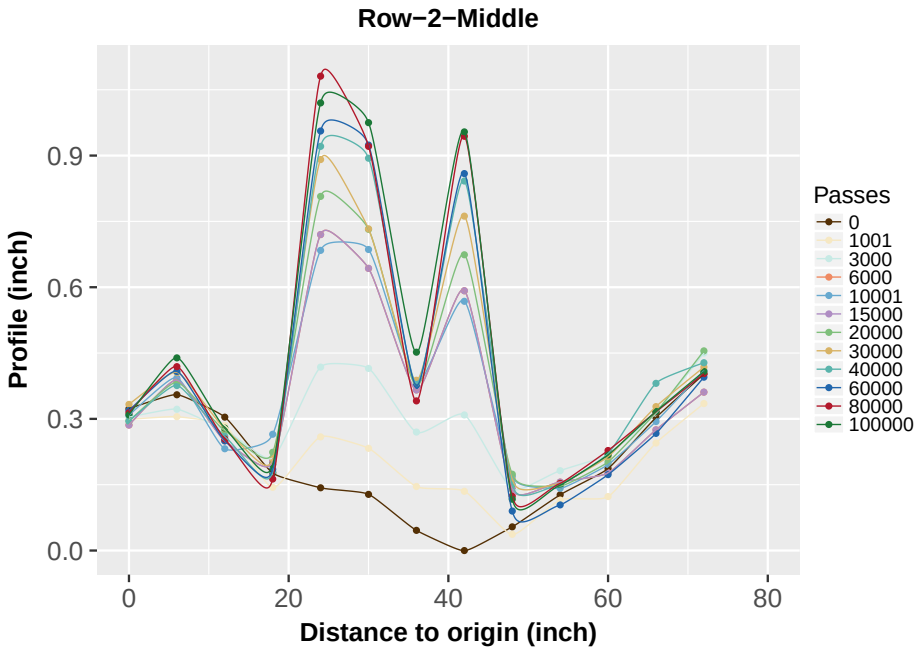

Figure 5.46: *Profile of Cross-Section-2 in Middle Lane (Row-2)*

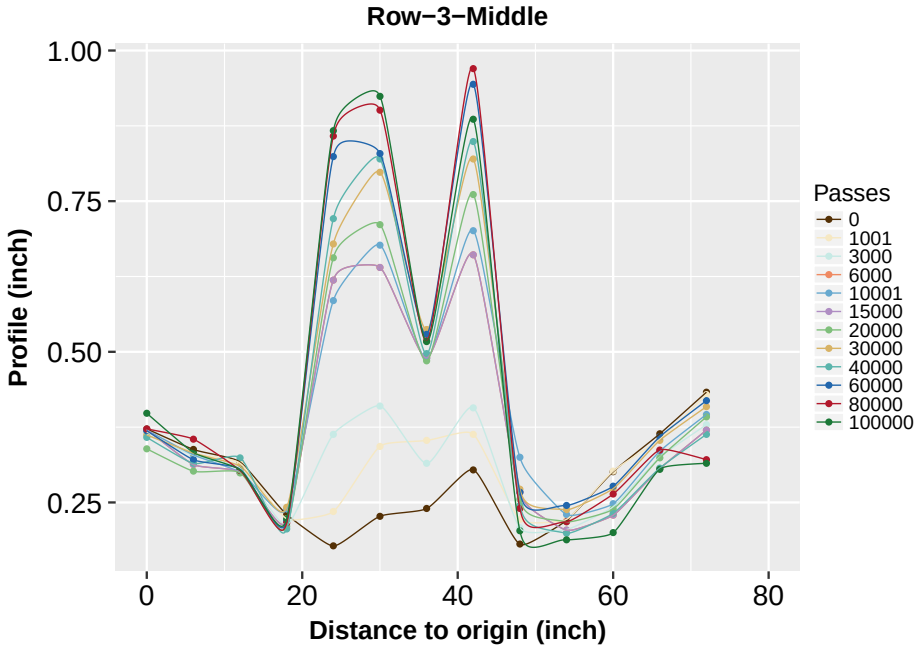

Figure 5.47: *Profile of Cross-Section-3 in Middle Lane (Row-3)*

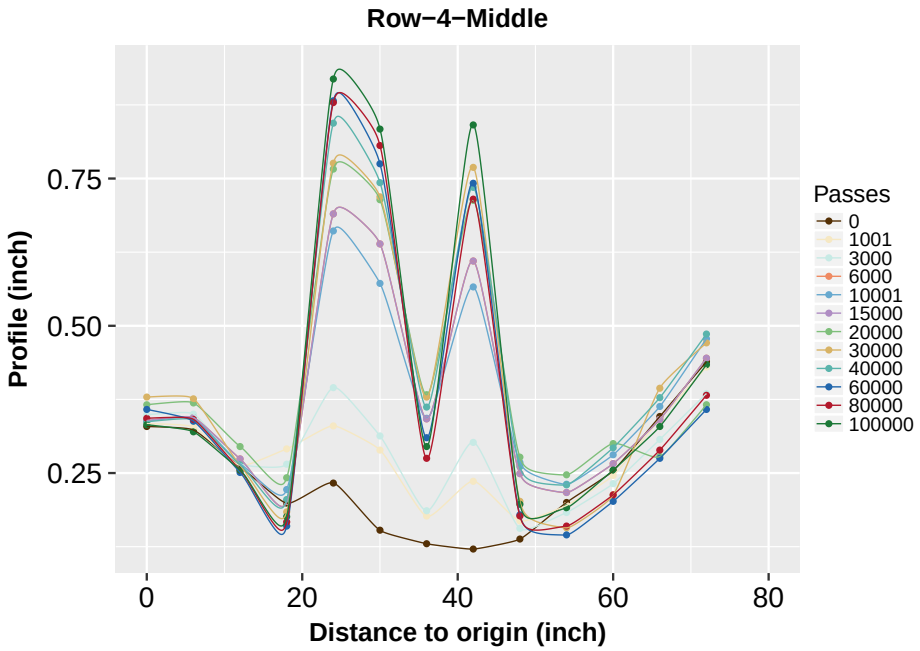

Figure 5.48: *Profile of Cross-Section-4 in Middle Lane (Row-4)*

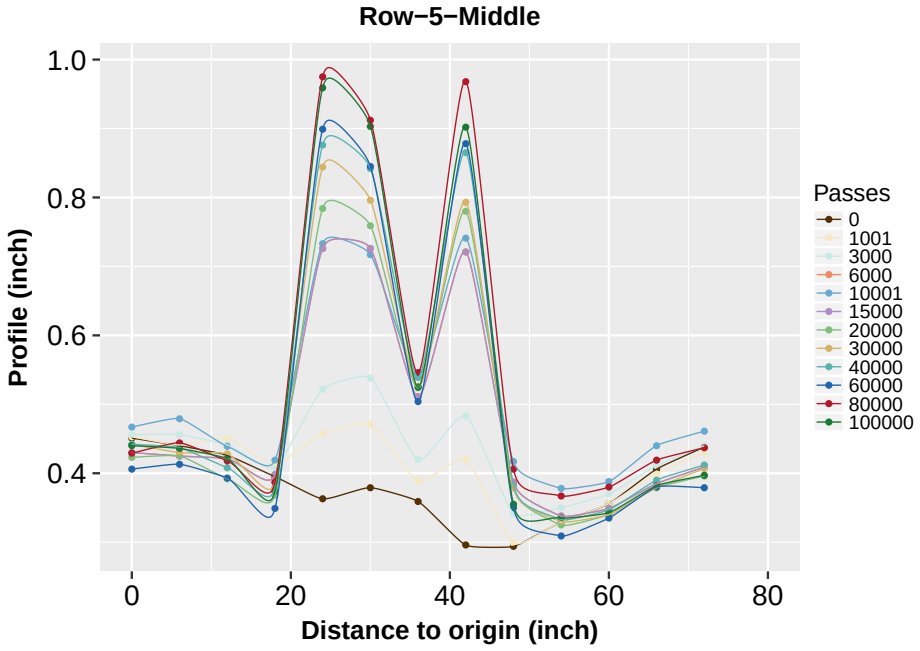

Figure 5.49: *Profile of Cross-Section-5 in Middle Lane (Row-5)*

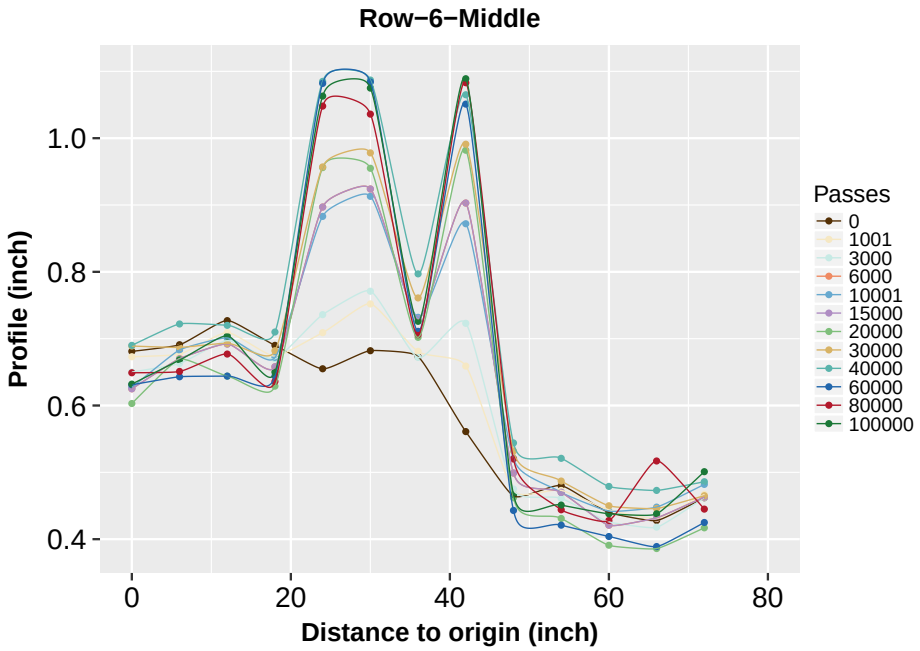

Figure 5.50: *Profile of Cross-Section-6 in Middle Lane (Row-6)*

deformation of 0.65 inch. Comparable deformations were also found in the 6^{th} and 8^{th} cross-section. Overall, after 100,000 axle repetitions, the average rutting (permanent deformation) in the lane-M was 0.6 inch.

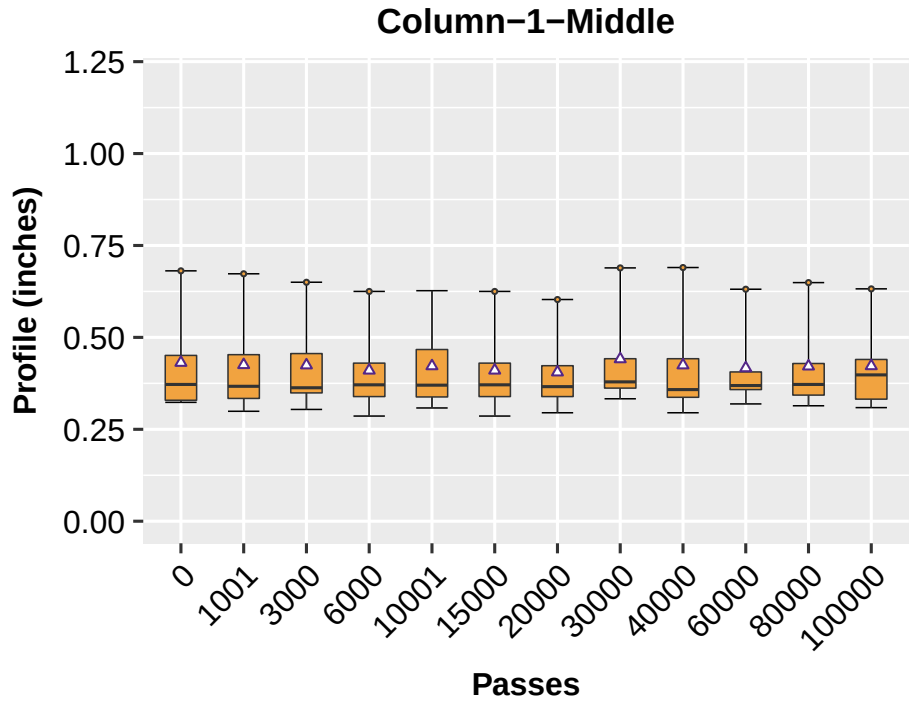

Figure 5.51: *Longitudinal profile change with axle load repetitions (Column-1)*

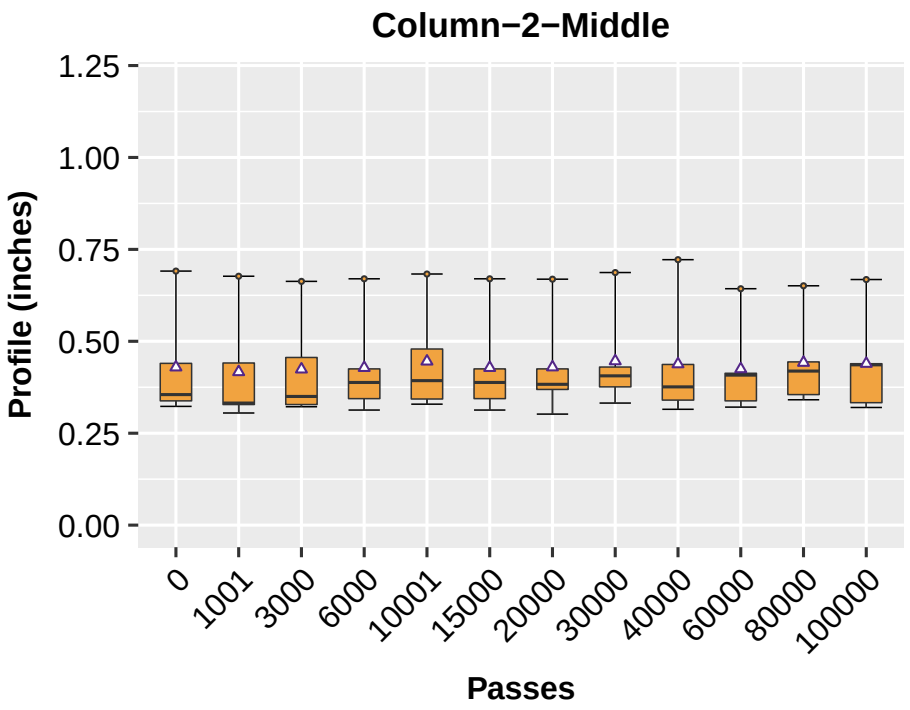

Figure 5.52: *Longitudinal profile change with axle load repetitions (Column-2)*

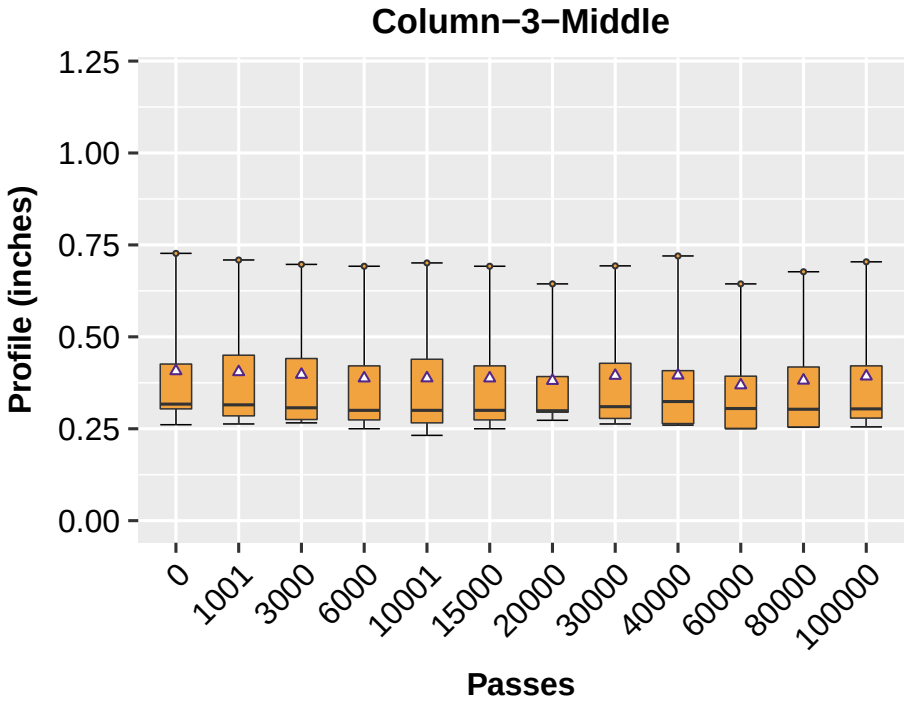

Figure 5.53: *Longitudinal profile change with axle load repetitions (Column-3)*

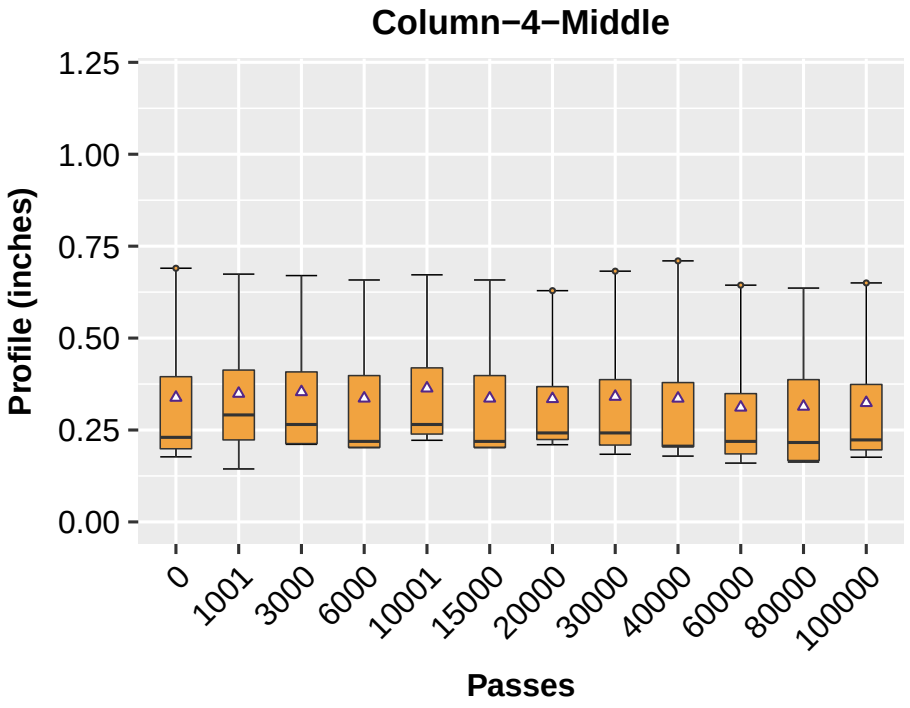

Figure 5.54: *Longitudinal profile change with axle load repetitions (Column-4)*

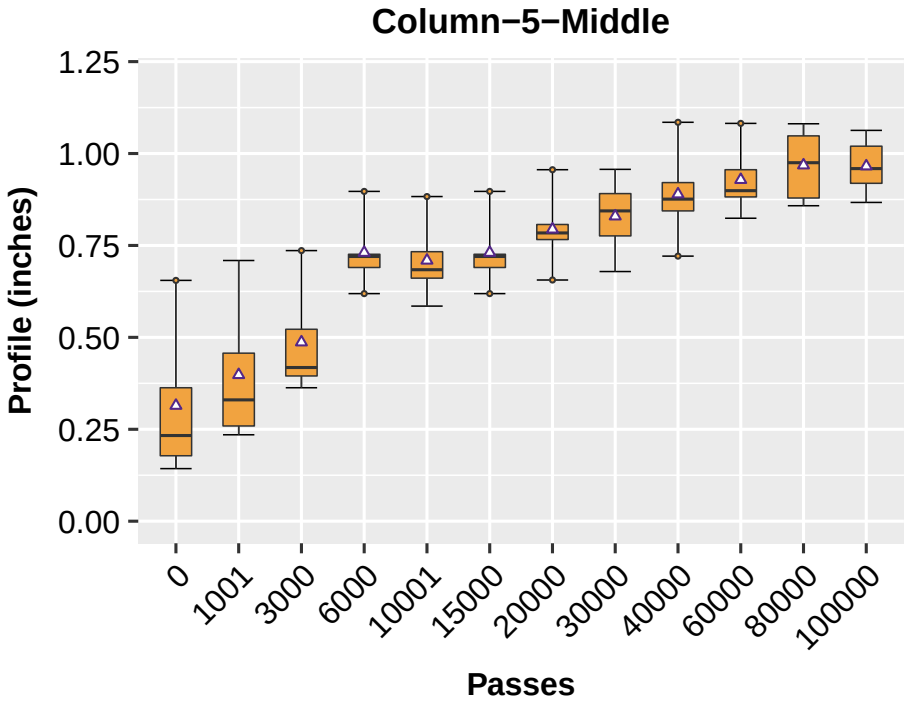

Figure 5.55: *Longitudinal profile change with axle load repetitions (Column-5)*

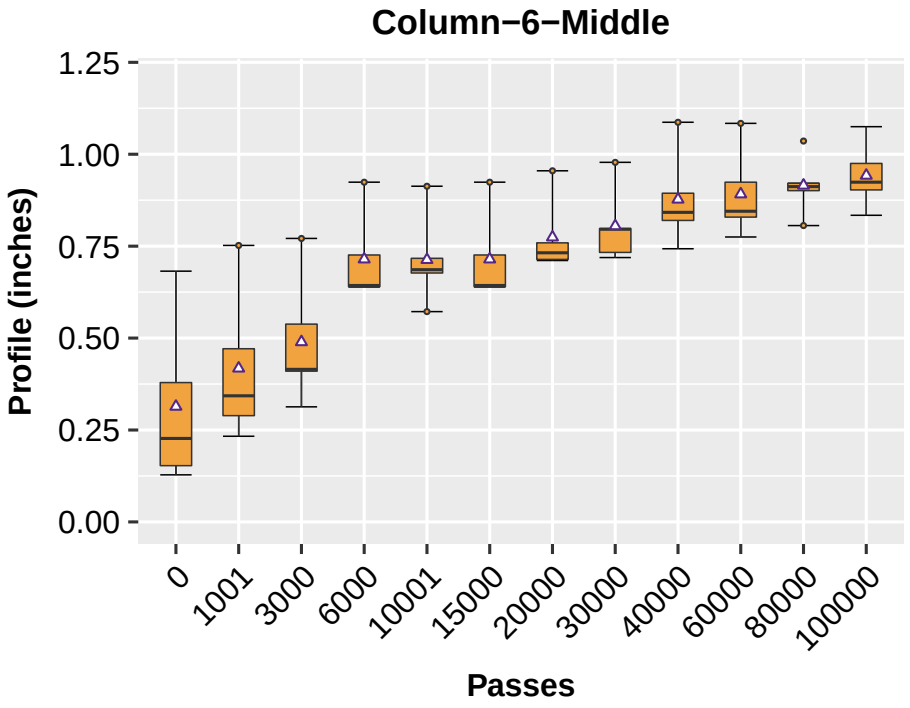

Figure 5.56: *Longitudinal profile change with axle load repetitions (Column-6)*

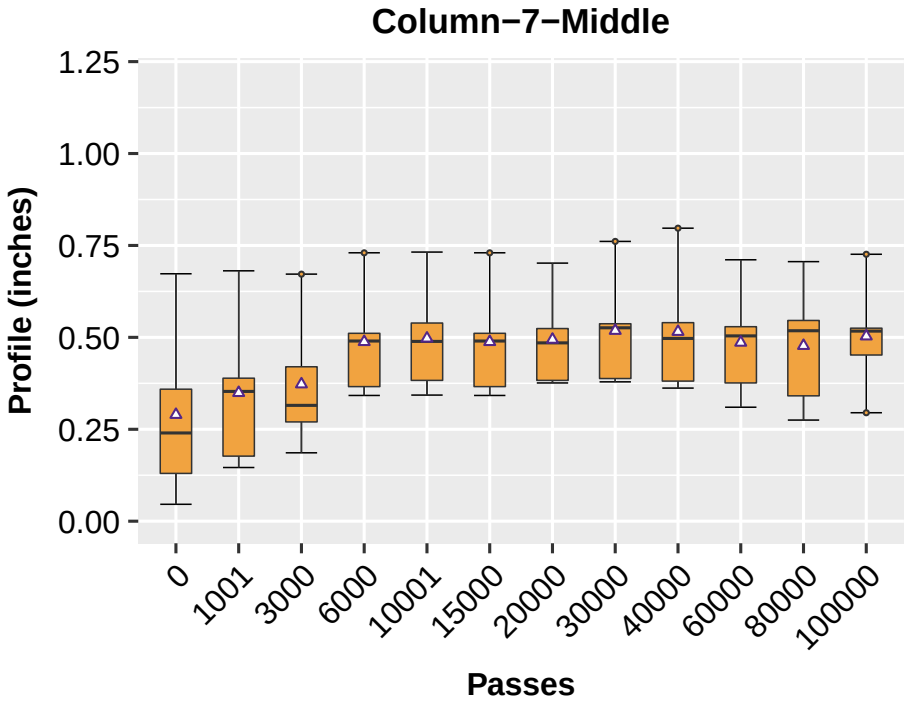

Figure 5.57: *Longitudinal profile change with axle load repetitions (Column-7)*

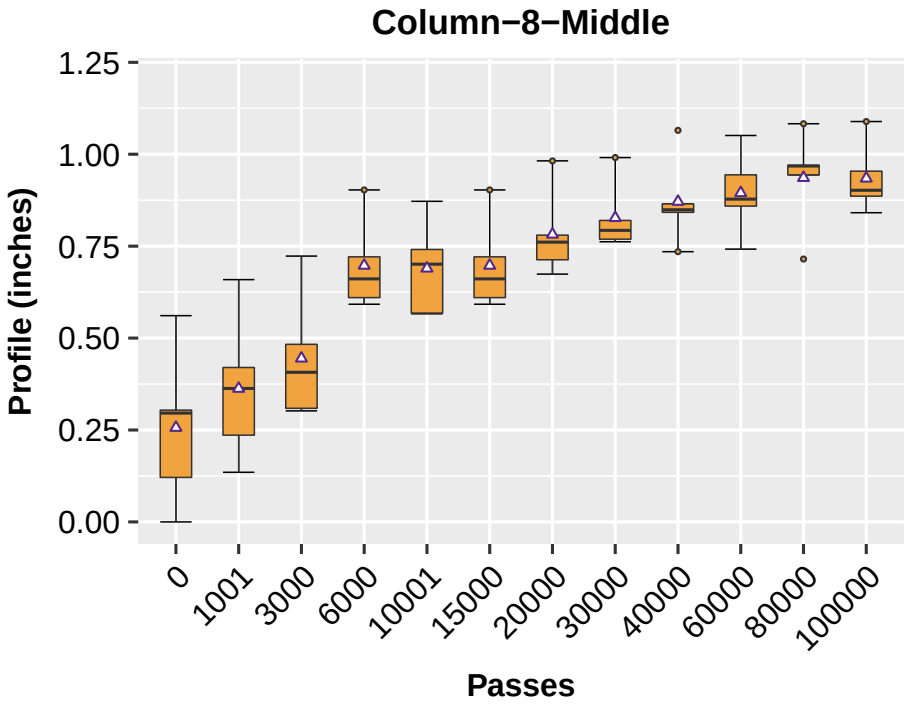

Figure 5.58: *Longitudinal profile change with axle load repetitions (Column-8)*

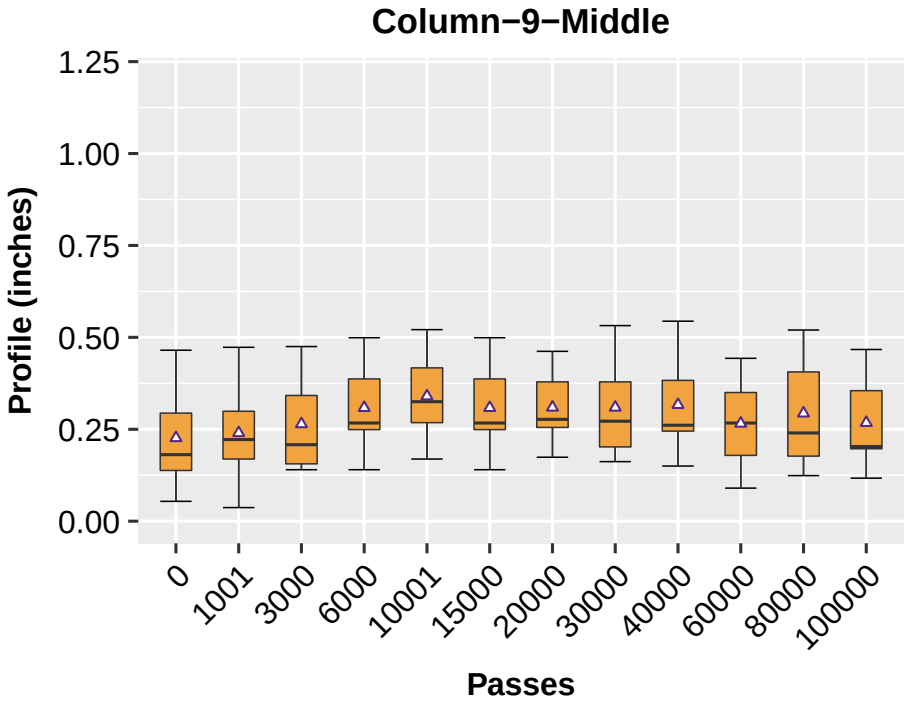

Figure 5.59: *Longitudinal profile change with axle load repetitions (Column-9)*

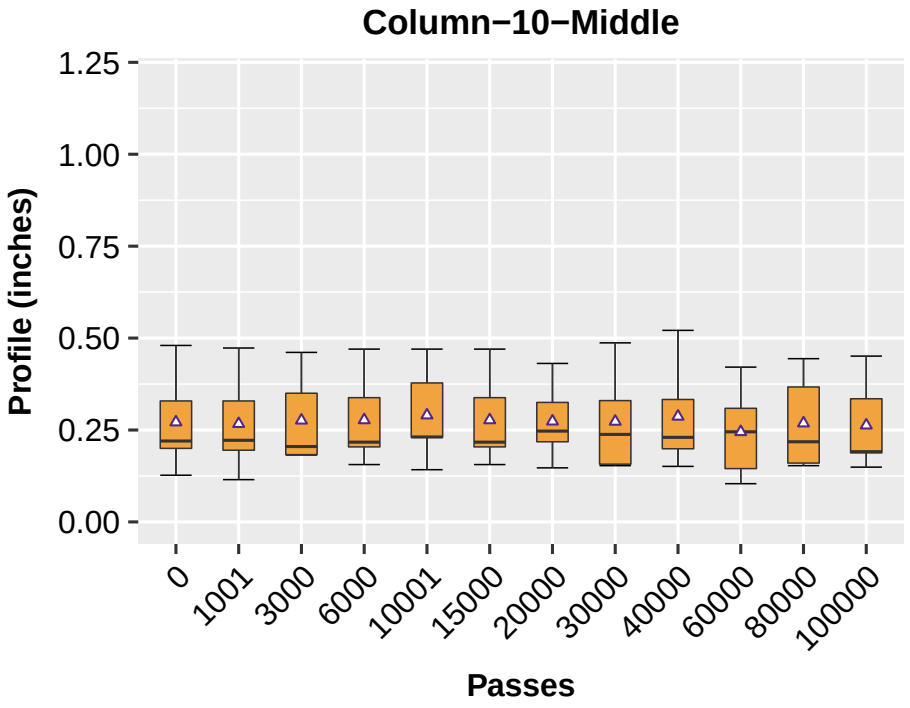

Figure 5.60: *Longitudinal profile change with axle load repetitions (Column-10)*

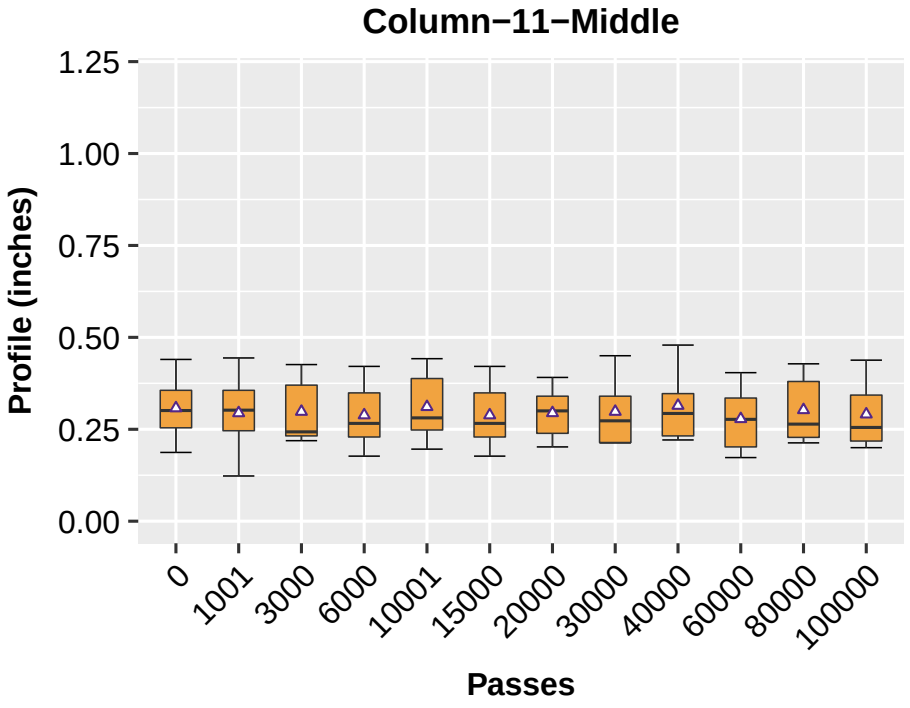

Figure 5.61: *Longitudinal profile change with axle load repetitions (Column-11)*

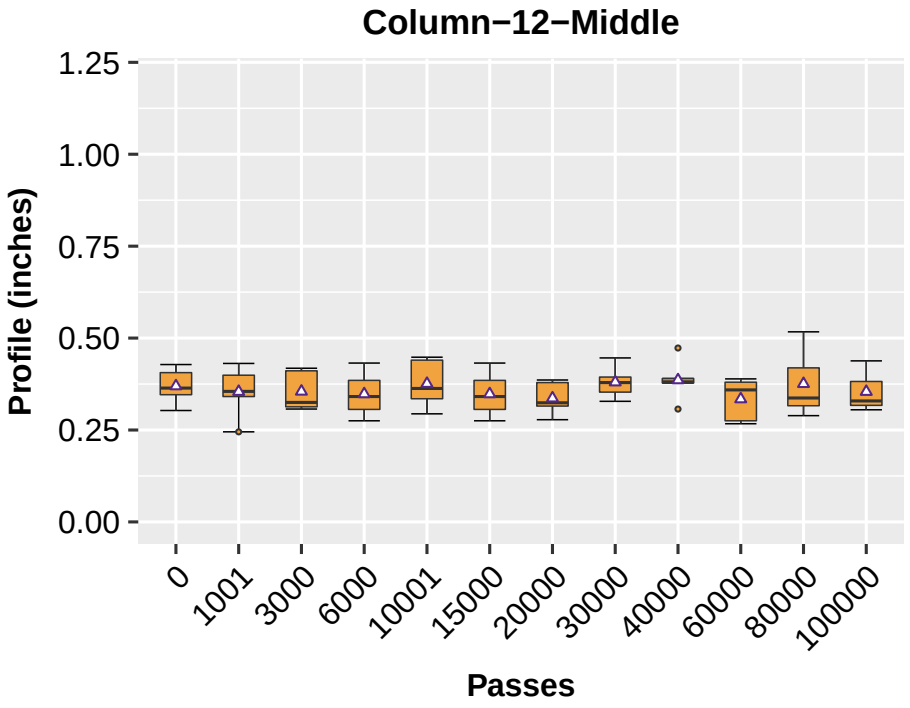

Figure 5.62: *Longitudinal profile change with axle load repetitions (Column-12)*

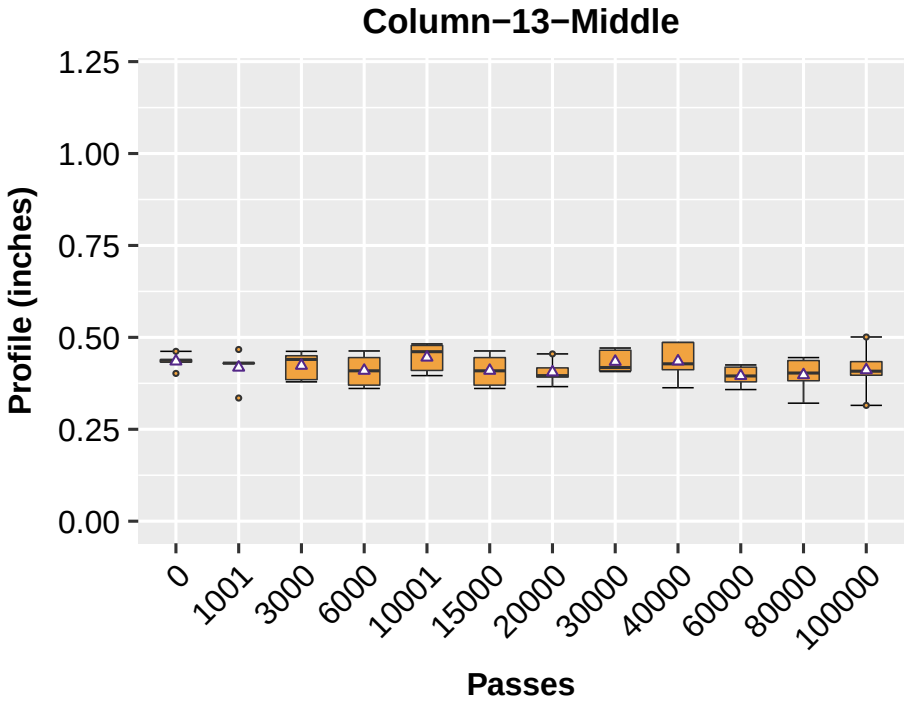

Figure 5.63: *Longitudinal profile change with axle load repetitions (Column-13)*

5.3.4 Forensic Trenching

Upon finishing trafficking pavement constructed in the second round, the pavement was trenched to identify the permanent deformation in each of the layer in the pavement structure. To obtain an even and neat surface, the pavement was cut and half towards to east direction of the test pit was removed, as shown in Figure 5.64. Figure 5.65 is the resulted cross section from the trench process, and the labels of the lanes are provided as well. In addition, the interfaces as marked in Figure 5.67 were delineated. The delineated profiles of the interfaces for each test section are shown in Figure 5.66. It noted that for the control lane, the deformation seems to be propagated from the pavement surface direct through the aggregate base to the subgrade soil, as noticeable deformation was found in the subgrade. However, for the two lanes with geogrid reinforcement, the deformation in the subgrade is very small. In particular, for Lane B, the deformation in the subgrade was barely noticeable.

Figure 5.64: *Trenched Test Sections of Second Round Testing*

Upon finishing trafficking pavement constructed in the second round, the pavement was trenched to identify the permanent deformation in each of the layer in the pavement structure. To obtain an even and neat surface, the pavement was cut and half towards to east direction of the test pit was removed, as shown in Figure 5.64. Figure 5.66 is the resulted cross section from the trench process, and the labels of the lanes are provided as well. In addition, the interfaces as marked in Figure 5.67 were delineated. The delineated profiles of the interfaces for each test section are shown in Figure 5.67. It noted that for the control lane, the deformation seems to be propagated from the pavement surface direct through the aggregate base to the subgrade soil, as noticeable deformation was found in the subgrade. However, for the two lanes with geogrid reinforcement, the deformation in the subgrade is very small. In particular, for Lane B, the de-

Figure 5.65: *Overview of Trenched Test Pit*

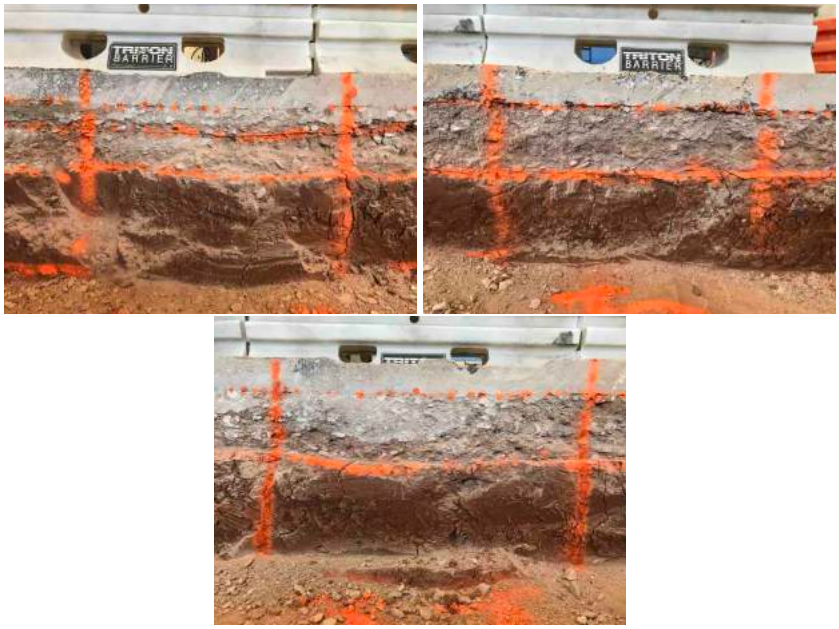

Figure 5.66: *Cross Section of Test Pit After Trenching*

formation in the subgrade is barely noticeable.

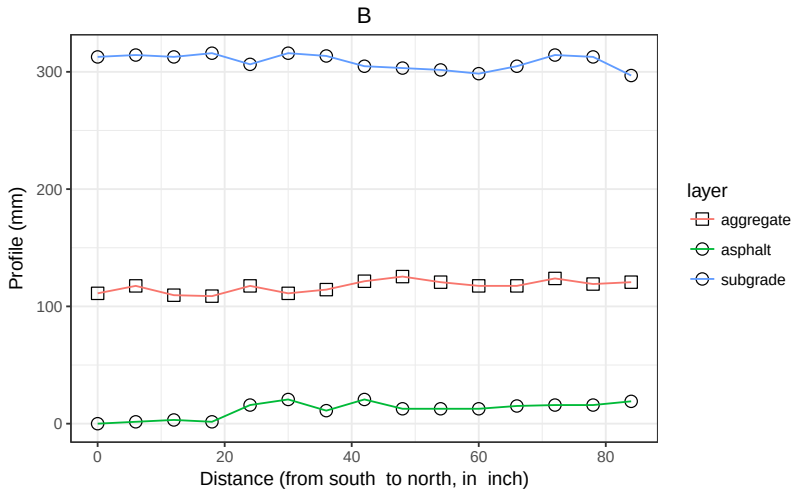

(a) *Lane B*

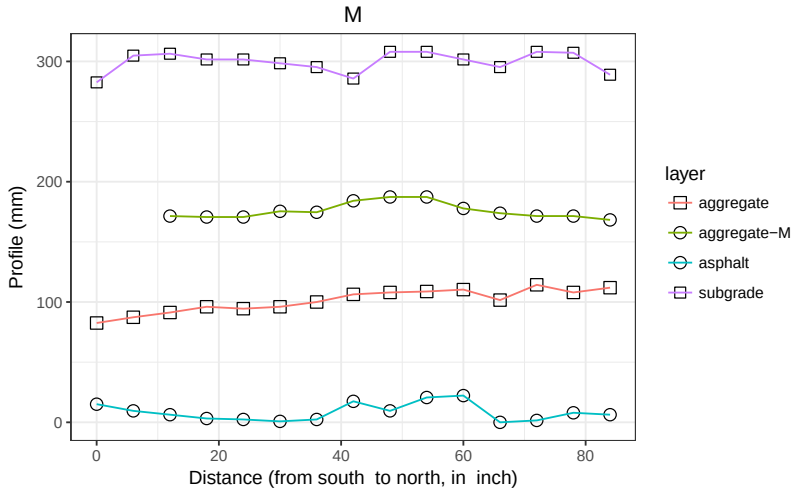

(b) *Lane M*

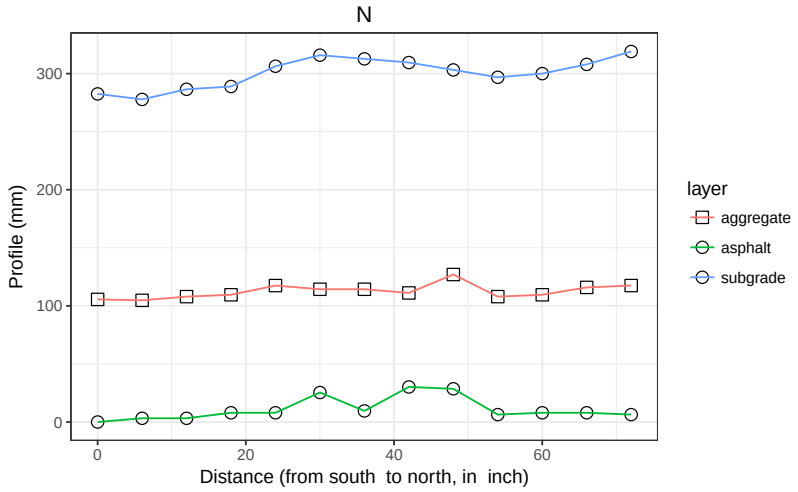

(c) *Control*

Figure 5.67: *Profiles for Interfaces of Cross Section*

5.4 Summary

During the second round of the APT testing, the rectangular geogrids were used as reinforcement for the aggregate base. Given the lesson learned in the first round, more cautions were used in controlling the quality of construction, so as to keep the actual thickness of the pavement structure as close as possible to the design. Further, to verify the thickness of the asphalt layer, a total of six cores were obtained, three from each end of the test sections. The heights of the cores indicated that there was no significant difference between the thickness of the asphalt layer. According to the measured profiles, the utilization of geosynthetics as the base reinforcement material significantly improved the rutting resistance of the test sections. Compared with the control lane, the permanent deformation at Lane B was reduced by 37%, and it was also reduced by 23% at Lane M.

Chapter 6 Third Round of APT Testing

6.1 Test Section Construction

6.1.1 Geosynthetics Product

After the trenching test, a similar procedure for constructing the second round of testing was followed. First, the asphalt layer, aggregate base layer, and one foot from the top of the subgrade were removed. Then, one foot of subgrade soil was refilled and compacted to construct a new subgrade of the pavement structure for the third round of testing. In order to control the construction quality, especially, for controlling the thickness of the asphalt layer, after compacting each layer of unbound granular materials, the thicknesses were checked at several cross sections. The geosynthetics product used in the third round was obtained from Huesker (Figure 6.1). Compared to the geogrids in the first and second rounds, the one used for the third round has a much smaller stiffness.

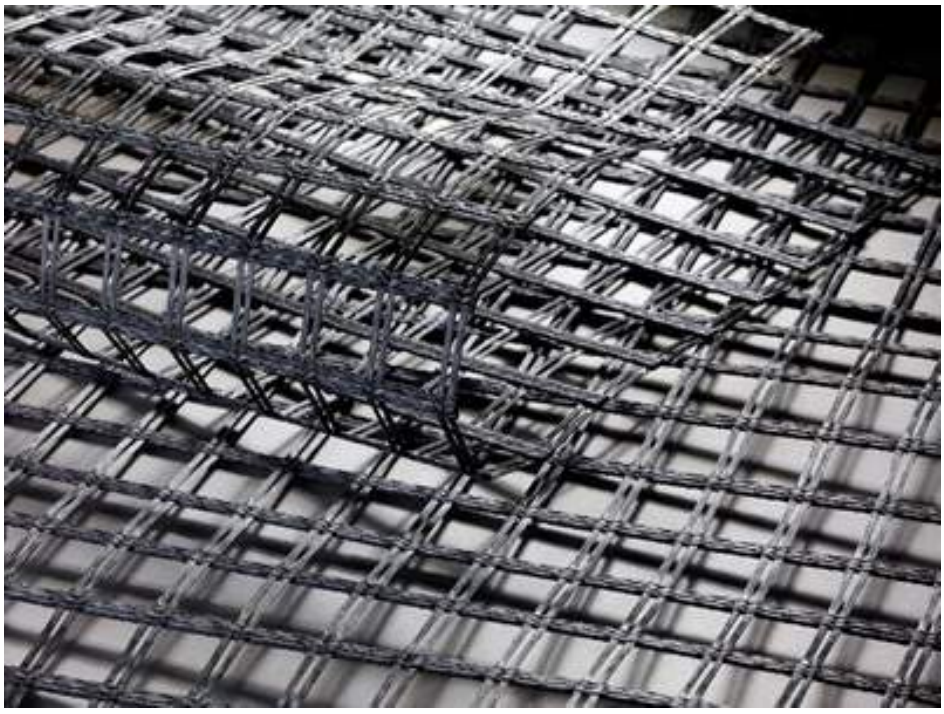

Figure 6.1: *Geogrid Used in the Third Round of APT Testing*

6.2 APT Testing Profiles

A denser pattern of grids than the one in the second round of testing was used for the third round. Figure 6.2 gives a diagram of illustrating the grids of the third round. As indicated, overall, a total of seven horizontal cross-sections (rows) and 24 longitudinal cross-sections (columns) were considered.

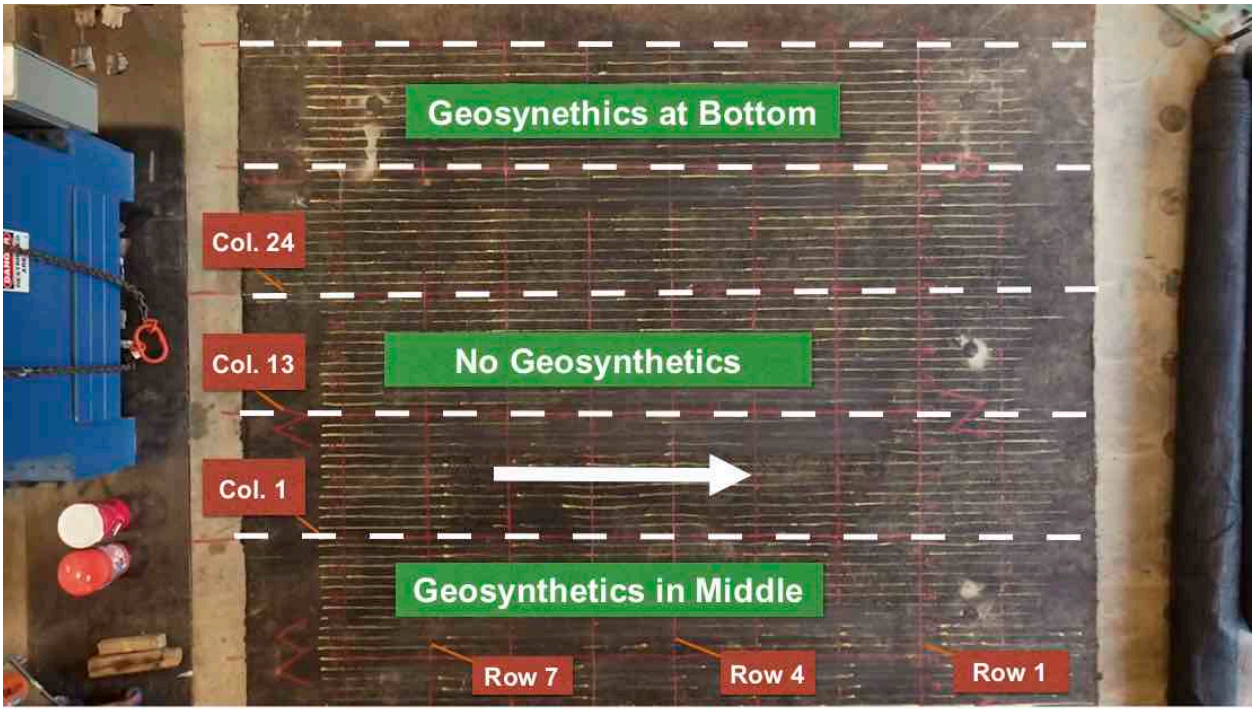

Figure 6.2: *Diagram of Profile Grids*

6.2.1 Lane M

Deformation Curves

Figures 6.3 through 6.7 are the profiles measured along the horizontal cross-sections, namely, from cross-traffic direction or from north to south of the test section. It is found that the largest deformation occurrs at the first cross section (Row-1 in Several very large rutting values were also found in the second cross-section (Row-2, Figure 6.3). According to the cores drilling test results, the cores taken around these areas revealed a thinner lift thickness of the asphalt mixture. This is a possible cause of the large rutting values in this area. With respect to the cross-section in the center of the lane, where the thickness was closer to the design (0.385-inch), the rutting values are only slightly over 0.5 inch. This pattern was observed in Figures 6.4 through 6.7.

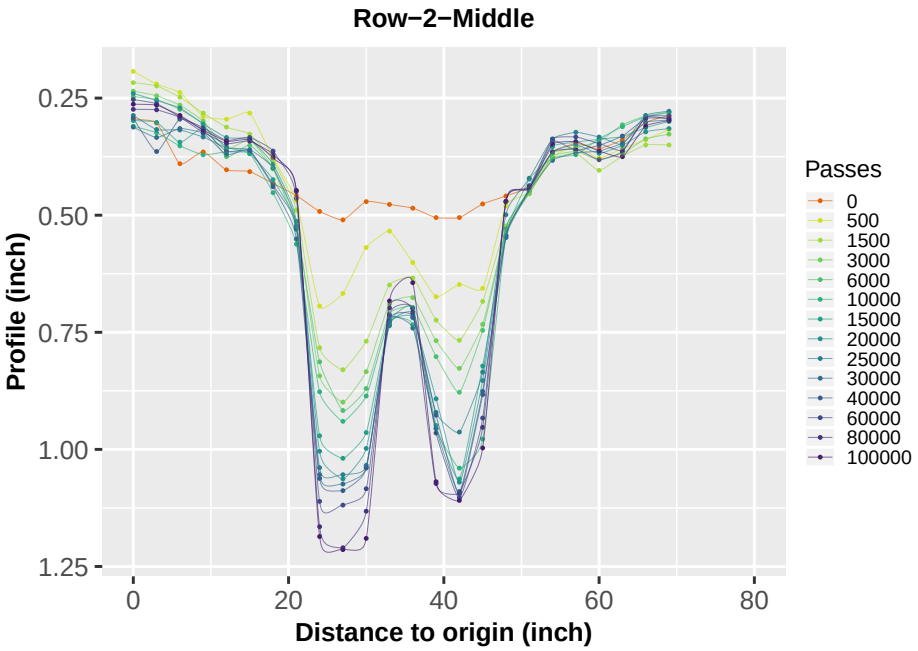

Figure 6.3: *Profile results for Lane-M (Row-2)*

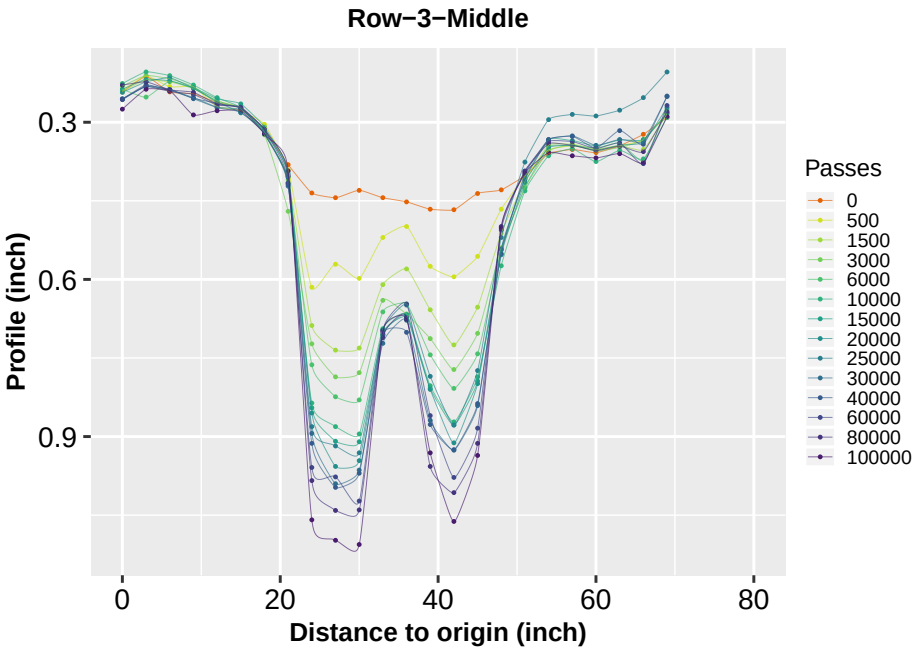

Figure 6.4: *Profile results for Lane-M (Row-3)*

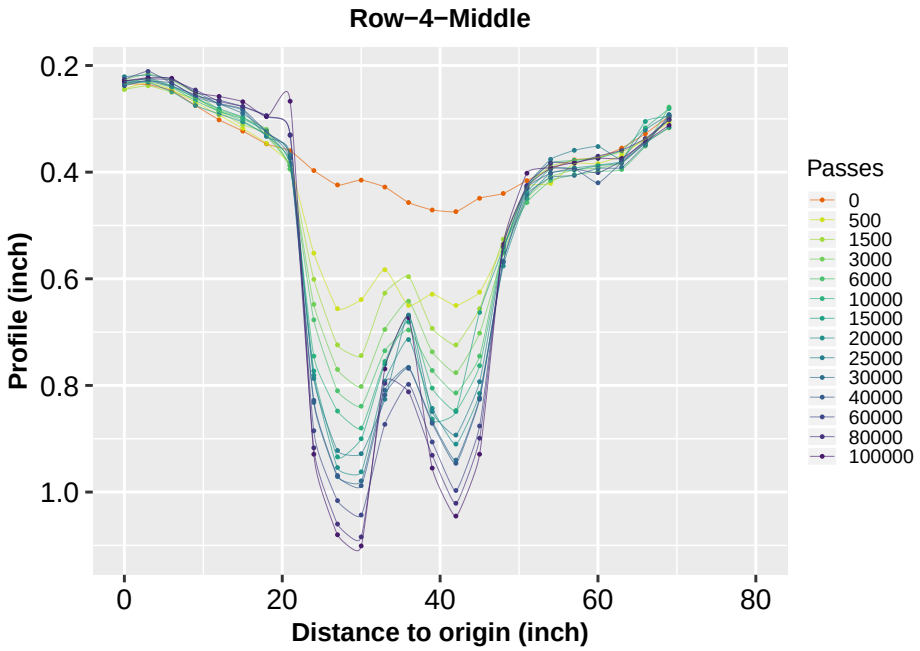

Figure 6.5: *Profile results for Lane-M (Row-4)*

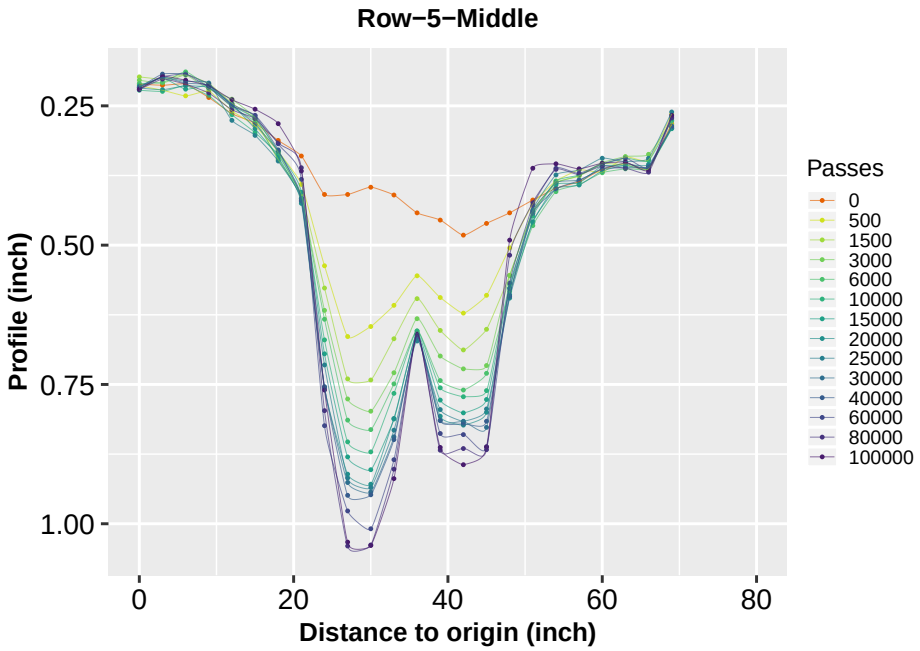

Figure 6.6: *Profile results for Lane-M (Row-5)*

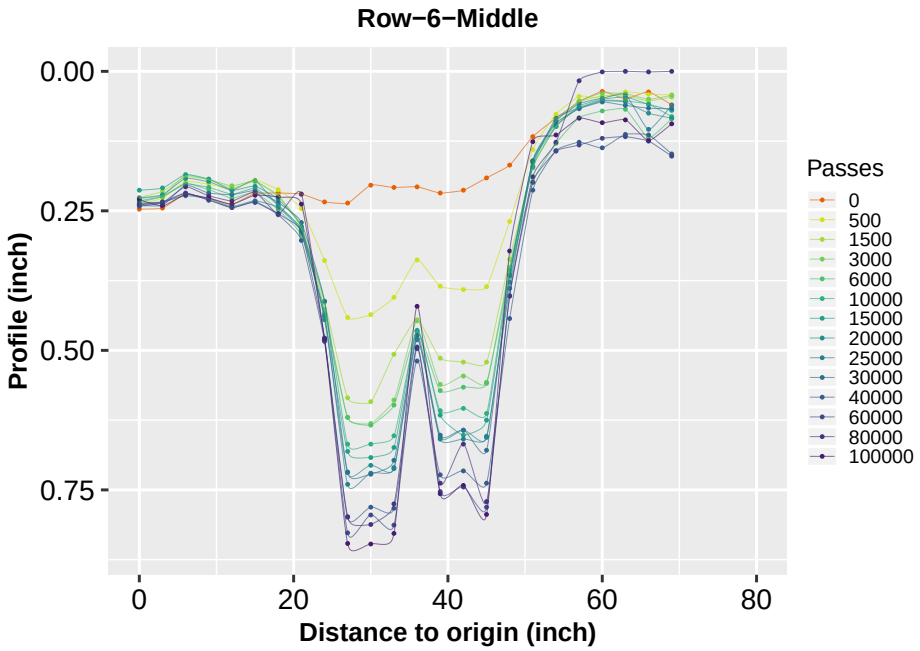

Figure 6.7: *Profile results for Lane-M (Row-6)*

Aggregated Longitudinal profiles

Figures 6.8 through 6.31 graph the longitudinal profiles of the Lane-M, which were measured along the traffic (east to west) direction. It is seen that from the Columns 1 through 8 (Figures 6.8 to 6.15), only a very small amount of deformation occurred. This is because these sections are far from the wheel path areas, thus are almost free from the effect of the wheel loading of the APT. Most of the deformation is seen taking place in the vicinity of the two wheel paths, as indicated in Figures 6.16 through 6.23. Regarding the longitudinal profiles, the largest averaged permanent deformation is found in the Column-10 (Figure 6.17), which is right in the center of the right wheel path. The largest rutting in this longitudinal cross section is around 0.5-inch. Similar deformation values were found in the Column-11 and the Column-16.

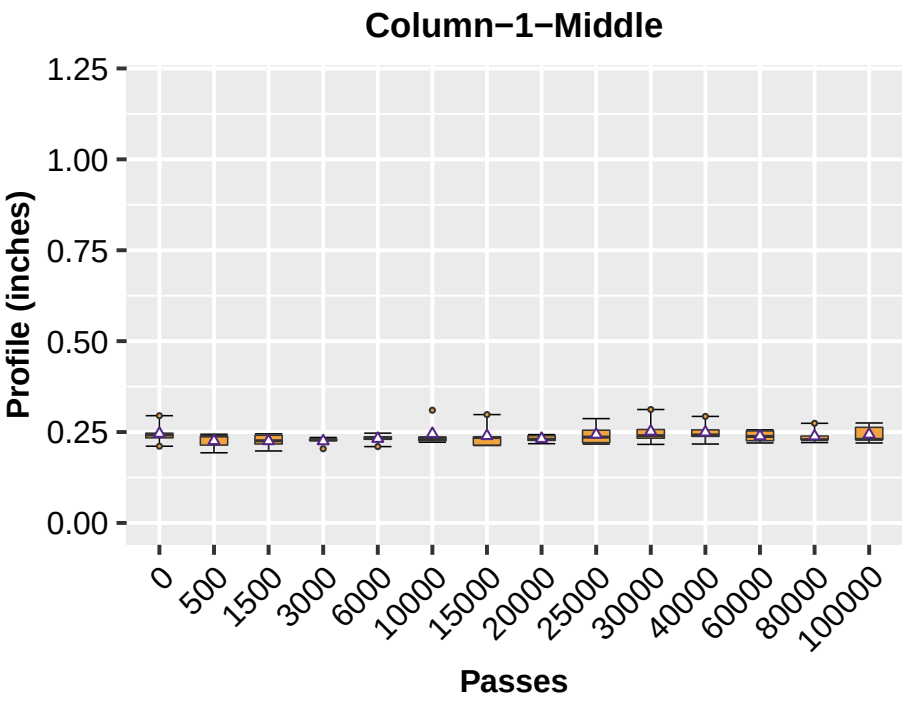

Figure 6.8: *Averaged Longitudinal Profiles (Column-1)*

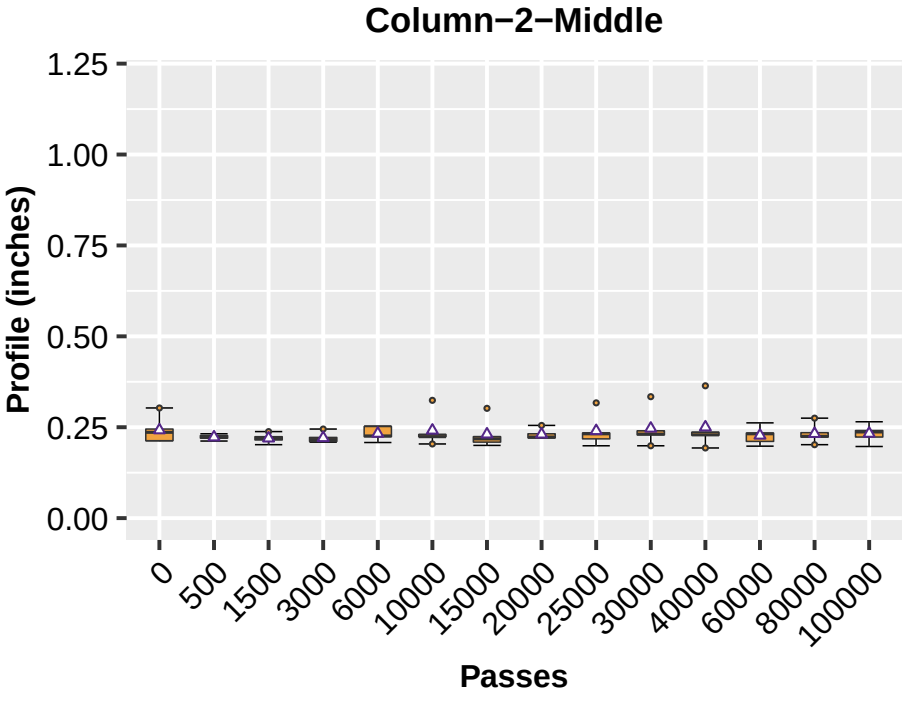

Figure 6.9: *Averaged Longitudinal Profiles (Column-2)*

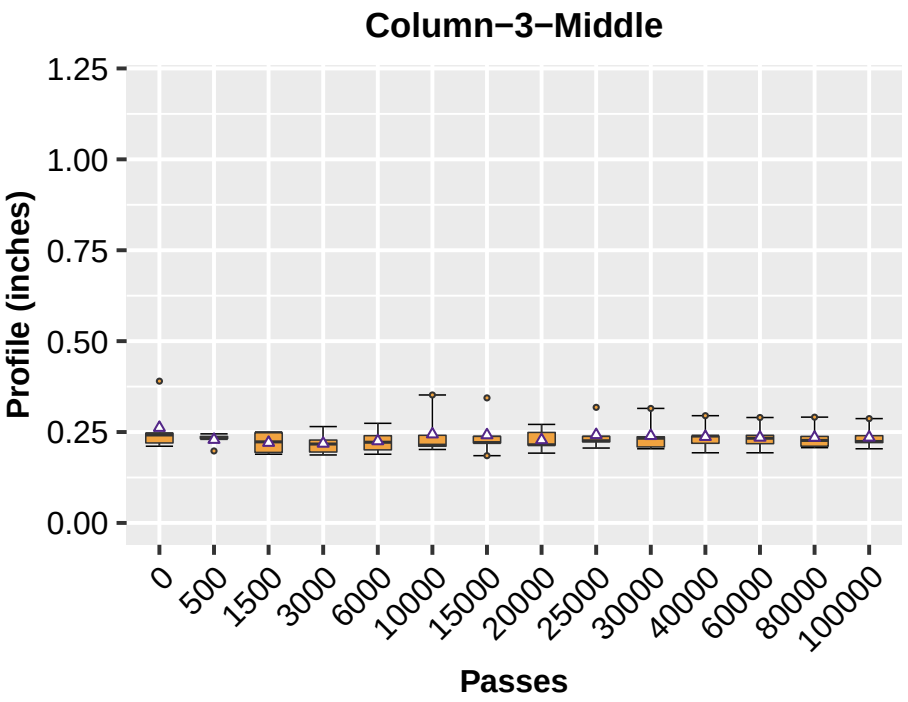

Figure 6.10: *Averaged Longitudinal Profiles (Column-3)*

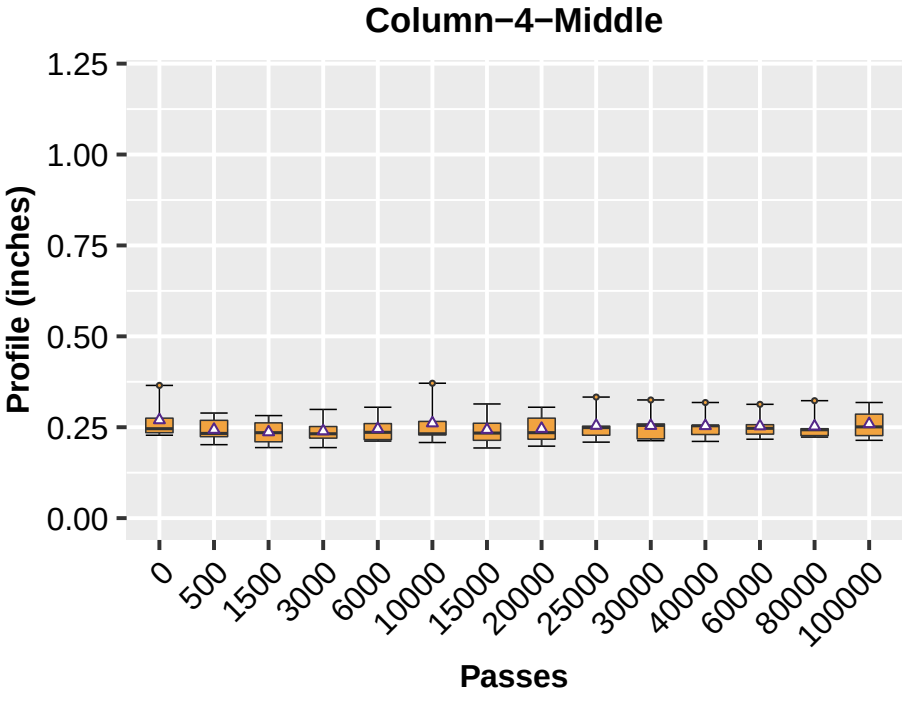

Figure 6.11: *Averaged Longitudinal Profiles (Column-4)*

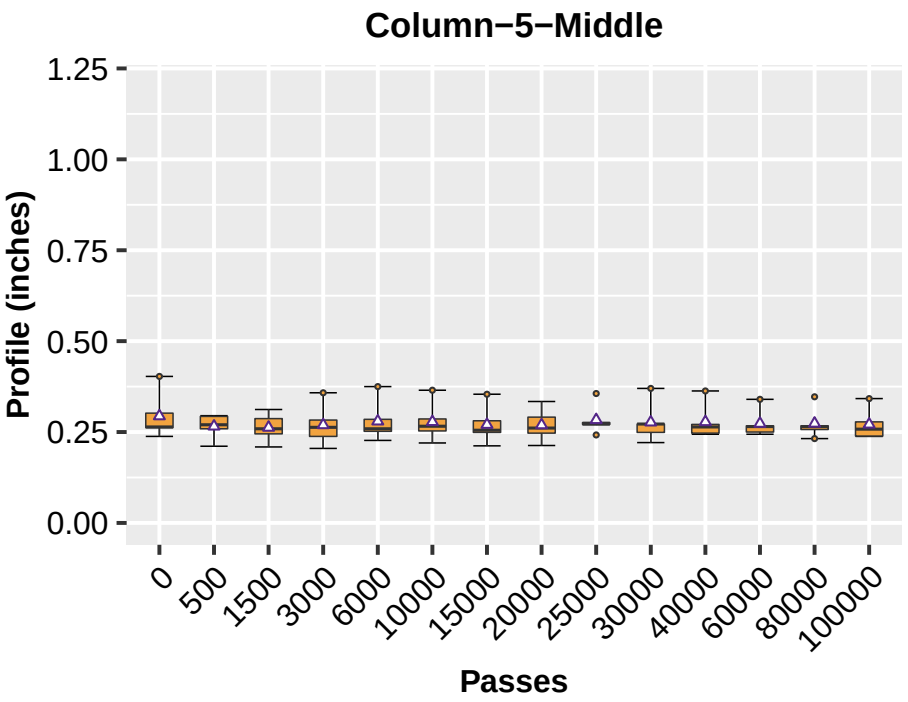

Figure 6.12: *Averaged Longitudinal Profiles (Column-5)*

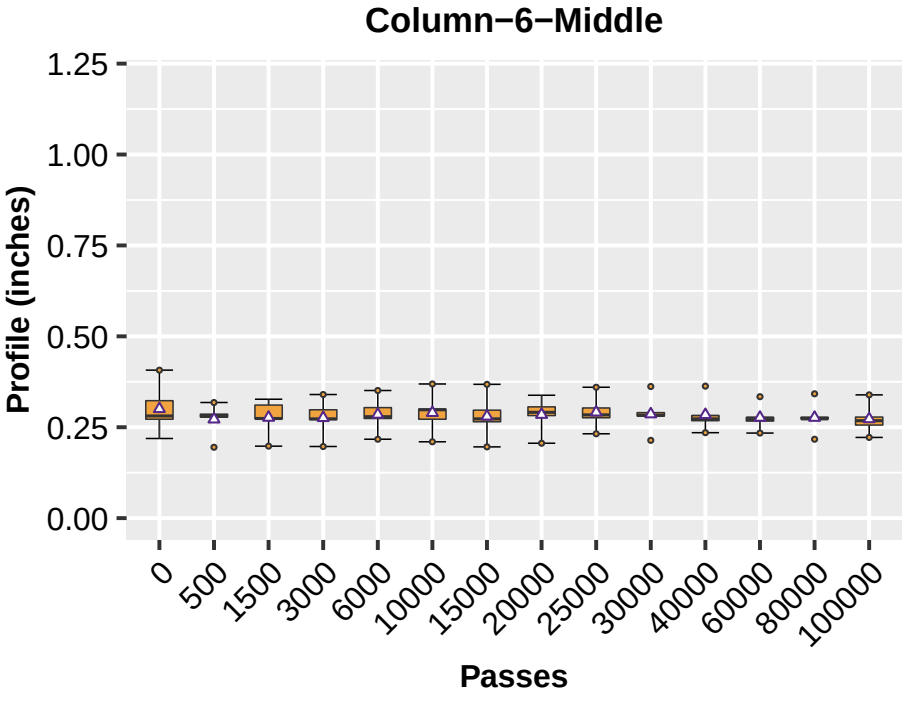

Figure 6.13: *Averaged Longitudinal Profiles (Column-6)*

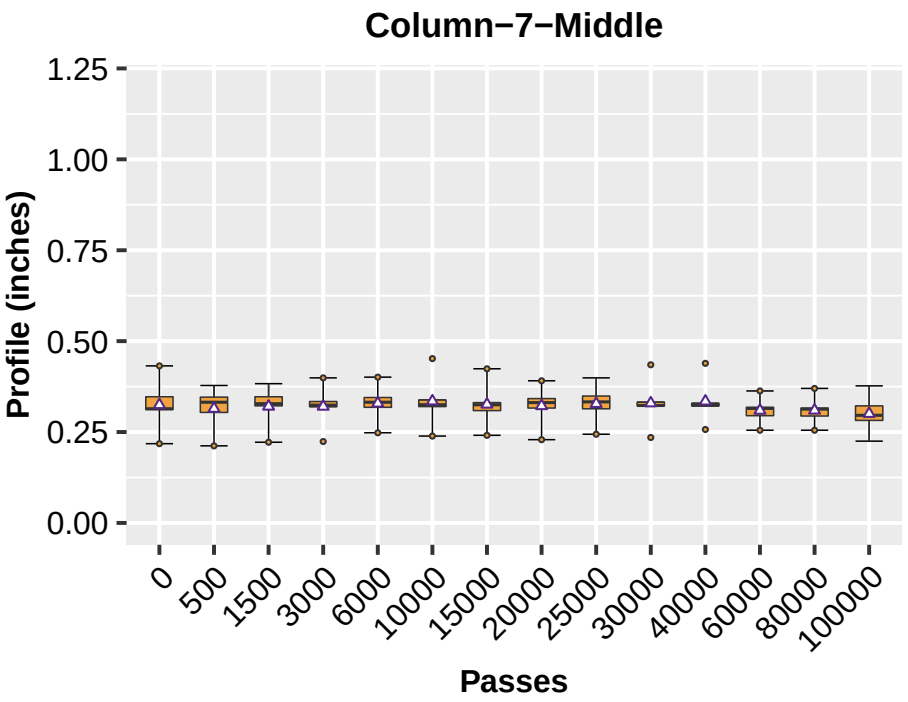

Figure 6.14: *Averaged Longitudinal Profiles (Column-7)*

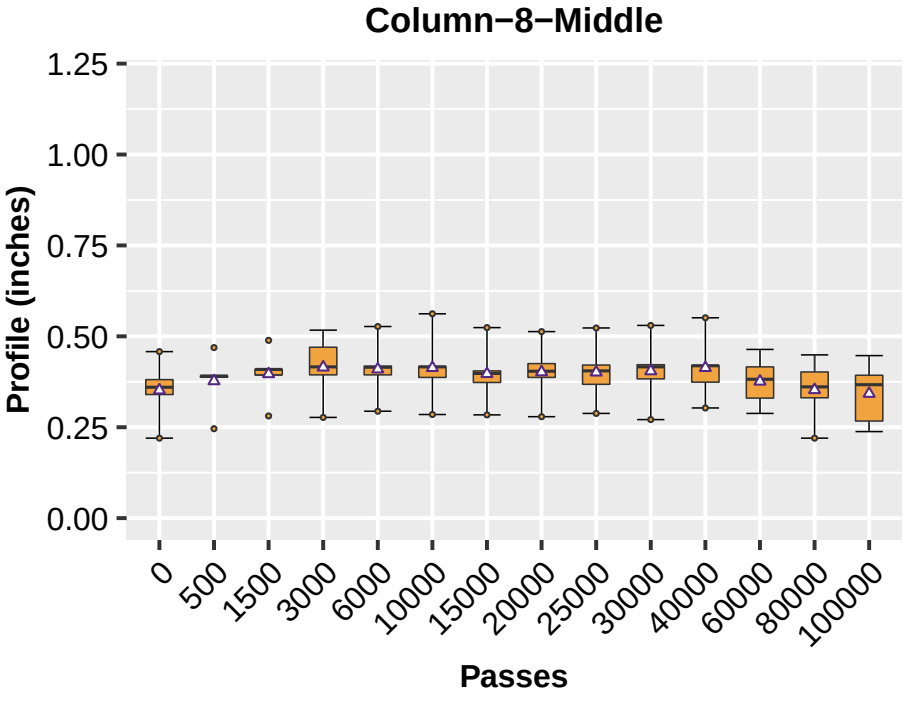

Figure 6.15: *Averaged Longitudinal Profiles (Column-8)*

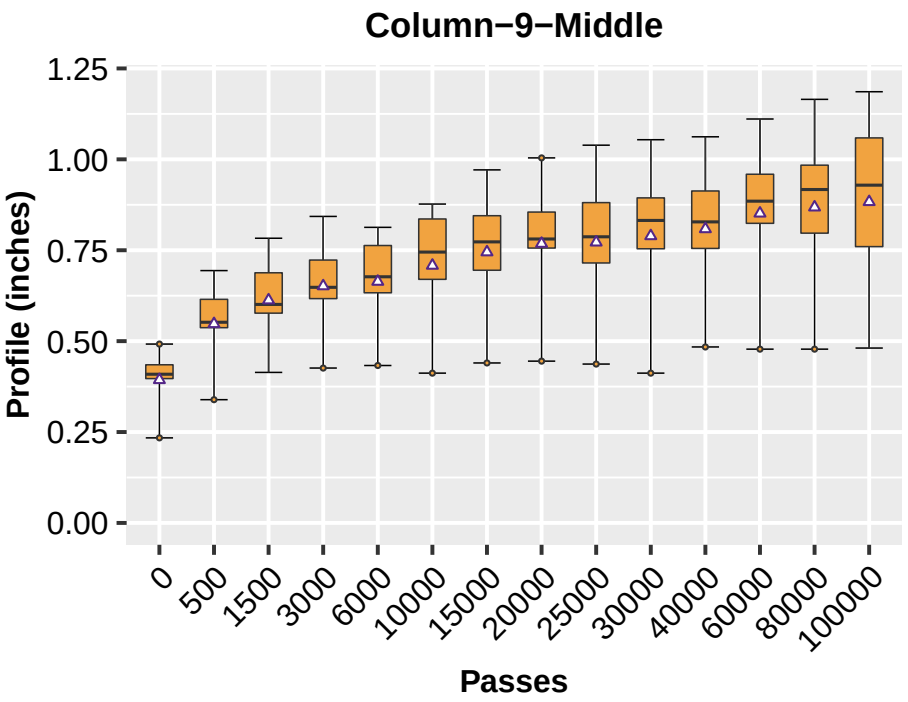

Figure 6.16: *Averaged Longitudinal Profiles (Column-9)*

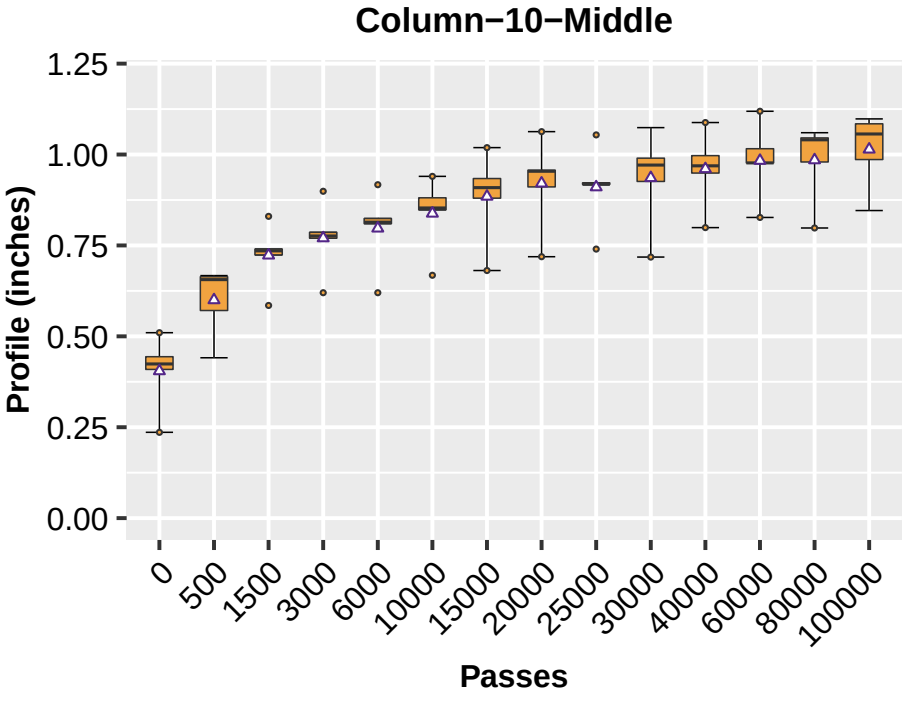

Figure 6.17: *Averaged Longitudinal Profiles (Column-10)*

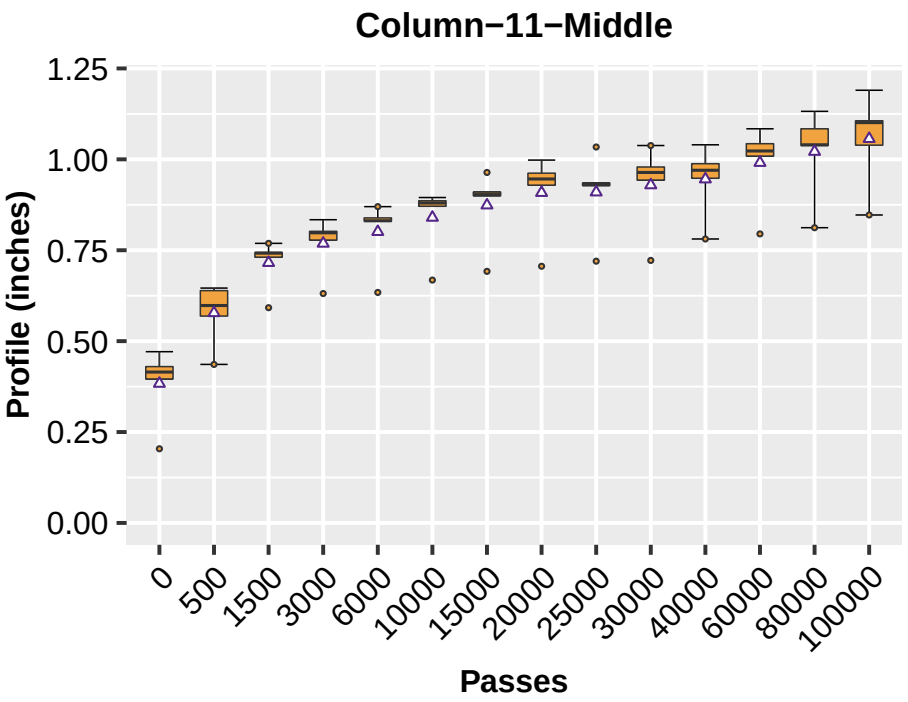

Figure 6.18: *Averaged Longitudinal Profiles (Column-11)*

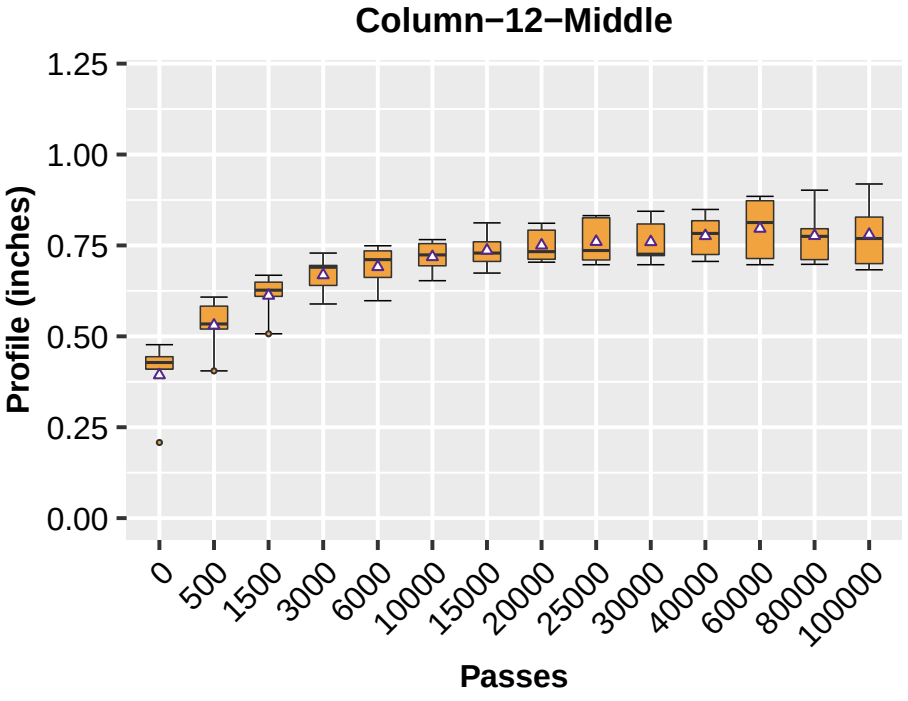

Figure 6.19: *Averaged Longitudinal Profiles (Column-12)*

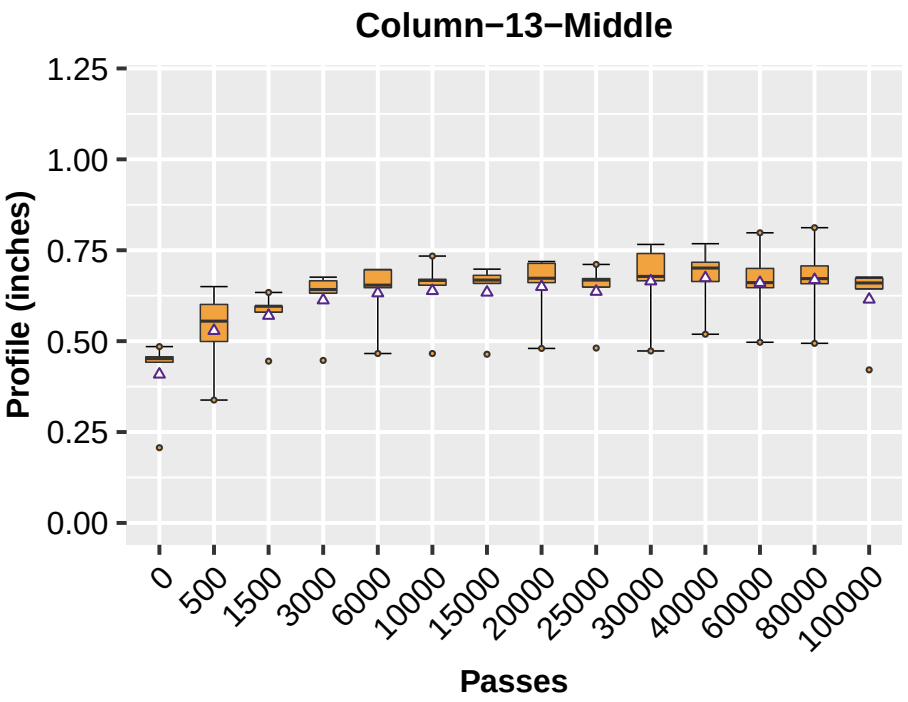

Figure 6.20: *Averaged Longitudinal Profiles (Column-13)*

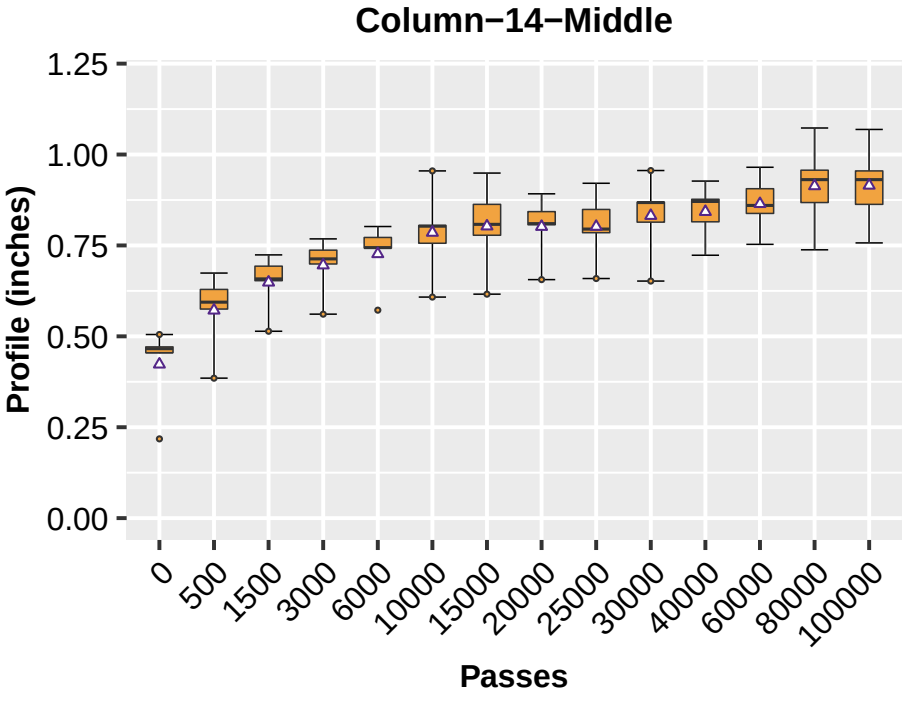

Figure 6.21: *Averaged Longitudinal Profiles (Column-14)*

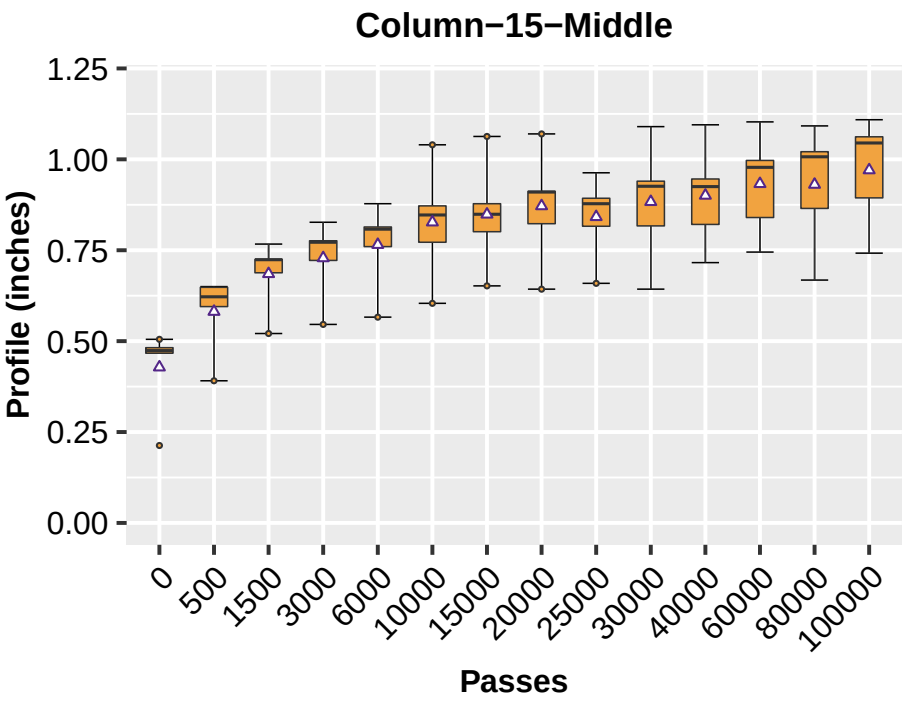

Figure 6.22: *Averaged Longitudinal Profiles (Column-15)*

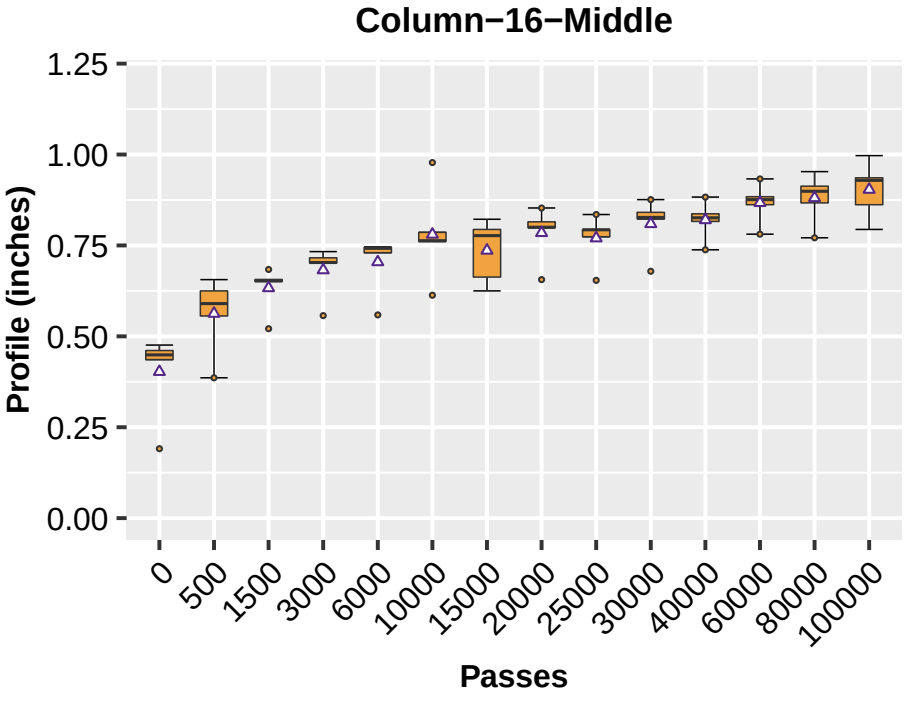

Figure 6.23: *Averaged Longitudinal Profiles (Column-16)*

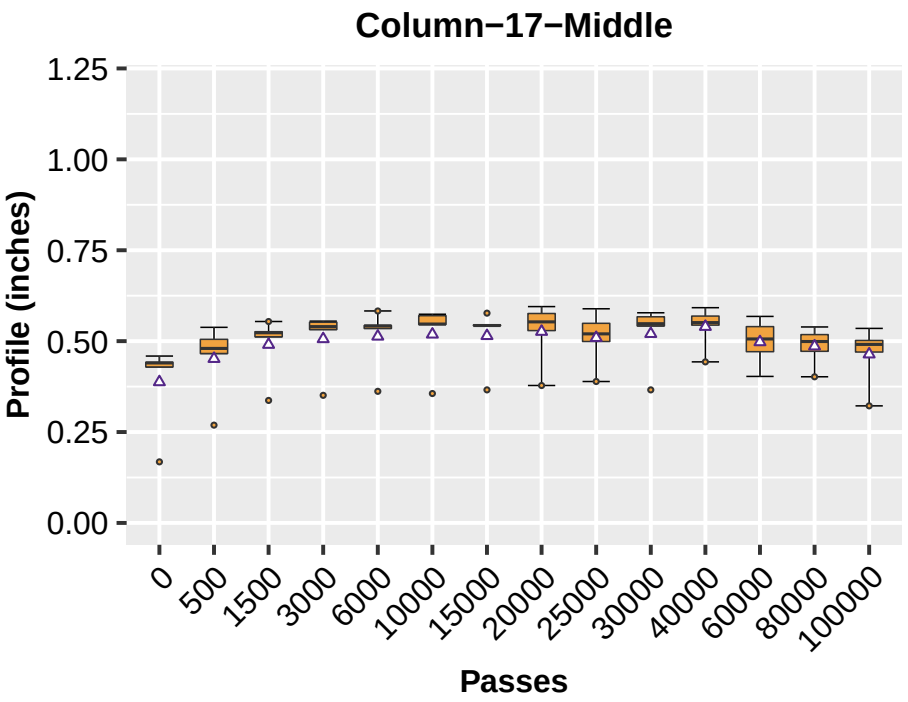

Figure 6.24: *Averaged Longitudinal Profiles (Column-17)*

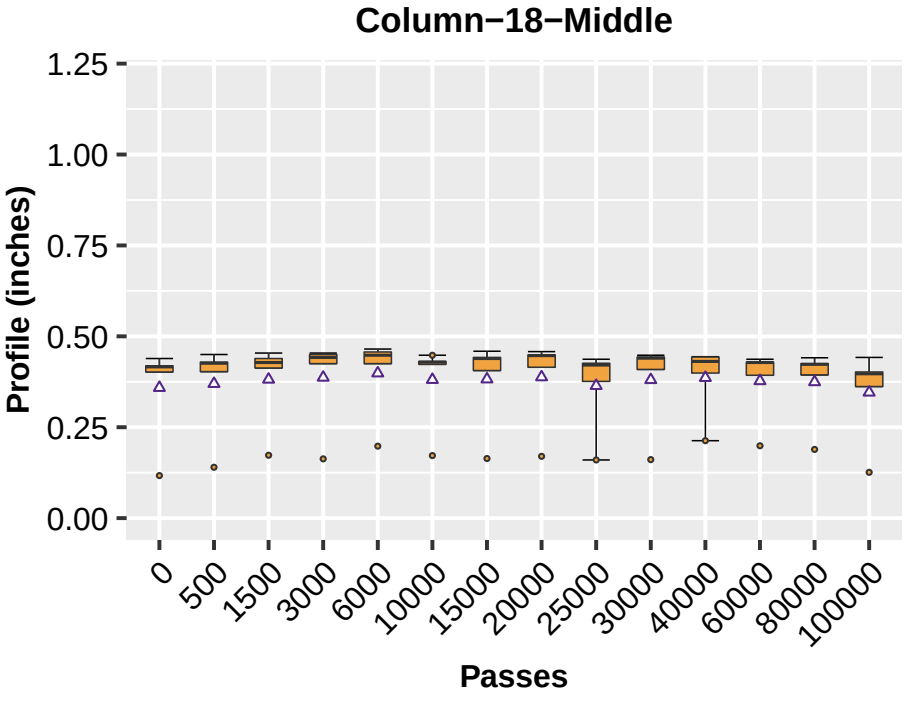

Figure 6.25: *Averaged Longitudinal Profiles (Column-18)*

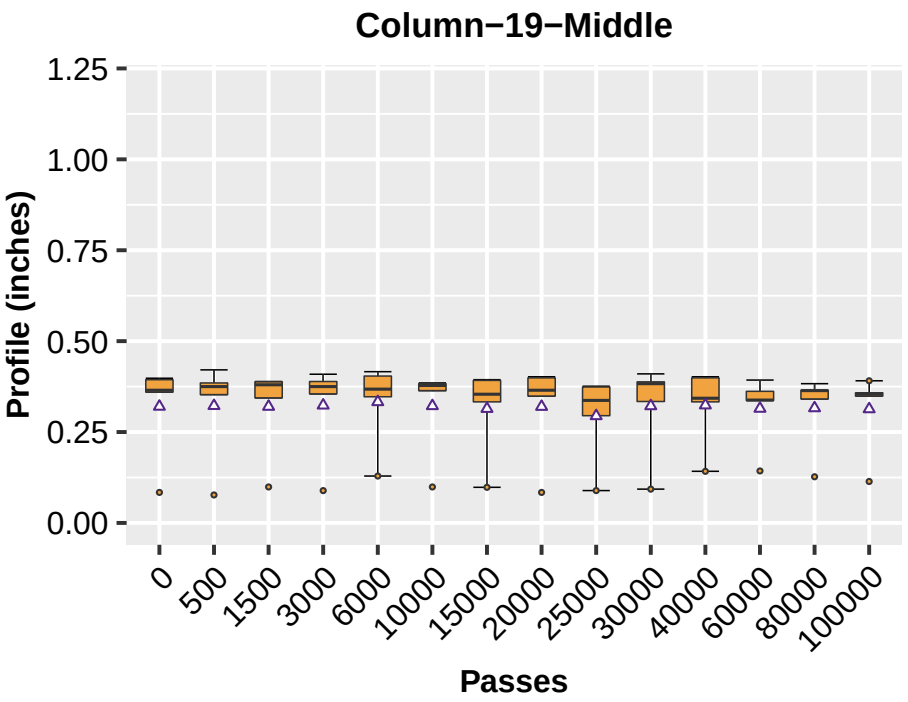

Figure 6.26: *Averaged Longitudinal Profiles (Column-19)*

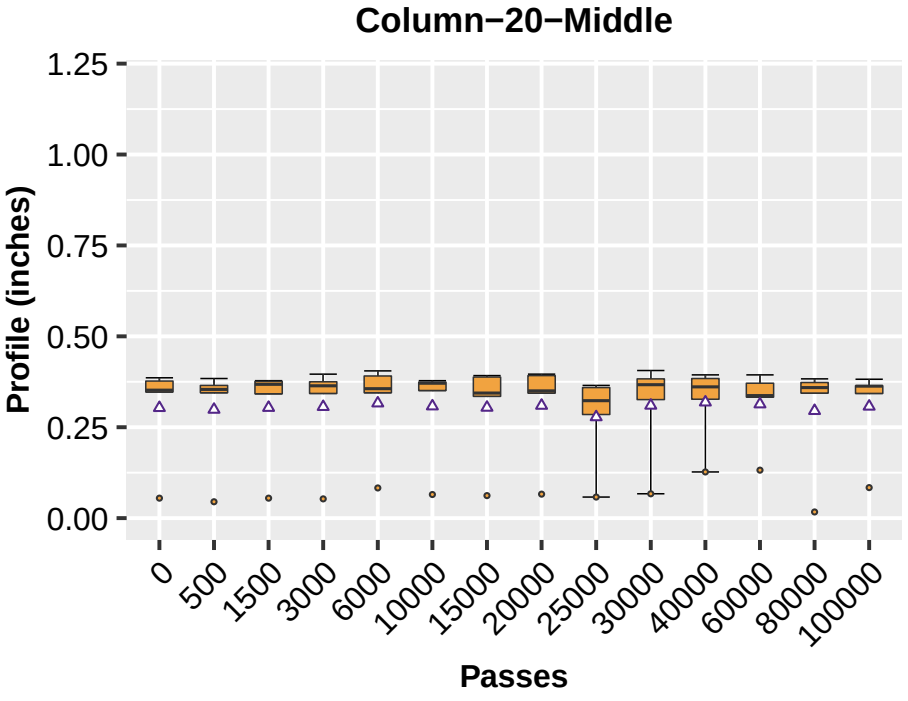

Figure 6.27: *Averaged Longitudinal Profiles (Column-20)*

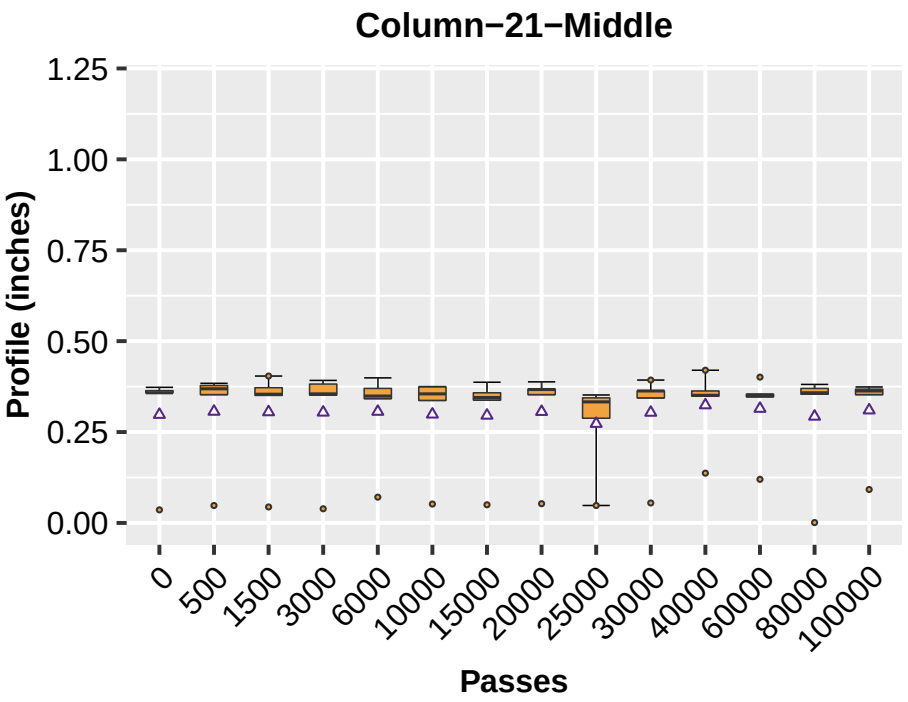

Figure 6.28: *Averaged Longitudinal Profiles (Column-21)*

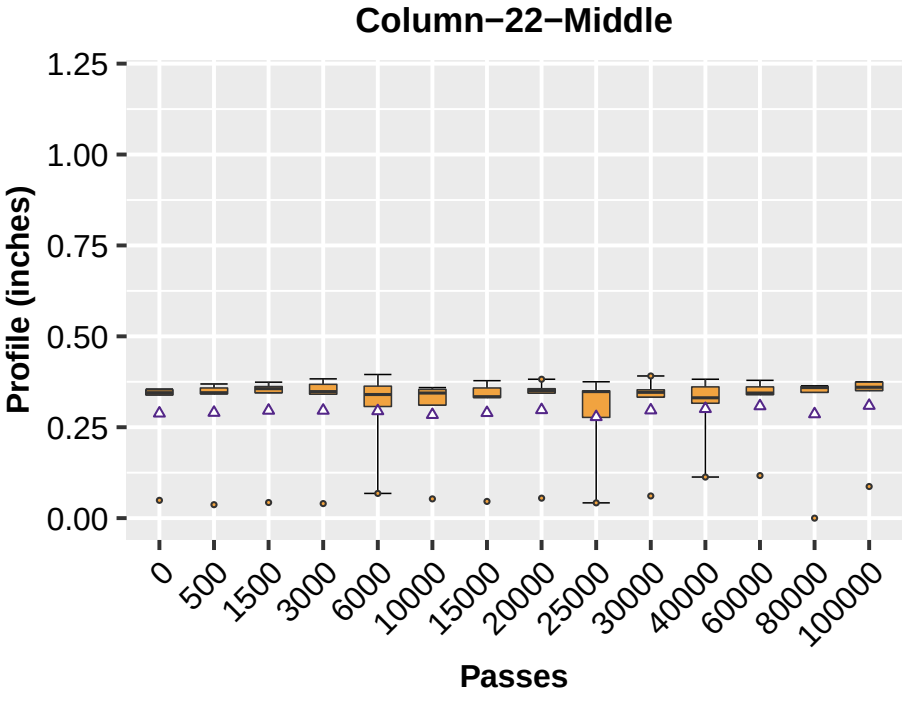

Figure 6.29: *Averaged Longitudinal Profiles (Column-22)*

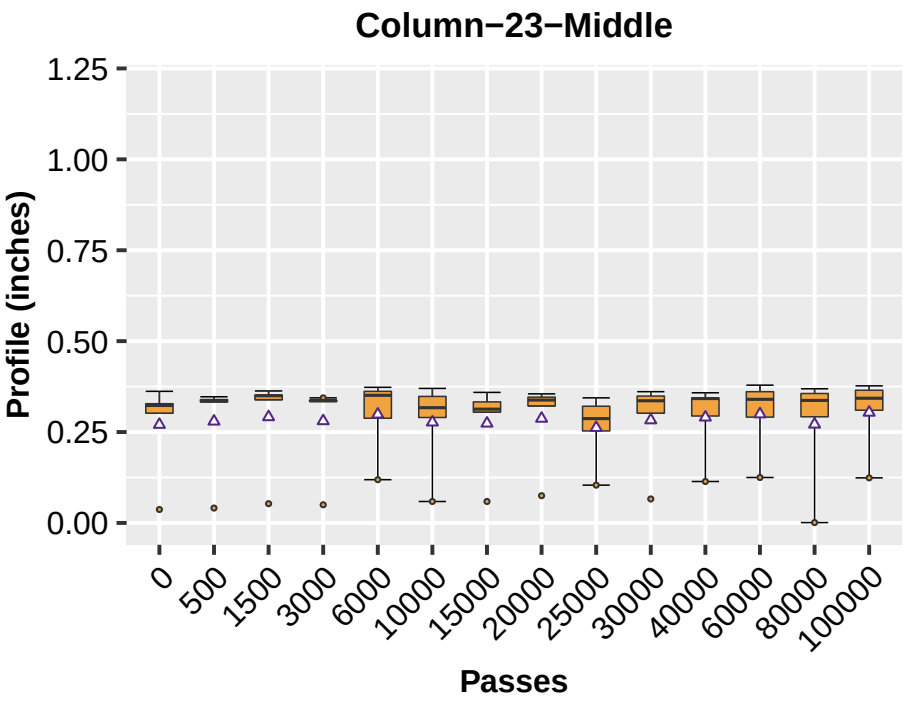

Figure 6.30: *Averaged Longitudinal Profiles (Column-23)*

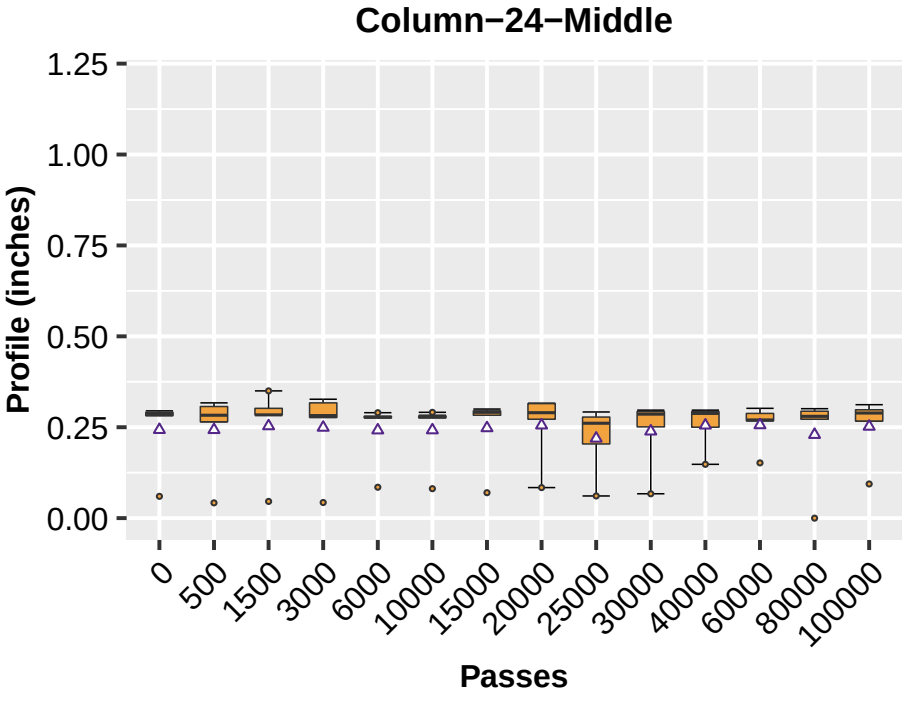

Figure 6.31: *Averaged Longitudinal Profiles (Column-24)*

6.2.2 Lane B

Deformation Curves

Figures 6.32 through 6.36 show the cross-section profiles for the lane with geogrids installed at the bottom of the stone base (Lane B). As indicated, the largest rutting value was found at the second row (Figure 6.32), which reaches 0.91 inch. The rutting value at the third cross-section, as shown in Figure 6.33, was only slightly smaller than that of the second row, which had a rutting value of 0.81 inch. The rutting at the cross-sections 4 through 6 were quite similar, which are all around 0.6 inch. It is noted that the thickness around east end (Rows 1 through 3) was relatively thinner than that of the center of the test section, which is probably the reason for the larger rutting values found in this area.

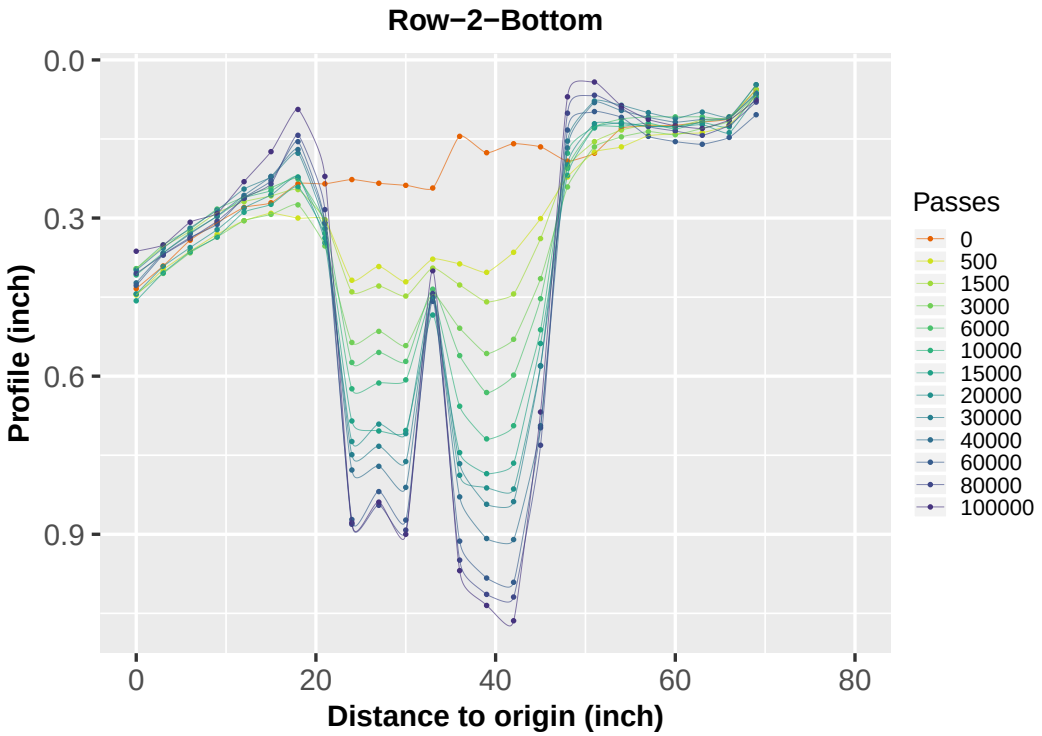

Figure 6.32: *Profile results for the Bottom Lane (Row-2)*

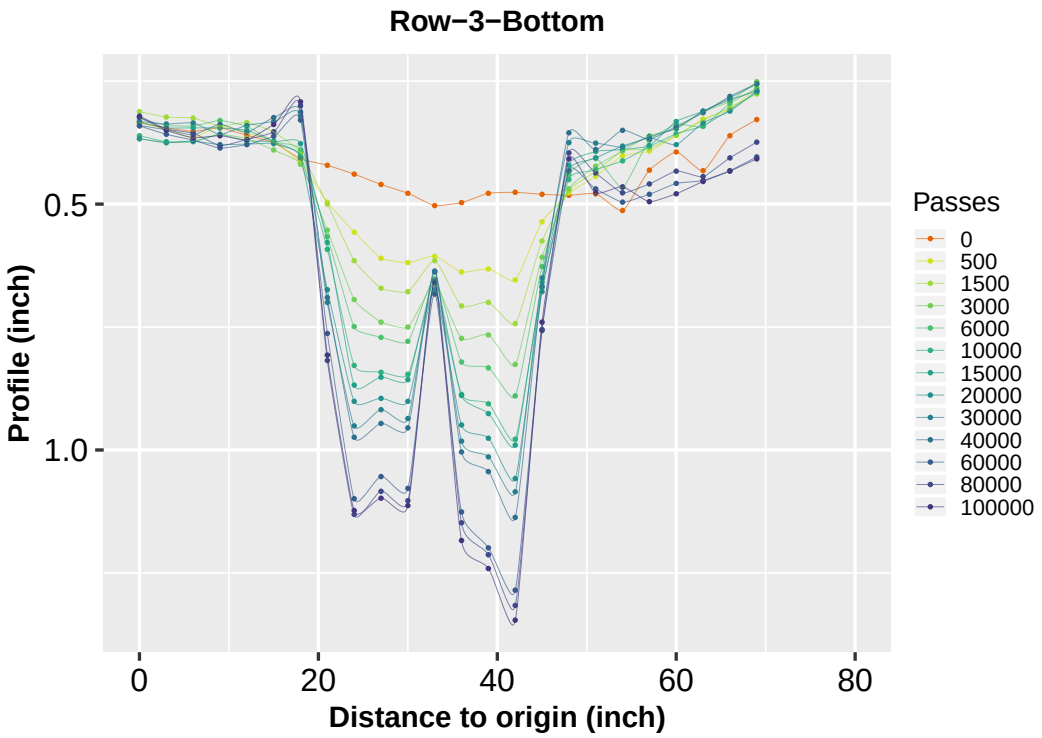

Figure 6.33: *Profile results for the Bottom Lane (Row-3)*

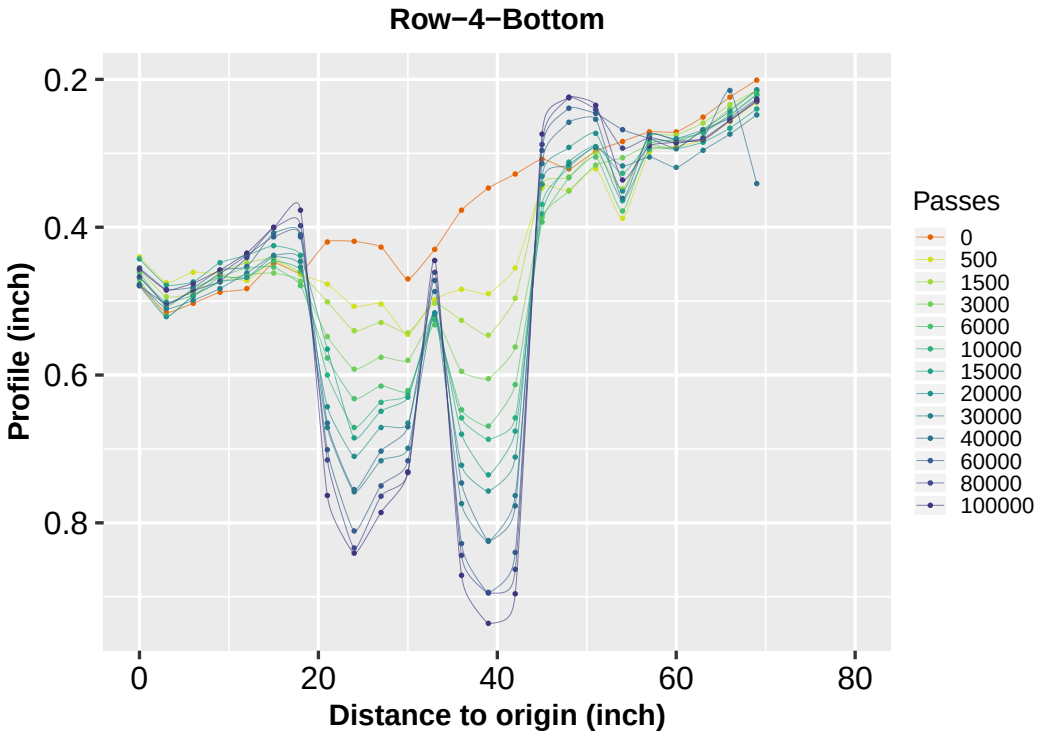

Figure 6.34: *Profile results for the Bottom Lane (Row-4)*

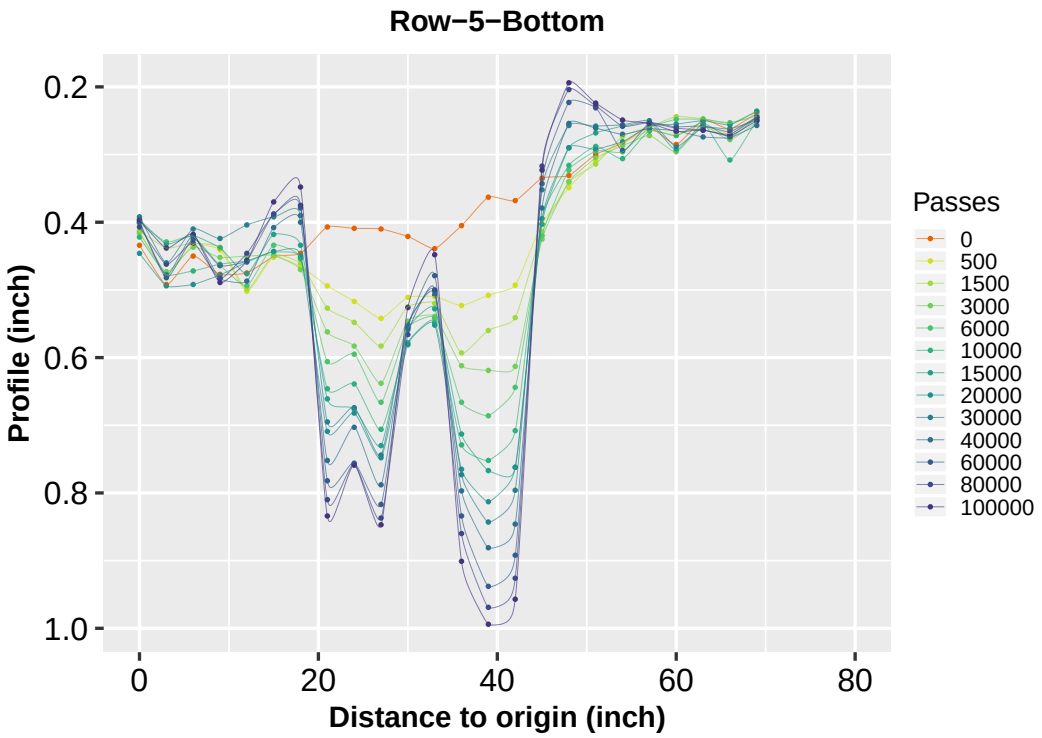

Figure 6.35: *Profile results for the Bottom Lane (Row-5)*

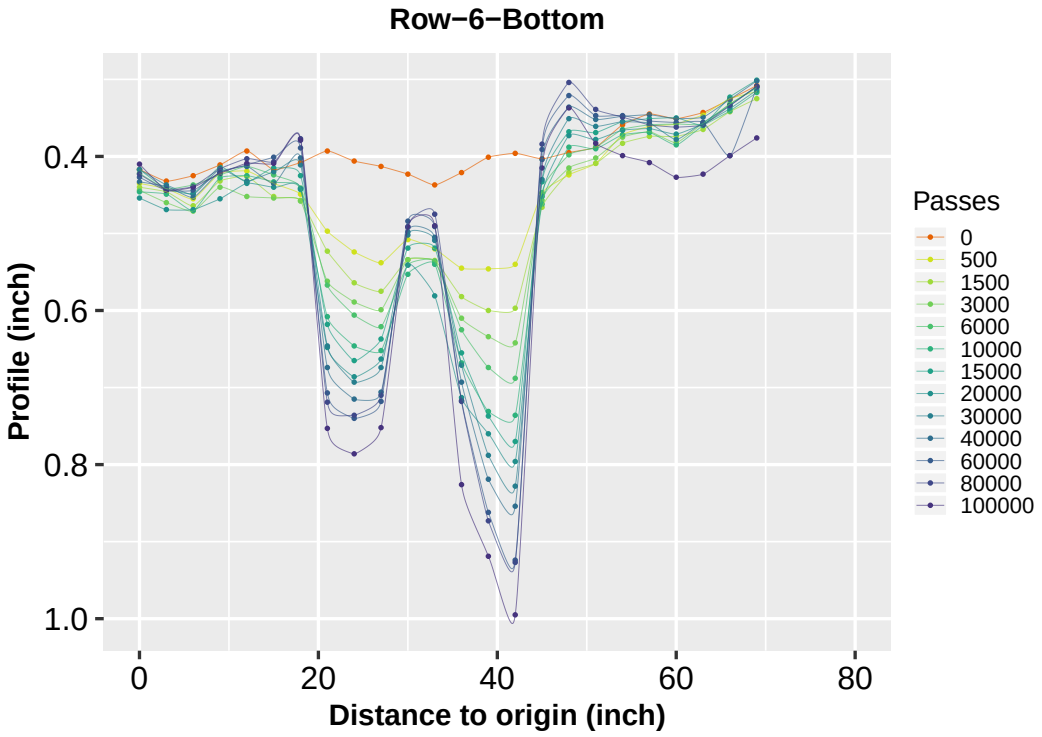

Figure 6.36: *Profile results for the Bottom Lane (Row-6)*

Aggregated Profiles

Figures 6.37 through 6.60 depict the longitudinal profiles for the Lane B. For the Lane M, similar to the other two lanes, the cross-sections that were far away from the two wheelpaths show very few deformations, as indicated in the Figures 6.37 through 6.43, and Figures 6.53 through 6.60. The largest average rutting was found at cross-section 11 (column 11, Figure 6.47), which reached 0.66 inch. A similar rutting value was found at cross-sections 10 and 15 (columns 10 and 15), which had rutting values of 0.64 inch and 0.59 inch, respectively. When considering the effects of thickness at the west end (rows 1 through 2) of the test section, the average rutting value of the Lane B was around 0.6 inch.

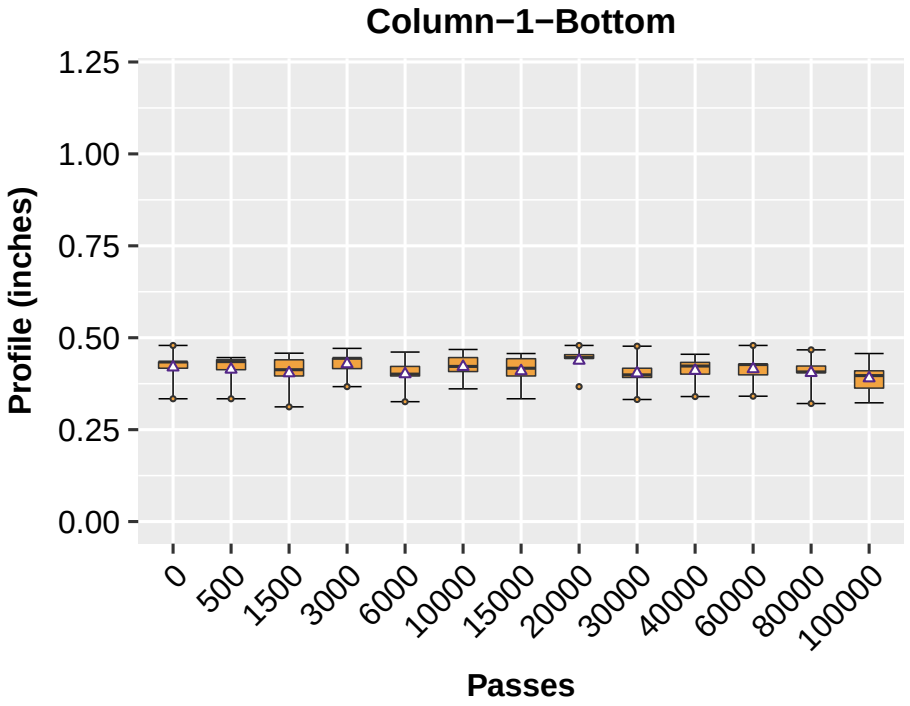

Figure 6.37: *Averaged Longitudinal Profiles (Column-1)*

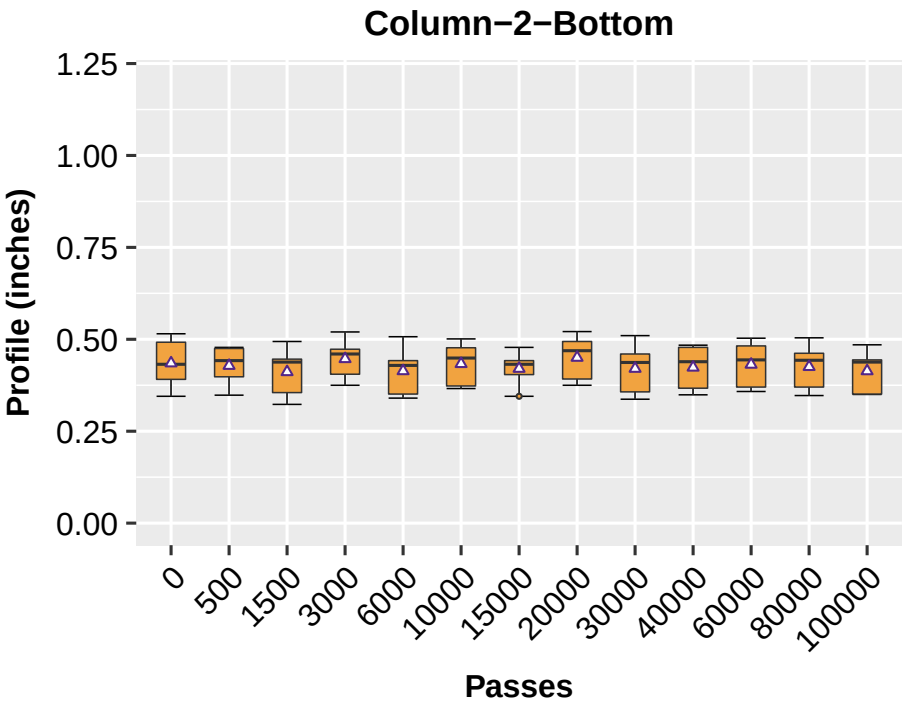

Figure 6.38: *Averaged Longitudinal Profiles (Column-2)*

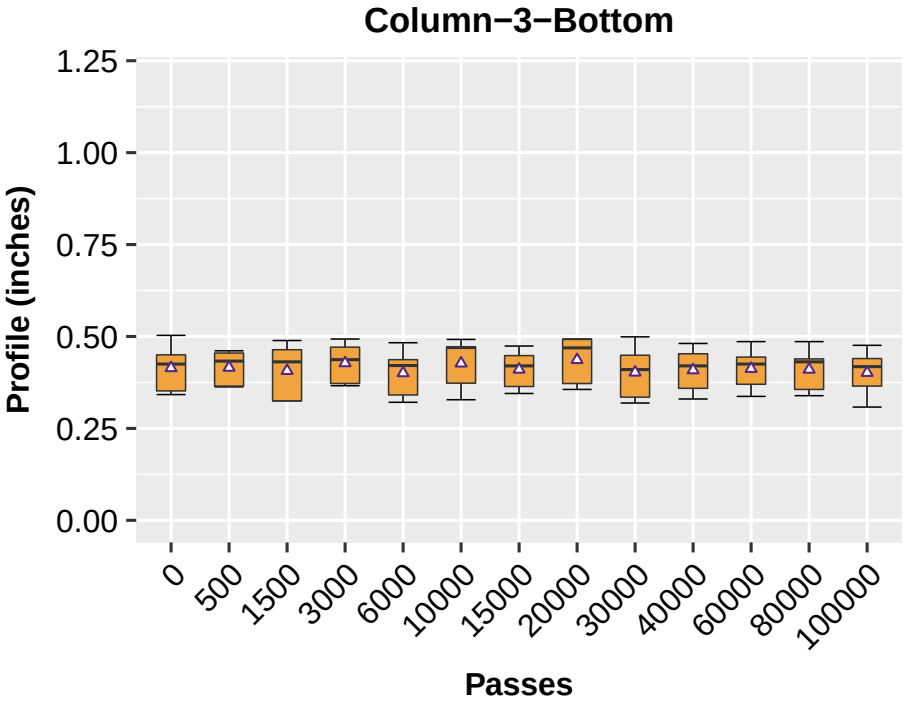

Figure 6.39: *Averaged Longitudinal Profiles (Column-3)*

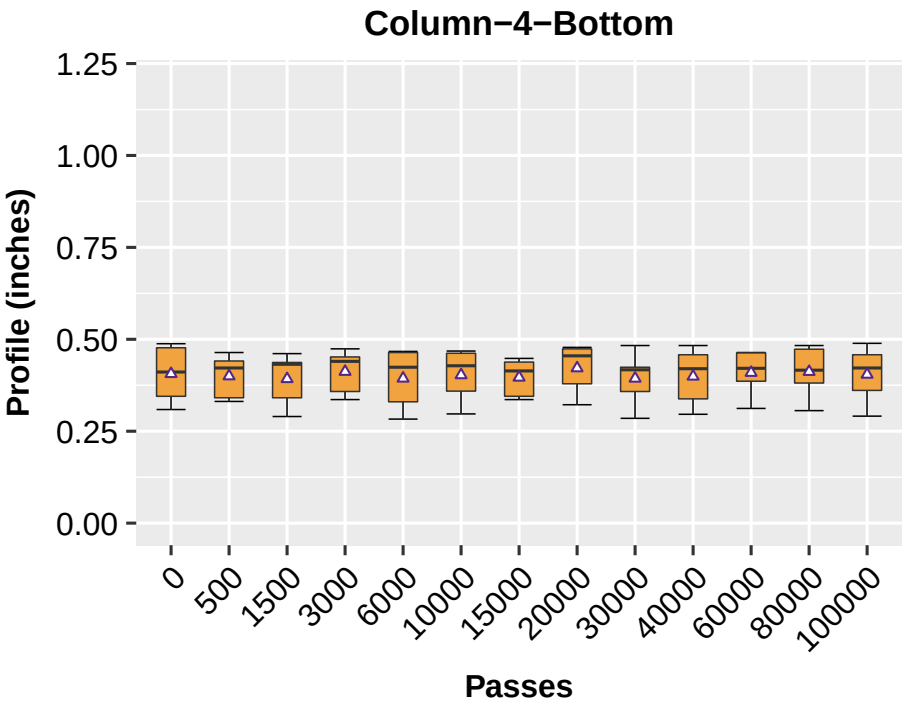

Figure 6.40: *Averaged Longitudinal Profiles (Column-4)*

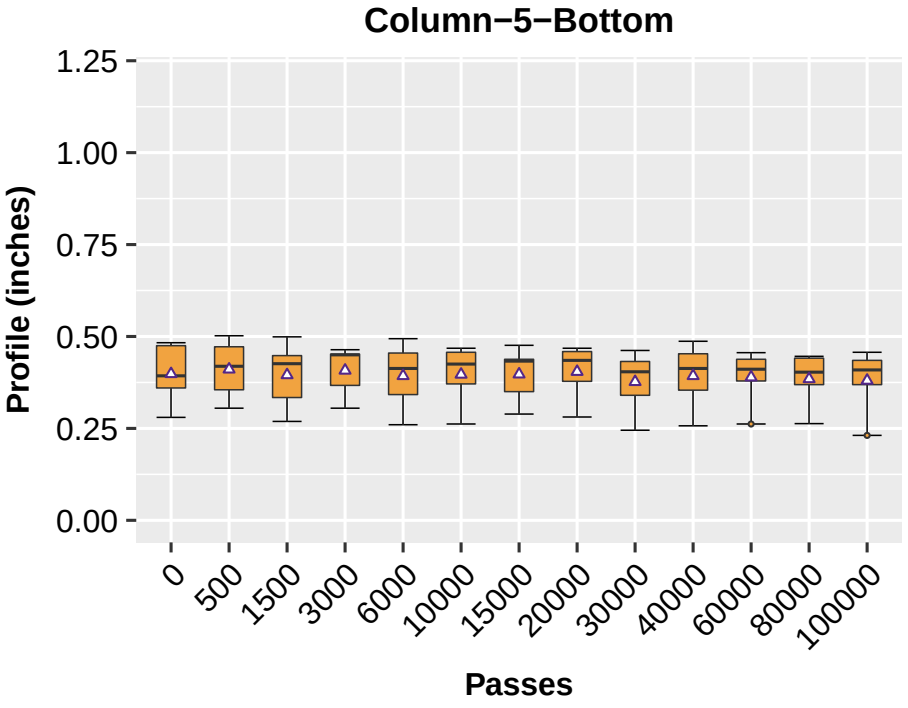

Figure 6.41: *Averaged Longitudinal Profiles (Column-5)*

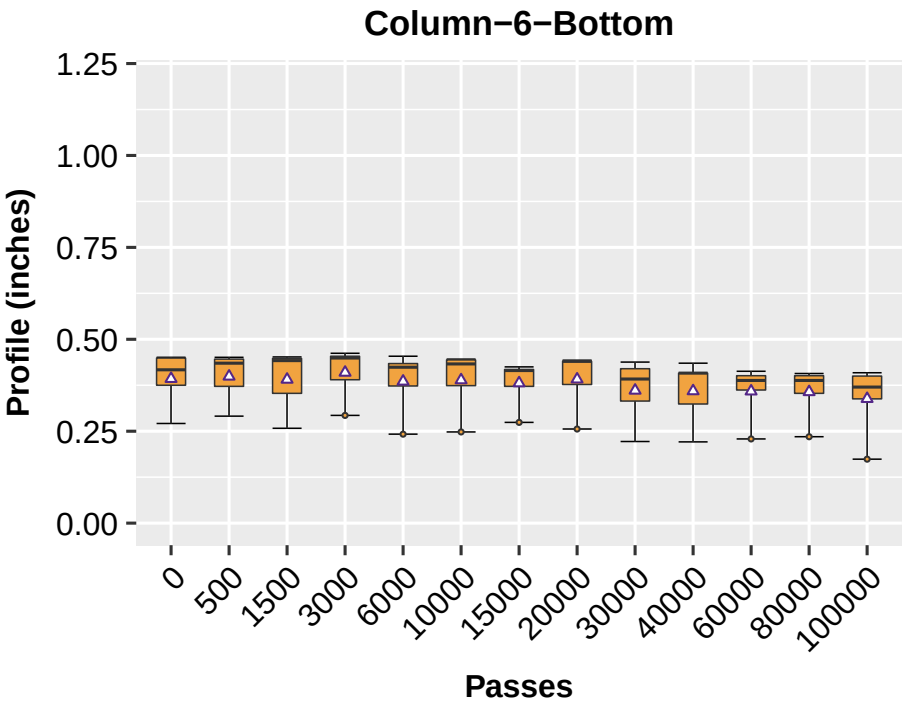

Figure 6.42: *Averaged Longitudinal Profiles (Column-6)*

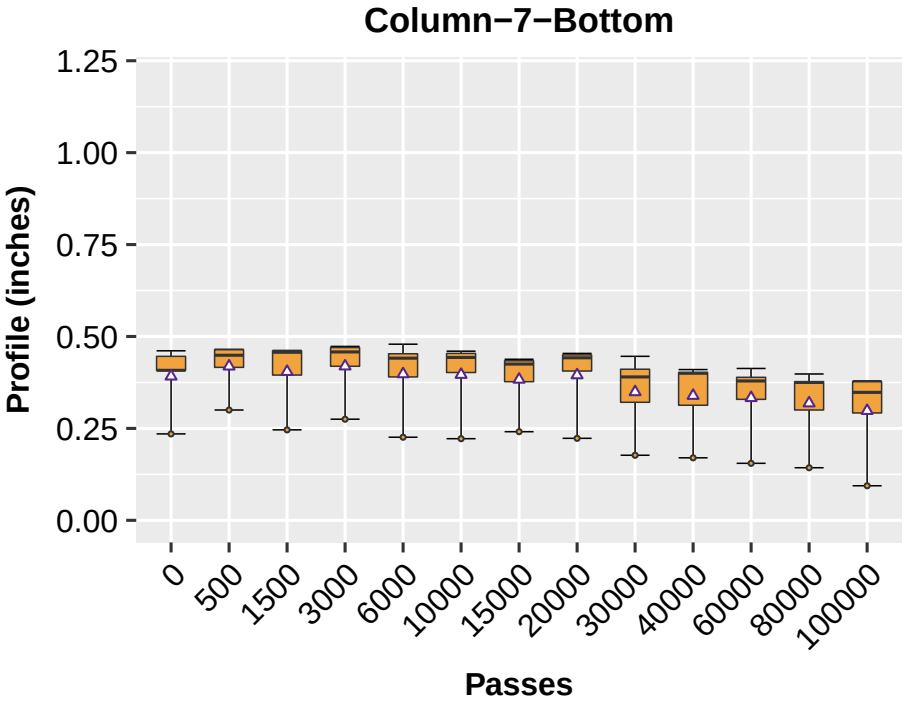

Figure 6.43: *Averaged Longitudinal Profiles (Column-7)*

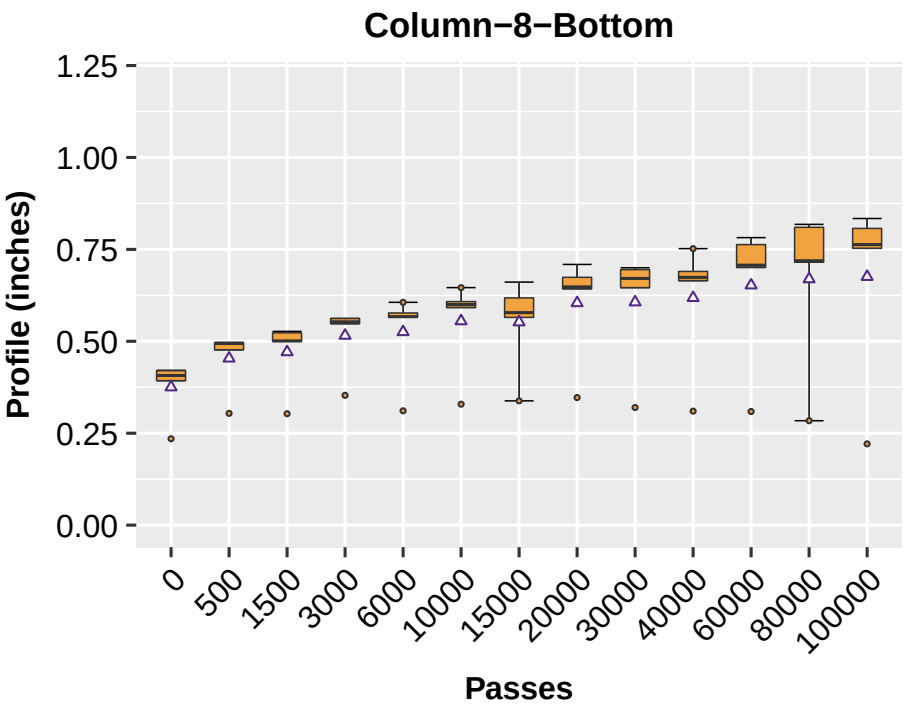

Figure 6.44: *Averaged Longitudinal Profiles (Column-8)*

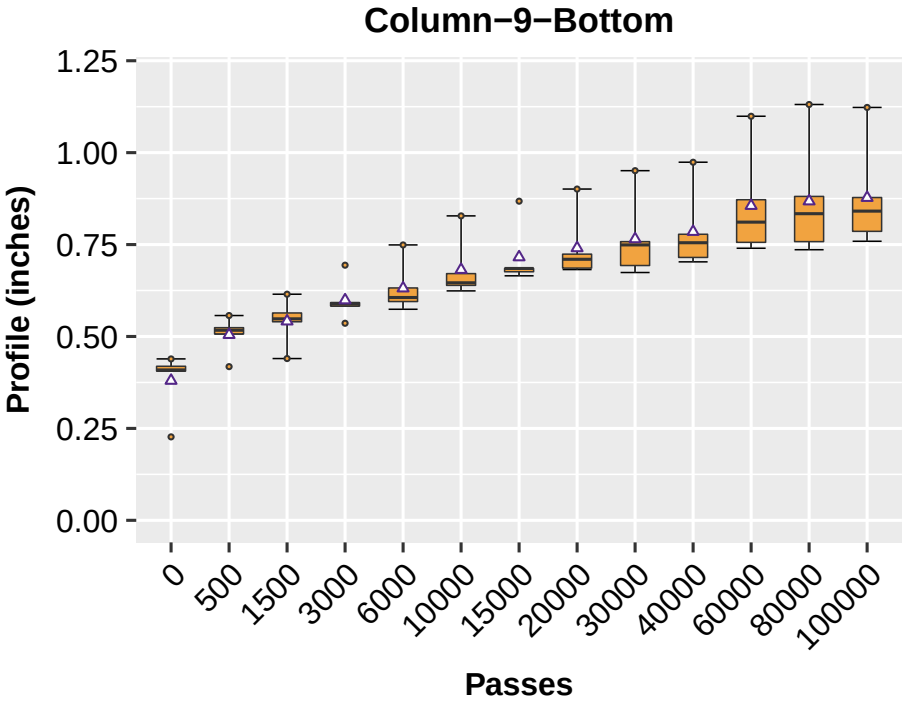

Figure 6.45: *Averaged Longitudinal Profiles (Column-9)*

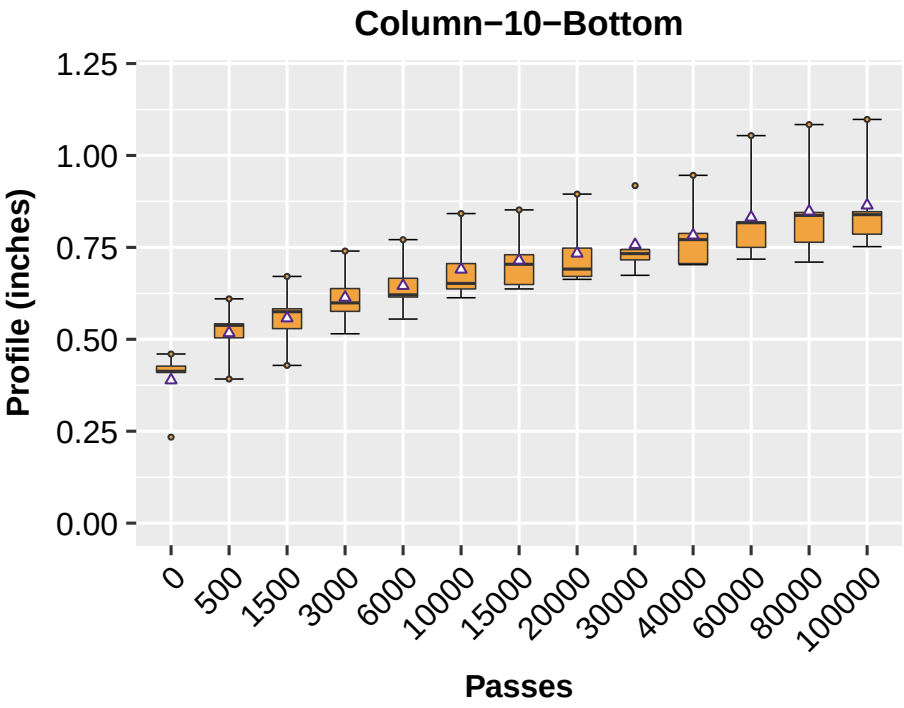

Figure 6.46: *Averaged Longitudinal Profiles (Column-10)*

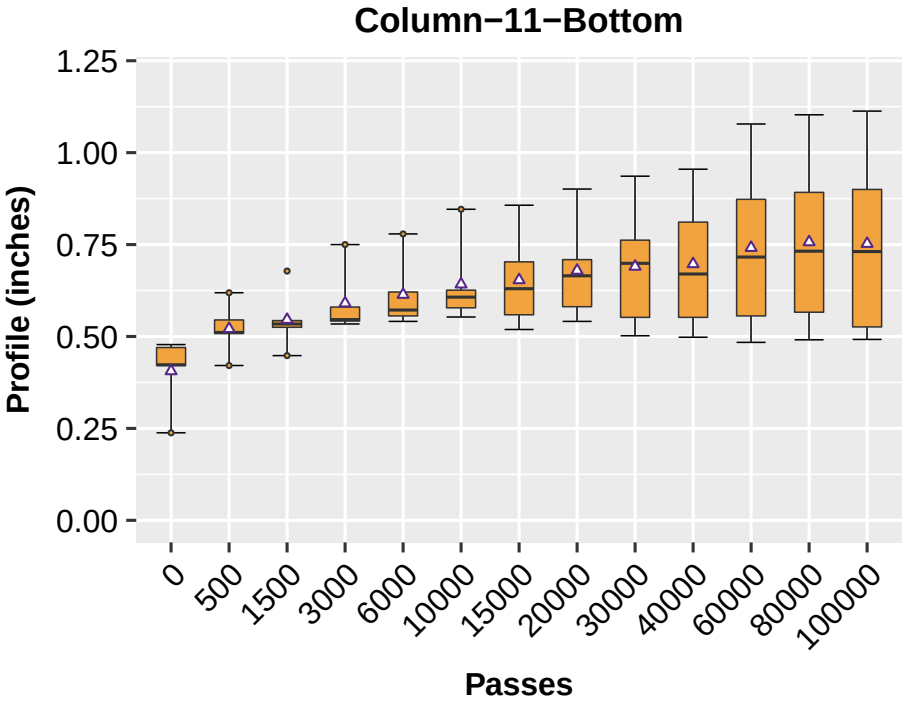

Figure 6.47: *Averaged Longitudinal Profiles (Column-11)*

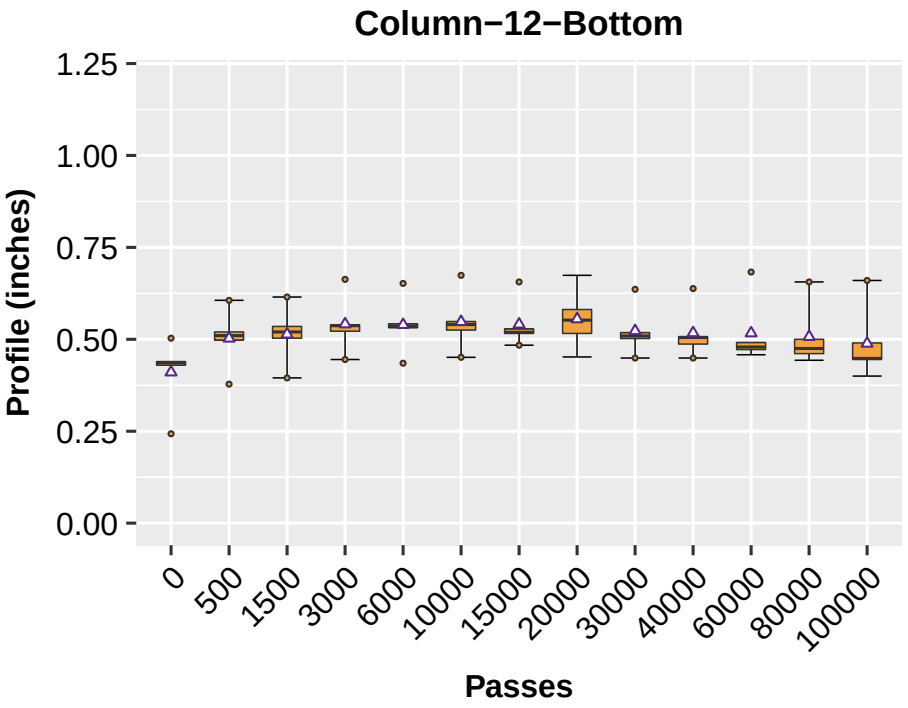

Figure 6.48: *Averaged Longitudinal Profiles (Column-12)*

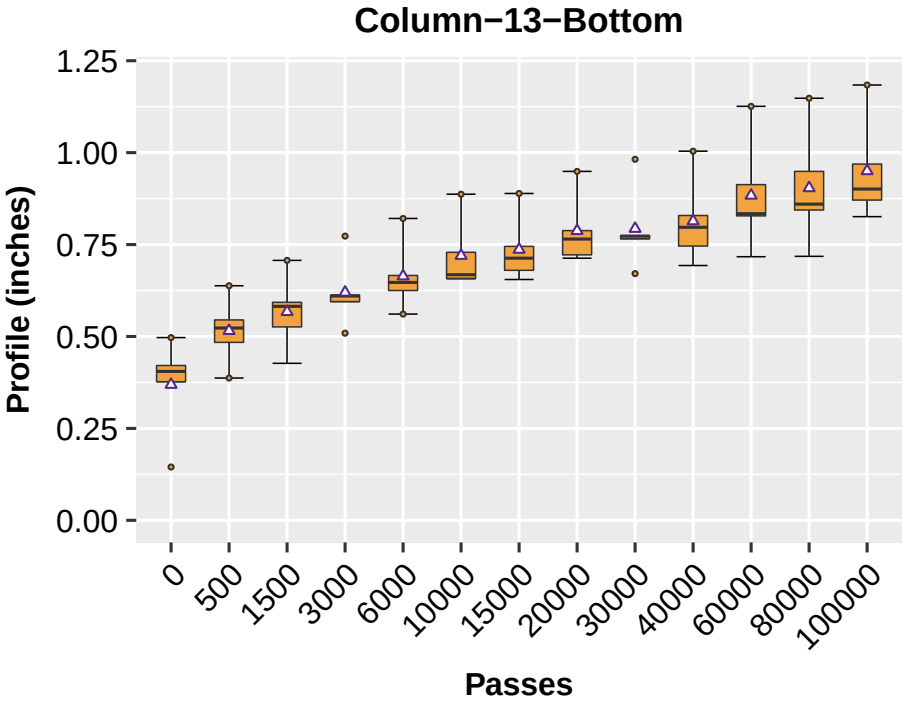

Figure 6.49: *Averaged Longitudinal Profiles (Column-13)*

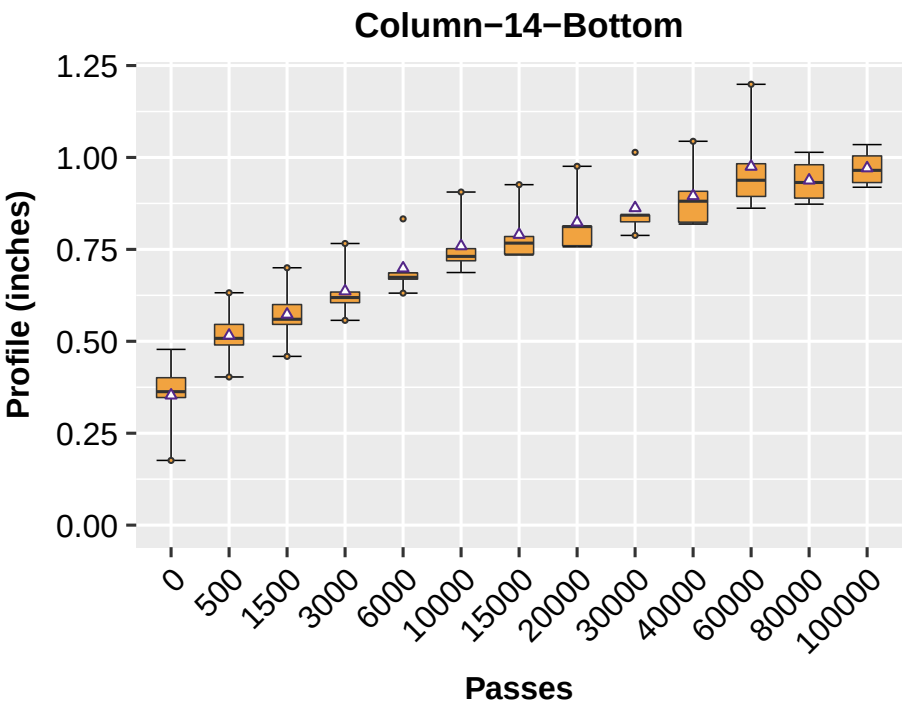

Figure 6.50: *Averaged Longitudinal Profiles (Column-14)*

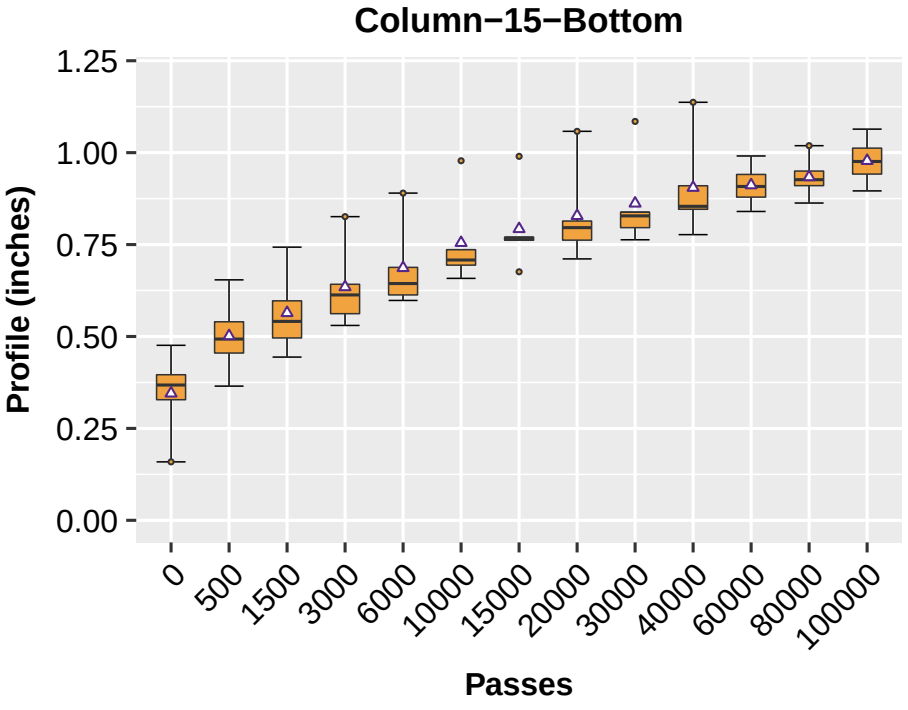

Figure 6.51: *Averaged Longitudinal Profiles (Column-15)*

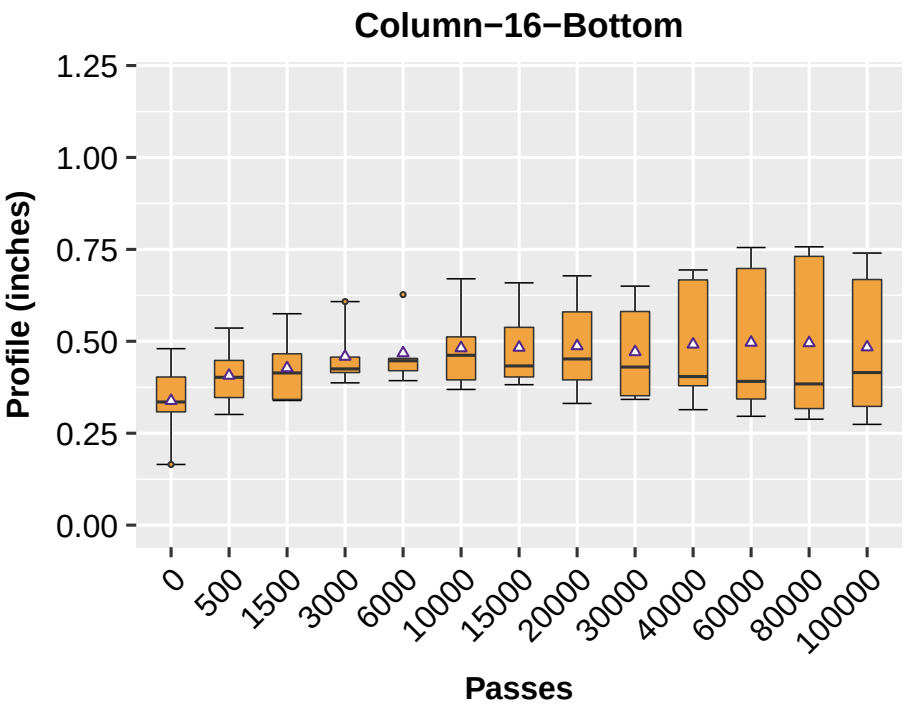

Figure 6.52: *Averaged Longitudinal Profiles (Column-16)*

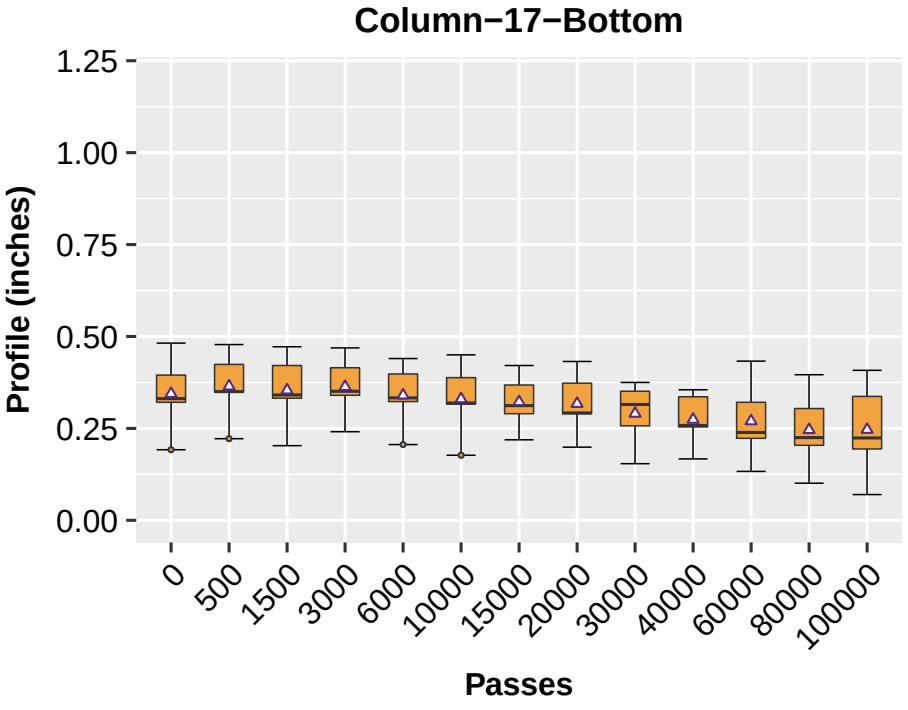

Figure 6.53: *Averaged Longitudinal Profiles (Column-17)*

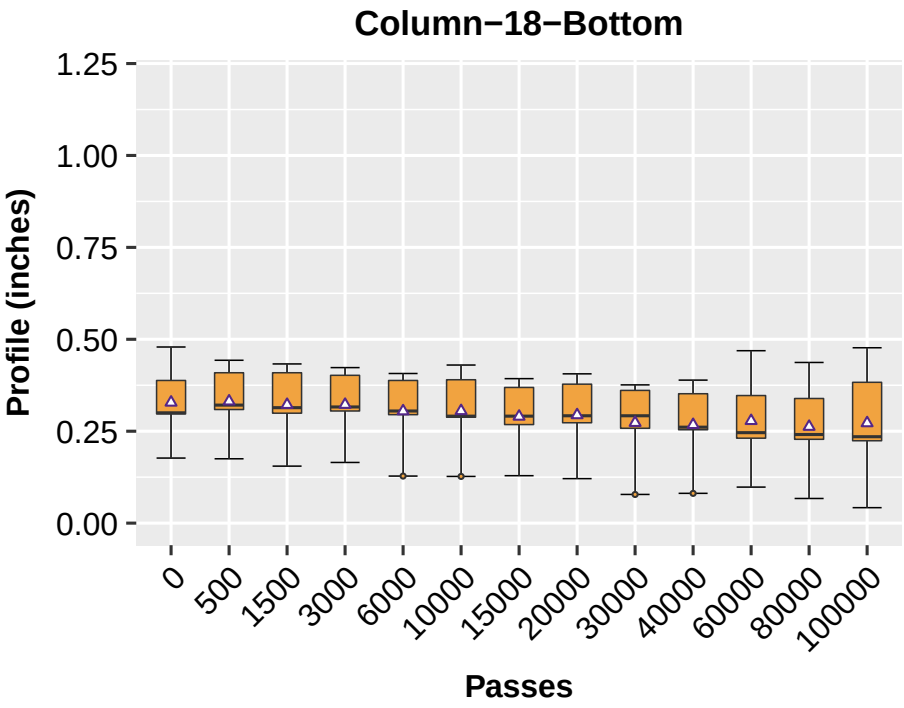

Figure 6.54: *Averaged Longitudinal Profiles (Column-18)*

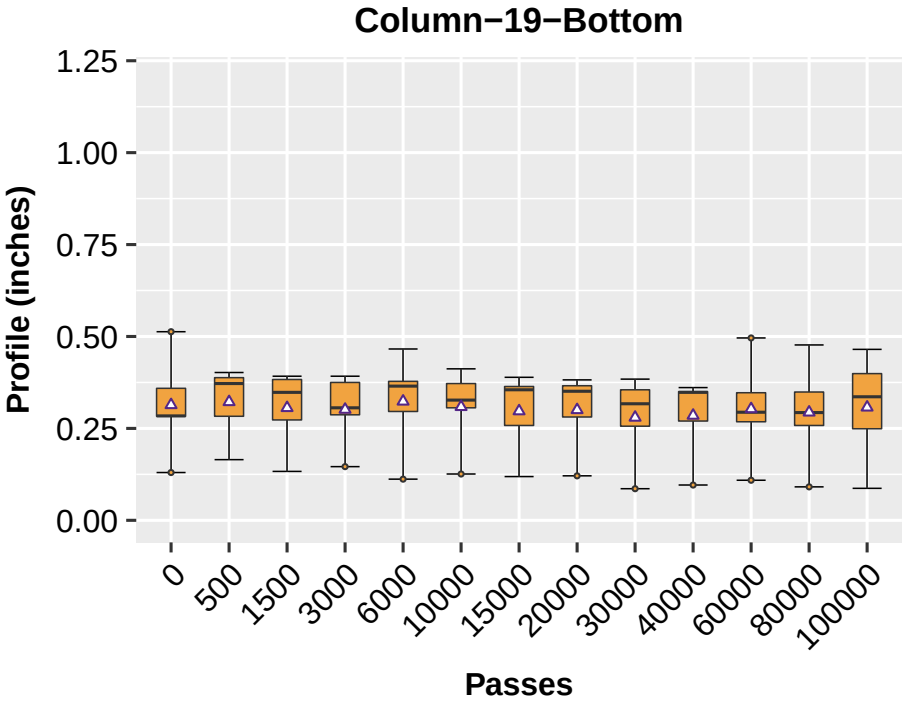

Figure 6.55: *Averaged Longitudinal Profiles (Column-19)*

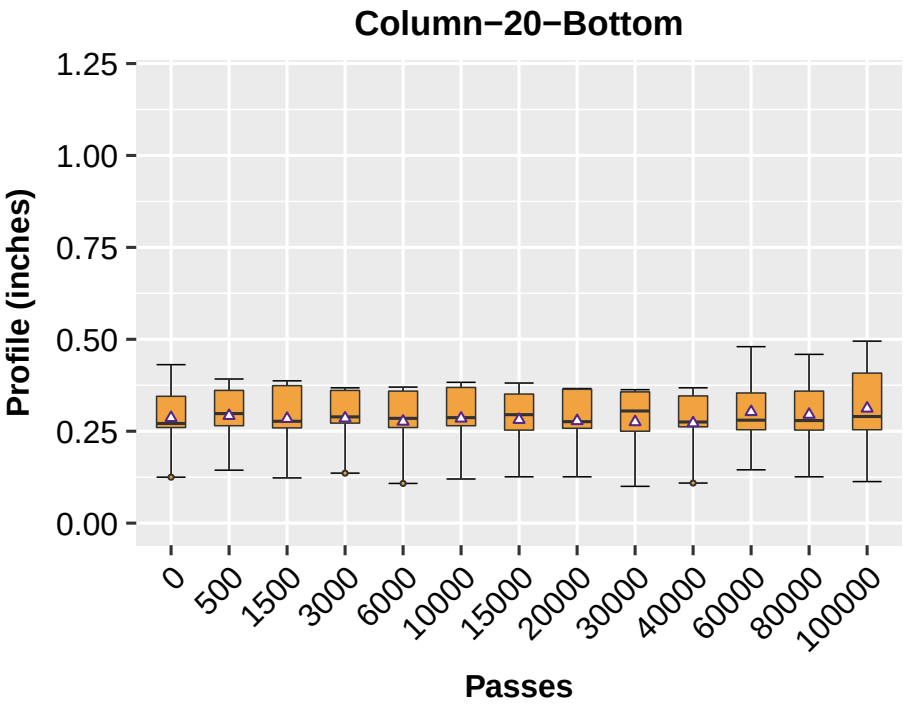

Figure 6.56: *Averaged Longitudinal Profiles (Column-20)*

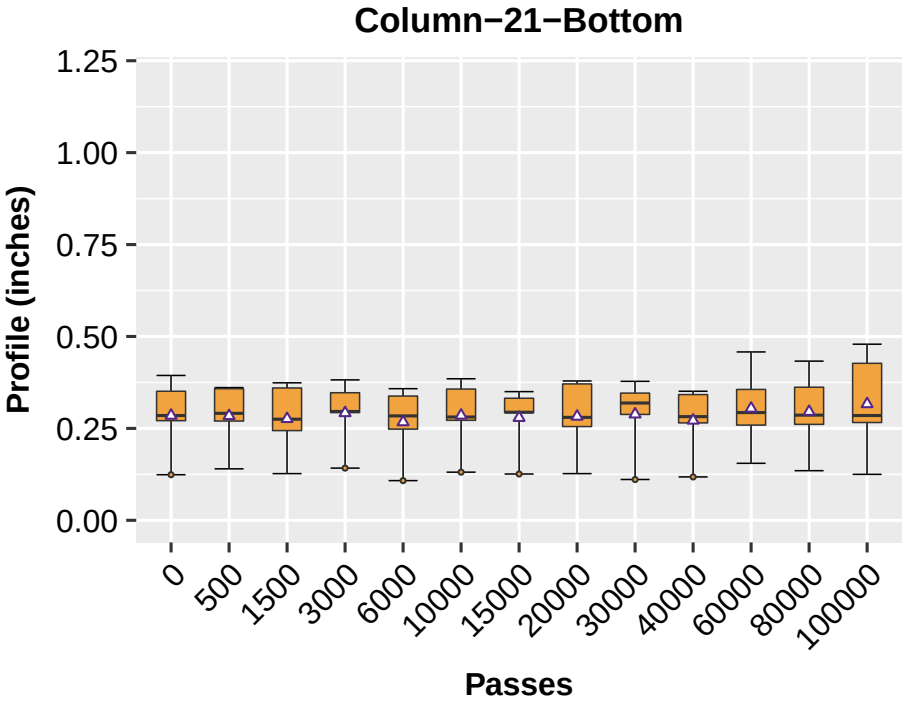

Figure 6.57: *Averaged Longitudinal Profiles (Column-21)*

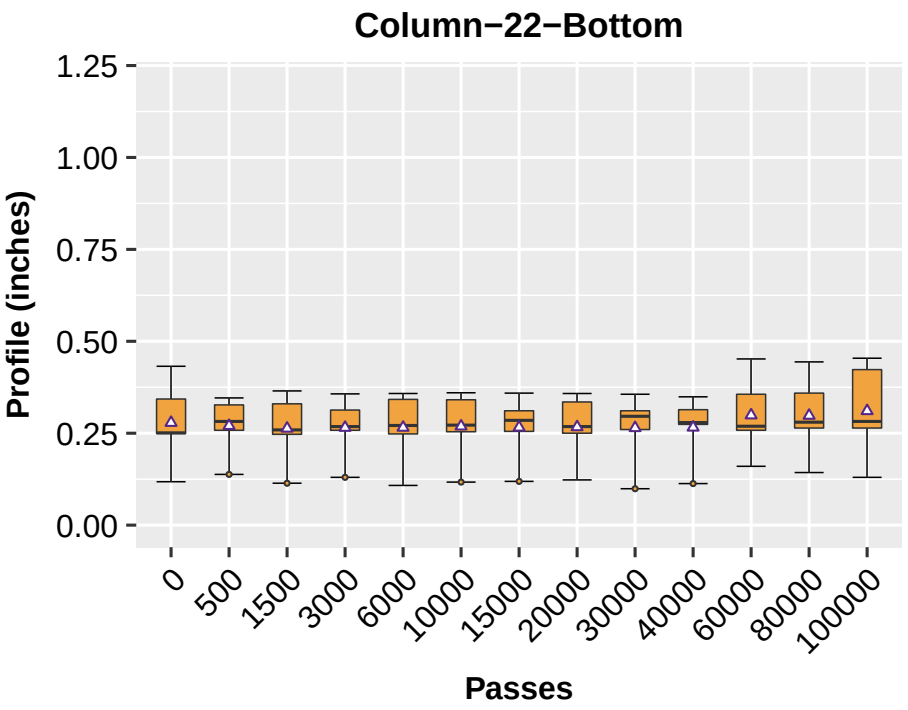

Figure 6.58: *Averaged Longitudinal Profiles (Column-22)*

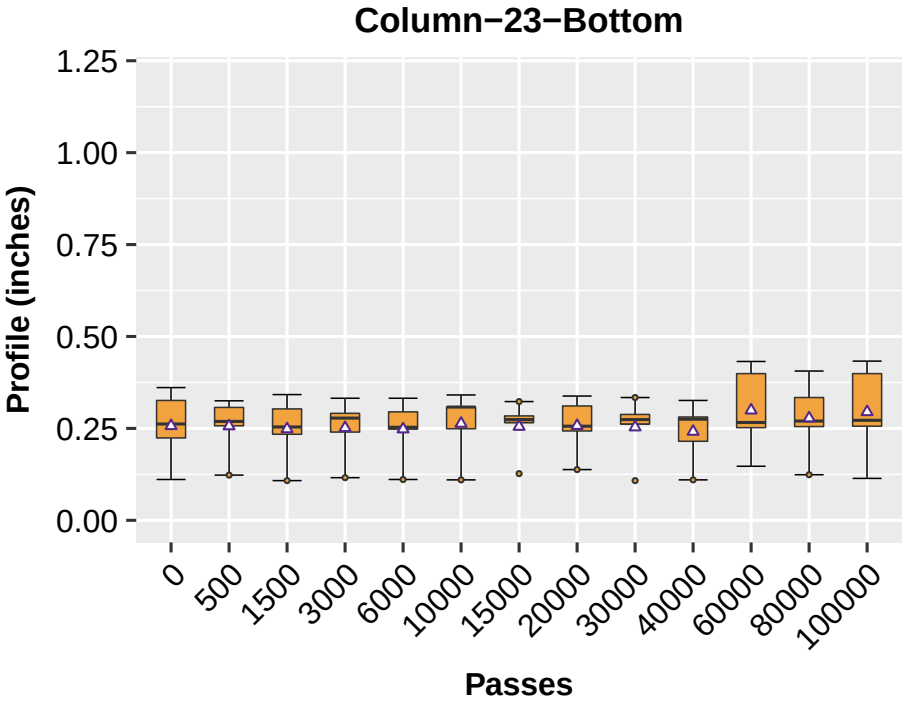

Figure 6.59: *Averaged Longitudinal Profiles (Column-23)*

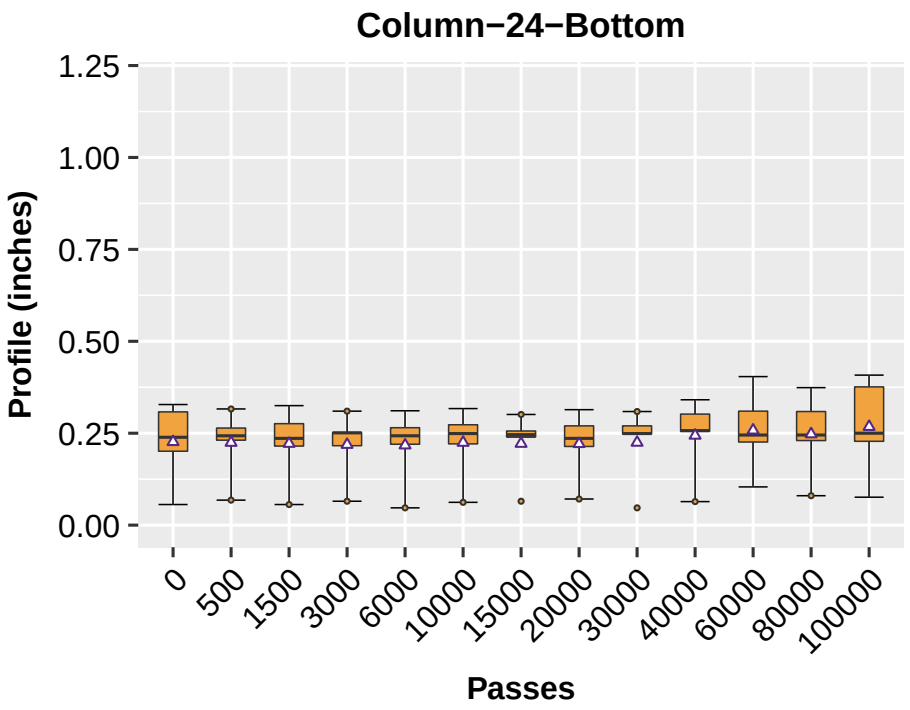

Figure 6.60: *Averaged Longitudinal Profiles (Column-24)*

6.2.3 Control

Deformation Curves

Figures 6.61 through 6.65 present the profiles measured along the horizontal cross-sections, that is, from the north to the south. Due to the similar reason to the Lane M, the largest rutting values were found in the second cross sections for the control lane (see Figure 6.61). After 10,000 wheel load repetitions, the largest rutting value is around 0.5 inch, which occurred around the cross section 2 (Row-2), as plotted in Figure 6.61. In the center of the control lane (Row-3 through Row-5), less rutting was currently observed. The rutting values in the center of the control lane are about 0.3-inch.

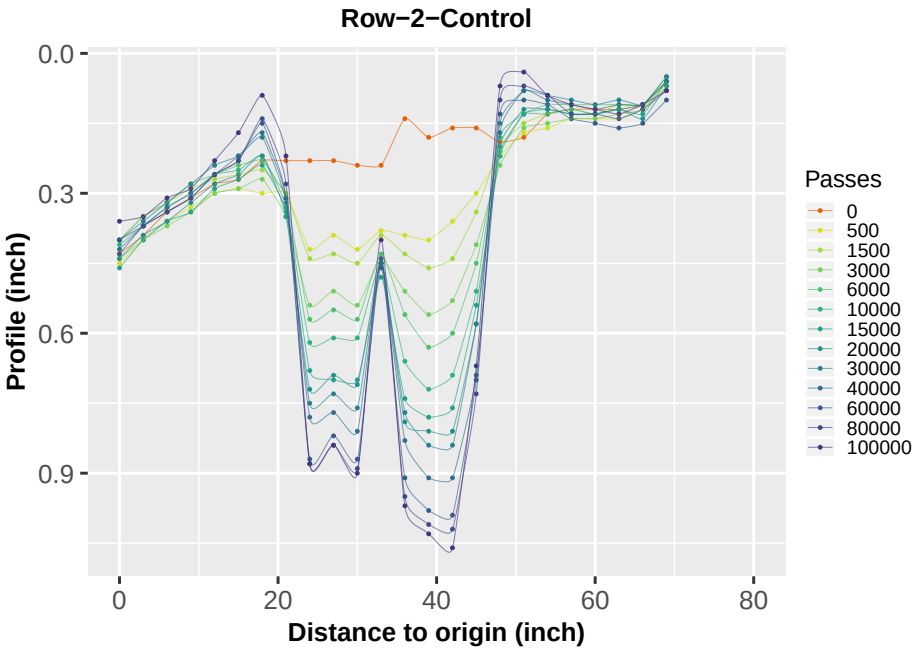

Figure 6.61: *Profile results for the Control Lane (Row-2)*

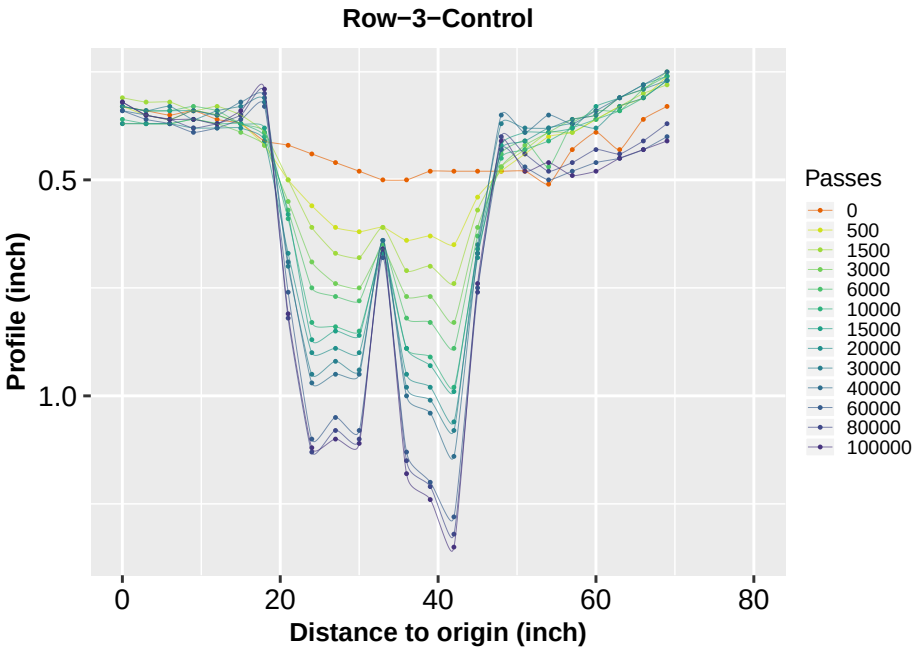

Figure 6.62: *Profile results for the Control Lane (Row-3)*

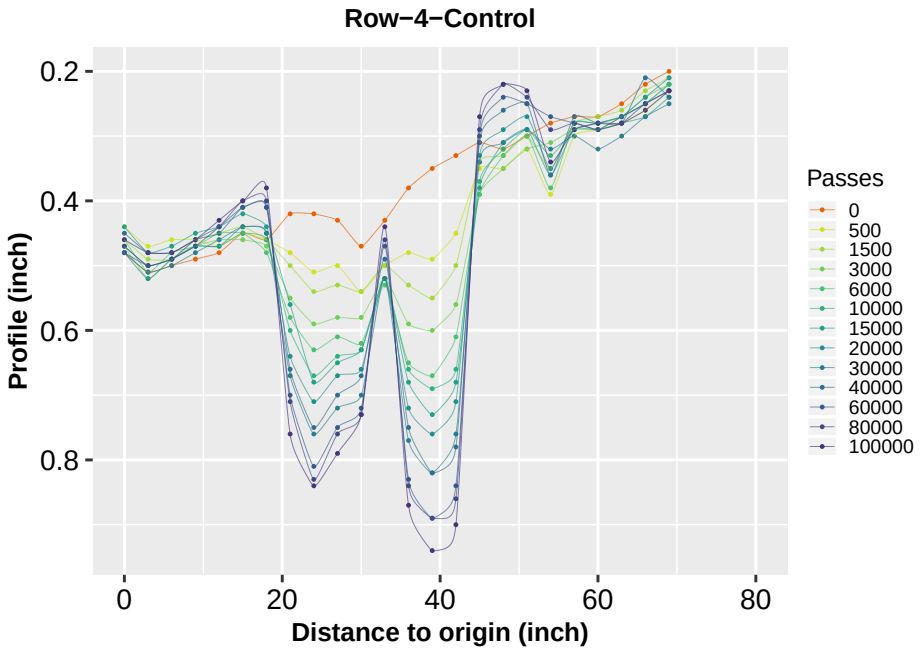

Figure 6.63: *Profile results for the Control Lane (Row-4)*

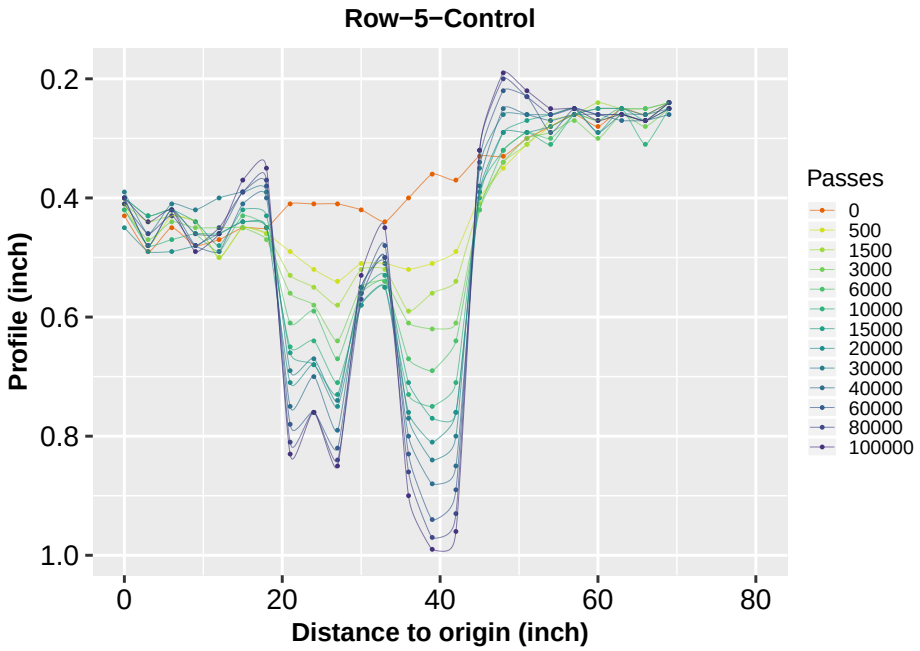

Figure 6.64: *Profile results for the Control Lane (Row-5)*

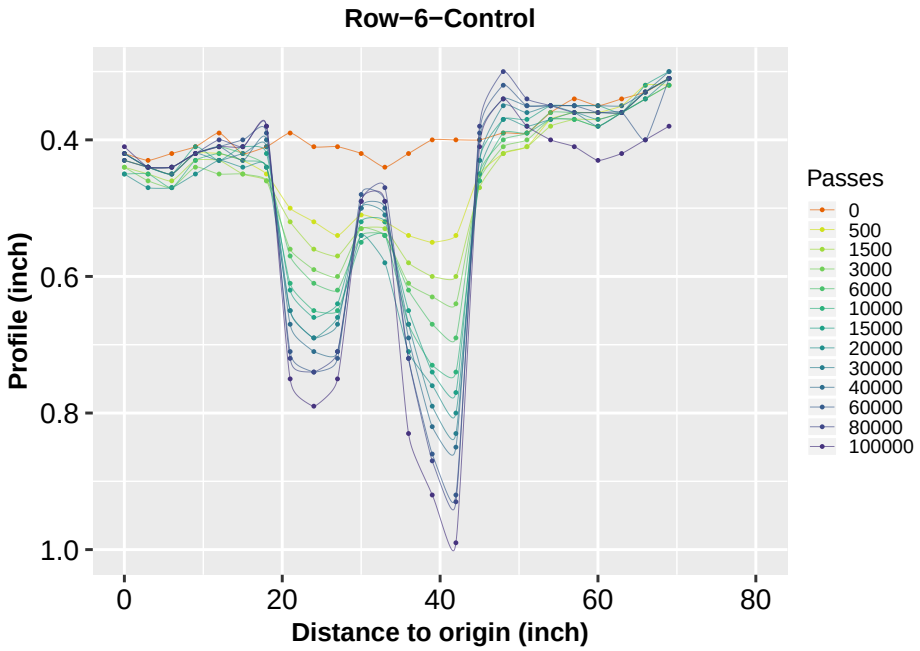

Figure 6.65: *Profile results for the Control Lane (Row-6)*

Aggregated Profiles

The measurements taken along the longitudinal cross sections were also included for the control lane, as shown in Figures 6.66 through 6.89. As it is still the early stage of testing on this lane, only a small amount of deformation was found. The largest averaged rutting along the longitudinal direction is seen in the Column-14, which is slightly greater than 0.3-inch. Compared to the Lane-M at 10,000 axle load repetitions, the deformation is quite similar. Therefore, at this stage, no definite conclusion can be made on the benefits of using this type of geogrid (Fornit 25 from HUESKER).

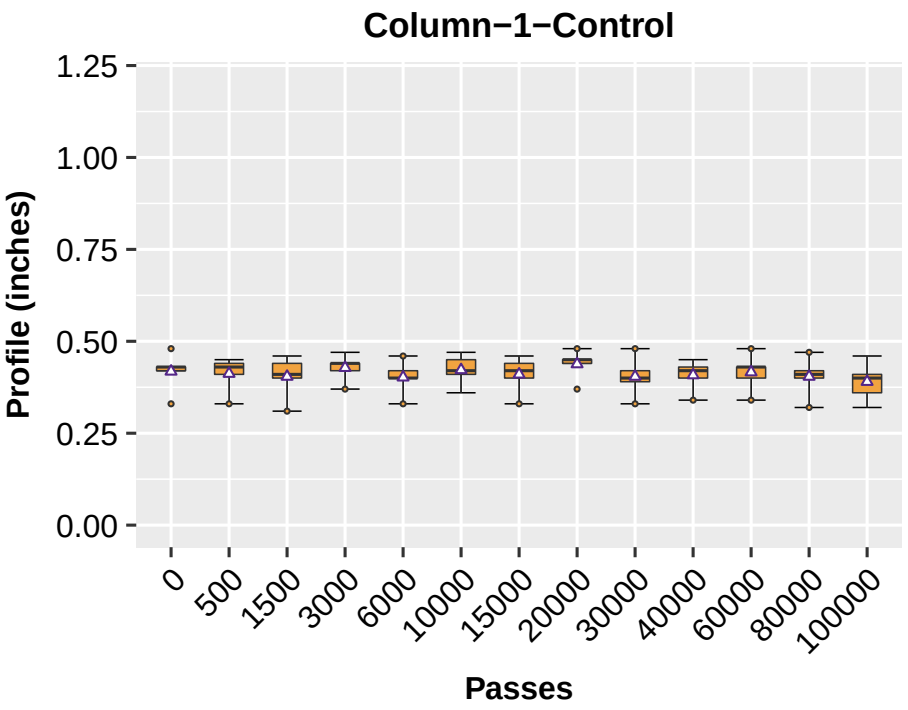

Figure 6.66: *Longitudinal Profiles for Control Lane (Column-1)*

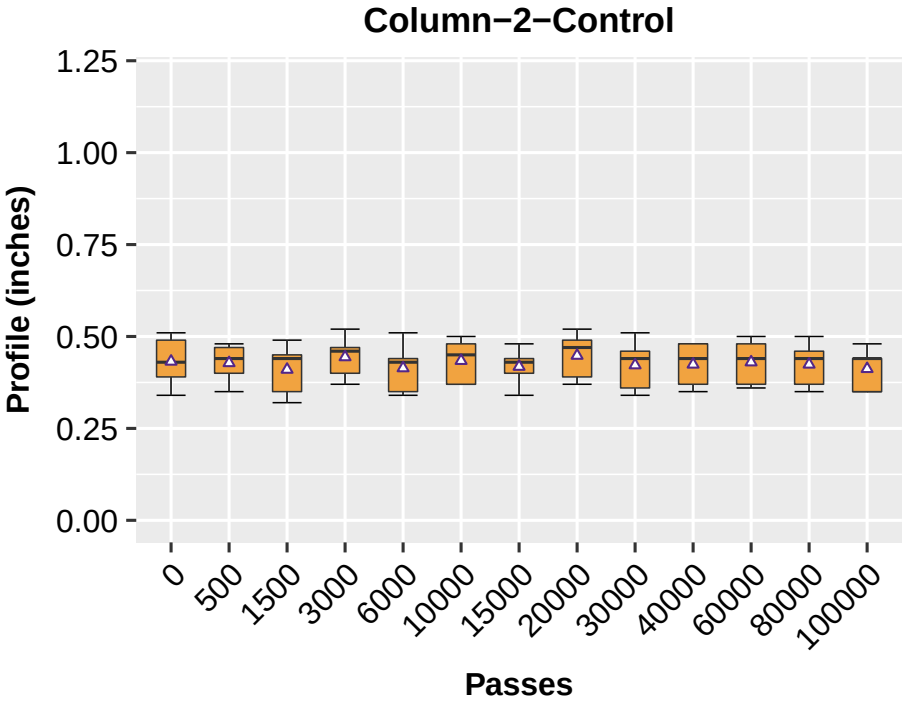

Figure 6.67: *Longitudinal Profiles for Control Lane (Column-2)*

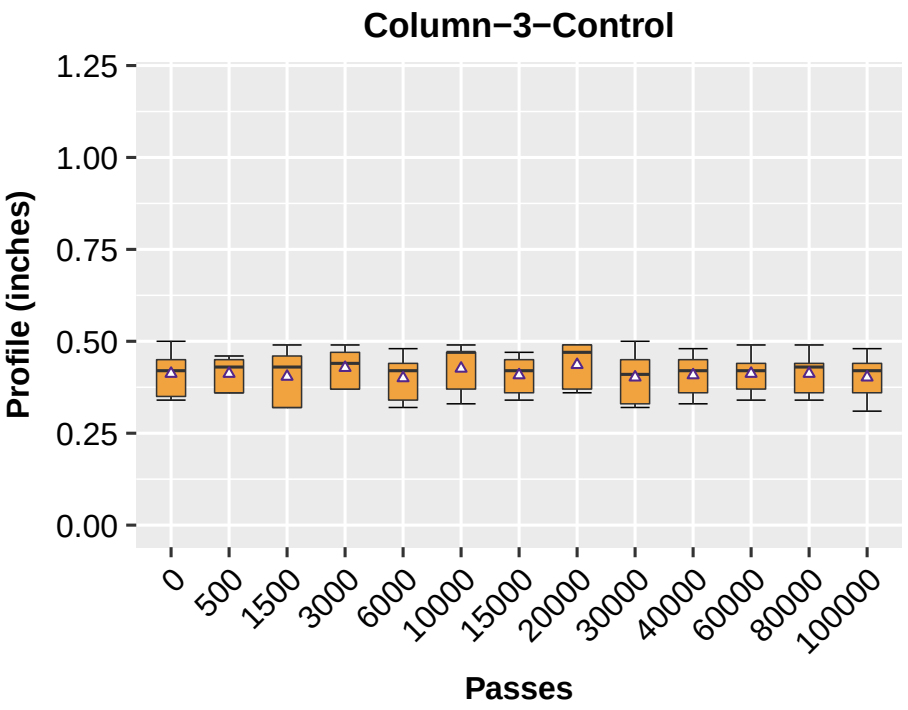

Figure 6.68: *Longitudinal Profiles for Control Lane (Column-3)*

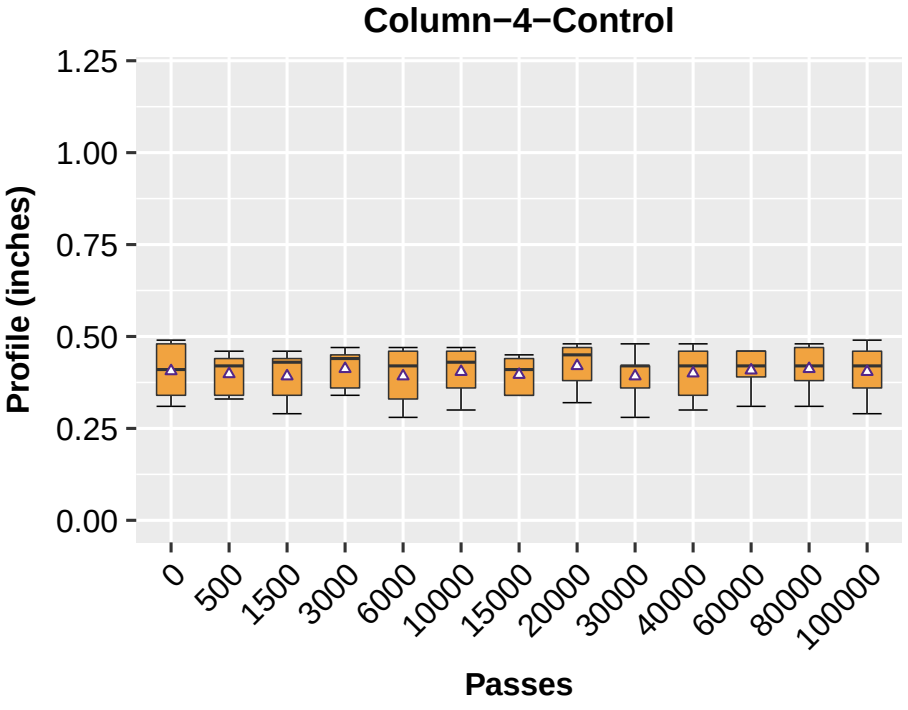

Figure 6.69: *Longitudinal Profiles for Control Lane (Column-4)*

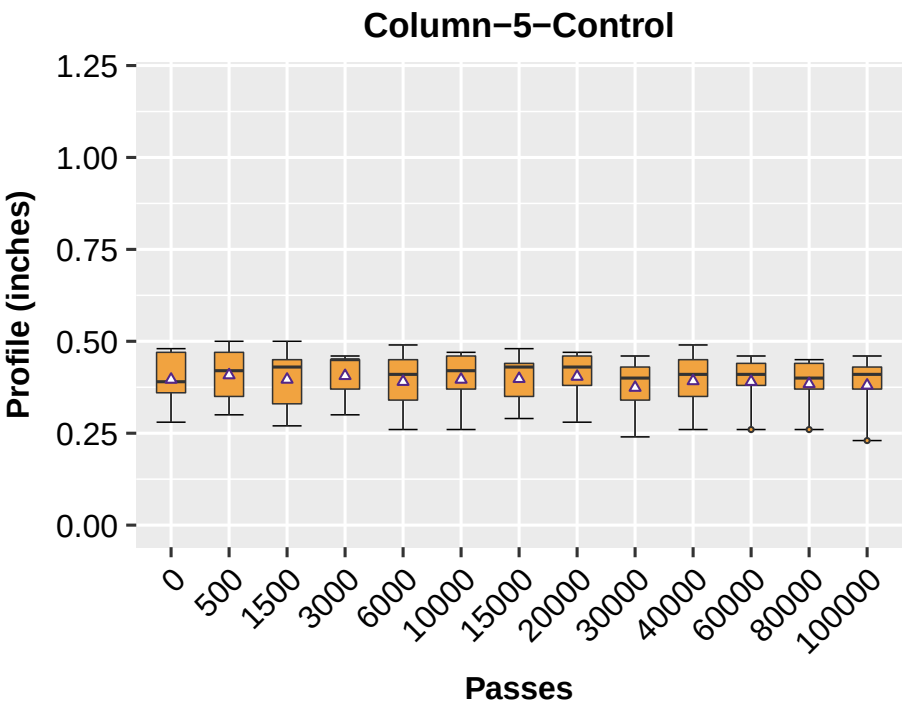

Figure 6.70: *Longitudinal Profiles for Control Lane (Column-5)*

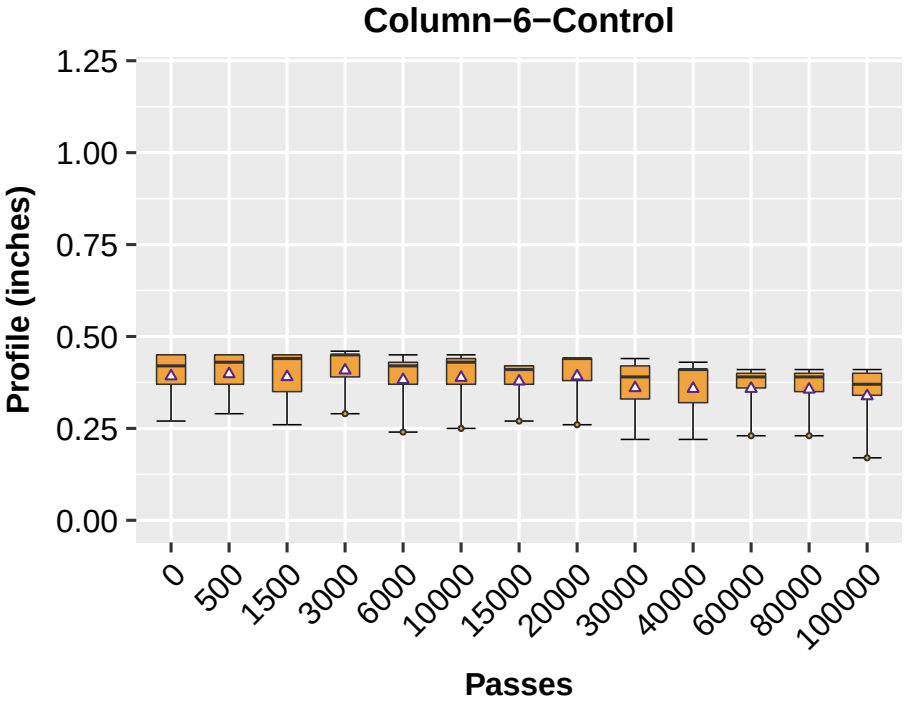

Figure 6.71: *Longitudinal Profiles for Control Lane (Column-6)*

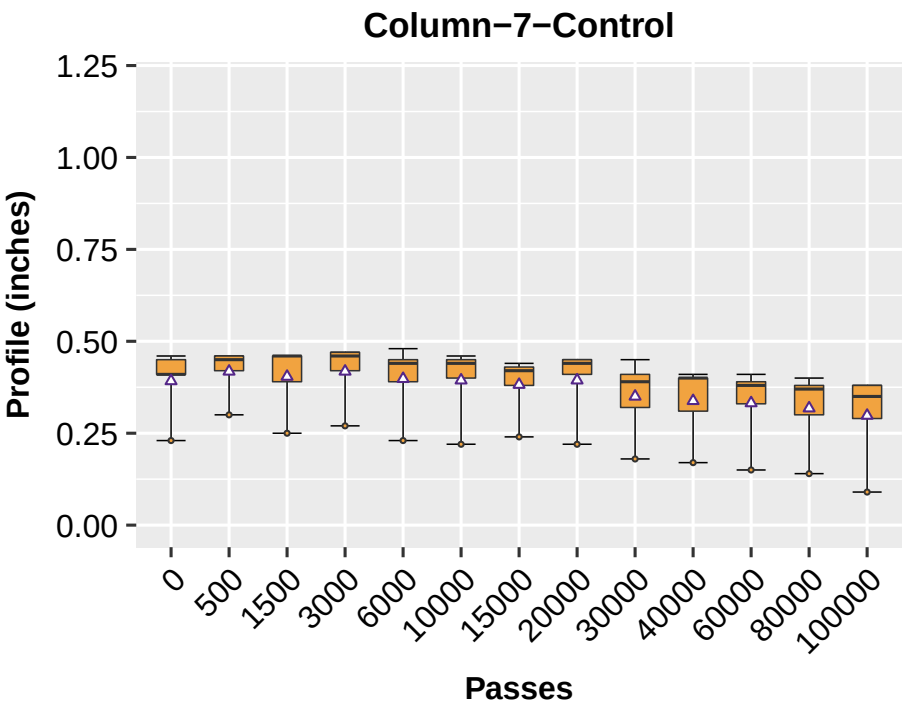

Figure 6.72: *Longitudinal Profiles for Control Lane (Column-7)*

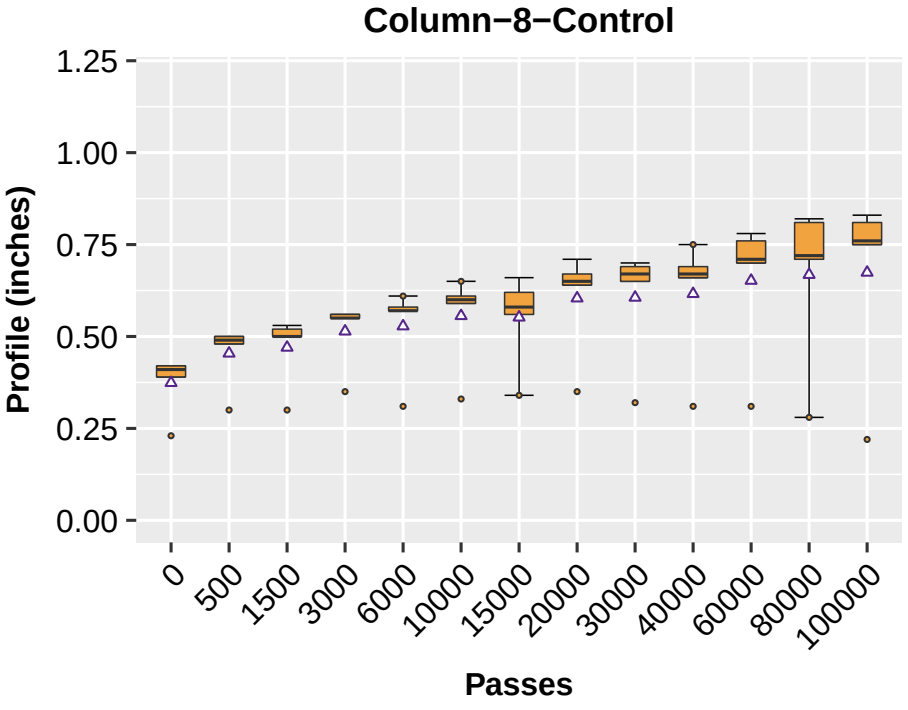

Figure 6.73: *Longitudinal Profiles for Control Lane (Column-8)*

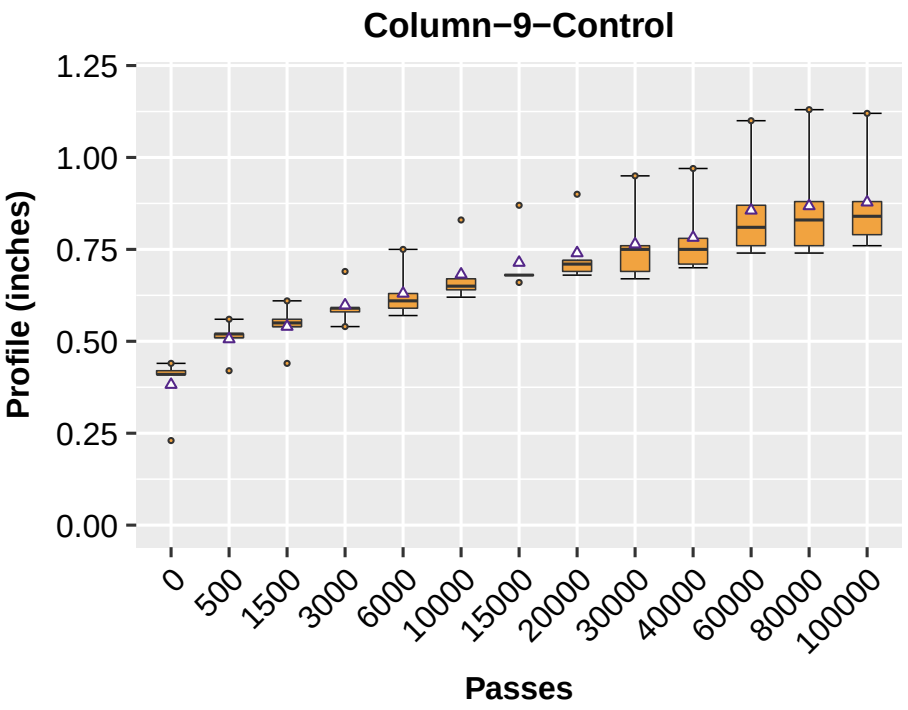

Figure 6.74: *Longitudinal Profiles for Control Lane (Column-9)*

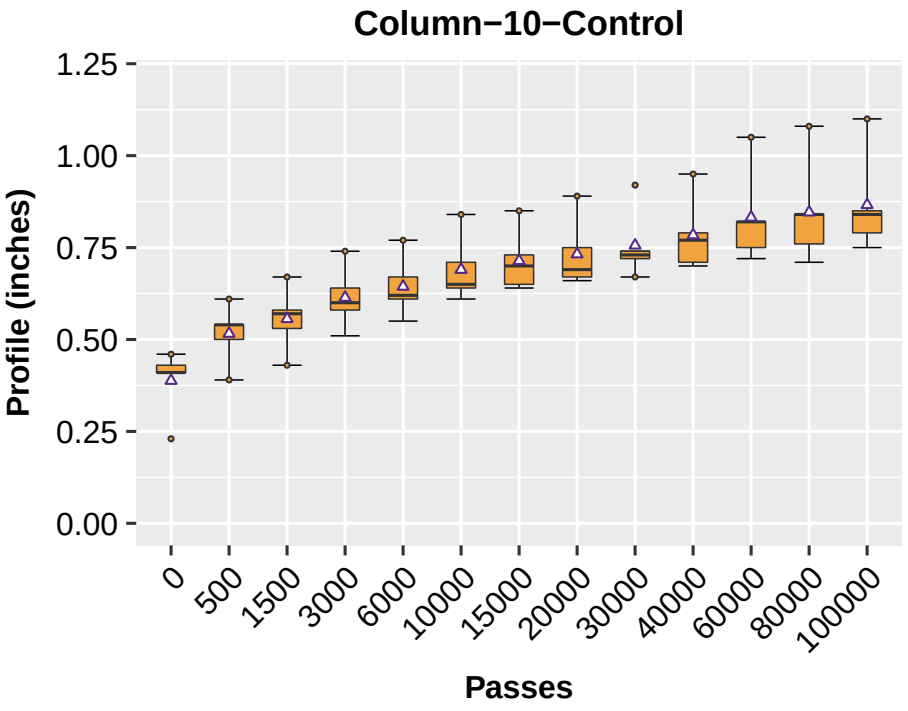

Figure 6.75: *Longitudinal Profiles for Control Lane (Column-10)*

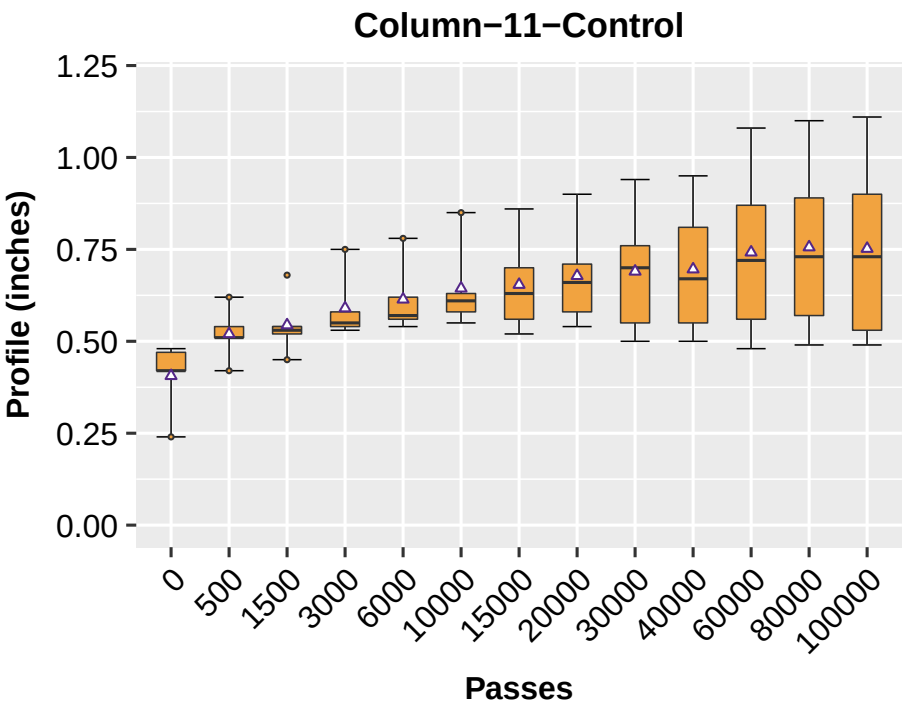

Figure 6.76: *Longitudinal Profiles for Control Lane (Column-11)*

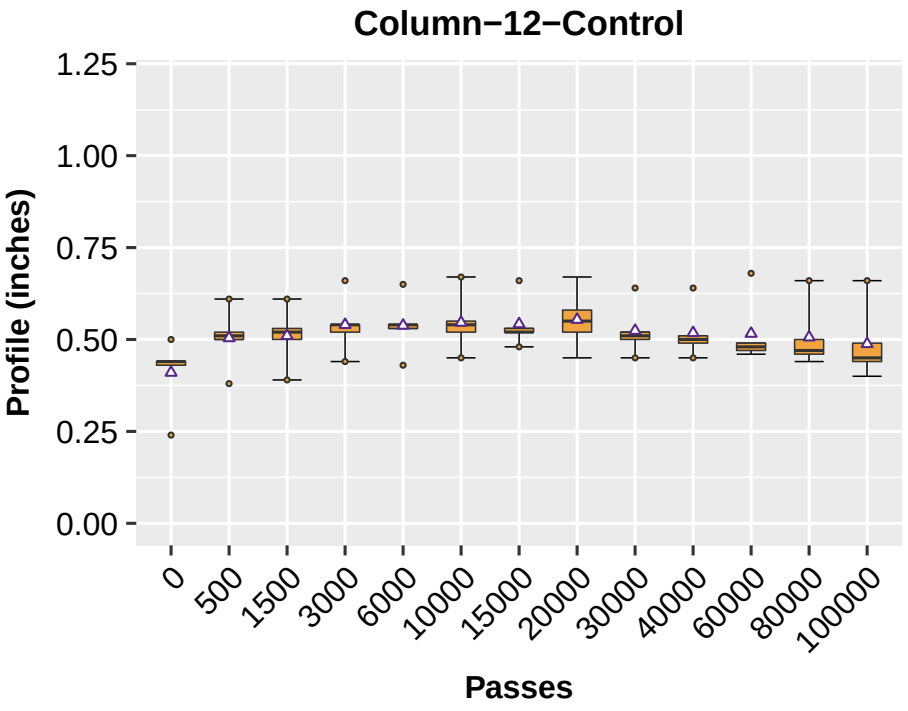

Figure 6.77: *Longitudinal Profiles for Control Lane (Column-12)*

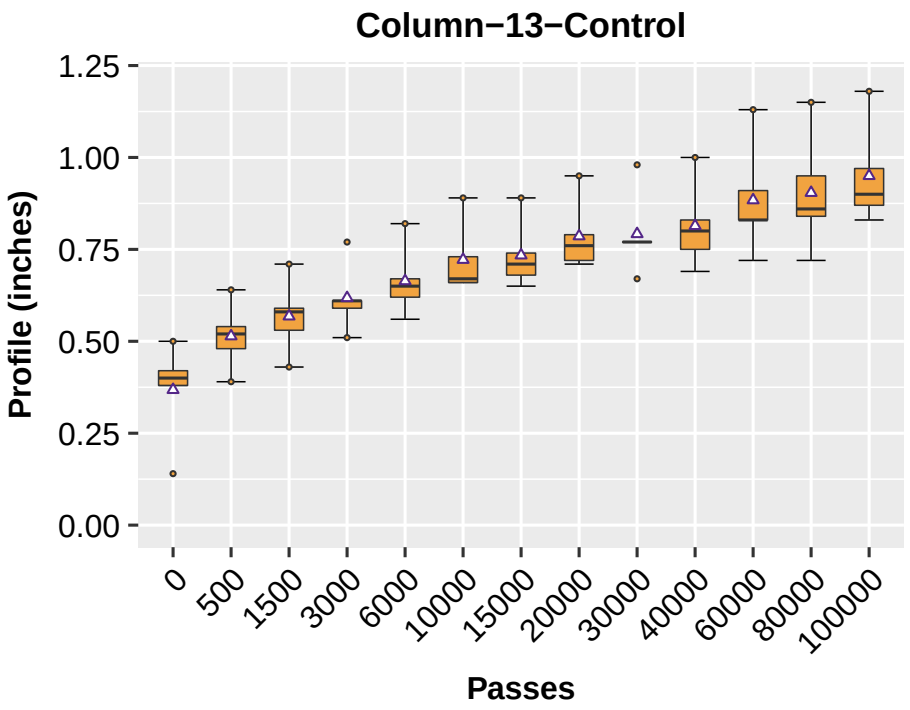

Figure 6.78: *Longitudinal Profiles for Control Lane (Column-13)*

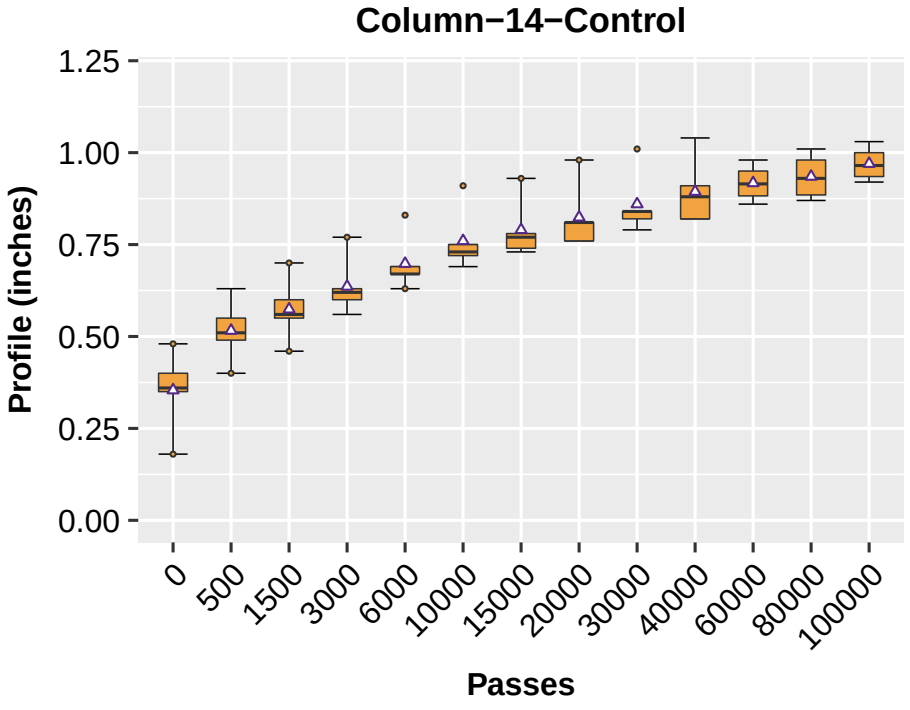

Figure 6.79: *Longitudinal Profiles for Control Lane (Column-14)*

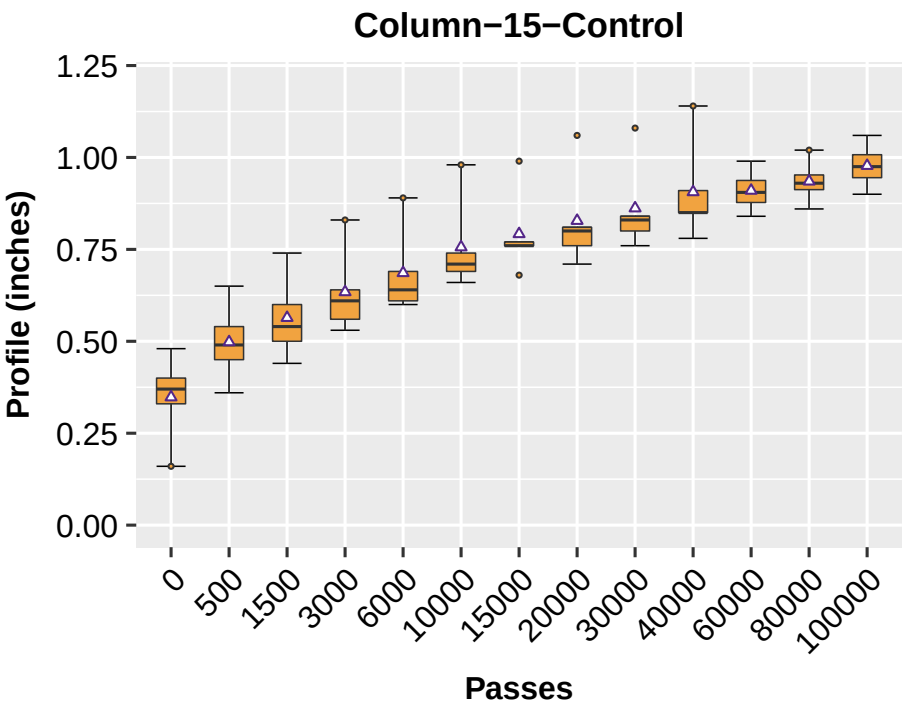

Figure 6.80: *Longitudinal Profiles for Control Lane (Column-15)*

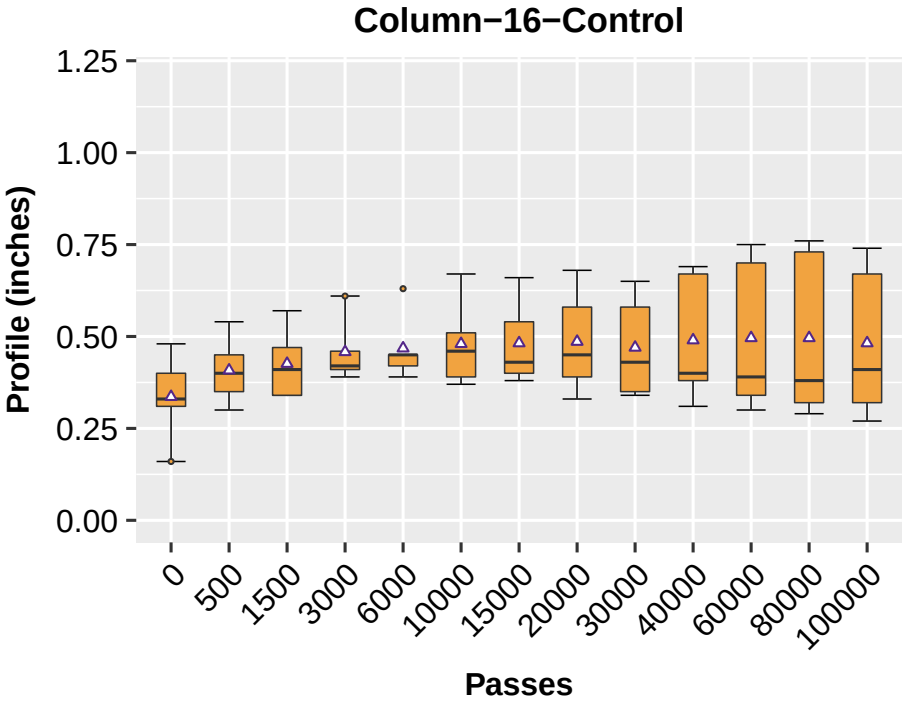

Figure 6.81: *Longitudinal Profiles for Control Lane (Column-16)*

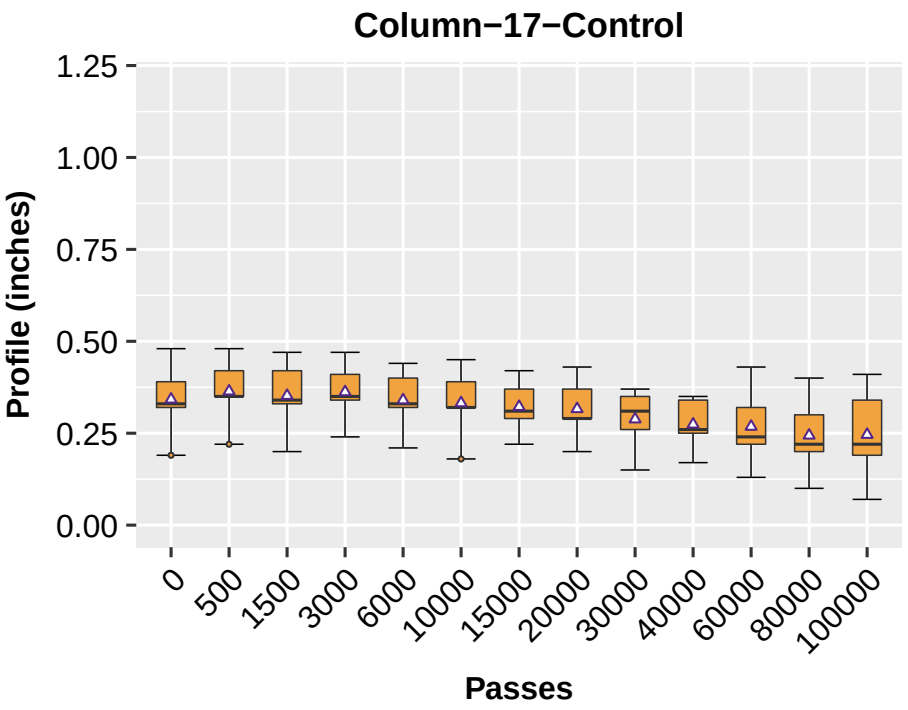

Figure 6.82: *Longitudinal Profiles for Control Lane (Column-17)*

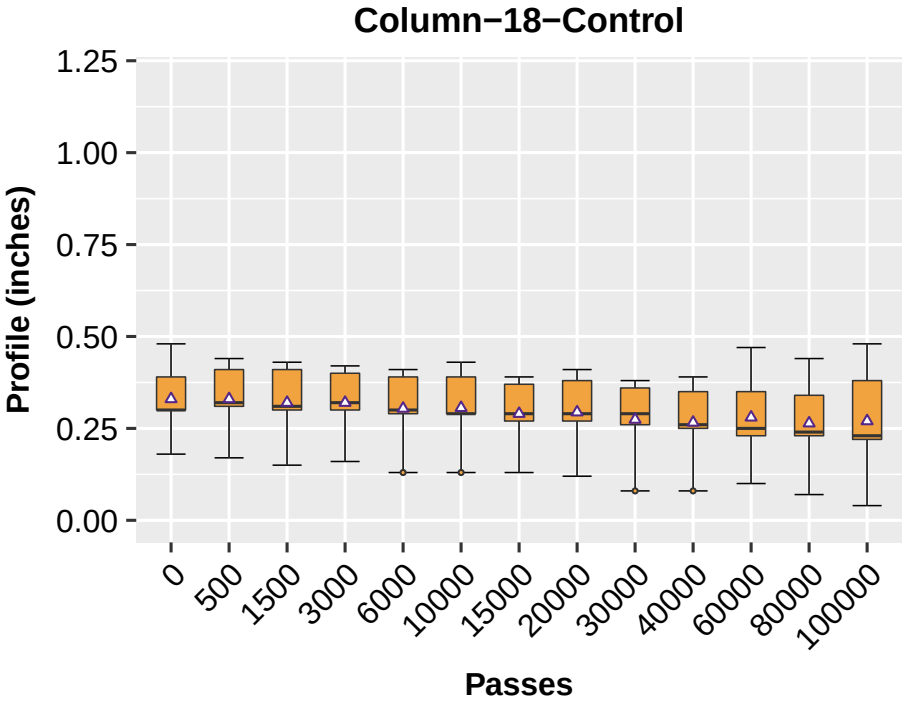

Figure 6.83: *Longitudinal Profiles for Control Lane (Column-18)*

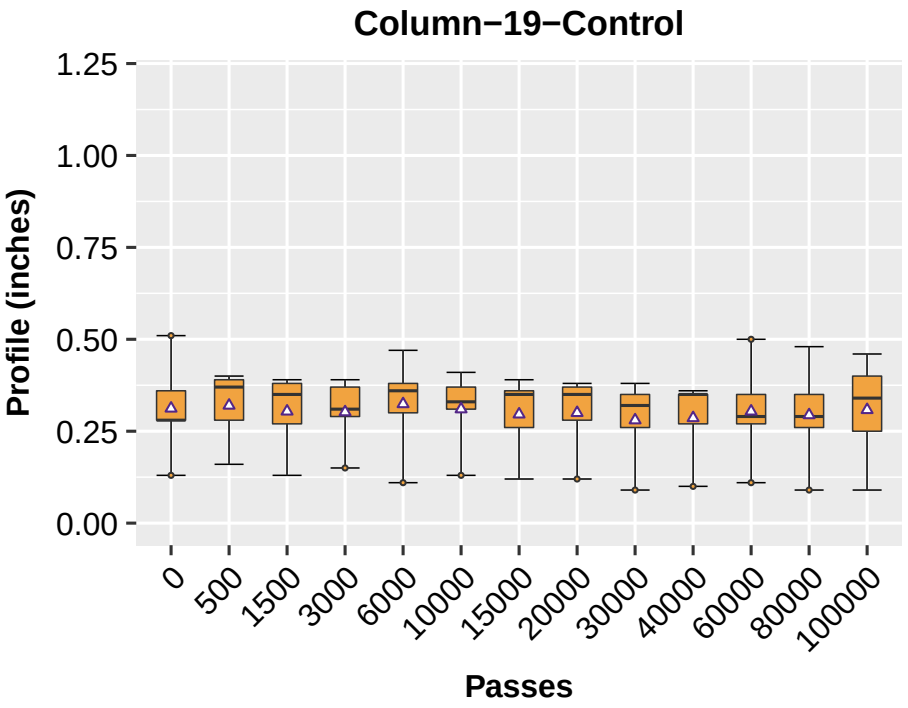

Figure 6.84: *Longitudinal Profiles for Control Lane (Column-19)*

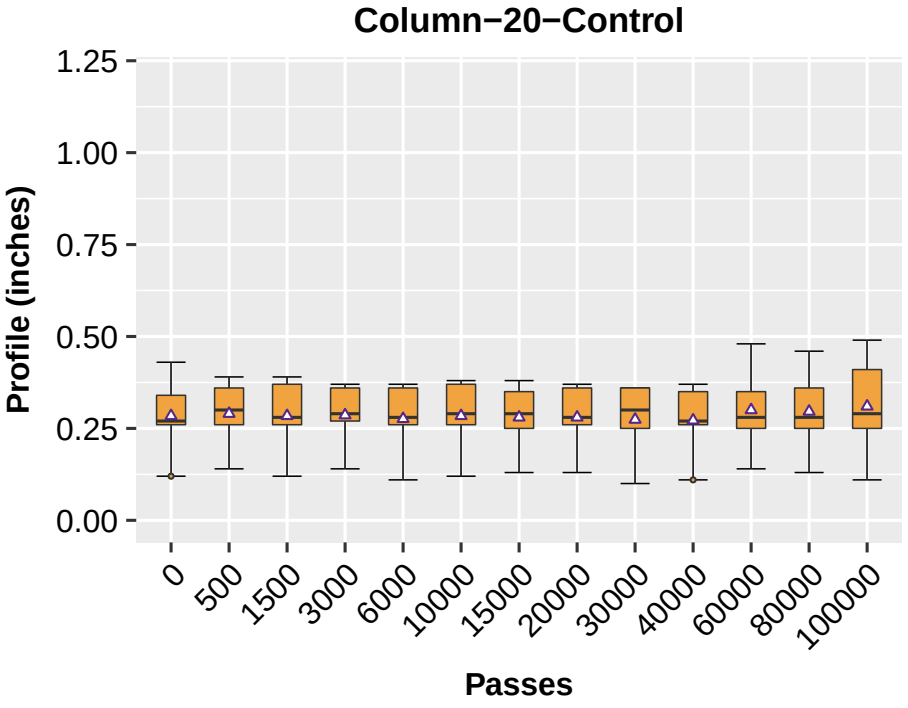

Figure 6.85: *Longitudinal Profiles for Control Lane (Column-20)*

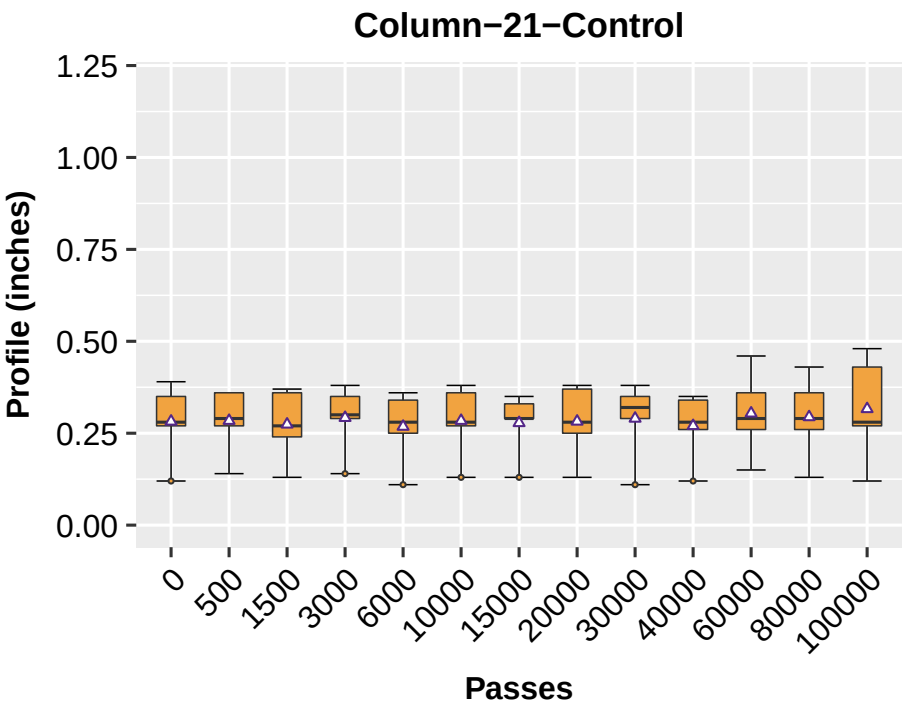

Figure 6.86: *Longitudinal Profiles for Control Lane (Column-21)*

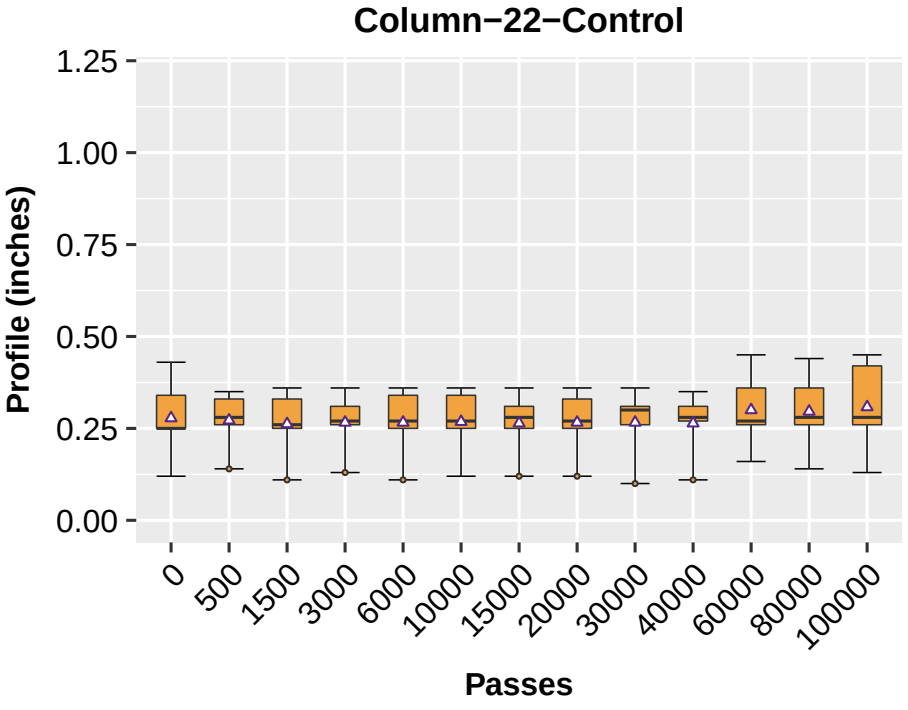

Figure 6.87: *Longitudinal Profiles for Control Lane (Column-22)*

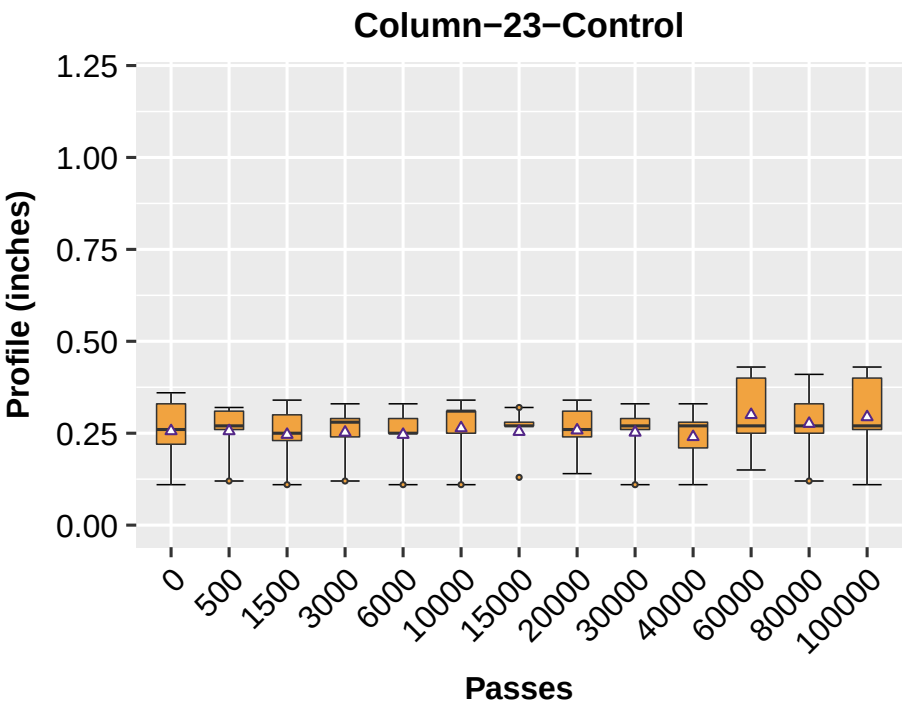

Figure 6.88: *Longitudinal Profiles for Control Lane (Column-23)*

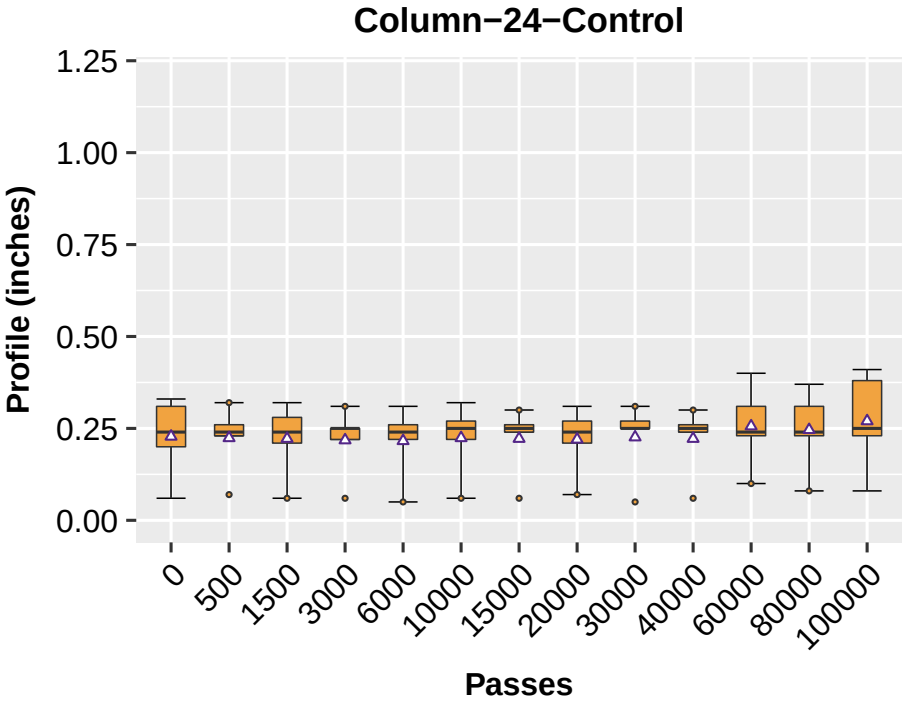

Figure 6.89: *Longitudinal Profiles for Control Lane (Column-24)*

6.2.4 Summary of rutting values in different lanes

Table 6.1: *Summary of rutting values at different lanes*

Lane	Max Rutting (inches)	Median Rutting (inches)
Control	0.82	0.69
Bottom	0.81	0.60
Middle	0.72	0.66

Since the lift thicknesses of the asphalt mixtures in different lanes significantly affect the rutting performance, using the maximum rutting as the performance criterion, which favors the thicker sections, is unreasonable. Hence, the median rutting was used as the criterion for comparing the rutting performance of different lanes. According to Table 6.1, compared with the control lane, the median rutting in the Lane B was reduced by 13%, and the median rutting in Lane M was reduced by 4%.

6.3 Core Testing

To verify the asphalt layer thickness of the test section, cores were taken at each end of the test section. As illustrated in Figure 6.90, a total of six cores were taken at each end of the test pit, namely, one at each end of each of the lanes. As indicated, overall, the thickness of the asphalt layer was quite uniform. The heights of cores drill at the west end of the lanes were close to 4 inches, while the cores at the east end were around 3.5 inches. It was noted that the core height at east end of the Lane M is less than 3 inches. To verify the thickness of this lane, another three cores were taken at the center of each lane (between rows 3 and 4, please see Figure 6.2), which revealed that the thickness at that location was around 4 inches (Figure 6.91). Hence, the overall asphalt layer thickness of all the three lanes was considered consistent.

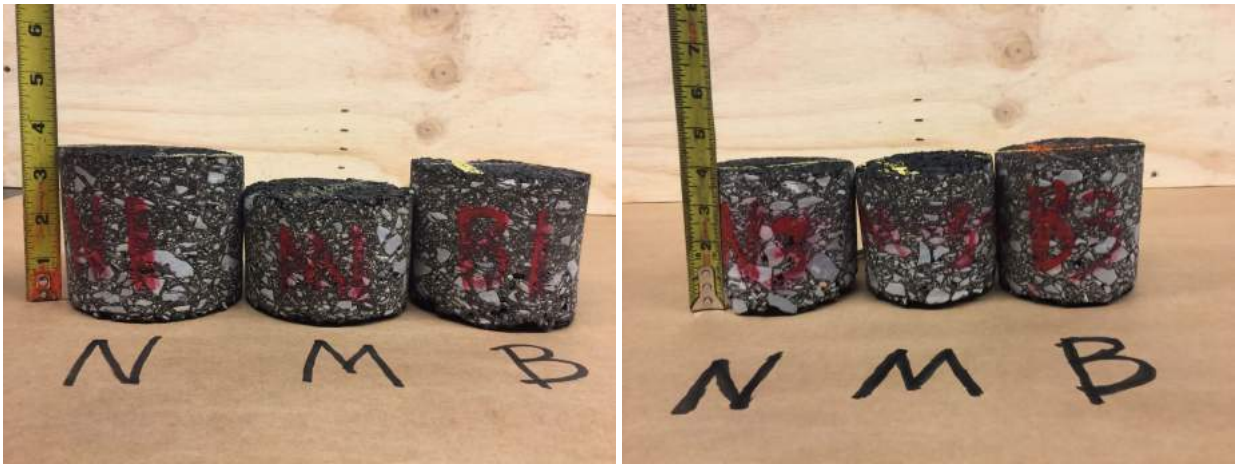

(a) *Cores Taken at East Side of Test Pit* **(b)** *Cores Taken at West Side of Test Pit*

Figure 6.90: *Visual Comparison of Cores Obtained at Each End of Test Pit*

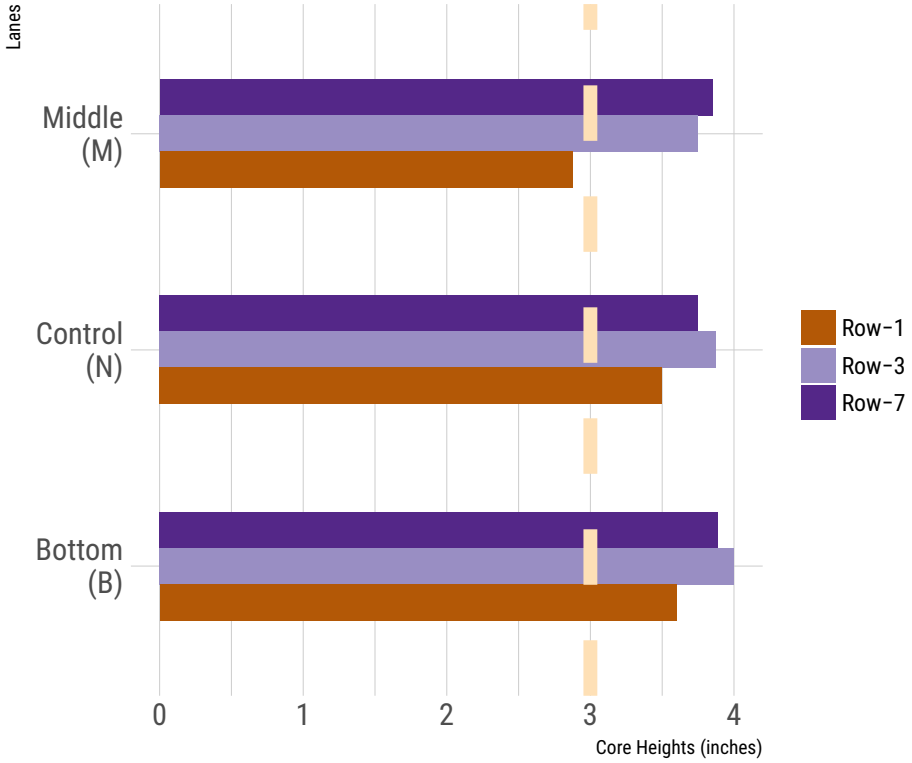

Figure 6.91: *Comparison of Core Heights at Different Locations*

6.4 Falling Weight Deflectometer Test

After trafficking all the lanes, a series of falling weight deflectometer (FWD) tests were conducted to evaluate the overall stiffness of the test sections. Figure 6.92 gives the deflections basins tested

at both the wheelpath and non-wheelpath areas of each of the lanes. Similar to the observations made in the previous two rounds of tests, the stiffness at the control lane was the largest, which could be attributed to the better compaction received at the control lane. A finite element analysis was further performed to explore the reason behind this phenomenon. A detailed explanation of this will be presented in the final report of this project.

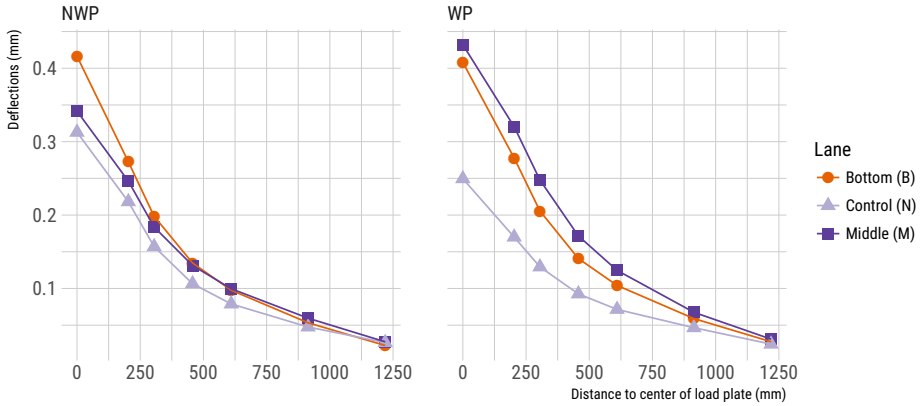

Figure 6.92: *FWD deflection basins at different lanes*

6.5 FEM Analyses

Considering the contradiction between the observed rutting performance of the test lanes and the results from the FWD testing, FEM analyses were conducted to investigated the reinforcement mechanism and address the disagreement.

6.5.1 FEM Model Configuration

The dimension of the used to simulate the each of the test lanes given as follows:

- Model Dimension: 6ft×6ft×6ft;
- Tire-Pavement Contact Pressure: 1.36 MPa (197 psi);
- Tire-Pavement Contact Shape and Dimension: 10 inches × 9.8 inches.
- Pavement Structure:
  - Asphalt Layer: 3 inches, Young's Modulus E = 1000 ksi, Poisson's Ratio $\nu = 0.3$;
  - Aggregate Base: 8 inches, Young's Modulus $E = 100$ ksi, Poisson's Ratio $\nu = 0.38$;
  - Subgrade Soil: Young's Modulus $E = 10$ ksi, Poisson's Ratio $\nu = 0.4$.

Figure 6.93b gives the mesh of the FEM model created. As indicated, a relatively denser mesh was used around the loading area, while a coarse mesh was used for regions far away from the loading area to increase the computation efficiency.

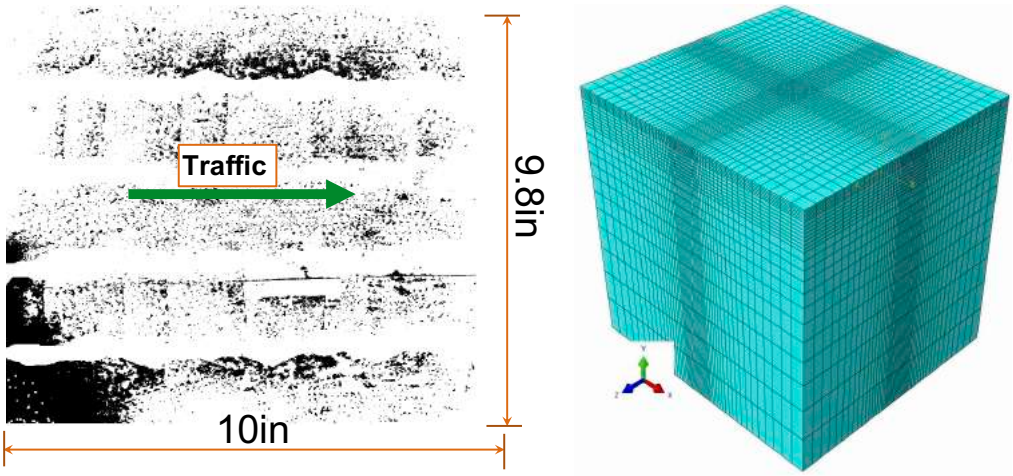

(a) *Tire-Pavement Contact Shape and Dimension* **(b)** *Meshing of FEM Model*

Figure 6.93: *FEM Model Configuration*

6.6 Forensic Trenching

After the failure of all the three lanes for the third round of APT testing, another round of forensic trench testing was conducted. Figure 6.94 illustrates the trenching process. A half of the test sections were removed, a flat surface was cut to measure to the profiles at each of the interfaces, including the interfaces at the top subgrade soil, in the middle of the aggregate base (Lane M), and at the top of the aggregate base. Figure 6.95 presents a overview of the trenched test pit. Figure 6.96 plots the measured the profiles at these interfaces along the cross section. As indicated by the deformation curve, the subgrade of the control lane that has no geogrids reinforcement seemed to be significant affected by the wheel load. However, the two lanes with geogrids were found only slighted impacted by the wheel loads.

(a) *Cutting Asphalt Layer*

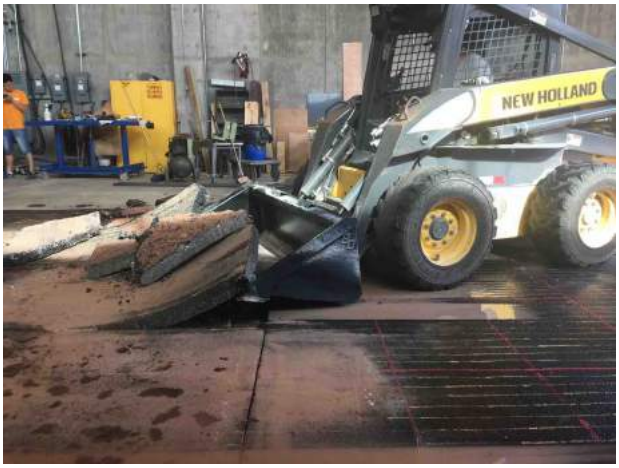

(b) *Removing Asphalt Layer*

(c) *Cleaning Asphalt Layer*

(d) *Removing Aggregate Base Layer*

Figure 6.94: *Removing Failed Pavement*

Figure 6.95: *Resulted Cross Section from Trenching*

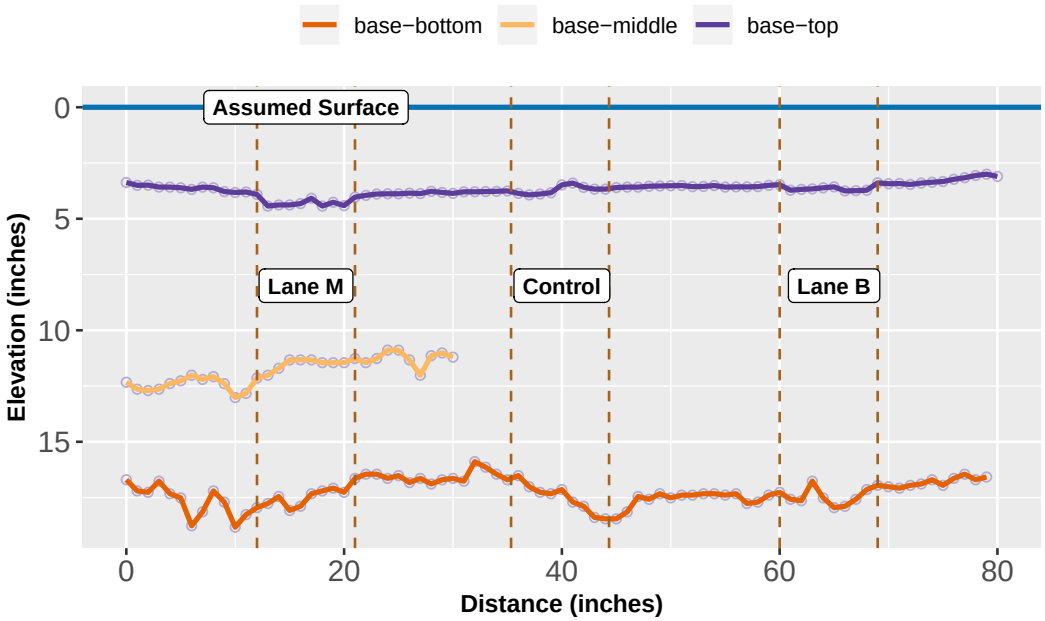

Figure 6.96: *Profile of Trenched Test Sections*

6.7 Summary

Table 6.2 gives a summary on the rutting performance of the lanes in the third round of APT testing. As indicated, the Lane B (geogrids in the middle of aggregate base) had the best overall rutting performance, followed by the Lane M (geogrids in the middle of aggregate base), and then the control lane. According to the results in Table 6.2, compared with the control lane, the maximum rutting depth in Lane B was reduced by 13%, and it was reduced by 4% in Lane M. Hence, the inclusion of geogrids reinforcement in the aggregate base is effective but it was not so as the performance achieved in the first two rounds of testing. Also, this implied that the stiffness the geogrids was critical to the overall rutting performance of the pavement. Additionally, the stiffness of back-calculated by the FWD may not be an effective approached to quantify the reinforcement performance of the geogrids, which seemed to significantly affected by the construction quality of the pavement, especially the compaction quality.

Table 6.2: *Rutting Performance of Different Lanes*

Lanes	Max Rutting Depth (Deformation Curve, inches)	Median Rutting Depth (Box-Plot, inches)
Control	0.82	0.69
Lane M	0.72	0.66
Lane B	0.81	0.60

Chapter 7 Cost Benefit Analysis

7.1 Introduction

Cost–benefit analysis (CBA), also called the benefit costs analysis (BCA), is a systematic method to estimate the strengths and weaknesses of alternatives (for example in materials, structures). It is often used to determine options or combinations of options that give the best approach to achieve benefits while preserving savings. In this study, the aim of CBA is to find the optimal combination(s) of materials and geosynthetics placements, and thus to achieve maximum benefit per unit cost. The benefit in this study was defined by the reduction in permanent deformation, and the cost benefit was given in Equation 7.1.

$$\text{Cost Benefit} = \frac{\text{Increase in Cost per Lane-Mile}}{\text{Increase in Service Life}} \tag{7.1}$$

7.2 Cost Benefit Analyses

Table 7.2 gives the unit prices of the products included in the study with the manufactures of products were omitted. The unit price of the triaxial geogrids was assumed to be twice that of the extruded biaxial geogrids. As indicated in Table 7.1, due to the higher price of the triaxial geogrids, the extra cost per lane mile of using this product was also the highest.

Table 7.1: *Cost Definition of Geogrids*

Products	Unit Price ($/Square Yard)	Extra Cost per Lane Mile ($)
Triaxial	3.5	1148
Biaxial Extruded	1.75	574
Biaxial Woven	0.8	262.4

Table 7.2 presents the overall benefits of using geosynthetics as reinforcement for the base materials. As indicated, due to the premature of the Lane B in the first round, the value for this entry was considered a missing value. Overall, considering the marginal benefit gained using the woven geogrids and the added cost, the unit cost per lane-mile per unit service life was thus the highest. Although, significant improvements in rutting resistance was achieved in using the

triaxial geogrids, the added cost had offset the benefits gained. Hence, regarding the overall benefits of using geosynthetics for base reinforcement, the extruded biaxial seemed to produce the best benefit per unit cost over the whole service lift period, followed by the triaxial geogrids, and then the woven biaxial geogrids.

Table 7.2: *Overall Benefits of Using Geosynthetics*

Products	Bottom unit cost ($) / (lane-mile/service life))	Middle unit cost ($) / (lane-mile/service life))
Triaxial	NA	4592
Biaxial Extruded	977	1922
Biaxial Woven	1756	25,978

7.3 Benefit-Reduction in Rut Depth

Table 7.3 lists the benefits of using geosynthetics according to the reduction in rut depth. Compared with the control section that had no geosynthetics reinforcement, the Lane with extruded geogrids installed at the bottom of the aggregate base achieved the highest rutting reduction per unit cost, followed by the lane with extruded geogrids placed in the middle of the base and the lane with triaxial placed in the middle of the base. Regarding the rutting reduction per unit cost, the Lane had woven geogrids placed in the middle of the base performed the worst, which was only slightly better than the control. For the lane with triaxial geogrids at the bottom of the base, if it had a similar asphalt layer thickness to the corresponding control section, its rutting reduction per unit cost would be close to or even better than that of the section with extruded biaxial in the middle of the base.

Table 7.3: *Rutting Reduction of Different Products at Varied Placements*

Products	Control	Bottom	Middle
Triaxial	100%	NA	80%
Biaxial Extruded	100%	63%	77%
Biaxial Woven	100%	87%	96%

7.4 Summary

According to the cost benefit analysis, the section with extruded biaxial geogrids installed at the bottom of the aggregate base attained the highest overall benefit per unit cost, followed by the lane with the same geogrids that had placed in the middle of the base layer, and the one with triaxial geogrids in the middle of the base layer. The section with woven biaxial geogrids at the bottom of the base layer achieved similar cost-benefit to the one with extruded biaxial geogrids in the middle of the base, while the one with woven biaxial geogrids in the middle of the base

performed only marginally better than the corresponding control section. If the section with triaxial geogrids installed at the bottom of the unbounded aggregate base had similar thickness to the corresponding control section, the cost-benefit of this section would then be close to or even lower than the one with extruded biaxial geogrids in the middle of the base, while it would be slightly higher than the one with extruded geogrids in the bottom of the base layer.

Chapter 8 Conclusions and Recommendations

8.1 Conclusions

This project investigated the reinforcement performance of different types of geosynthetics placed at two locations of the aggregate base through a series of well-controlled accelerated pavement testing. To attain the target of accelerating the tests in a relatively short time period, a weak soil with a CBR value of 3 (%) was used to construct the subgrade of the pavement. A full-scale accelerated pavement testing facility was utilized to carry out all the accelerated tests, which has the ability to apply a bidirectional load and a loading capacity higher than 9000 kips on each of the two wheels. A total of three rounds of tests were conducted to evaluate three different types of geosynthetics, which differed in their aperture shape, stiffness, and manufacturing mechanism. During the test of each round, the deformations at a certain interval of axle load passed were measured manually. The failure criterion of the testing was defined as reaching 1 inch of permanent deformation in the wheel path or reaching 100,000 axles, depending on whichever occurred first.

According to the tests and analyses in the study, the following conclusion were reached:

- The utilization of geosynthetics to reinforce an unbounded aggregate base that rested on a weak subgrade was very efficient, while the effectiveness of the geosynthetical materials depended significantly on their aperture shape, stiffness, and manufacturing mechanism.
- Overall, in terms of the rutting performance, the lanes with geogrids installed at the bottom of the aggregate base performed the best, followed by the one with geogrids placed at the bottom of the aggregate base, and then the control that had no reinforcement in the base.
- Compared with the control lane, the permanent deformation of the lane with extruded biaxial geogrids placed in the middle of the aggregate base was reduced by 24%, and it was reduced by 37% for the lane had geogrids installed at the bottom of the base layer.
- Compared with the control lane, the rutting at the lane with woven biaxial geogrids installed at the bottom of the aggregate base was reduced by 13%, and it was reduced by 4% for the one with geogrids placed in the middle of the base layer.
- The cost benefit analysis revealed that geogrids placed at the bottom of the aggregate base generated the highest overall benefit per unit cost. Compared with the control that had no reinforcement, the extruded biaxial geogrids placed at the bottom of the base produced the highest overall benefit per unit cost and the highest rutting reduction per unit cost, followed by the triaxial geogrids placed at the same location if it had a similar thickness

to its corresponding control section. The woven biaxial geogrids installed at the bottom of the base generated similar cost-benefit to the triaxial geogrids placed at the middle of the base. The woven biaxial geogrids that were placed in the middle of the base achieved only marginally higher benefit per unit cost than the corresponding control.

- The construction quality is extremely critical to the success of the APT testing. During the construction process, great caution should be used in controlling the thickness of each of the layers, especially the thickness of the asphalt layer.

8.2 Recommendations

Given the limited time for the project, it is impossible to include more combination of materials, such as different types of asphalt mixtures, varied gradation of aggregate base materials, and soils of varied properties. It is thus recommended in the future to include more materials combinations in the study, and thus to present a more comprehensive picture on the performance of geosynthetics as a reinforcement for the unbound granular base. Due to the limited space in the laboratory, attention should be taken in controlling the thickness of each layer of the pavement, so as to keep the thickness of the pavement layers as accurate as possible.

Bibliography

Imad Al-Qadi, Samer Dessouky, Jayhyun Kwon, and Erol Tutumluer. Geogrid in flexible pavements: validated mechanism. *Transportation Research Record: Journal of the Transportation Research Board*, (2045):102–109, 2008.

Imad L Al-Qadi, Thomas L Brandon, Richard J Valentine, Bruce A Lacina, and Timothy E Smith. Laboratory evaluation of geosynthetic-reinforced pavement sections. *Transportation Research Record*, (1439), 1994.

Imad L Al-Qadi, Samer Dessouky, Erol Tutumluer, and Jayhyun Kwon. Geogrid mechanism in low-volume flexible pavements: accelerated testing of full-scale heavily instrumented pavement sections. *International Journal of Pavement Engineering*, 12(02):121–135, 2011.

DA Beranek. Use of geogrids in pavement construction. department of the army. *US Army Corps of Engineers, Washington DC, Technical Letter No. ETL*, pages 1110–1, 2003.

EV Cuelho and SW Perkins. Resilient interface shear modulus from short-strip, cyclic pullout tests. In *Slopes and Retaining Structures Under Seismic and Static Conditions*, pages 1–11. 2005.

Peter A Cundall and Otto DL Strack. A discrete numerical model for granular assemblies. *geotechnique*, 29(1):47–65, 1979.

Ahmet Demir, Mustafa Laman, Abdulazim Yildiz, and Murat Ornek. Large scale field tests on geogrid-reinforced granular fill underlain by clay soil. *Geotextiles and Geomembranes*, 38:1–15, 2013.

RJ Fannin and DM Raju. On the pullout resistance of geosynthetics. *Canadian geotechnical journal*, 30(3):409–417, 1993.

RJ Fannin and Of Sigurdsson. Field observations on stabilization of unpaved roads with geosynthetics. *Journal of Geotechnical Engineering*, 122(7):544–553, 1996.

Jean-Pierre Giroud and Laure Noiray. Geotextile-reinforced unpaved road design. *Journal of Geotechnical and Geoenvironmental Engineering*, 107(ASCE 16489), 1981.

JP Giroud and Jie Han. Design method for geogrid-reinforced unpaved roads. ii. calibration and applications. *Journal of Geotechnical and Geoenvironmental Engineering*, 130(8):787–797, 2004.

J Han, Y Zhang, and RL Parsons. Quantifying the influence of geosynthetics on performance of reinforced granular bases in laboratory. *Geotechnical Engineering*, 42(1):75, 2011.

Hayssam Itani, George Saad, and Ghassan Chehab. The use of geogrid reinforcement for enhancing the performance of concrete overlays: An experimental and numerical assessment. *Construction and Building Materials*, 124:826–837, October 2016.

G Kennepohl, N Kamel, J Walls, and RCG Haas. Geogrid reinforcement of flexible pavements design basis and field trials (with discussion and closure). In *Association of Asphalt Paving Technologists Proc*, volume 54, 1985.

Thomas Kinney, Danielle Stone, and John Schuler. Using Geogrids for Base Reinforcement as Measured by Falling Weight Deflectometer in Full-Scale Laboratory Study. 1611:70–77, January 1998.

Robert M Koerner. *Designing with geosynthetics*, volume 1. Xlibris Corporation, 2012.

J Kwon, M Kim, and E Tutumluer. Interface modeling for mechanistic analysis of geogrid reinforced flexible pavements. In *Advances in pavement engineering*, pages 1–15. 2005.

Jayhyun Kwon and Erol Tutumluer. Geogrid base reinforcement with aggregate interlock and modeling of associated stiffness enhancement in mechanistic pavement analysis. *Transportation Research Record: Journal of the Transportation Research Board*, (2116):85–95, 2009.

Jayhyun Kwon, Erol Tutumluer, and H Konietzky. Aggregate base residual stresses affecting geogrid reinforced flexible pavement response. *International Journal of Pavement Engineering*, 9(4):275–285, 2008.

Jayhyun Kwon, Erol Tutumluer, and Imad L Al-Qadi. Validated mechanistic model for geogrid base reinforced flexible pavements. *Journal of Transportation Engineering*, 135(12):915–926, 2009.

Jianjun Leng and Mohammed Gabr. Characteristics of geogrid-reinforced aggregate under cyclic load. *Transportation Research Record: Journal of the Transportation Research Board*, (1786):29–35, 2002.

Wenting Liu and Tom Scullion. MODULUS 6.0 for windows: User's manual. Technical report, Texas Transportation Institute, Texas A & M University System, 2001.

GR McDowell, O Harireche, H Konietzky, SF Brown, and NH Thom. Discrete element modelling of geogrid-reinforced aggregates. *Proceedings of the Institution of Civil Engineers-Geotechnical Engineering*, 159(1):35–48, 2006.

Nicola Moraci and Giuseppe Cardile. Deformative behaviour of different geogrids embedded in a granular soil under monotonic and cyclic pullout loads. *Geotextiles and Geomembranes*, 32: 104–110, 2012.

Antonio A Munjiza. *The combined finite-discrete element method*. John Wiley & Sons, 2004.

Angelica Maria Palomino, Xiaochao Tang, Shelley Marie Stoffels, et al. Determination of structural benefits of penndot approved geogrids in pavement design. Final report, Pennsylvania Transportation Institute, 2010.

Steven W Perkins. Evaluation of geosynthetic reinforced flexible pavement systems using two pavement test facilities. Technical report, Montana Department of Transportation, 2002.

Steven W Perkins and Michael Q Edens. Finite element and distress models for geosynthetic-reinforced pavements. *International Journal of Pavement Engineering*, 3(4):239–250, 2002.

Steven W Perkins and M Ismeik. A synthesis and evaluation of geosynthetic-reinforced base layers in flexible pavements-part i. *Geosynthetics International*, 4(6):549–604, 1997a.

SW Perkins and MQ Edens. A design model for geosynthetic-reinforced pavements. *International Journal of Pavement Engineering*, 4(1):37–50, 2003.

SW Perkins and M Ismeik. A synthesis and evaluation of geosynthetic-reinforced base layers in flexible pavements-part ii. *Geosynthetics International*, 4(6):605–621, 1997b.

SW Perkins, BR Christopher, Eli L Cuelho, GR Eiksund, CS Schwartz, and G Svanø. A mechanistic–empirical model for base-reinforced flexible pavements. *International Journal of Pavement Engineering*, 10(2):101–114, 2009.

DM Raju and RJ Fannin. Load-strain-displacement response of geosynthetics in monotonic and cyclic pullout. *Canadian Geotechnical Journal*, 35(2):183–193, 1998.

Xiaochao Tang, Ghassan R Chehab, and Angelica Palomino. Evaluation of geogrids for stabilising weak pavement subgrade. *International Journal of Pavement Engineering*, 9(6):413–429, 2008.

Jacob Uzan. Characterization of granular material. *Transportation research record*, 1022(1):52–59, 1985.

Steve L Webster. Geogrid reinforced base courses for flexible pavements for light aircraft: Test section construction, behavior under traffic, laboratory tests, and design criteria. Technical report, DTIC Document, 1993.

Hao Wu, Baoshan Huang, Xiang Shu, and Sheng Zhao. Evaluation of geogrid reinforcement effects on unbound granular pavement base courses using loaded wheel tester. *Geotextiles and Geomembranes*, 43(5):462–469, 2015.

Bing Xu, S Ranji Ranjithan, and Y Richard Kim. New relationships between falling weight deflectometer deflections and asphalt pavement layer condition indicators. *Transportation Research Record: Journal of the Transportation Research Board*, (1806):48–56, 2002.

Yuze Zhang. *Investigation of geosynthetic-soil confinement using asphalt pavement analyzer*. PhD thesis, University of Kansas, 2007.